NNT/NL : 0000AIXM0000/000ED000

THÈSE DE DOCTORAT

Soutenue à Aix-Marseille Université
le 04 Avril 2023 par

Sandra GYASI

Contribution to the Thermodynamics of Key Zirconium-Based Binary Systems for Severe Nuclear Accident Assessment

Discipline

Physique et Sciences de la Matière

Spécialité

Matière Condensée et Nanosciences

École doctorale

ED 352- Physique et Sciences de la Matière

Laboratoire/Partenaires de recherche

LETR - Laboratoire d'Etude des Transferts de radioéléments
SYMME - SYstèmes et Matériaux pour la MÉcatronique
IM2NP - Institut Matériaux Microélectronique Nanosciences de Provence

Composition du jury

Mme. Christine GUENEAU Commissariat à l'Energie Atomique et aux Energies Alternatives	Rapporteur
M. Alexander PISCH Université Grenoble Alpes	Rapporteur
M. Olivier TOUGAIT Université Lille 1	Président du jury
Mme. Caroline ANTION Université Savoie Mont Blanc	Examinatrice
M. Jérôme ANDRIEUX Université Lyon 1	Examinateur
M. Marc LOMELLO Université Savoie Mont Blanc	Examinateur
M. Jean-Marc JOUBERT Université Paris-Est Créteil	Examinateur
M. Pierre BENIGNI Aix Marseille Université	Directeur de thèse
M. Marc BARRACHIN Institut de Radioprotection et de Sûreté Nucléaire	Encadrant et Invité

Affidavit

I, undersigned, Sandra GYASI, hereby declare that the work presented in this manuscript is my own work, carried out under the scientific direction of Pierre BENIGNI, in accordance with the principles of honesty, integrity and responsibility inherent to the research mission. The research work and the writing of this manuscript have been carried out in compliance with both the French national charter for Research Integrity and the Aix-Marseille University charter on the fight against plagiarism.

This work has not been submitted previously either in this country or in another country in the same or in a similar version to any other examination body.

Place Annecy, date 25 janvier 2023

List of publication and participation in conferences

1) Liste des publications réalisées dans le cadre du projet de thèse :
    1. Gyasi S., Benigni P., Rogez J., Barrachin M., About the enthalpy of formation of the UZr_2 compound. *Journal of Nuclear Materials* 562 (2022): 153580. https://doi.org/10.1016/j.jnucmat.2022.153580.

2) Participation aux conférences et écoles d'été au cours de la période de thèse :
    1. Journées annuelles du GDR - Thermodynamique des Matériaux à Haute Température (TherMatHT) – présentation orale
    2. Ecole sur la diffusion dans les solides
    3. Journées des thèses (IRSN- SAM/SEREX) - présentation orale
    4. Colloque NEEDS -Recherche amont pour les réacteurs et les cycles de combustible - présentation orale
    5. NUMAT2022- The Nuclear Material Conference – presentation poster

Résumé

Cette thèse porte sur l'étude expérimentale des systèmes binaires à base de zirconium pour l'étude des accidents graves dans les réacteurs à eau pressurisée. Des mélanges de différentes compositions Ag-Zr-In-O, Fe-Cr-Ni-Zr-O et Fe-O-U-Zr sont susceptibles de se former lors d'un accident. La thermodynamique de ces systèmes joue un rôle clé dans la compréhension et la simulation de la progression de la dégradation du cœur et des rejets de produits de fission. Ce travail apporte une contribution expérimentale à certains systèmes binaires importants de ces diagrammes de phase complexes, In-Zr qui était inconnu jusqu'à présent et Ag-Zr, Fe-Zr et U-Zr pour lesquels peu de données sont disponibles, les données existantes étant même parfois controversées. Le système binaire In-Zr est difficile à étudier expérimentalement en raison à la fois du point de fusion élevé du zirconium et de sa grande réactivité, notamment à l'état liquide. Des alliages In-Zr de différentes compositions à différentes températures de recuit ont été analysés par microscopie électronique à balayage (MEB) et par diffraction des rayons X (DRX) pour identifier les phases et mesurer leurs compositions. Les températures de décomposition des composés existants dans le système In-Zr ont été déterminées pour la première fois par analyse thermique différentielle (ATD). La solubilité du zirconium dans l'indium liquide a également été révisée. Les enthalpies standard de formation de In_3Zr et In_2Zr ont été mesurées ainsi que celles de UZr_2, Fe_2Zr et AgZr par calorimétrie de dissolution dans l'aluminium liquide à haute température. Ces nouvelles données thermodynamiques seront introduites dans la base de données NUCLEA actuellement développée à l'IRSN et utilisée pour la modélisation des accidents graves.

Mots clés : Accident grave, Système binaire au zirconium, Thermodynamique, Expériences, Diagramme de phase

Abstract

This thesis was focused on the experimental investigation of key zirconium-based binary system for the study of severe accidents in pressurized water reactors. Melts of different Ag-Zr-In-O, Fe-Cr-Ni-Zr-O and Fe-O-U-Zr compositions form during an accident. Thermodynamics of these systems plays a key role in the understanding and the simulation of the progression of the degradation in the core and the fission product releases. This work brings forth an experimental contribution to some important binary systems of these complex phase diagrams, In-Zr which was unknown and Ag-Zr, Fe-Zr and U-Zr for which few data are available, the existing data being sometimes controversial. The binary In-Zr system was difficult to study experimentally because of both the high melting point of zirconium and its high reactivity, particularly at the liquid state. In-Zr alloys of different compositions at different annealed temperatures were analyzed by scanning electron microscopy (SEM) and X-ray diffraction (XRD) to identify the phases and measure their compositions. The decomposition temperatures of the existing compounds in the In-Zr system have been determined for the first time by differential thermal analysis (DTA). The solubility of zirconium in liquid indium has been also revised. The standard enthalpy of formation of In_3Zr and In_2Zr have been measured as well as those of UZr_2, Fe_2Zr and AgZr by dissolution calorimetry in liquid aluminium at high temperature. These new thermodynamic data will be introduced in the NUCLEA database currently developed at IRSN which is used for severe accident modelling.

Keywords: Severe accident, Zirconium binary system, Thermodynamics, Experiments, Phase diagram

Résumé

Le principal risque associé à l'exploitation des réacteurs nucléaires de puissance, qui utilisent la fission nucléaire, concerne la dispersion de substances radioactives et l'exposition potentielle de l'homme et de l'environnement à ces substances. Afin de réduire ces risques, la plus grande responsabilité de l'industrie nucléaire est d'exploiter les centrales nucléaires dans des conditions de sûreté [1]. Malgré toutes les mesures prises pour réduire la probabilité de survenance d'un accident nucléaire, trois accidents nucléaires majeurs ont eu lieu au cours des dernières décennies : Three Mile Island (TMI) aux Etats Unis, Tchernobyl en ex-Union Soviétique et Fukushima Daiichi au Japon. Ces accidents, qui ont entraîné la fusion partielle ou complète du cœur du réacteur et les relâchements de produits de fission très importants pour les deux accidents les plus récents, ont attiré l'attention sur la nécessité de prendre en compte la survenance d'un accident grave et ses conséquences au stade de la conception du réacteur.

D'un point de vue général, lorsqu'un accident grave se produit dans un réacteur dont l'eau est le caloporteur (réacteur à eau sous pression REP ou réacteur à eau bouillante REB), la puissance résiduelle produite pendant l'exploitation ne peut plus être évacuée par cette eau, ce qui implique que le cœur n'est plus refroidi. Le cœur est alors exposé à une température élevée et à l'oxydation de la vapeur, conduisant à une montée très rapide des températures et à une dégradation progressive du cœur pouvant évoluer vers la fusion complète de celui-ci comme cela s'est produit dans l'Unité 1 de Fukushima Daichi. Dans cette situation, les éléments du cœur, comprenant les crayons absorbants et les barres de combustible ainsi que les structures internes en acier inoxydable, se relocalisent vers les parties inférieures du cœur où ils se mélangent pour former un bain liquide appelée *corium*. Dans le même temps, les produits de fission libérés par le combustible sont transportés par le circuit primaire jusqu'à l'enceinte de confinement et pour une partie, sont relâchés dans l'environnement.

À la lumière des accidents majeurs qui ont eu lieu par le passé, les principaux axes de recherche actuels pour une amélioration de la sûreté ont trait à la réduction des rejets de produits de fission à l'extérieur de la centrale nucléaire en cas d'accident et au maintien du corium à l'intérieur de la cuve ou, si cela n'est pas possible, la mise en place d'un système à l'extérieur de la cuve capable de refroidir le cœur à long terme.

Plus précisément, cette recherche s'inscrit dans le cadre général des deux thèmes importants pour la compréhension et la mitigation des accidents graves dans les réacteurs nucléaires.

- La première est liée à la détermination du terme source (le terme source désigne la quantité et la forme chimique des radionucléides qui sont relâchés dans l'environnement en conditions accidentelles) dans des conditions d'accident et plus particulièrement à l'évaluation des produits de fission, tels que l'iode, ayant des conséquences radiologiques importantes à court et moyen terme. Au début d'un accident grave dans un réacteur à eau sous pression, on s'attend à ce que le crayon de contrôle Ag-Cd-In interagisse avec le tube guide en zircaloy à haute température en raison de la rupture de du gainage du crayon absorbant en acier inoxydable, entrainant de facto la formation de mélanges de compositions complexes Ag-In-Zr-O et Fe-Zr-Cr-Ni-O et la vaporisation

partielle de l'argent et du cadmium dont on sait qu'ils ont un impact important sur la spéciation et le transport de l'iode dans le circuit primaire du réacteur. Pour aborder la question des interactions entre les barres de contrôle et le Zircaloy et son impact sur les rejets d'indium et d'argent, une connaissance précise des sous-systèmes binaires et ternaires du diagramme de phase quaternaire Ag-In-Zr-O ainsi que ceux du quinaire Fe-Zr-Cr-Ni-O est nécessaire.

- La seconde est liée à l'interaction du corium avec la partie inférieure de la cuve. Dans la phase tardive de l'accident, lorsque le corium s'est massivement relocalisé vers le plénum inférieur de la cuve, une question importante est de pouvoir calculer le flux thermique imposé par le corium sur la cuve afin de déterminer le moment et le lieu de la rupture de la cuve et les conditions initiales de l'interaction corium-béton. La thermodynamique du système multiphase complexe (U-O-Zr-Fe) du corium joue un rôle clé dans ce calcul.

Cette recherche a débuté entre l'IRSN, l'IM2NP (Université de Marseille), le SYMME (Université Savoie-Mont-Blanc) et le SIMAP (Université de Grenoble) en 2013. Dans ce cadre, d'importants travaux ont été réalisés lors des deux précédentes thèses [2, 3] pour répondre à la première problématique. Ces deux études ont porté sur la détermination expérimentale du système Ag-Cd-In à haute température. Les déterminations du liquidus [3] obtenues par une approche originale (Interrupted Heating Differential Technique Analysis permettant de mieux approcher les conditions d'équilibre) combinées aux données existantes de la littérature et aux mesures d'enthalpie de mélange de la phase liquide réalisées précédemment obtenues par Bénigni et al. [4] ont permis de proposer pour la première fois une modélisation Calphad du système ternaire Ag-Cd-In [5].

L'objectif de cette thèse est d'apporter une contribution expérimentale à la thermodynamique des systèmes binaires clés à base de zirconium, In-Zr, Ag-Zr, Fe-Zr et U-Zr permettant d'avoir une description plus complète et plus précise de la thermodynamique des systèmes Ag-Cd-In-Zr-O, Fe-Zr-Cr-Ni-O et U-O-Zr-Fe.

Système In-Zr

Pour le système In-Zr, système pratiquement inconnu au début de notre étude, une grande partie du travail de Gajavalli [3] avait été consacrée à l'élaboration des échantillons, élaboration qui avait été identifiée au début de ce travail comme un problème important en raison des difficultés suivantes :

- ✓ la différence de point de fusion entre les deux éléments In et Zr,
- ✓ leur relative immiscibilité avérée à l'état liquide,
- ✓ la pression partielle significative de l'indium au point de fusion du zirconium,
- ✓ l'affinité des deux éléments avec l'oxygène.

L'existence de divers composés intermétalliques In_3Zr, In_2Zr, InZr, $InZr_2$, et $InZr_3$ était établie. S'ils avaient été caractérisés d'un point de vue structural, les données thermodynamiques expérimentales faisaient défaut puisque seules deux mesures de l'enthalpie standard de formation de In_2Zr par Gajavalli [3] et Meschel et Kleppa [6] étaient disponibles dans la littérature. Il y avait également peu d'informations sur les transformations invariantes tant du côté riche en Zr que du côté riche en In du système.

Le travail présenté dans cette thèse vise à contribuer, par l'expérience, à une description plus complète de ce système. Cet objectif a été atteint en utilisant de nombreuses techniques expérimentales, à savoir la mise à l'équilibre de différents alliages In-Zr de différentes compositions à température constante suivie d'analyses métallographiques (MEB, microsonde), d'analyses par diffraction des rayons X (DRX) et d'analyses thermiques différentielle (ATD). Ce travail a été complété par des mesures calorimétriques de type dissolution en bain d'aluminium liquide à haute température.

Nous avions anticipé des résultats plus nombreux au début de ce travail, mais nous avons rencontré de nombreuses difficultés dans la préparation des échantillons, ce qui était quelque peu attendu compte-tenu des tentatives de synthèse infructueuses précédentes des travaux antérieurs. Malgré ces difficultés, une méthode d'élaboration à partir de la métallurgie des poudres a finalement été développée, ce qui nous a permis d'obtenir de nouveaux résultats très importants pour une première modélisation du système In-Zr, résultats qui sont décrits et discutés dans ce travail. Les principaux résultats obtenus sur le système In-Zr sont résumés ci-après :

- L'existence des composés intermétalliques (In_3Zr, In_2Zr, InZr, $InZr_2$ et $InZr_3$) précédemment rapportés par Schubert et al. [7-9] a été confirmée. Une phase additionnelle de composition In_3Zr_2 a été identifiée par analyse MEB des alliages 20-40 at.%Zr. L'existence de cette phase (possiblement de structure tP10) est également prédite par les calculs de stabilité effectués par approche ab-initio de type DFT [10]. A ce jour, nous n'avons pas pu la confirmer par DRX.

- Les températures et la nature des transition des différentes composés intermétalliques ont été déterminées. Nous avons mis en évidence :
  - ✓ la réaction péritectique (In) $\leftrightarrow$ αIn_3 Zr + liquide à basse température (156.8 ± 0.3 °C) par la technique bi-différentielle, contrairement à la réaction eutectique anciennement proposée dans l'évaluation d'Okamoto [11].
  - ✓ la décomposition péritectique de $In_3Zr \leftrightarrow In_2Zr + L$ à 591.6 ± 2.4 °C, inférieure à la valeur de 660 °C reportée précédemment par G. Collins [12].
  - ✓ la décomposition péritectique de $In_2Zr \leftrightarrow In_3Zr_2 + L$ à 1132.9 ± 1.8 °C. La décomposition péritectique de In_2Zr identifiée dans ce travail n'est pas conforme à l'hypothèse de fusion congruente à 1370°C proposée dans la modélisation très préliminaire du système In-Zr de la base de données NUCLEA développée à l'IRSN [13].
  - ✓ la décomposition péritectique $In_3Zr_2 \leftrightarrow InZr + L$ à 1279 ± 6 °C.

  En raison de problèmes d'élaboration pour les échantillons (de compositions comprises entre 40 < at% Zr < 75) très sensibles à l'oxygène, la partie centrale du diagramme de phase reste aujourd'hui largement incertaine et devrait être l'objectif principal des futures investigations pour le système In-Zr.

Enfin, Collins [12] avait indiqué que la température de transition à l'état solide entre α-In_3Zr et β-In_3Zr était située autour de 270 ± 50°C mais il a été impossible dans ce travail d'identifier cette transition par ATD, notamment car impliquant deux phases α-$In_3Zr(D0_{23})$ et β-$In_3Zr(D0_{22})$ dont les énergies (calculs DFT) sont très proches, rendant de facto très difficile la détection de cette transition de phase quasi-athermique par ATD.

- Une analyse de type Tamman des signaux ATD appliquée aux plateaux péritectiques à 592°C et à 1133°C a permis de déterminer les solubilités de zirconium dans l'indium liquide. Les solubilités sont de 1.0 ± 0.1 at.% et ~ 3.7 ± 1.7 at.% respectivement. Ces valeurs limites de solubilité du zirconium sont plus élevées que les limites de solubilité, 0.02 at.% Zr et 0.5 at.% Zr, qui pouvaient être calculées aux mêmes températures à partir de la corrélation de Dieva [14].

- Dans la partie riche en Zr, même si la réaction péritectoïde rapportée par Betterton et Noyce [15] a été retenue dans la version finale de notre diagramme de phase, de manière surprenante, des microstructures présentant des structures lamellaires, suggérant donc une réaction eutectoïde $\beta Zr \leftrightarrow InZr_3 + \alpha Zr$, ont été observées lors de l'analyse de diverses compositions dans la gamme 74-82 at.%Zr après ATD. Cependant, à ces compositions, les analyses DTA elles-mêmes n'étant pas assez concluantes pour démontrer le caractère eutectoïde de cette réaction, les conclusions de Betterton et Noyce [15] ont été conservées pour cette partie riche en Zr du diagramme de phase, qui reposent sur un grand nombre d'échantillons. De futures études pourraient être conduites dans cette gamme de composition afin de mieux interpréter ces observations contradictoires.

- Les enthalpies standard de formation des composés In_3Zr et In_2Zr ont été déterminées par calorimétrie de dissolution en bain liquide d'aluminium (respectivement 39.7 ± 2.9 $kJ.mol^{-1}.at^{-1}$ et -38.2 ± 3.3 $kJ.mol^{-1}.at^{-1}$). L'enthalpie standard de formation de In_2Zr a été également déterminée par réaction directe dans ce travail et un accord a été obtenu entre les valeurs obtenues par les deux techniques. Elles sont également en accord avec la valeur antérieure obtenue par Meschel et al. [16] pour In_2Zr. Il faut souligner que les valeurs pour In_2Zr et In_3Zr sont néanmoins significativement plus exothermiques que les valeurs calculées obtenues en DFT. Une tendance analogue est observée dans le système "similaire" Ga-Zr [10] et fera probablement l'objet d'un débat en termes de validation des approches théoriques pour ce type de systèmes chimiques.

- Ces nouveaux résultats (diagramme de phase et données thermodynamiques, combinés aux données de la littérature) seront utilisés pour établir une première description CALPHAD précise du système, modélisation qui sera intégrée à la base de données NUCLEA.

Système Ag-Zr

Pour le système Ag-Zr, les limites des domaines de phase, en particulier le liquidus, avaient été déterminées par Decreton [2] et ce, sur toute la gamme de composition. L'un des principaux résultats avait été l'identification de la nature (jusqu'à présent controversée) des décompositions des deux composés du système, AgZr et $AgZr_2$. Ils se décomposent de manière congruente et péritectique respectivement, en désaccord avec certaines évaluations récentes du système Ag-Zr [17, 18]. Dans notre travail, l'enthalpie standard de formation de AgZr a été déterminée, en utilisant la technique de calorimétrie de dissolution à haute température dans l'aluminium liquide. L'enthalpie de formation du composé équiatomique AgZr mesurée est en bon accord avec la valeur obtenue par Decreton [2] qui a utilisé un bain d'acide comme solvant. Notre valeur (-21.8 ± 5.7 $kJ.mol^{-1}$ $.at^{-1}$) est en revanche beaucoup plus exothermique que la valeur précédemment obtenue par réaction directe [19], communément acceptée dans les évaluations Calphad du système Ag-Zr publiées même récemment. Dans la limite de l'erreur expérimentale, notre valeur est néanmoins cohérente avec le modèle le plus récent du système Ag-Zr réalisé par le laboratoire SIMAP à Grenoble [20] dans le cadre du développement de la base NUCLEA et intégrant l'étude du diagramme de phase de Decreton [2] et les décompositions congruente et péritectique respectives de AgZr et $AgZr_2$. Pour ce système, les travaux futurs devraient être consacrés aux mesures de l'enthalpie de formation de $AgZr_2$ par calorimétrie de dissolution.

Système Fe-Zr

Dans le système Fe-Zr, notre travail a porté sur la détermination des propriétés thermodynamiques du composé intermétallique Fe_2Zr, et plus précisément sur la mesure de son enthalpie standard de formation. Cette grandeur a été déterminée, comme pour les autres composés considérés dans cette étude, en utilisant la technique de calorimétrie de dissolution en bain d'aluminium liquide à haute température. L'enthalpie standard expérimentale de formation du Fe_2Zr déterminée dans ce travail est en accord avec les valeurs expérimentales [21-23] déjà disponibles. La valeur obtenue (-32.2 ± 3.3 $kJ.mol^{-1}.at^{-1}$) est en accord avec les valeurs calculées par DFT et celles retenues dans les modélisations Calphad disponibles pour ce système. Malgré l'importance de ce système, il n'existe pas, à notre connaissance, de données thermodynamiques expérimentales pour les autres composés de ce système. Cette première étude en calorimétrie de dissolution pourrait donc être étendue à ces derniers.

Système U-Zr

Malgré de nombreuses études sur le système U-Zr, il existe quelques controverses sur les données disponibles du système. Parmi ces données, les propriétés thermodynamiques liées aux phases du système U-Zr, notamment l'enthalpie standard de formation de δ-UZr_2 (seule phase intermétallique du système) ont fait l'objet d'un débat intense entre différentes équipes théoriques dans le cadre de la validation des approches ab initio. La solution solide δ est une phase clé pour la description du système U-Zr. Pour UZr_2, il existait une valeur standard d'enthalpie de formation déterminée par calorimétrie de dissolution dans l'aluminium liquide par Nagarajan et al. [24] à partir de laquelle de nombreuses évaluations Calphad du système U-

Zr ont été construites. Elle a également été le support d'intenses échanges entre équipes théoriques sur la méthodologie DFT (GGA ou GGA+U) à appliquer pour calculer l'enthalpie de formation de cette phase à 0 K. Une réinterprétation complète de cette valeur a été conduite dans ce document. Notre réinterprétation montre que cette détermination résulte d'une combinaison de différentes valeurs erronées ou imprécises. Cela nous a conduit à mesurer à nouveau l'enthalpie de dissolution de l'UZr_2 dans l'aluminium liquide qui, combinée à celles de l'uranium et du zirconium, donne une valeur plus exothermique (-11.9 ± 6.7 $kJ.mol^{-1}.at^{-1}$). A ce stade, cette valeur doit être confirmée par un examen MEB des lingots solidifiés pour s'assurer de la complétude du processus de dissolution des échantillons UZr_2 dans l'aluminium liquide. La cohérence de cette nouvelle valeur avec les autres données expérimentales disponibles sur ce système doit être vérifiée. En parallèle, la capacité thermique de cette phase entre 0 et 298.15 K devra être mesurée pour avoir une estimation de son entropie de formation à 298.15 K et ensuite une valeur fiable de son énergie de formation de Gibbs qui pourrait être considérée dans une modélisation future du système.

Références

1. Jacquemain D., Les Accidents de Fusion du Cœur des Réacteurs Nucléaires : État actuel des connaissances. EDP Sciences (2015).
2. Decreton A. Contribution Expérimentale à l'Etude Thermodynamique des Systèmes Ag-Zr et Ag-Cd-In. Thèse de doctorat, Aix Marseille Université, (2016).
3. Gajavalli J., Contribution Expérimentale à la Thermodynamique des systèmes Ag-Cd-In, In-Zr et In_2O_3-ZrO_2. Thèse de doctorat, Aix Marseille Université (2019).
4. Benigni P., Hassam S., Decreton A., Mikaelian G., Gajavalli K., Barrachin M., Fischer E., Rogez J., Enthalpy of Mixing in the Ag-Cd-In Ternary Liquid Phase. The Journal of Chemical Thermodynamics.107: 0715 (2017).
5. Fischer E., Gajavalli K., Mikaelian G., Benigni P., Rogez J., Decreton A., Barrachin M., Experimental Study and Thermodynamic Modelling of the Ag-Cd-In System. Calphad 64: 292305 (2019).
6. Meschel S.V., Kleppa O.J., Standard Enthalpies of Formation of Some Transition Metal Indium Compounds by High Temperature Direct Synthesis Calorimetry. J Alloys Compound. 333:91-98 (2002).
7. Schubert, K., Meissner H.G., Raman A., Rossteutscher W., Einige Strukturdaten Metallischer Phasen (9). Die Naturwissenschaften. 51 (12): 287-287 (1964).
8. Schubert K., Frank K., Gohle R., Maldonado A., Meissner H.G., Raman A., et al. Einige Strukturdaten Metallischer Phasen (8). Die Naturwissenschaften. 50 (2): 41-41 (1963).
9. Schubert K., Meissner H.G., Potzschke M., Rossteutscher W., Stolz E., Einige Strukturdaten Metallischer Phasen (7). Die Naturwissenschaften. 49 (3): 57-57 (1962).
10. Colinet C. Communication privée (2019).
11. Okamoto H., The In-Zr (Indium-Zirconium) System. Bulletin of Alloy Phase Diagrams. 11(2):150-152 (1990).
12. Gary S. Collins. "Communication privée (2021)".
13. Fischer E., Base de données thermodynamiques NUCLEA (IRSN) (2014).
14. Dieva E.N., Solubility of Metals of the Fifth and Sixth Periods in Liquid Indium: Physicochemical Studies of Liquid Metals and Alloys, V.G. Bamburov, Ed., Izd. Ural'sk. Nauch. Tsentra Akad. Nauk SSSR, Sverdlovsk. 105-110 en russe (1974).
15. Betterton J.O., Noyce W.K. The Equilibrium Diagram of Indium-Zirconium in the Region 0-26 at. pct. In. Transactions de la société métallurgique de l'AIME. 212 (6): 340-342 (1958).
16. Meschel S.V., Kleppa O.J., Standard Enthalpies of Formation of Some Transition Metal Indium Compounds by High Temperature Direct Synthesis Calorimetry. J Alloys Compound. 333:91-98 (2002).
17. Hsiao H-M., Liang S-M, Rainer S-F., Yen Y., Thermodynamic Assessment of the Ag-Zr and Cu-Zr Binary Systems. CALPHAD. 55(2): 77-87 (2016).
18. Jin C., Hu B., Zeng G., Xie J., Sheng S., Liu S., Hu J., Experimental investigation and CALPHAD modeling of phase equilibria of the Cu-Ag-Zr system. Calphad 79: 102487 (2022).

19. Fitzner K., Kleppa O.J., James F., Thermochemistry of Binary Alloys of Transition Metals: the Me-Titanium, Me-Zirconium and Me-Hafnium (Me = argent, or) Systems. Metall Trans A. 23(3): 997-1003 (1992).
20. E. Fischer, Base de données thermodynamiques NUCLEA pour le corium ; Institut de Radioprotection et Sûreté Nucléaire : St Paul lez Durance, France, 2022.
21. Gachon J.C., Hertz J., Enthalpies of Formation of Binary Phases in the Systems FeTi, FeZr, CoTi, CoZr, NiTi, and NiZr, by direct reaction calorimetry. Calphad. 7:1-12 (1983).
22. Rosner-Kuhn M., Qin J.P., Schaefers K., Thiedemann U., Frohberg M.G., Temperature-Dependence of the Mixing Enthalpy and Excess Heat-Capacity in the Liquid-System Iron-Zirconium. Z. Metallkd. 86: 682-685 (1995).
23. Schneider A., Klotz H., Stendel J., G. Strauß, Zur thermochemie von Legierungen, Pure Appl. Chem. 2: 13-16 (1961).
24. Nagarajan K., Babu R., Mathews C., Enthalpy of Formation of UZr_2 by Calorimetry. J. Nucl. Mater. 203: 221-223 (1993).

Acknowledgement

According to Albert Einstein, “if we knew exactly what we were doing, it would not be called research”. This implies that there is vast knowledge waiting to be discovered. I couldn't agree more that sometimes the journey teaches you a lot more about the destination when I reflect back on this journey and how quickly three very lovely years have passed. I've had the good fortune to come across some truly lovely people along the way, and they have all been extremely supportive. The list of people to whom I am most grateful to could go on and on but that does not go by without mention.

First and foremost, I owe my deepest gratitude to IRSN for its logistical and financial support and the Radioelement Transfer Research Laboratory (LETR). Big thanks to SYstèmes et Matériaux pour la MÉcatronique laboratory (SYMME) and Institut Matériaux Microélectronique Nanosciences de Provence (IM2NP) where the experimental research was carried out.

I would like to sincerely appreciate Pierre BENIGNI from IM2NP- Marseille and Marc BARRACHIN from Institute for Radioprotection and Nuclear Safety - Cadarache for providing support and guidance as my director and supervisor respectively. They have not only played the role of supervisors but also as advisors and role models. I have learnt so much from them, which has enabled me to grow not only as a researcher but also as a person.

Playing this role alongside were my thesis supervisors from SYMME lab - Annecy, Marc LOMELLO, Amin JANGHORBAN and Caroline ANTION. Most of all the things I have learnt relating to technical and experimental techniques were acquired during my study by their due diligence. The discussions, analysis and comments have been critical in arriving at this point and I could not have made it without them. A special thanks to Benedicte MICHEL of Institute for Radioprotection and Nuclear Safety - Cadarache, for her extensive input in the In-Zr phase diagram calculations.

I also would like to express my gratitude to other co-supervisors, Georges MIKAELIAN from IM2NP- Marseille with whom I carried out some of my calorimetry experiments at IM2NP as well as some technical discussions, Yannick MUGNIER from SYMME lab- Annecy who helped me in the Rietveld analysis and Gary Collins from Washington state university for his help in synthesizing the indium rich samples.

Another person whom I extend my deepest gratitude is Jean-Christophe MARTY who is the technical responsible of the SYMME lab- Annecy. He took me through the sample synthesis, XRD and DTA investigations even in the tightest of schedules. All his efforts are deeply appreciated.

Special appreciation also goes to Jerome ANDRIEUX from Université Claude Bernard Lyon 1, for his assistance and effort. He dedicated part of his precious time in sealing the samples that were used for DTA.

A heartfelt gratitude goes to Sylvie CHATAIN from the LM2T laboratory of CEA Saclay who supplied Fe_2Zr samples and Olivier TOUGAIT from the UCCS laboratory of Lille University who supplied UZr_2 samples for dissolution calorimetry.

A special thanks to Evelyne FISCHER of Laboratoire de Science et Ingénierie des Matériaux et Procédés – Grenoble. She has been an unseen driving force for our experiments and her contributions to the project are highly cherished.

Notable mention is also made of my colleagues both PhD students and interns and the many others with whom I share some unforgettable memories.

Table of contents

Affidavit **2**
List of publication and participation in conferences **3**
Résumé **4**
Abstract **5**
Résumé **6**
    Références 12
Acknowledgement **14**
Table of contents **16**
1. Introduction **19**
  1.1. Context of studies 24
    1.1.1. Pressurized water reactor 24
    1.1.2. Absorber Rods 25
    1.1.3. Absorber materials description 27
    1.1.4. Phenomenology of a severe accident 29
  1.2. Choice and motivation of studies 35
  1.3. References 36
2. Experimental methods **39**
  2.1. Sample synthesis 39
    2.1.1. Powder Metallurgy 39
    2.1.2. Arc melting 41
    2.1.3. Annealing 42
  2.2. Sample preparation and analysis techniques 43
    2.2.1. X-ray diffraction (XRD) 43
    2.2.2. Polishing 45
    2.2.3. Scanning Electron Microscopy (SEM) 45
    2.2.4. Electron Probe Microanalysis (EPMA) 45
  2.3. Thermal Analysis 46
    2.3.1. Principle 46
    2.3.2. Experimental protocols 47
  2.4. Drop solution calorimetry 49
    2.4.1. Drop solution method 49
    2.4.2. Description of the Calorimeter 50
    2.4.3. Procedure 51
    2.4.4. Thermogram processing 52
  2.5. High temperature direct reaction calorimetry 52
    2.5.1. High temperature direct synthesis method 52

2.5.2. Procedure 53
2.6. Experimental difficulties 53
2.7. References 54
3. Study of the In-Zr system 55
3.1. Introduction 55
3.2. Bibliography 56
3.2.1. In-Zr System 56
3.2.2. Thermodynamic properties 61
3.2.3. Calphad modelling 62
3.3. In-Zr binary phase diagram investigation 66
3.3.1. Phase equilibria of In-Zr system 67
3.3.2. Phase transformation temperatures 75
3.4. Thermodynamics contribution 83
3.4.1. Dissolution calorimetry measurements 83
3.4.2. Direct reaction calorimetry 92
3.5. Discussion 93
3.6. Conclusion 100
3.7. Appendix 101
3.8. References 102
4. Enthalpies of formation of the AgZr and Fe_2Zr intermetallic compounds 105
4.1. Introduction 105
4.2. Bibliography 106
4.2.1. Fe-Zr system 106
4.2.2. Ag-Zr System 109
4.3. Dissolution calorimetry measurements 113
4.3.1. Dissolution of Fe_2Zr in liquid Al at 1173 K 113
4.3.2. Enthalpy of formation of Fe_2Zr 115
4.3.3. Dissolution of AgZr in liquid Al at 1173 K 117
4.3.4. Enthalpy of formation of AgZr 120
4.4. Metallographic examinations 120
4.1. Discussion 123
4.2. Conclusion 129
4.3. Appendix 130
4.4. References 132
5. Enthalpy of formation of UZr_2 137
5.1. Introduction 137
5.2. Bibliography 138
5.3. Reinterpretation of the measured thermal effect in Nagarajan et al.'s [9] experiments 141
5.3.1. Zirconium solution in liquid aluminium 141
5.3.2. Uranium solution in liquid aluminum 143

5.3.3. UZr_2 solution in liquid aluminum 149
5.4. New measurements of UZr_2 dissolution in liquid Al 152
5.5. New determination the enthalpy of solution of UZr_2 155
5.6. Summary and discussion 156
5.7. Conclusion 159
5.8. Appendix 161
5.9. References 164
Conclusion 169
References 173
Table of figures 175

1. Introduction

The main risk associated with the operation of nuclear power reactors using nuclear fission involves radioactive substance dispersion, and potential human and environmental exposure to radiation. In order to reduce these risks, the nuclear industry greatest responsibility is to operate the nuclear plants under safety conditions [1].

Despite all the measures taken to reduce the probability of the occurrence of a nuclear accident, for the past years there have been three major nuclear accidents of which the causes, effects and consequences are briefly discussed here. These accidents which lead to the partial or complete core melting have drawn attention on the necessity to take into account the occurrence of a severe accident and its consequences at the design stage.

The Three Mile Island (TMI) nuclear accident was the first major nuclear accident recorded. The Three Mile Island (TMI) Pressurized Water Reactor (PWR) power plant is located near Harrisburg, Pennsylvania, in the USA. The accident at the Three Mile Island Unit 2 (TMI-2) occurred on March 28, 1979, when the Unit was operating at 97 % power [2]. The accident was caused by a sequence of events during which equipment malfunctions, design-related problems, and worker errors occurred, which resulted in loss of reactor coolant, and partial meltdown of the TMI-2-unit core. The releases of radioactive noble gases and iodine to the environment were limited. No deaths or injuries to plant workers or members of the nearby community related to the accident have been recorded. However, the impact of the TMI-2 nuclear accident in the public opinion was very high forcing the U.S government to cancel all plans already adopted for the construction of new nuclear power reactors in the country [2]. For safety experts, the Three Mile Island accident remains a major source of lessons that help understanding of the complex phenomena that occur during a core melt accident.

The second major nuclear accident recorded was the Chernobyl nuclear accident, which occurred on April 26, 1986, in Ukraine. The Chernobyl reactors were pressurized water cooled reactors of the Soviet-designed, Reaktor Bolshoy Moshchnosty Kanalny (RBMK), which use graphite as moderator, designed to produce both plutonium and electric power. The accident was as a result of flawed reactor design combined with human errors. It occurred during a test to check if the turbine could provide enough energy to keep the cooling pumps running in case of loss of power until emergency diesel generators takeover. Control of the reactor power was lost, leading to overheating of the fuel and a steam explosion that collapsed the reactor building during the exercise. Considering the radioactive releases in the environment, the area contaminated, the number of countries involved, and the amount of people affected by the accident, it was concluded that the Chernobyl nuclear accident is the worst nuclear accident which has ever occurred in a nuclear power plant [2]. After the occurrence of this accident, the pressure of the international community to close nuclear power plants in operation, in particular those of RBMK type, in many countries was increased [2].

The Fukushima Daiichi nuclear accident was considered the second world major nuclear accident after Chernobyl, and the third major accident that has affected the world nuclear industry in the last forty-three years. The accident in a Boiling Water Reactor (BWR) was caused by an earthquake, followed by a tsunami on March 11, 2011. The earthquake caused damage to the electric power supply lines to the site, and the tsunami resulted in failures of equipment and a loss-of-coolant event with nuclear meltdown (overheating and damage to the reactor core with melting of fuel rod components) [2]. The accident at the Fukushima Daiichi nuclear plant in Japan, has increased again the necessity to take into account a possible occurrence of a severe accident in the reactor design and to foresee mitigation means to reduce as low as possible the consequences of radioactive releases on the populations and the environment.

From a general perspective, whenever severe accident occurs in reactors (PWR or BWR) with water being the coolant, the residual power produced during the operation can no longer be evacuated by water, implying that the core is no longer cooled. When there is loss of coolant, the core is exposed to high temperature and steam oxidation, until progressing to core meltdown. In this situation, the core elements comprising of the absorber and fuel rods as well as the stainless steel internal structures, get relocated to lower parts of the core where they mix to form a molten pool called *corium*. In the same time, fission products are released from the fuel, are transported through the primary circuit until the containment and eventually into the environment.

From the above-mentioned major accidents, two of the significant areas of improvement in terms of safety are to reduce the fission product release outside the nuclear power plant in case of accident conditions and to maintain the melted core inside the vessel or if not possible to foresee a system outside the vessel able to cool the corium at the long term.

To achieve the objective related to the first issue, i.e. the fission product release limitation, the key point is the determination of the so-called source term, thus, quantifying the nature (i.e. chemical species), release rate and global released fraction of fission products and other radioactive materials that will be transferred into the environment. In this framework, several experimental safety research programs have been performed by various entities worldwide as well as numerous computer models have also been developed to simulate a core melt accident sequence, assess the consequences, and determine the effectiveness of various systems (e.g. filtration devices) that could be implemented to mitigate the consequences of such an accident [1]. As an example, IRSN in France has launched a very important experimental program (Phebus FP program) focused on core melt accidents for water-cooled reactors with an objective of a better understanding of the phenomenology of the degradation processes and the fission product behaviour occurring in a nuclear core during an accidental sequence. The Phebus FP tests were performed to study at a reduced scale compared to the reactor one, fuel degradation until the formation of a molten pool, hydrogen production (from the oxidation of fuel zircaloy-4 cladding by steam), the release and transport of fission products in the Reactor Coolant System (RCS), aerosol physics, and iodine chemistry in the RCS and containment. Knowledge obtained from this program as well as the other different experimental programs has put in evidence the particular role of the absorber rods in the fission product chemistry in the primary circuit.

In a reactor, the function of the absorber rods is to control the reactivity of the core. Most PWR absorber rods are composed of silver-indium-cadmium alloy, with a composition of 80wt.% Ag, 15wt.% In, 5wt.% Cd (so-called SIC alloy or composition), inserted inside a stainless steel (SS) (AISI 304 or 316) cladding and itself inserted into a Zircaloy-4 guide tube. During an accident sequence, the progressive melting of the Ag-In-Cd alloy between 1016K and 1104K [3] is the first event of the core degradation. This does not induce any absorber rod degradation as long as the molten SIC alloy remains inside its stainless steel cladding. In a low-pressure scenario, as the temperature keeps on increasing, the absorber rods cladding made of stainless steel, fails, as a result of internal pressurization (high Cd and filling gas, usually He, vapor pressures) and eutectic interactions with the Zircaloy-4 guide tube (bowing of the rods at high temperatures). In a high-pressure scenario, over-pressurization of the absorber rod presumably does not occur, and the absorber rod fails at higher temperature, around, 1720K, as a result of stainless steel melting.

Early in the accidental sequence, there is then formation of melts containing the absorber elements (Ag, Cd, and In), zirconium from the guide tube, and oxygen resulting of the interaction of these melts with steam. The stainless steel elements are in low quantities in these melts due to the immiscibility of these elements with the absorber rod elements at the liquid state. The composition of these mixtures, as they are progressively relocated to the bottom of the vessel, may change because of oxidation of indium and zirconium but also because there is a potential vaporization of the absorber elements, the most volatile one being Cd. These gases resulting from the absorber rod degradation are then transported to the primary circuit of the reactor, where they can interact with the fission products vaporized from the fuel.

Knowledge of the nature of these gases and their quantity are important for the studies that are currently being conducted in case of severe accidents, for the following reasons. Firstly, silver and indium significantly contribute in terms of presence of aerosols in the primary circuit. Secondly, Cd and Ag are very reactive with iodine. As a consequence, the release kinetics and the composition of these gases are of primary importance in assessing the gas speciation in the primary circuit and more particular the fraction of iodine gas which is key to predict the source term.

Related to this issue, the particular questions which have to be solved regarding the behavior of absorber rods in accident conditions are:

- What are the composition and the amount of the gas phase when the absorber rod begins to degrade?
- What are the composition and the amount of the gas phase when the absorber alloy interacts with zirconium guide tubes in the mixture?
- What is the solid/liquid fraction of zirconium in absorber alloy mixtures in order to be able to estimate the flow rates of the mixtures to the bottom of the core?

Thermodynamics of the Ag-In-Cd-Zr-O system and its modelling can help to provide some answers to these questions. For several years, IRSN, with the support of SIMAP (Grenoble University), has been developing the NUCLEA thermodynamic database dedicated to the corium thermochemistry using the CALPHAD method, which is the approach commonly used for the modelling of systems including many chemical elements. This approach has the advantage of being able to predict the thermodynamic behaviour of a complex multiphase system based on the modelling of the subsystems. For each phase, it allows to aggregate in a unique Gibbs free enthalpy function, the experimental information deduced from the study of the equilibria between phases (nature of the phases in equilibrium, limits of stability domain, transition temperatures...) and the one resulting from measurements of thermodynamic quantities (enthalpy of formation, activity, chemical potential, heat capacity...) and thus to ensure a global coherence between these various data. The scrupulous optimization of binary and ternary systems constitutes the basis of validity of the approach. For this task, to acquire experimental data in terms of phase diagram as well as thermodynamic properties on the subsystems is the key point.

In two previous theses [4,5], numerous experimental data have been acquired on thermodynamics of the Ag-Cd-In system, at high temperature, allowing to determine the nature of the equilibria with the liquid phase. From these data, a CALPHAD modelling of the Ag-Cd-In ternary system was built [6]. It allows to calculate the vapor pressures of Cd, Ag and In above the Ag-Cd-In melts as a function of composition and temperature. This significant work already contributes to answer the first question, since in the very beginning of the degradation process of the absorber rod, it is not expected that the melts contain a significant amount of zirconium. As far as the degradation process progresses, more zirconium can be potentially incorporated into the absorber melts as the consequence of the interaction between the absorber material and the guide tube, and the impact of this composition modification on the vapor pressures of Cd, Ag and In has to be assessed. Also, the interaction with surrounding steam atmosphere has to be considered, regarding the relatively high affinity of indium and zirconium with oxygen. These two previous theses [4, 5] also brought a significant contribution to the Ag-Zr and In_2O_3-ZrO_2 phase diagrams.

The objective of this thesis is to bring an experimental contribution allowing to have a more complete description of thermodynamics of the Ag-Cd-In-Zr-O system. The present study will be focused on the In-Zr (phase diagrams and thermodynamic properties) and Ag-Zr (thermodynamic properties) systems in order to better estimate the impact of the degradation of the guide tubes on the vaporization of the silver and indium known to interact with fission products in the primary circuit, in particular iodine.

This experimental work of importance for the early phase of a severe accident will be completed by thermodynamic studies of the Fe-Zr and U-Zr systems which is of great importance for the core degradation, but in this case for the late phase of the accident. With sustained loss of water inventory in the reactor core, the residual energy (due to the decay heat) as well as the chemical energy (due to the zirconium oxidation) results in a heat up of fuel assemblies and neighboring structures during the progression of severe accidents as evidenced in the TMI-2, Chernobyl, and Fukushima Daiichi Nuclear Power Plant (FDNPP) accidents. Various materials in the reactor vessel including UO_2 pellets of fuel, zirconium-based cladding, control rod materials, and stainless steel internal structures may melt and interact between each other and these interactions results in the formation of a sort of magma, so-called corium. The morphology and phases of molten core in the lower plenum of the reactor vessel are of interest, as it determines the paths of accident progression including the failure modes of the reactor vessel and the phases and composition of molten core released out of the reactor vessel which determine the initial conditions of the interaction between the corium and the concrete of the reactor basemat. From the TMI-2 experience, it was suggested that crusts were able to support melt pools, this phenomenon could probably explain why the vessel failure was not observed. On the contrary it can be assumed that if there was no water reflooding, the crust would have failed leading to massive relocation of molten material and debris into the lower plenum. On the other hand, in the FDNPP accident, molten core materials relocated to the lower plenum of the reactor vessel resulted in a failure of the reactor vessel due to an interaction of high temperature molten corium with the reactor vessel lower head structure, hours and days after the loss of safety systems. In all three units of FDNPP, the reactor vessels were breached. As a consequence, substantial amount of molten core materials was released out of the reactor vessel.

Today, the knowledge on the end state of fuel debris in the reactor vessel is essential not only for the understanding of the phenomenology of core damage progression in the different accidents but also for the development of proper strategies to confine the corium inside the vessel in case of severe accidents for future reactors. To reach this objective, a complete knowledge of thermodynamics of the U-Fe-O-Zr system (including the elements of the main core components, UO_2 fuel, Zircaloy cladding and stainless structures) is key. Even if many studies have been devoted to this system some lacks still exist on the binary metallic systems, in particular Fe-Zr and U-Zr. The work presented in this document will contribute to reduce the uncertainties on these chemical systems.

The format of this manuscript begins with a presentation of the context of the work, which includes a brief description of the operation of a pressurized water reactor (PWR), the description of the behavior of SIC absorber rod in a PWR during normal and accidental conditions and the choice and motivation behind our studies. Then the different experimental methods implemented in the work and the experimental difficulties related to the studied systems are presented in Chapter 2. In Chapter 3, a critical analysis of bibliography available for the In-Zr system and the experimental results obtained for the In-Zr system are presented. These results are discussed in relation to the state of the art and new perspectives are proposed.

Finally, the thermodynamic investigation of additional systems (Ag-Zr, Fe-Zr and U-Zr) in conjunction with my work are presented in Chapters 4 and 5. For these systems, the experimental work is mainly focused on thermodynamic properties of binary compounds (AgZr, Fe_2Zr and UZr_2, respectively). In Chapter 4, thermodynamic data available for Fe-Zr and Ag-Zr system are presented, together with the experimental results obtained for the Fe_2Zr and AgZr intermetallic compounds in this work. In Chapter 5, the bibliography and results obtained for U-Zr system, with a focus on the UZr_2 intermetallic phase are presented.

1.1. Context of studies

1.1.1. Pressurized water reactor

The nuclear power plants that are currently in operation in France are the pressurized water reactors (PWR) which belong to the second generation (so-called Gen II) of nuclear power reactors. These reactors use enriched uranium dioxide that may be mixed, for some reactors (900 Mwe ones), in the so-called MOX fuel with plutonium oxide recovered from reprocessing of spent fuel. The water used as the heat-transfer fluid is maintained under high pressure (155 bar) and remains at liquid state at its operating temperature (300 °C) [1].

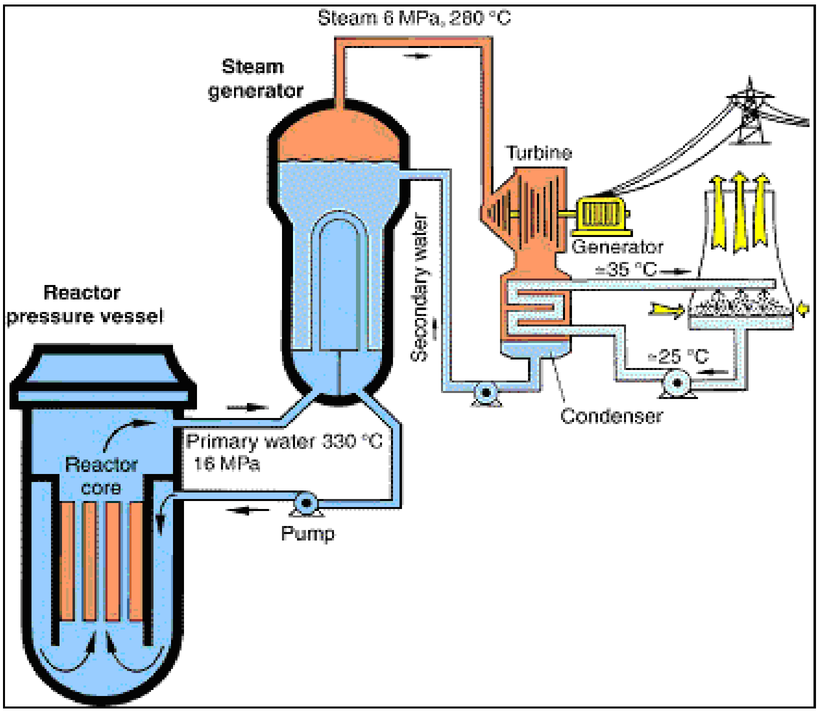

Figure 1. Schematic representation of a PWR reactor [7].

The operation of pressurized water reactor can be described in a very simplified way as follows (**Figure 1**):

- The reactor core is the source of energy and produces heat,
- The heat generated by the core, is carried to the steam generator by the pressurized water,
- Inside the steam generator, heat from the primary coolant loop vaporizes the water in a secondary circuit, to produce steam,
- The steam passes through the main turbine causing it to drive an alternator which then produces electricity,
- The secondary steam is condensed at the outlet of the turbine, before being recycled into the steam generators.

The reactor core is made up of fuel assemblies, with each assembly consisting of 264 fuel rods, 24 tubes to contain the absorber rods suspended to a structural part called “spider”, which simultaneously controls their movements shown in **Figure 2**. These rods (fuel and absorber) are arranged in a 17 × 17 square lattice. About one-third of the fuel assemblies contain absorber rod guide which are incorporated into them. The fuel rods are made up of zirconium alloy (Zircaloy-4) tubes also known as “cladding” (this alloy has low neutron-absorbing properties and good corrosion resistance). Inside these tubes are pellets made of uranium dioxide (UO_2) or a mixture of uranium and plutonium oxides ((U, Pu) O_2 which make up the nuclear fuel [1].

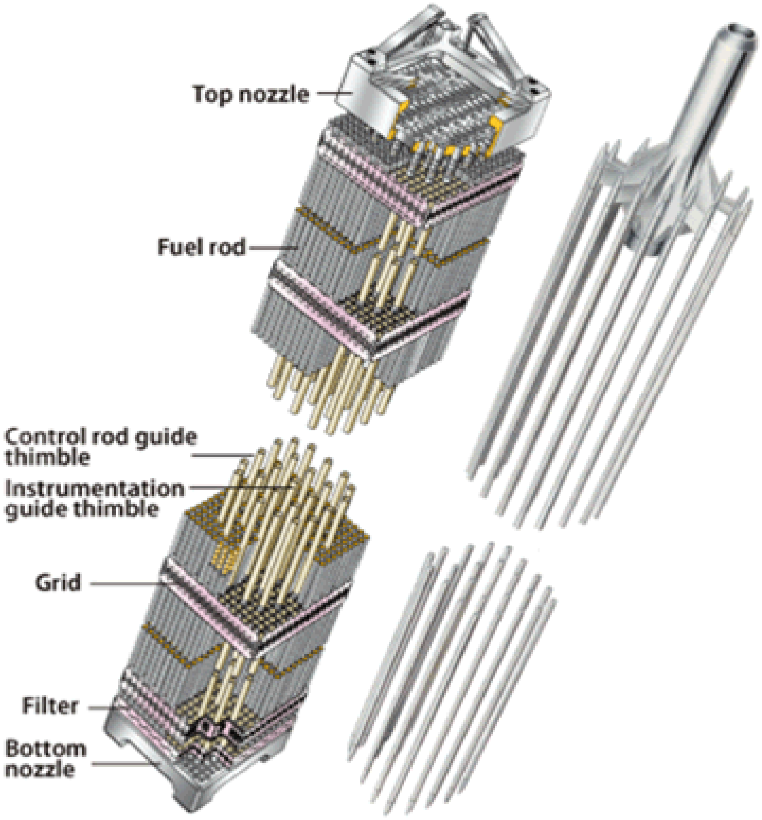

Figure 2. The nuclear fuel assembly with the rod cluster control assembly [8].

1.1.2. Absorber Rods

Absorber rods are used to control the fission rate of the nuclear fuel by adjusting the number of slow neutrons present to keep the rate of the chain reaction at a safe level. The reactivity of the reactor is controlled by moving the absorber rods into or out of the core allowing to vary the thermal power of the reactor, the amount of steam produced, and hence the electricity generated. Absorber rods may contain different materials with selective neutron capture cross sections, depending on the reactor’s neutron spectrum [9]. In PWRs, absorber material is selected to absorb a larger fraction of slow (thermal) neutrons when move into the fuel assembly in the reactor core, thereby slowing the rate of the fission reaction and decreasing the power produced. Conversely, if the absorber rods are removed, fewer neutrons are absorbed, and the fission rate and energy production increase. When there is an emergency situation, the absorber rods are fully inserted into the nuclear core between the fuel rods to shut down the chain reaction.

In PWRs, the absorber rods are usually made up of the following elements (boron, silver, cadmium, hafnium, and indium) that capture thermal neutrons. As previously mentioned, the absorber rods are grouped together in clusters known as “clusters of control ", made up of 24 rods and distributed inside the reactor core. The absorber rod drive mechanisms are mounted on the reactor pressure vessel head and are inserted into the core from above.

The reactors have different number of clusters control depending on their power. The reactor power regulation takes place through 57 of these clusters for the core of French 900 MWe reactors with absorber material (Ag-Cd-In) and 65 of them for 1300 MWe reactors with absorber material (Ag-Cd-In+ B_4C). The number of absorber rods is therefore, 1368 for 900 MWe reactor and 1560 for 1300 MWe reactor. To give an order of magnitude, these numbers can be compared to those of fuel rods, i.e. 41448 for a 900 MWe reactor and 50952 for a 1300 MWe reactor. The total mass of absorber material is approximately 1.7% of the mass of fuel of the core of a 900 MWe reactor [9].

Considering a 900MWe reactor, the absorber rod (height 4.3m, internal diameter 8.75mm and an external diameter of 9.75mm, **Figure 3**) which contains silver, indium and cadmium (SIC alloy), is inserted into a 316L stainless steel sheath. Helium fills the space between the absorber material and the stainless steel cladding for efficient cooling of the absorber elements [9]. The absorber rod (absorber alloy together with stainless steel casing) is placed in the center of a Zircaloy-4 (98.23 wt.% Zr alloy, 1.45 wt.% Sn, 0.21 wt.% Fe, 0.1 wt.% Cr) guide tube in order to guide the movements of the rod during the reactor operations. There is a gap between the stainless steel sheath and its guide tube. The gap is filled with the heat transfer fluid (water in this case for PWR), which circulates and extracts the heat produced by neutron reactions and γ-radiation. Therefore, there is no direct contact between the stainless steel sheath and the Zircaloy-4 guide tube during normal operations.

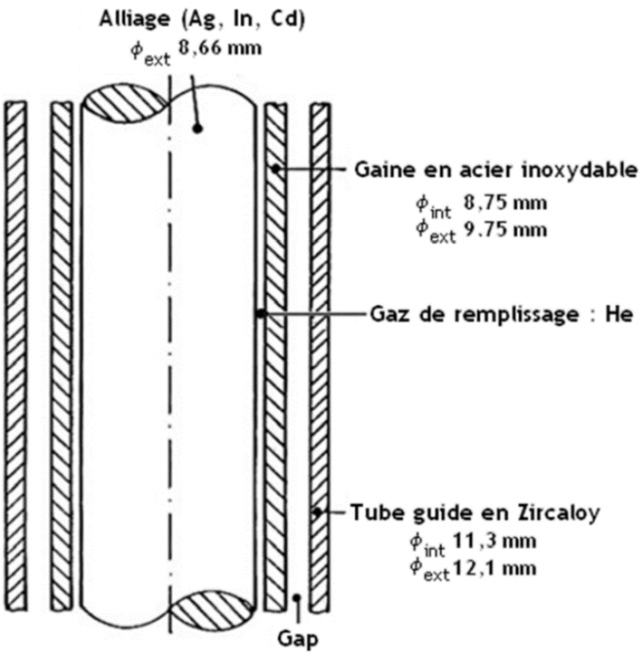

Figure 3. Structure of an SIC absorber rod in a 900 MWe reactor [9].

1.1.3. Absorber materials description

In the manufacturing of control rods for nuclear reactors, there are certain criteria and requirements that govern the choice of the absorber materials:

- The effective neutron absorption cross section of the material must have a cross section of at least 100 barns for thermal neutrons, a few barns for fast neutrons. Based on this idea **Table 1** lists some elements that fit these criteria and can be used for the fabrication of absorber rods for different reactors.
- Metallurgical stability under neutron irradiation and absence of harmful irradiation damage that could prevent proper functioning during reactor operation.
- Good resistance to corrosion when used in high temperature pressurized water.
- Substantial absence of thermal distortion under non-uniform temperature conditions during reactor operation.
- Sufficient mechanical strength and ductility to withstand scramming loads during operation.

Table 1. Neutron absorption elements used in the 900 and 1300 MWe reactors [11].

Elements	Atomic Number	Atomic Mass (u)	Cross-section at 20°C for thermal neutrons (barns)	Comments
B	5	10.811	766	Used in the form of B_4C and HfB_2
Ag	47	107.87	68	Used in the form of SIC ternary alloy, Density; 9.93 $g.cm^{-3}$
Cd	48	112.41	2349	
In	49	114.82	193	

In addition to the above requirements, the availability of the metals comprising the alloy has to be considered, how easy it will be to fabricate the absorber material into complex shape, the cost and the manufacture of absorbent elements, related to the service life in reactor.

There are different materials used in manufacturing of the absorber rods for the French nuclear reactors. Two types of material are currently used for the absorber material. Silver, indium, and cadmium elements are alloyed (SIC alloy) for 900 MWe reactors. Other possible absorber material is B_4C (used in combination with SIC in the French 1300MWe reactors) [10].

The nominal composition of the SIC absorber material is 80 wt% Ag, 15 wt% In, 5 wt% Cd. The composition was adjusted to fulfill the needed requirements of a material with high absorption over a wide range of neutron energy and acceptable mechanical properties. In order to obtain an absorber alloy in the solid state under nominal conditions of the reactor, silver is chosen as the main element of the alloy. The SIC ternary alloy forms a single solid solution of face centered cubic (fcc) structure which is metallurgically stable for operating conditions of reactors and a liquefaction range between 1016 and 1104K [3]. SIC alloy has the lowest melting temperature among all metallic and ceramic materials used in the PWR nuclear reactors, and hence will melt first during beyond design basis nuclear accidents [10].

As stated earlier, the initial composition of the SIC alloy is located in a single-phase domain (fcc) of the Ag-Cd-In ternary phase diagram. During the operation of the nuclear reactor, the absorber rod is heated by the γ-rays and irradiated by the neutron flux. For the neutron irradiation process [9, 11], the neutron capture reaction involving indium (reaction 1.1) leads to the stable tin formation. The neutron capture reactions of silver (reactions 1.2 and 1.3) create new cadmium nuclei. Therefore, the composition of the alloy evolves under irradiation with enrichment in tin and cadmium and a depletion of silver and indium compared to the nominal composition as can be illustrated in **Table 2**.

The various neutron capture reactions are summarized here:

$$^{115}In + n \rightarrow {}^{116}In \rightarrow {}^{116}Sn + e- + \bar{v}\,e \tag{1.1}$$

$$^{107}Ag + n \rightarrow {}^{108}Ag \rightarrow {}^{108}Cd + e- + \bar{v}\,e \tag{1.2}$$

$$^{109}Ag + n \rightarrow {}^{110}Ag \rightarrow {}^{110}Cd + e- + \bar{v}\,e \tag{1.3}$$

$$^{113}Cd + n \rightarrow {}^{114}Cd \tag{1.4}$$

Above an average concentration of around 2 wt% Sn, a second phase rich in indium and tin, with a hexagonal structure and less dense than the initial SIC alloy, forms an intergranular precipitate which begins to melt at 623 K [12]. The formation of this secondary phase and the irradiation defects induced by fast neutrons contribute to the swelling of the material. This swelling linked to irradiation remains limited because the operating temperature of the reactor is higher than the recrystallization temperature of the alloy, hence promoting recombination of the created defects. The expansion and irradiation-induced swelling of the alloy are accommodated during operation, because of the space between the stainless steel cladding and the absorber material [13].

Table 2. Average chemical composition of the absorber alloy (at. %) [9].

Alloy	Ag	In	Cd	Sn
Nominal composition (initial)	80.8	14.3	4.9	-
8 PWR cycles, thus about 8 years	68.1	7.0	17.8	7.1

1.1.4. Phenomenology of a severe accident

1.1.4.1. General description

Severe accidents in nuclear power plant are unlikely events but with serious consequences since they have the potential to cause large release of radioactive material thereby posing a risk to public health and safety as well as to the environment. In these situations, the reactor faces conditions in terms of temperatures more severe than a design basis accident and these conditions lead to significant core degradation, i.e. partial or complete melting of the fuel assemblies [14]. Severe accidents may be caused by so-called internal initiators (such as complete loss of power supply for an extended period, complete loss of feed water for an extended period of time, loss of coolant etc..), external initiators (as extreme natural events) or human errors such as initiating events not considered in the design. Severe accidents are typically identified through probabilistic safety assessments performed for each plant [15].

The phenomenology of a severe accident involving the loss of coolant will be considered thereafter and briefly described here. Loss of Coolant Accidents (LOCA) are usually initiated by breaks in the reactor coolant system or any of the connecting circuits and leads to an increase in core temperature because the residual power is no longer evacuated. When the reactor core remains uncovered by water for a long period of time, the nuclear fuel is progressively overheated due to the residual power, and temperatures as high as the melting point of the fuel(3120 K) can be reached if no water becomes again available to cool the core. **Figure 4** is indicative of the different material melting temperatures and potential interactions in a reactor core under such conditions (left side of the figure) and the potential consequences in terms of core degradation (right side of the figure).

At first, the metal components of the core such as absorber rod components, steel internal structures, either melt or/and partially vaporize depending on temperatures reached in the core. They produce only local damages in the core as experimentally shown in the Phebus FP Programme. During this short-term phase most of the fuel rods remains in place. As the temperature rises, the steam produced initiates an exothermic oxidation of Zircaloy fuel cladding, resulting in considerable production of hydrogen and thermal power (Equation (1.5)).

$$Zr_{(s)}+2H_2O_{(g)}\rightarrow ZrO_{2\,(g)}+2H_{2\,(g)} \tag{1.5}$$

with a reaction enthalpy about -600 kJ.mol^{-1} (at 1500 K) and 0.0442 kg of hydrogen is produced per kg of oxidized zirconium [4]. The heat produced associated to the transformation of the metallic Zr into ceramic ZrO_2 then becomes comparable to the decay heat. It leads to a considerable increase of temperatures in the core. When the temperature reaches the melting temperature of the cladding (2030 K for the onset of the melting of Zircaloy-4 [16]) chemical reaction between fuel and its cladding producing low-melting point mixtures occurs, resulting in relocation of molten material until forming a corium in the lower part of the vessel. Depending on the conditions and the accumulation of core materials, this corium may cause after some times the rupture of the vessel. During this process, the corium may come into contact with residual water either in the vessel or out of the vessel. As it has higher temperature than the boiling water temperature, the water vaporizes with a potential steam explosion with severe consequences in terms of loss of confinement. The corium can also continue its progression and may interact with the concrete of the basemat, which constitutes the ultimate containment barrier of the reactor.

During all this progression, the fission products are released depending on their volatility and the temperature and atmospheric conditions (i.e. oxygen partial pressure). Most volatile fission products (rare gases, iodine, cesium, tellurium ...) are released from the fuel still intact, then the so-called semi-volatile fission products (barium, molybdenum, palladium, etc.) under the effect of heating and the variation of the oxygen potential (e.g. hydrogen-rich atmospheres increase the barium volatility whereas steam-rich atmospheres do the same for molybdenum).

During the core degradation, standby water supply delivered by the containment sprays as seen in **Figure 5** water can be used for cooling the system (also for reducing the pressure inside the containment) but later may lead to an increase in hydrogen production. The hydrogen produced from the exothermic oxidation of fuel cladding released in the containment burns on contact with the oxygen which may finally damage the containment building [1] as it was observed at Fukushima Daiichi. The damage of the containment building initiates the release of fission products into the environment. **Figure 5** shows the phenomena as well as the possible modes of rupture of the various confinement barriers (fuel cladding, primary circuit and containment) of the reactor likely associated to the fission product release paths to be caused by such an accidental situation.

In the following sections, we are going to make a focus on the degradation of Ag-In-Cd control rods and on the molten corium interaction with steel which takes place during the early times accident and during the late phase of the accident, respectively.

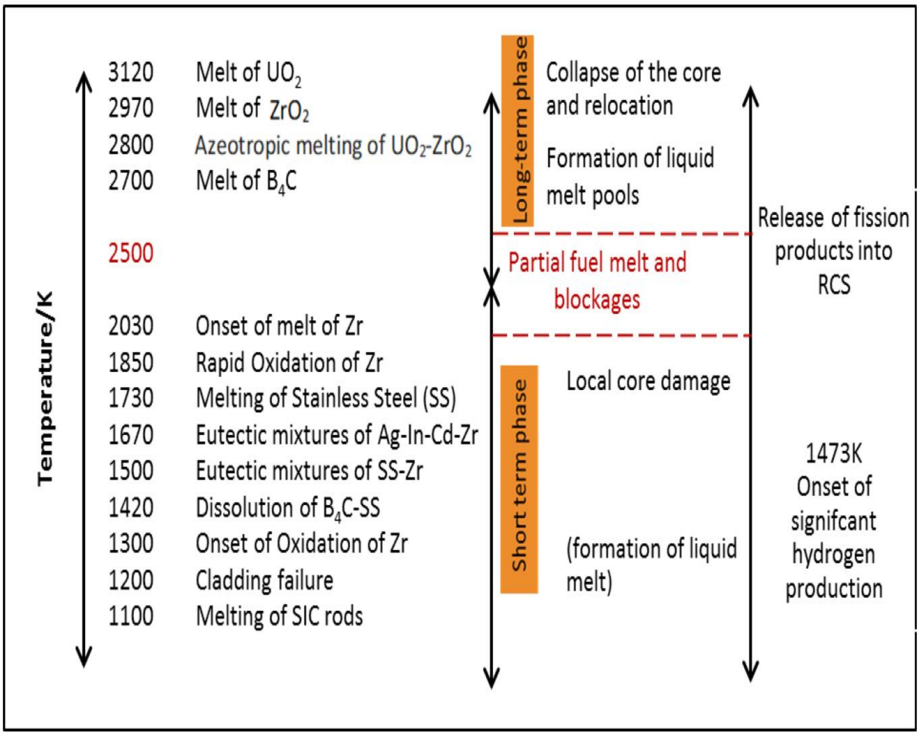

Figure 4. Reactor core degradation phenomena in relation to temperature [1].

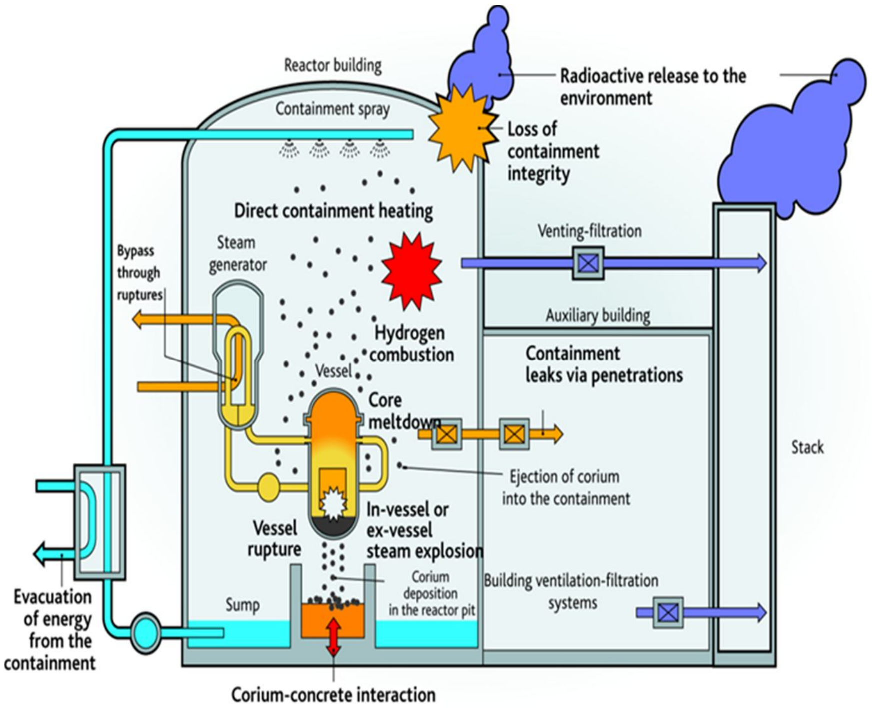

Figure 5. Main physical phenomena during a severe accident [17].

1.1.4.2. Early phase of the accident: degradation of Ag-In-Cd control rods in accident conditions

When a severe accident occurs, the increase in the core temperature causes the absorber alloy with a nominal composition 80 wt% Ag, 15 wt% In and 5 wt% Cd, to begin to melt at a temperature of 1016 K [3]. The melting of the alloy does not cause absorber rod degradation as long as there is no failure of the stainless-steel cladding, since liquid absorber material practically does not interact with stainless steel. At the same time, the internal pressure of the filling gas encapsulated in absorber rod increases gradually with the increase in temperature. To a lesser extent, the volatility of the absorber alloy, in particular cadmium, also contributes to the pressure rise.

In a low-pressure scenario, failure of the stainless steel occurs, because of internal pressurization (high Cd and filling gas vapor pressure) and eutectic interactions (by bending or ballooning) with the Zircaloy-4 guide tube. Eutectic liquefaction is due to the existence of low temperature binary eutectics between zirconium and stainless steel components at 1201, 1605, and 1233 K in the Fe-Zr [18], Cr-Zr [19], and Ni-Zr [20] systems, respectively. When the stainless steel cladding fails, the liquefied absorber alloy (Ag-In-Cd) interacts with the Zircaloy-4 guide tube and chemically dissolves it around 1273 K to 1373 K resulting in the formation of a metallic melt of typical composition Ag-In-Zr or Ag-In-Zr-(O) under oxidizing atmosphere. There is no cadmium or a very low amount of Cd in the mixtures, since this element is substantially and quickly vaporized due to its high vapor pressure in the very beginning of the degradation process of the absorber rod. The different steps of degradation of the absorber rod are schematically shown in **Figure 6**.

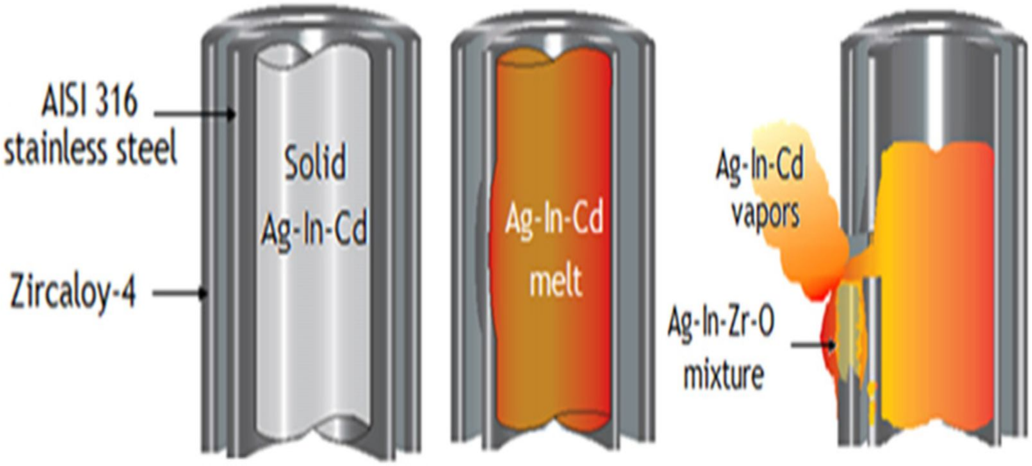

Figure 6. Schematic representation of the degradation of the control rod in a severe accident scenario in case of low pressure primary circuit. (a) Control rod in nominal conditions, (b) Rise of internal pressure in the rod following the loss of cooling and progressive swelling of the stainless steel (SS) sheath, (c) SS sheath and Zry-4 guide tube rupture, and (d) relocation and vaporization of absorber materials. [4].

The mixtures formed can interact with the fuel rods, especially in low pressure scenarios due to overpressure inside the control rod and the resulting ejection of materials, when relocating to the lower region of the core [21, 22]. These melts then weaken some of the still-intact surrounding fuel rods as a result of chemical interactions. The more volatile elements of these melts (Ag and In gaseous species) progressively vaporize if they remain at sufficiently high temperatures before finally flowing out of the hot regions of the core. As stated earlier, volatile fission products like iodine, cesium or tellurium, can be easily released from the fuel and transported to the reactor primary circuit. During the transportation, these fission products may react with vaporized chemical elements from the structural materials (such as absorber materials, internal structures of core, and surfaces of the primary circuit etc..) and the carrier gas, which is for most accidents a mixture of steam and hydrogen, with a variable composition depending on the accidental sequence. Since a PWR contains up to 2 tons of Ag-In-Cd alloy, it is very important to understand and model the behavior of this material which is likely to react (in particular Ag) with iodine fission product, which is a major contributor of the source term during the first weeks after the accidents. In particular, the vaporization of the various absorber elements (Ag-In-Cd) must be estimated from the initiation of the absorber rod degradation, till the formation of Ag-In-Zr-O mixtures and its relocation in the colder part of the reactor. From a theoretical point of view, the intensity of this vaporization depends on the thermodynamic activities of each of the components in the mixtures which are function of the compositions of the mixtures and the temperature.

The thermodynamic investigation of the Ag-In-Zr-O chemical system has started at IRSN [4,5] with the collaboration of IM2NP (Marseille), SYMME (Annecy), SIMAP (Grenoble), and JRC Karlsruhe with the study of the Ag-Cd-In, Ag-Zr and In_2O_3*-*ZrO_2 *systems. The work presented in this document aims to improve the knowledge of Ag-Zr and an extensive investigation of the In-Zr system.*

1.1.4.3. Late in-vessel phase of the accident: molten corium interaction with the vessel

In the simulations of the advanced phase of severe nuclear reactor accidents, an important issue is to be able to calculate the heat flux imposed by the corium on the vessel in order to determine the time and location of the vessel rupture and the initial conditions of the corium-concrete interaction. From a general point of view, the configuration of the corium is determined by the concentration of the components (UO_2, Zircaloy-4/M5 and steel, considering only the main components of the core of a pressurized water reactor) as well as by the evolution of the partial pressure of oxygen and temperature during the accident. Under strongly oxidizing conditions, all the oxides initially present, such as UO_2, as well as those formed by reaction with steam (zirconia and the oxides of the steel components) should be intimately mixed and form a homogeneous bath. This is the situation that probably occurred during the TMI-2 accident in the USA [23]. Under less oxidizing conditions, part of the steel may remain in metallic form, the corium separating above 2800 K into two distinct liquid phases, one containing the refractory oxides (UO_2 and ZrO_2) and the second the metallic elements of the steel (Fe, Ni, Cr). This separation results from the fact that the steel and the refractory oxides are thermodynamically immiscible at the liquid state. The density of the oxide phase being higher than that of the metal phase, the latter could theoretically float above the oxide phase.

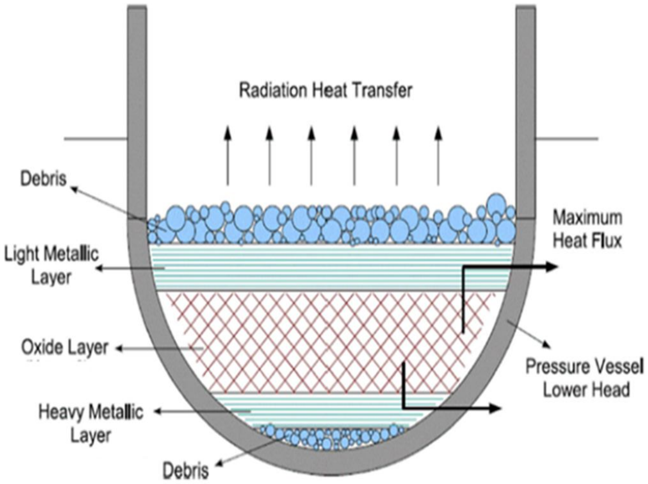

Figure 7. Lower head geometry—stratification and interface heat exchange fluxes

This situation is potentially critical, if the metallic layer will impose a concentration of heat flux on a reduced portion of the inner surface of the reactor vessel wall [24, 25]. This phenomenon can lead to failure of the vessel. Under even more reducing conditions, not only the stainless steel elements, but also part of the zirconium, are maintained in the metallic state. The unoxidized zirconium fraction has the ability to reduce the UO_2 fuel so that the metallic phase contains not only steel components but also uranium and zirconium, resulting in densification of the metallic phase (**Figure 7**). This densification can temporarily lead to the formation of three phases: a metallic phase of low density (mainly composed of the elements of the steel), an oxide phase (with UO_2 and ZrO_2) and a dense metallic phase (containing uranium and zirconium) [26]. A transient reduction in the thickness of the upper metallic layer then contributes to create a situation that is even more penalizing than the previous situation in terms of focusing of the heat flux (so-called focusing effect) [24, 25, 26]. Thus, it appears that the development of scenarios more or less critical for the integrity of the vessel results from the complex interactions between the corium components, which cannot be treated independently. Recently, approaches combining thermal-hydraulics and a description of the thermochemistry of the U-O-Zr-Fe system have been developed, for example at IRSN, in the ASTEC severe accident code, in order to predict these situations [27]. In spite of many studies, there is an uncertainty related to the chemical composition of the metallic and oxide liquids that can affect the predictions that can be made on the vessel performance. A better thermodynamic description of the in-vessel corium system, in first approximation U-Zr-Fe-O, is necessary today to improve the quality of calculations and the accuracy of simulations. By constructing thermodynamic models, the scrupulous optimization of binary systems constitutes the basis of validity of the CALPHAD approach.

Among the different binary systems of interest for the modeling of the high-temperature corium and more particularly of the thermodynamics of the metallic phase of the corium, the U-Zr and the Fe-Zr systems are key subsystems to be considered for which few data are available, some of these data being moreover controversial and some data are missing. Some part of this work will contribute to improve the knowledge of these systems.

1.2. Choice and motivation of studies

The work presented in this document is a contribution to the thermodynamics of key zirconium-based binary systems, In-Zr, Ag-Zr, Fe-Zr and U-Zr for severe nuclear accident assessment. The importance of their investigation related this context is recalled here:

- **During the early times of a severe accident**, vaporization of metallic elements from the Ag–In–Cd control rods at the initiation of core degradation has an effect on the speciation of chemical fission products and their transport in the primary circuit. In particular, silver released during the degradation is very reactive with iodine which is a major contributor to the source term to environment, at least at short time. Kinetic release of silver and evolution of its content through the reactor coolant system is very significant to study, in order to estimate its potential interaction with iodine and in fine the gaseous fraction of gaseous iodine reaching the containment and eventually the atmosphere in case of confinement loss of the containment building. The interaction between the Ag-In-Cd melts and the Zircaloy of the guide tubes is expected to have a strong impact on the quantities of Ag, Cd, In released into the primary circuit, which should finally influence the iodine chemistry. Taking into account the previous experimental works in the two preceding theses, we have chosen to study the **In-Zr and Ag-Zr systems** experimentally to establish in a future a complete thermodynamic modeling of the Ag-In-Zr-O system. The study will help to better estimate the quantity of the absorber elements vaporized during the accidental conditions and the progression of the degradation of the absorber rod and of the mixtures (Ag-In-Zr-O) to the bottom of the core.
- **In the case of late phase of the accident**, knowledge of the end state of fuel debris in the reactor vessel is essential for understanding the progression of the accident and in particular the conditions (time and locations) of the eventual rupture of the vessel. If there is no water in the vessel, and if the corium pool is overlaid by a steel liquid layer, then the heat flux might focus on the vessel in front of the steel layer ("focusing effect"). It is more penalizing for thin top metal layers, so that one of the critical point is linked to the determination of the height of the molten steel layer that stratifies above the oxidic pool. The strong influence of material effects on core material mixtures has been demonstrated by several authors [28, 29]. It has been shown [30] that when enough non-oxidized zirconium is available, then metallic uranium migrates to the metal layer. The transfer of species between the U, O, Zr melt and the steel results in a significant density increase of the metallic phase. This increase of density leads to inverse stratification with a metallic layer relocating below the oxidic pool and then a reduction of the thickness of the top metallic layer (even more penalizing situation). In this framework, the knowledge of the complex multiphase system (U-O-Zr-Fe) of the corium will allows to calculate the distribution of chemical elements between the different phases. Even a lot of work has been done on this topic, some uncertainties remain. Among the binaries, U-Zr and the Fe-Zr systems which are key subsystems will be studied in this work.

1.3. References

1. Jacquemain D., Nuclear Power Reactor Core Melt Accidents: Current State of Knowledge. EDP Sciences (2015).
2. Morales Pedraza J., World Major Nuclear Accidents and Their Negative Impact in the Environment Human Health and Public Opinion. International Journal of Energy, Environment and Economics. 21(2):1-23 (2013).
3. Steinbruck M., Stegmaier U., Grosse M., Experiments on Silver-Indium-Cadmium Control Rod Failure During Severe Nuclear Accidents. Ann. Nucl. Energy. 101: 341-357 (2017).
4. Decreton A., Contribution Expérimentale à l'Etude Thermodynamique des Systèmes Ag-Zr et Ag-Cd-In. PhD Thesis, Aix Marseille University (2016).
5. Gajavalli K., Experimental Contribution to Thermodynamics of the Ag-Cd-In, In-Zr and In_2O_3-ZrO_2 Systems. PhD Thesis, Aix Marseille University (2019).
6. Fischer E., Gajavalli K., Mikaelian G., Benigni P., Rogez J., Decreton A., et al., Experimental Study and Thermodynamic Modeling of the Ag-Cd-In System. CALPHAD J. 64: 292-305(2019).
7. Vinson D., Inventory and Description of Commercial Reactor Fuels within the United States: Fuel Cycle Research and Development (2011).
8. The Nuclear Fuel Assembly with the Rod Cluster Control Assembly. Source: www.world-nuclear.org.
9. Bailly H., Ménessier D., Prunier C., Le Combustible Nucléaire des Réacteurs à Eau sous Pression et des Réacteurs à Neutrons Rapides : Conception et Comportement. Eyrolles Editions (1996).
10. Steinbruck M., Barrachin M., Control Rod Behavior During Beyond Design-Basis Accidents in LWRs. Comprehensive Nuclear Materials, Elsevier. 2: 466-498 (2020).
11. Gosset D., Absorber Materials for Generation IV Reactors: Structural Materials for Generation IV Nuclear Reactors. Edited by P.Yvon, Woodhead Publishing (2017).
12. Desgranges C., Comprehension et Prediction du Comportement sous Irradiation Neutronique d'Alliages Absorbants à Base d'Argent. PhD Thesis, Paris XI University-Orsay (1998).
13. International Atomic Energy Agency, Advances in Control Assembly Materials for Water Reactors: Proceedings of a Technical Committee Meeting, IAEA-TECDOC-813, IAEA, Vienna (1993).
14. Adorni M., Carenini L., Mazzini G.et al., Severe Accident Phenomenology, European Technical Safety Organizations Network (2013).
15. International Atomic Energy Agency, Accident Analysis for Nuclear Power Plants with Pressurized Water Reactors, Safety Reports Series No. 30, IAEA, Vienna (2003).
16. Hayward P.J., George, I.M., Determination of the Solidus Temperatures of Zircaloy-4/oxygen Alloys. J. Nucl. Mater. 273(3): 294-301 (1999).
17. Van Dorsselaere J.P., Albiol T., Micaelli J.C., Research on Severe Accidents in Nuclear Power Plants: Nuclear Power - Operation, Safety and Environment, Edited by P. Tsvetkov, (2011).
18. Okamoto H., Fe-Zr (Iron-Zirconium). J. Phase Equilibria and Diffus. 18: 361 (1997).
19. Okamoto, H., Cr-Zr (Chromium-Zirconium). J. Phase Equilibria and Diffus. 14: 768 (1993).

20. Okamoto, H., Ni-Zr (Nickel-Zirconium). J. Phase Equilibria and Diffus. 28: 409 (2007).
21. Luze O. D., Haste T., Barrachin M., Repetto G., Annals of Nuclear Energy Early Phase Fuel Degradation in Phébus FP: Initiating Phenomena of Degradation in Fuel Bundle Tests. Ann. Nucl. Energy. 61: 23–35 (2013).
22. Sepold L., Lind T., Csordás A.P., Stegmaier U., Steinbrück M., Stuckert J., Ag-In-Cd Control Rod Failure in the QUENCH-13 Bundle Test. Ann. Nucl. Energy. 36: 1349–1359(2009).
23. Akers D.W., TMI-2 Core Materials and Fission Product Inventory. Nucl. Eng. Des. 118: 451–461 (1990).
24. Seiler J.M., Tourniaire B., Defoort F., Froment K., Consequences of Material Effects on In-Vessel Retention. Nucl. Eng. Des. 237: 1752–1758 (2007).
25. Bechta S.V., et al., Corium Phase Equilibria Based on MASCA, METCOR and CORPHAD Results. Nucl. Eng. Des. 238: 2761–2771 (2008).
26. Almjashev V.I., et al., Experimental Study of Transient Phenomena in the Three-liquid Oxidic-Metallic Corium Pool. Nucl. Eng. Des. 332: 31–37 (2018).
27. Nandan S., Fichot F., Piar B., A Simplified Model for the Quaternary U-Zr-Fe-O System in the Miscibility Gap. Nucl. Eng. Des. 364: 110608 (2020).
28. Hofmann P., Reactions und Schmelzverhalten der LWR-Corekomponenten UO_2, Zircaloy and Stahl warhend des Abschmelzperiode. KFK 2220, Kernforschungszentrum Karlsruhe. (1976).
29. Gueneau C., Dauvois V., Perodeaud P., Gonella C., Dugne O., Liquid Immiscibility in a (U, O, Zr) Model Corium. J. Nucl. Mater. 254: 158–174 (1998).
30. Bechta S. and Asmolov V., Zr Partitioning Tests in the Cold Crucible Test MA-1, in Proceedings of the OECD MASCA Meeting, Helsinki, Finland (2001).

2. Experimental methods

2.1. Sample synthesis

2.1.1. Powder Metallurgy

The raw materials used for the synthesis of the In-Zr alloys were pure zirconium and indium powders. The purities of these powders are given in **Table 3**. A mechanical mixture of the elemental powders in the appropriate molar ratio is prepared for each alloy composition. The powder mixture is thoroughly blended and pressed into pellets using a press of 5 mm diameter shown in **Figure 8 a**. The whole process is performed inside the glovebox (**Figure 9**) under argon gas atmosphere. This 5 mm diameter press allows to obtain samples with a mass of ~300 mg, which is a sufficient quantity to perform, after annealing, both X-ray diffraction (XRD) analyses and metallographic observations by scanning electron microscopy (SEM). In-Zr samples prepared for thermal analysis, direct reaction and dissolution calorimetry were pressed into pellets of 3 mm diameter using the press shown in **Figure 8 c**.

Each In-Zr binary alloy pellet was wrapped in tantalum foil and sealed under argon in silica tubes with a piece of zirconium acting as an oxygen trap (**Figure 8 b**). The sealed ampoules were then annealed at different temperatures for varying lengths of time. The synthesized compositions and the corresponding annealing conditions are summarized in **Table 4**.

(a) (b) (c)

Figure 8. (a) Powder pellet pressing die set for 5 mm diameter cylindrical sample. (b) Samples wrapped in Ta foils and sealed in a quartz ampoule under inert atmosphere, ready for subsequent annealing (c) Powder pellet pressing die set for 3 mm diameter cylindrical sample.

Table 3. Purities of the materials used in the experiments.

Utility	Chemical name	Supplier	Commercial grade	Purity (mass)	Purification method
Powder reagent	In	Alpha Aesar	325 mesh	0.9999	None
Powder reagent	Zr	Cerac TM Incorporated	325 mesh	0.998	None
Zr used for AgZr synthesis	Zr	Alpha Aesar	Crystal bar (Van Arkel)	0.995	None
Silver shots used for AgZr synthesis	Ag	Alpha Aesar		0.999	None
Fe pieces used for Fe_2Zr synthesis	Fe			0.9997	
Zr used for Fe_2Zr synthesis	Zr		Crystal bar (Van Arkel)	0.9999	
U pieces used for UZr_2 synthesis	U		Nuclear		
Zr used for UZr_2 synthesis	Zr		Crystal bar (Van Arkel)		
Solvent and heat calibration material	Al	Alfa Aesar	-	0.9995	None
Crucible for dissolution calorimetry	Al_2O_3	Umicore	C799 ALSINT alumina	> 0.997	None
Atmosphere	Ar	Air Liquide	Alphagaz 1	> 0.99999 (mole)	Sertronic© O_2, H_2O < 1 ppb
Crucible for direct reaction calorimetry	Alumina	Setaram©	AL23	>0.995	none
Oxide powder bed	HfO_2	CTTC, Limoges	-	0.999	600°C for 4h in air
Reference material	Al_2O_3	Degussit©	AL23	>0.995	none

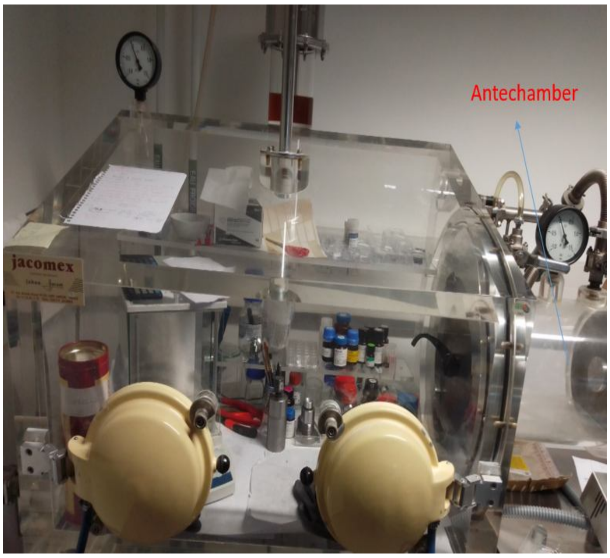

Figure 9. Glove box of the SYMME laboratory.

Table 4. Annealing conditions and compositions of the In-Zr samples used for subsequent phase diagram investigations by SEM and XRD.

1000°C (24 hours) at%Zr	800°C (1 week) at%Zr	600°C (2 months) at%Zr	400°C (1 month) at%Zr	400°C (2 months) at%Zr	330°C (1 month) at%Zr	200°C (1 month) at%Zr
24.90	25.19	23.68	25.53	25.53	25.76	25.63
27.65	27.93	28.44	27.79			30.35
33.17	40.61	35.02				
39.64	50.21	39.99				
55.00		44.96				
75.38		54.89				
80.92		60.00				
		66.00				

2.1.2. Arc melting

The AgZr samples used for dissolution calorimetry were made by arc melting.

The arc melting furnace of the SYMME laboratory that was used for this synthesis is shown in **Figure 10**. It consists of a tungsten electrode and a water cooled movable copper crucible inside a small chamber put under inert argon atmosphere. An external generator controls the electric power supply.

Zr alloys are very sensitive to oxidation at high temperature, particularly at the liquid state. It is therefore important to work in an atmosphere free from of oxygen. Before each melting, the furnace chamber, initially under air, is flushed three times with high purity argon: for each purge, after reaching a residual vacuum of 10^{-3} mbar, the furnace is back filled with argon. Then a piece of zirconium is first melted to trap residual oxygen before melting the sample itself.

Each sample is melted several times to enhance homogeneity. A loss of mass due to silver evaporation is observed after each melting operation, so the number of melts was adjusted on a case by case basis to obtain the desired nominal composition.

Fe_2Zr samples for dissolution calorimetry were not prepared at the SYMME laboratory but supplied by S. Chatain from the LM2T laboratory of CEA Saclay. These samples were also synthesized by arc melting stoichiometric mixtures of Van Arkel Zr and high purity Fe under argon.

UZr_2 samples for dissolution calorimetry were supplied by O. Tougait from the UCCS laboratory of Lille University and were also prepared by arc-melting.

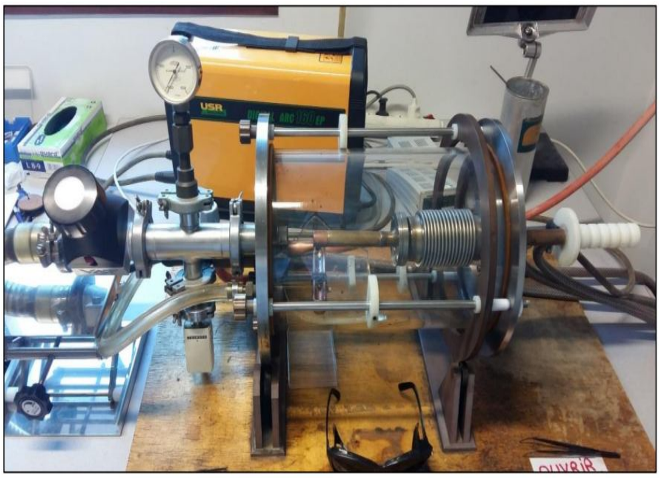

Figure 10. Arc melting furnace of the SYMME laboratory.

2.1.3. Annealing

The ampoules containing the In-Zr samples listed in **Table 4** were first put together in a furnace and heated at 5°C/min to 1000°C and annealed 24 h at this temperature for equilibration. Some of them were then water quenched whereas the rest of the samples were transferred to a 3-zone furnace better suited for long annealing times. The selected temperature and annealing time are given for each alloy in **Table 4**.

Sealed In_3Zr samples prepared for dissolution experiments were heated at 5°C/min in a resistive furnace from room temperature to 1000°C to ensure indium-zirconium reaction and then annealed at 400°C for 2 months. Sealed In_2Zr samples prepared for dissolution calorimetry and heat increment measurements were heated from room temperature to 600°C at 3°C/min and annealed for 48 h at this temperature.

The AgZr alloy for dissolution calorimetry experiments was annealed 40 days at 900°C. The UZr_2 alloy was annealed at 580°C for 2 hours. After annealing and quenching, X-ray diffraction analysis (XRD) and scanning electron microscopy (SEM) were performed on all samples to examine the phases that had formed. In addition, EPMA was performed on some of the oxygen-sensitive In-Zr alloys.

The Fe_2Zr alloys was not annealed. It was characterized by XRD and used at the as-cast state.

2.2. Sample preparation and analysis techniques

2.2.1. X-ray diffraction (XRD)

Phase identification in the alloys was performed using X-ray diffraction. Pure indium and pure zirconium powders used for the synthesis of In-Zr pellets were first characterized at room temperature under vacuum to check for oxidation (see **Figure 11**). **Figure 11** shows that all the X-ray reflections originated from In and Zr metal except few additional peaks from the sample holder (platinum) with no peak related to the oxide.

Next, the binary In-Zr alloys were examined using the same procedure to check the phases present after annealing.

The following protocol was adopted. After quenching, the annealed quartz tubes were broken up in the glove box. The pelleted samples were ground by hand in an agate mortar using a pestle to obtain fine, homogeneous grains. The ground samples were transferred from the glove box to the X-ray diffractometer. Isopropanol was poured over the surface of the samples to prevent oxidation during transfer, and then analysis was carried at room temperature under vacuum to avoid oxidation of the powders.

XRD patterns were collected with a Panalytical X'Pert PRO Multi-Purpose X-Ray diffractometer (40 kV and 40 mA), some of them using Co $K\alpha_1$ and $K\alpha_2$ radiation ($\lambda = 1.7903$ Å) under vaccum while others were acquired using Cu $K\alpha$ radiation ($\lambda = 1.5406$ Å). The 2θ range from 5° to 120° was scanned with a stepsize of 0.01313° and timestep of 150.45 seconds. XRD patterns of the samples were systematically compared to reference patterns from literature using ICS Database (ICSD) and PowderCell software. For In-Zr samples, lattice parameters of the various phases were refined by the Rietveld method with the aid of the Rietica program [1].

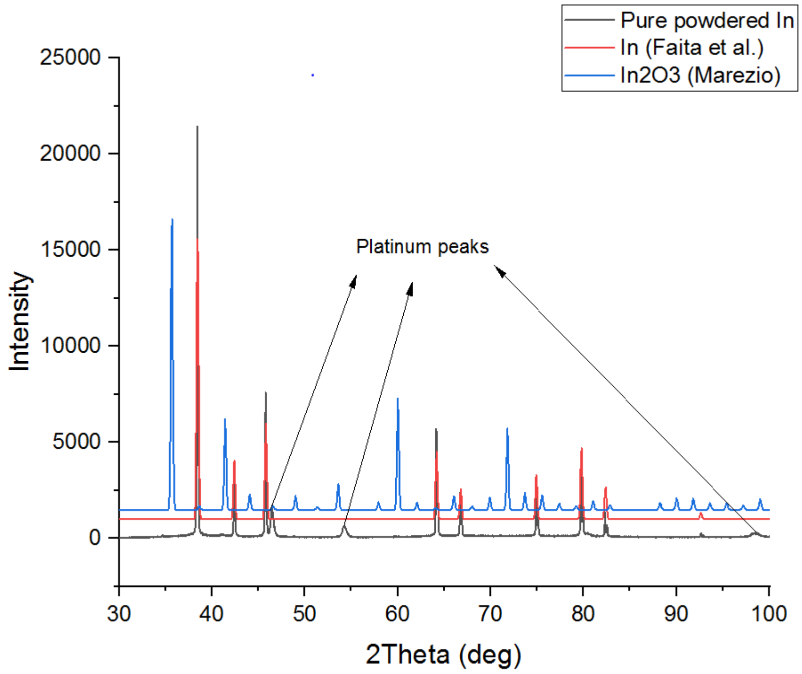

(a)

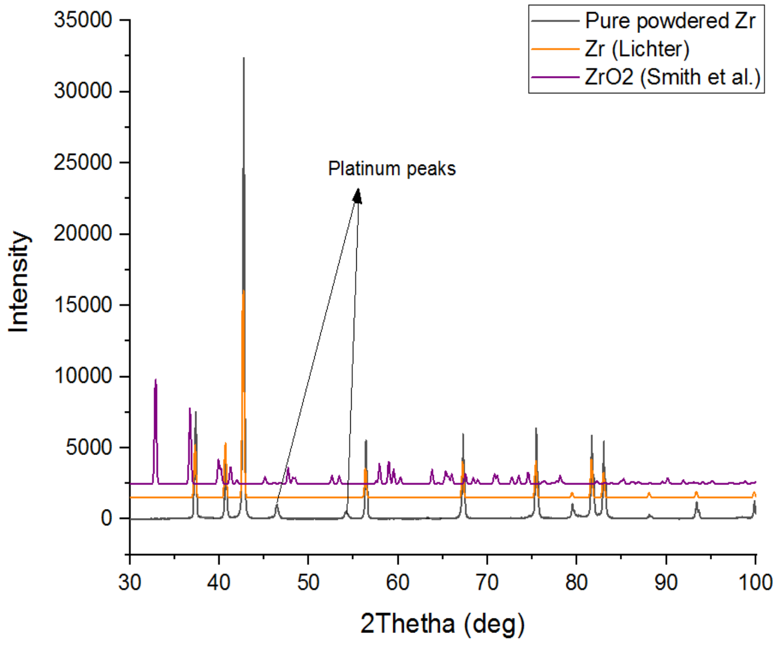

(b)

Figure 11. Comparison of XRD spectra of (a) pure powdered indium with XRD spectra of In by Faita et al. [2] and In_2O_3 by Marezio [3] and (b) pure powdered zirconium with Zr spectra of Lichter [4] and ZrO_2 by Smith and Newkirk [5]. The XRD pattern belongs to indium and zirconium, with no trace of the oxide peaks. All spectra were taken with Co K-α radiation at room temperature.

2.2.2. Polishing

To allow safer and more convenient handling of the samples for metallographic observations and microscopy, the samples were first embedded in cold resin (**Figure 12**).

Figure 12. Mounting of samples using cold resin.

Polishing was carried out using different grades of silicon carbide abrasive paper, starting with P240, followed successively by P600, P800, P1200, P2400 and P4000. During the polishing process, ethanol was frequently poured over the plate to reduce friction and thus the heat generated. Before each change to a finer abrasive paper, the samples were cleaned with ethanol and dried with compressed air. After the polishing with P4000 grade paper, the samples were cleaned with ethanol in an ultrasonic bath for a few minutes to remove impurities from the polishing papers, then rinsed with ethanol and dried with compressed air.

Afterwards, the samples were further polished using diamond sprays and polishing clothes of 6 µm, 3 µm and 1 µm. Again, samples were washed in ultrasonic bath and dried with compressed air before each change to a finer diamond suspension.

2.2.3. Scanning Electron Microscopy (SEM)

After polishing, analyses of the samples were carried out using Scanning Electron Microscopes (SEM): TESCAN Vega in Secondary Electron (SE) and Back-Scattered Electron (BSE) detectors. Chemical compositions of individual phases were obtained by Energy Dispersive spectroscopy (EDS) without standard. The acceleration voltage was adjusted to 20 kV to enhance topological or chemical information.

2.2.4. Electron Probe Microanalysis (EPMA)

Electron probe microanalysis (EPMA) was performed on the most oxygen-sensitive In-Zr compositions (39 - 40 at%Zr) in order to determine the compositions of the phases detected in these samples with greater accuracy.

The composition of the samples was measured by wavelength□dispersive spectrometry (WDS). The oxygen Kα line, zirconium Lα and indium Lα were measured respectively with LPCI (W/Si), LPET ($C_5H_{12}O_4$) and LPET crystals. An accelerating voltage of 15 kV, beam current of 40 nA and an electron beam with diameter of 1 µm were used. For lines and points, the peak counting time for each determined element was set to 20 s, with the background counting time equaling one half (10 s) of the peak counting time at high and low energy background positions. For maps, the dwell time was set to 300 ms. The calibration was done using Titanium oxide (TiO_2) (PI-KEM Ltd. UK, 99.999%, Yew Tree House, Tilley, Wem U.K.) as a standard reference for oxygen, Indium antimony (InSb) (NewMet –Rue de St. Lawrence, Waltham Abbey, Essex, EN9 1PFN U.K., 99.999%, Batch No. 1369 - In) for indium and zirconium (Alpha products, 99.5%, Johnson Matthey GmbH, Karlsruhe, Germany, Batch No E26E10) which was zone refined to remove Hf (99.99%) as a standard reference for zirconium. In order to obtain accurate results and to ensure the absence of calibration drift, intensities over standards considered as samples (Ix) were repeatedly measured between two consecutive In-Zr samples, and it was checked that the ratio of the intensities Ix/Istd was equal to 1. Randomly distributed points and lines were selected for quantification and cartography was done at different areas on the samples.

2.3. Thermal Analysis

2.3.1. Principle

Differential thermal analysis (DTA) consists of measuring the difference in temperature between the sample to be analyzed and an inert reference material showing no transformation in the temperature interval explored. The sample and reference are submitted to the same thermal program. Usually, the heating and cooling rates are kept constant. The differential signal can be plotted as a function of time or temperature and these plots are called thermograms. In thermograms, endothermic or exothermic phase transitions in the sample are detected by deviations from the baseline forming peaks from which characteristic temperatures can be defined.

According to Boettinger et al. [6], during the heating of a sample having an invariant melting, the onset of melting corresponds to the first deviation from the baseline. Experimentally, the determination of this onset temperature is made tricky due to the noise affecting the signal. For this reason, an alternative method of determining the melting temperature is commonly used, which consists of measuring the so-called “extrapolated onset temperature (T_T^{extrap})”. This temperature is taken as the intersection between the descending linear section of the melting peak and the extrapolation of the baseline. [6] (see **Figure 13**).

Boettinger et al. [6] further showed that onset temperature determined by the extrapolation method (T_T^{extrap}) has a higher deviation from the true melting point and a higher heating rate dependence than the onset temperature determined by first deviation from baseline method (T_T^{Onset}) (see Appendix D of [6]). Also considering the fact that alloys usually have a melting range and, therefore, do not melt with a linear section of the DTA curve, using the first deviation from baseline method is more accurate.

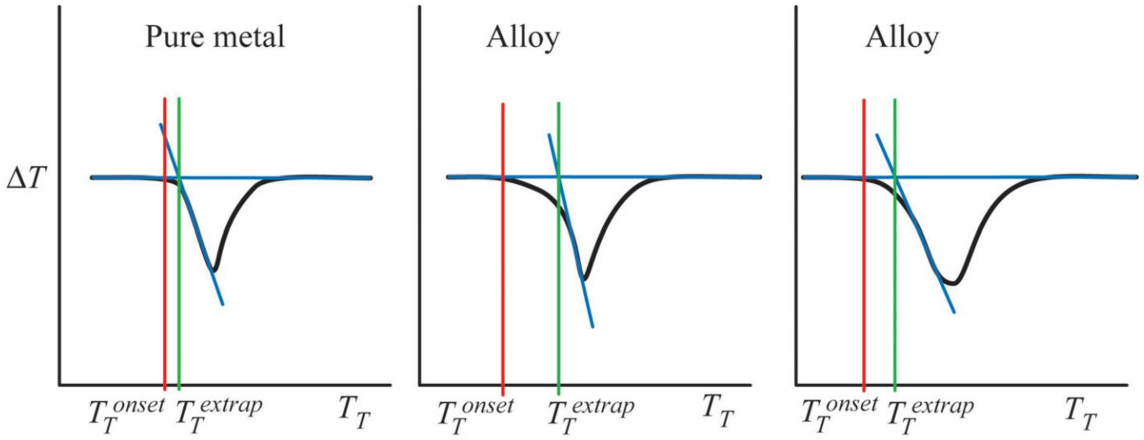

Figure 13. Graphical construction for determination of melting temperatures by the extrapolation method (T_T^{extrap}) or first deviation from baseline method (T_T^{Onset}) [2].

Considering the proposition by Boettinger et al. [2], onset temperature determined by first deviation from baseline method was used to determine the transition temperatures of the calibrants and alloys used in this work. In determination of the onset temperature of indium (see **Figure 15**), using the Calisto software, firstly the peak was extrapolated, of which we could find the point of intersection between extrapolated linear portion and the extrapolated baseline (onset temperature from extrapolation method). Afterwards, using the same software a line was placed at the point which was detected as onset from extrapolation and another line at any point on the baseline in order for the horizontal line to be at the same position of the baseline (see **Figure 15**). This yielded a circle which is at the exact position where we observe deviation of the signal from the baseline in **Figure 15**. This was taken as the onset temperature (T_T^{Onset}) for the melting of the indium, which is lower than the onset temperature detected from extrapolation (T_T^{extrap}) but closer to the reference melting temperature of indium [7].

On heating, for an alloy whose melting takes place through a multiphase domain, the liquidus temperature is taken at end of the melting process. At this point there is an abrupt change of thermal regime therefore a more or less clear break in slope of the differential signal.

2.3.2. Experimental protocols

The phase transitions temperatures in the In-Zr system were determined using three different protocols.

- For samples with composition in the range 20-40 at% Zr, the DTA experiments were carried out with a SETARAM TGA92 instrument equipped with a B-type sensor and sealed tantalum crucibles (see **Figure 14 b**) under an argon atmosphere. The samples were heated from room temperature to 1500°C and then cooled to room temperature at 2 rates, namely 5 and 10°C/min. This DTA setup was temperature calibrated towards the melting transitions of pure metals (Zn, Ag, Au, and Cu) at the same heating and cooling rates. Three heating–cooling runs were performed on each sample to check the reproducibility of the detected transition temperatures.

- For samples with composition in the range 0-10 at%Zr, DTA experiments were carried out with the same instrument but equipped with a S-type sensor and unsealed alumina crucibles (see **Figure 14 c**). These samples were heated from room temperature to 250°C at rates of 5 and 10°C/min. This DTA setup was temperature calibrated towards the melting transitions of pure elements (In, Sn, Bi, Pb, Zn and Al) heated under the same conditions (5 and 10 °C/min). Five heating– cooling runs were performed on each sample.

- For the sample with composition 25.53 at% Zr, the thermal analyses were repeated using a Setaram DSC 111 of Tian-Calvet type (see **Figure 14 d**) having higher sensitivity than conventional DTA instruments. The sample was encapsulated in a sealed stainless steel crucible and the reference was an empty crucible of the same type. The experiments were performed under flowing argon. The sample was heated from 25 to 700°C and cooled from 700 to 25°C at rates of 0.5, 1, 2, 5 and 10 °C/min. Equilibrium temperatures were obtained by extrapolating the characteristic temperatures to zero rate. The temperature calibration of the DSC device was carried out using pure In, Zn, Sb and Al.

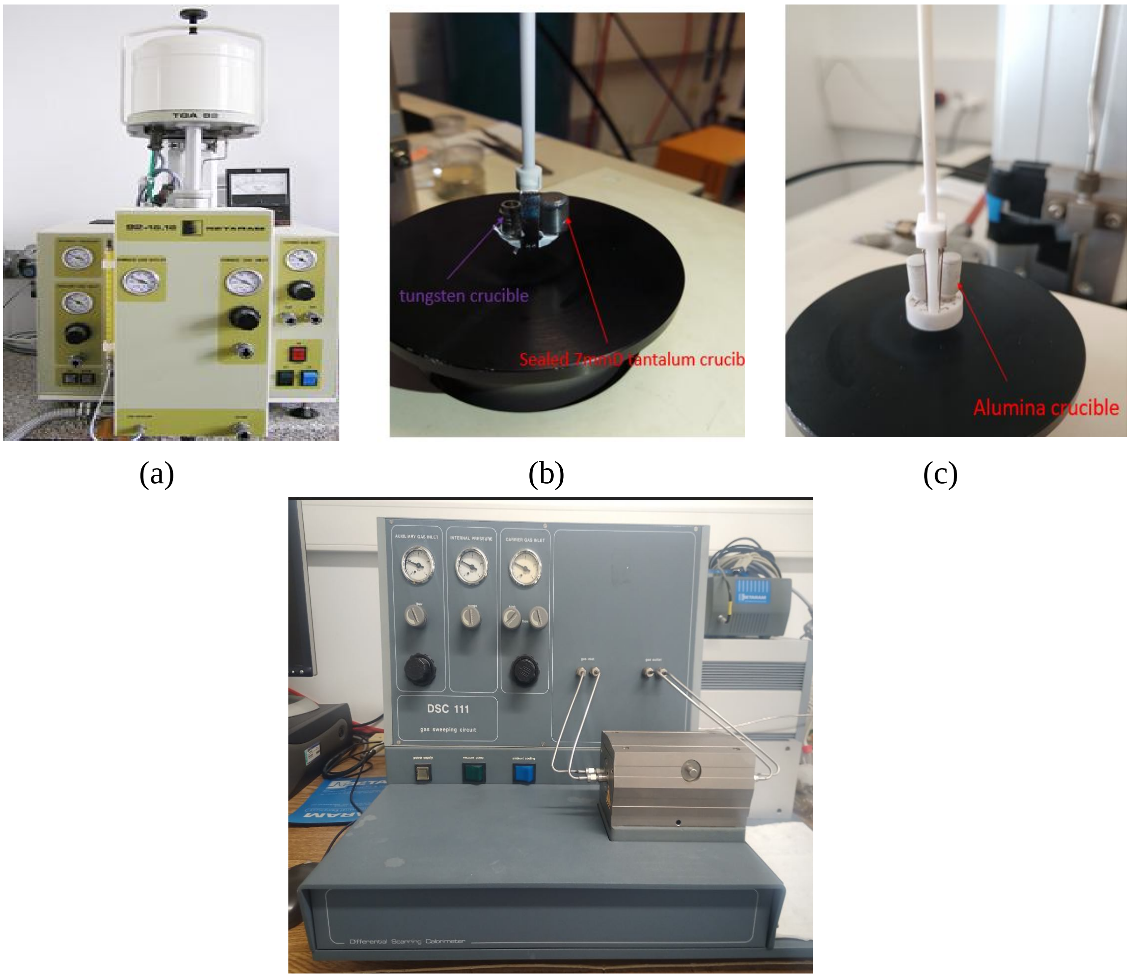

(a) (b) (c)

(d)

Figure 14. (a) SETARAM TGA92 DTA instrument equipped with (b) type B sensor and tantalum crucible and (c) type S sensor and unsealed alumina crucibles (d) Setaram DSC 111 having 3-D Tian-Calvet sensors.

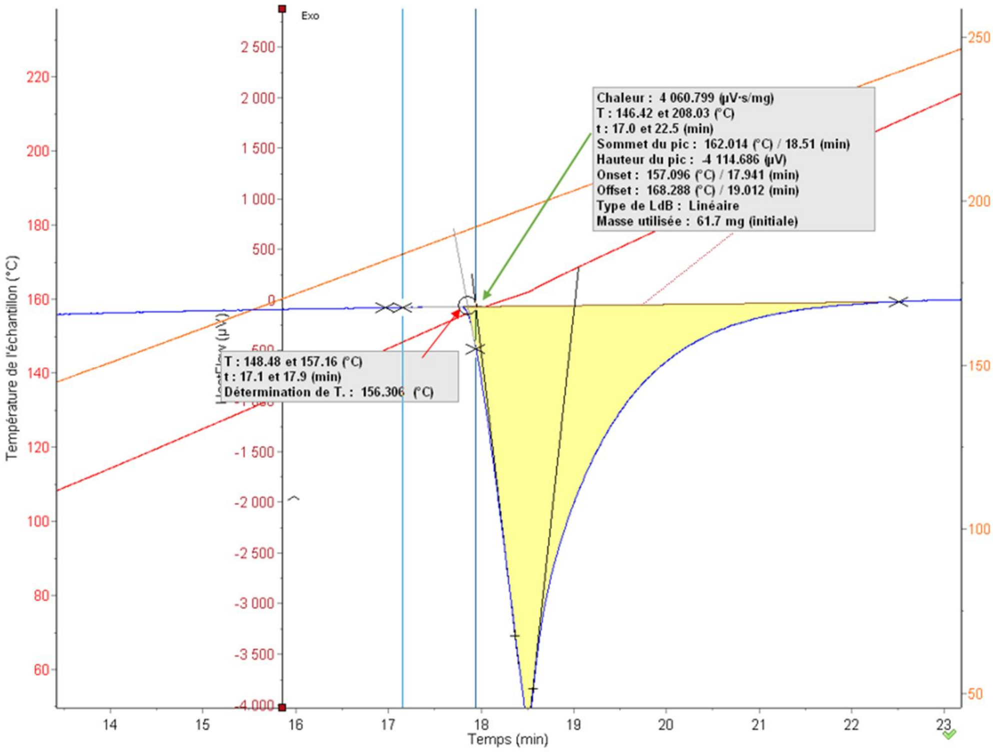

Figure 15. Onset temperature determination on DTA curve for temperature calibration performed with pure indium under purified argon (10°C/ min). It is shown that the temperature measured by the extrapolation method (T_T^{extrap} = 157.09°C) has a higher deviation from the true melting point (156.59 °C) than the temperature measured by first deviation from baseline method (T_T^{Onset} = 156.30 °C). Green arrow: extrapolated onset temperature (T_T^{extrap}). Red arrow: first deviation from baseline (T_T^{Onset}).

2.4. Drop solution calorimetry

2.4.1. Drop solution method

The standard enthalpy of formation can be determined indirectly by drop solution calorimetry. In this method, the enthalpy of formation of $A_\alpha B_\beta$ is calculated using a Hess cycle from the partial drop solution enthalpies at infinite dilution, $\Delta_{ds}H^{\infty,T}_{X,298.15\ K}$, of the elements (X = A or B) and the compound studied (X = $A_\alpha B_\beta$) respectively, in the same solvent with the same so-called working temperature, according to the following equation:

$$\Delta_f H^o_{(A_\alpha B_\beta)}\ (298.15\ K) = \alpha\Delta_{ds}H^{\infty T}_{A,298.15\ K} + \beta\Delta_{ds}H^{\infty T}_{B,298.15\ K} - \Delta_{ds}H^{\infty T}_{A_\alpha B_\beta,298.15\ K} \qquad (2.1)$$

where:

- α and β are the stoichiometric coefficients of the $A_\alpha B_\beta$ compound,
- $\Delta_f H°$ ($A_\alpha B_\beta$), the standard enthalpy of formation of the $A_\alpha B_\beta$ compound,
- $\Delta_{ds}H^{\infty,T}_{X,298.15\ K}$, the partial drop-solution enthalpy of X = A (or B or $A_\alpha B_\beta$) at infinite dilution in the solvent at T.

In solution calorimetry, the choice of solvent-temperature pair is a critical step because it affects measurement feasibility and, ultimately, the uncertainty in the value of the standard enthalpy of formation. In general, the chemical bonds in the solvent must be of the same nature as those in the solute in order to obtain the same order of magnitude for the values of the formation and dissolution enthalpies and, as a result, to reduce measurement uncertainty as much as feasible. In this work, the solvents that best meet this criterion are metallic solvents.

Regarding the choice of temperature, it is necessary that:

- Pure elements and investigated compounds all dissolve in the solvent at the working temperature.
- The dissolutions are sufficiently rapid with regard to the thermal stability of the calorimeter.

At this temperature, the solvent must be in the liquid state, and its vapor pressure must be low enough. Indeed, a calorimetric run lasts between 15 and 24 hours, and significant losses of solvent could distort the calculation of the concentration of solute and therefore the extrapolation of the enthalpy of dissolution at infinite dilution. Furthermore, the enthalpy of vaporization of the solvent would affect the measurement of the enthalpy of dissolution.

In the case of a metallic solvent, to overcome the effects of dilution and the possible solute-solute interaction, it is necessary to determine the partial enthalpy of drop dissolution of the compound and the elements, as a function of composition and extrapolate the results to infinite dilution $\Delta_{sol}H^{\infty}$. It is therefore necessary to study a large number of compositions (it means several drops) for this value to be determined with precision. The solubility of both elements in the solvent must therefore also be sufficiently extensive.

2.4.2. Description of the Calorimeter

A high-temperature Tian Calvet isothermal calorimeter (**Figure 16**) was used. The calorimeter consists of an oven surrounded by a series of insulators to achieve a high thermal inertia. The calorimeter core contains two cylindrical cells, one serving as a reference and the other as a sample cell, both surrounded by thermopiles having more than 200 Pt10%Rh-Pt thermocouples. The temperatures of the reference and sample cells are measured using a Pt10%Rh-Pt thermocouple inserted between the cells in the isothermal alumina block. The thermopiles achieve accurate measurement of the heat flows absorbed or produced in the reaction and reference cells. The thermopiles are connected in a differential circuit, and the differential voltage is measured and digitized using a Keithley 2182 Nanovoltmeter and then recorded on a computer.

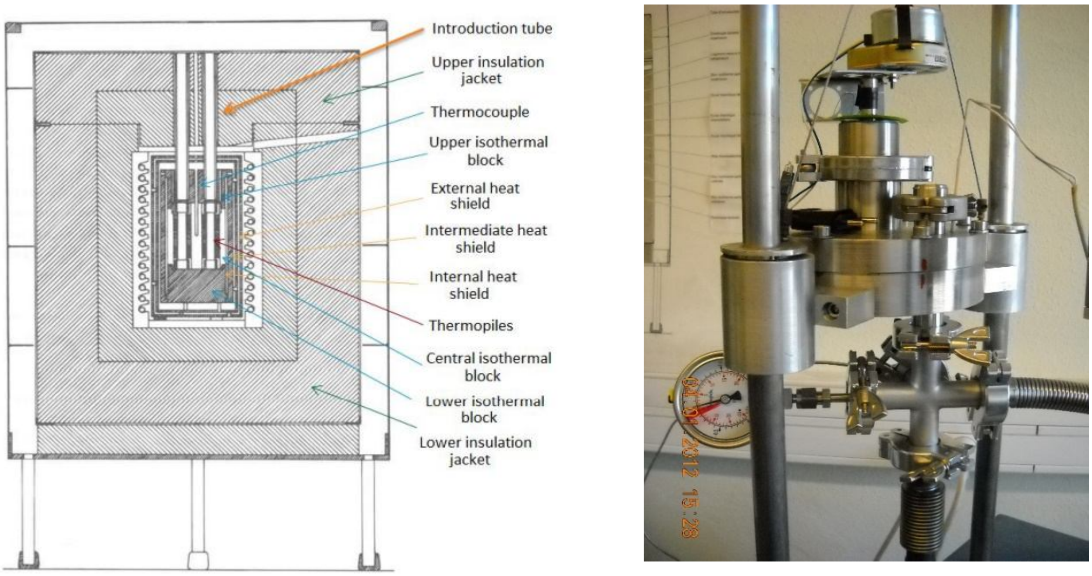

a) General drawing of the calorimeter b) Sample introduction device

Figure 16. High temperature Tian-Calvet calorimeter.

This calorimeter measures, by the Seebeck effect, the differential heat flux exchanged between each thermopile and the thermostatic chamber. The amount of heat is then obtained by integrating the differential heat flux measured over the duration of the phenomenon.

2.4.3. Procedure

The alumina crucible containing the solvent is placed in a silica tube. The samples are kept outside the calorimeter in a barrel that is connected to the silica tube and positioned vertically over it (**Figure 16 b**). The barrel was operated manually to drop the sample into the bath.

In order to prevent the oxidation of the metallic solvent as well as that of the samples, the entire experimental set-up is first put under an argon atmosphere (Alphagaz 1) at room temperature, by means of five cycles of purges at a primary vacuum and filling at atmospheric pressure. To minimize the risk of oxidation due to the residual amount (<2 ppm) of oxygen present in the commercial argon a short section of Ti or Zr tube acting as an oxygen getter can be placed on top of the crucible inside the silica tube.

The reference cell is permanently loaded with an alumina tube whilst the vitreous silica tube containing the bath of aluminum (Alfa Aesar, 99.99%) in an alumina crucible is inserted into the reaction cell. The choice of an alumina crucible was based on the fact that no significant reaction between the crucible and bath is expected to occur up to the temperature range of measurement (996-1273K). The silica tube is gently lowered into the calorimeter, which is kept at the experiment temperature, and after a transient thermal regime, the entire assembly reaches thermal equilibrium, yielding a stable baseline. After obtaining a stable thermal regime, calibration was done by dropping pure aluminum samples maintained at ambient temperature, 298 K into the bath at the calorimeter temperature to check the linearity response of the calorimeter. Then, the samples (In_3Zr, In_2Zr, AgZr, Fe_2Zr and UZr_2), initially maintained at ambient temperature were dropped successively into the liquid aluminum. Between each fall, there is sufficient stabilization time (~ 1 hour) so that the dissolution ends and the calorimetric signal returns to the level of the initial base. The temperature of the samples was measured before each drop. The differential signal of the calorimeter is recorded vs. time during the whole experiment. When a sample is dropped, the recorded heat effect corresponds to the heating of the sample from room temperature to the calorimeter temperature and its dissolution in liquid aluminum at the calorimeter temperature. The silica tube assembly is removed from the calorimeter at the end of the experiment, and the bath cooled down to room temperature under inert atmosphere for further investigations.

2.4.4. Thermogram processing

The thermogram recorded during a complete experiment comprises a series of calibration and sample peaks. For each peak the amount of heat released or absorbed during the thermal effect is proportional to the area under the peak. The acquisition data file is processed off-line by computing the area of each recorded peak by numerical integration using the Simpson method after subtracting the baseline from the calorimetric signal. This processing is done with a homemade Python software.

The shape of the sample peaks depends mainly on the exothermic or endothermic character of the dissolution reaction and also possibly of the dissolution kinetics if it is slow. The time interval between a sample drop and the return to the baseline gives an estimate of the duration of the dissolution process.

The thermal coupling between the silica tube and the thermopile of the sample cell calorimeter varies slightly from one manipulation to another hence the calorimeter must be recalibrated at each experiment to avoid the influence of these variations.

2.5. High temperature direct reaction calorimetry

2.5.1. High temperature direct synthesis method

Another way of determining the standard enthalpy of formation of a compound is by direct reaction calorimetry.

The reaction which occurs in the calorimeter after dropping sample pellets of an A + B mechanical mixture, initially at room temperature T_0, in the calorimeter maintained at temperature T_c, corresponds to an isothermal reaction of formation of the AB compound given by:

$$\alpha\langle A\rangle_{s,T_0} + \beta\langle B\rangle_{s,T_0} \rightarrow \langle A_\alpha B_\beta\rangle_{s,T_c};\ \Delta H_2 \qquad (2.2)$$

The heat effect (ΔH2) corresponding to the above reaction includes both the enthalpy of formation of the compound $A_\alpha B_\beta$, at T_c as well as the heat increment of the compound from room temperature to T_c. The standard enthalpy of formation can be obtained from a Hess cycle if the heat increment of the compound from room temperature T_0 to T_c is known. It is determined by dropping the formed alloy sample $A_\alpha B_\beta$ into the calorimeter with the corresponding reaction:

$$\langle A_\alpha B_\beta \rangle_{s,T_O} \rightarrow \langle A_\alpha B_\beta \rangle_{s,T_c}; \Delta H_3 \qquad (2.3)$$

Combining the two previous reactions, the standard molar enthalpy of formation of the $A_\alpha B_\beta$ compound at room temperature is obtained as:

$$\Delta_f H^o_{(A_\alpha B_\beta)} = \Delta H_2 - \Delta H_3 \qquad (2.4)$$

2.5.2. Procedure

Heat increment measurements were performed by drop calorimetry using a MHTC-96 Setaram© calorimeter used in isothermal mode. The calorimetric cell was heated by a vertical furnace. The experiments were carried out under flowing argon atmosphere purified using a subtronic 500 getter from Sertronic© that decreases water and oxygen impurities down to 1 ppb. A small layer (~ 5 mm thick) of hafnia (HfO_2) powder was placed inside the alumina crucible in order to homogenize the thermal coupling between the sample and the sensor. The calibration of the calorimeter was achieved by dropping α-alumina pieces (60-100 mg) into the crucible before and after each In_2Zr sample drop. The sensibility of the calorimetric cell was obtained using α-alumina data compiled by Sabbah et al. [8]. The room temperature was kept constant using an air conditioner, the temperature of the Ar-tight container prior to each drop was measured with a thermometer. The temperature of the calorimetric cell was calibrated towards the melting points of pure Al, Ag and Au. The uncertainty of the temperature of the cell is then estimated to be ± 1 K at $T_c = 1273$ K. The fluctuations of the thermopile are ± 0.1 µV at 1273 K. The baseline choice and the peak integration were done using the CALISTO Setaram© software.

The experimental standard deviation of the mean (u) was obtained from the experimental standard deviation on the data set (s) using a Type A evaluation method. Due to the small number of measurements used to estimate the expanded uncertainty, a coverage factor ($k = t_{\upsilon,p}$) according to Student's Law was applied. The later depends on the effective degrees of freedom (ν) that was calculated using the Welch-Satterthwaite formula given in the Guide to the Expression of Uncertainty in Measurement [9] and in [10]. Finally, the expanded uncertainty ($U = t_{\upsilon,p} \frac{s}{\sqrt{N}}$) was calculated with a confidence level of 95%.

2.6. Experimental difficulties

In this section, the main difficulties encountered during the experiments are summarized.

The samples were prepared from high purity starting materials, in particular using high quality pure Zr (van Arkel). However, Zr has a high affinity to oxygen. For this reason, the In-Zr and Ag-Zr alloys were synthesized in an inert atmosphere of purified Ar. For the annealing step, the samples were wrapped in tantalum foil to prevent the reducing action of Zr on the silica, and then sealed in silica tubes under argon with a piece of zirconium acting as an oxygen trap. Despite these precautions, oxide phases were found in some of the samples during characterization.

In addition to the high reactivity of the alloys towards oxygen, the high melting point of pure zirconium and the existence of some intermetallic compounds with a high melting point was a second experimental difficulty. At these high temperatures, the vapor pressure of pure indium is also high (e.g. 0.13 atm at 2000 K) and indium loss by vaporization is hardly avoidable. In the synthesis of alloys by arc melting, this phenomenon made it difficult to achieve the desired molar ratios. The immiscibility of the elements In and Zr in the liquid state also contributed to this problem. To limit indium loss by vaporization during the thermal analyses of In-Zr alloys, samples were hermetically sealed in tantalum crucibles.

2.7. References

1. Hunter B.A., Howard C.J., RIETICA: A computer program for rietveld analysis of X-ray and neutron powder diffraction patterns, (Lucas Heights, Australia). (1998).
2. Faita F.L., Ersching K., Acuna J.J.S., Campos C.E.M., Pizani P.S., Structure and Microstructure of In_4Te_3 Nano-Powders Prepared by Solid State Reaction. Materials Chemistry and Physics. 130 (3): 1361-1365 (2011).
3. Marezio M., Refinement of the Crystal Structure Of In_2O_3 at Two Wavelengths. Acta Crystalographica. 20(6): 723-728 (1966).
4. Lichter B.D., Precision Lattice Parameter of Zirconium Oxygen Solid Solution. Transactions of the Metallurgical Society of AIME. 218:1015 -1018 (1960).
5. Smith D. K., Newkirk W., The Crystal Structure of Baddeleyite (Monoclinic Zro_2) and its Relation to the Polymorphism of Zro_2. Acta Crystalographica. 18(6): 983-991 (1965).
6. Boettinger W.J., Kattner U.R., Moon K.W., Perepezko J.H., NIST Recommended Practice Guide: DTA and Heat-Flux DSC Measurements of Alloy Melting and Freezing, (2006).
7. Preston-Thomas H., The International Temperature Scale of 1990 (ITS-90). Metrologia. 27: 3-10 (1990).
8. Sabbah R., Xu-Wu A., Chickos J.S., Leitão M.L.P., Roux M.V., Torres L.A., Reference materials for calorimetry and differential thermal analysis, Thermochimica Acta. 331: 93–204 (1999).
9. Guide to the Expression of Uncertainty in Measurement, International Organization for Standardization(Geneva,Switzerland)1995. https://www.iso.org/sites/JCGM/GUM/JCGM100/C045315e-html/C045315e.html?csnumber=50461.
10. Expression of the Uncertainty of Measurement in Calibration - European co-operation for Accreditation, Report. EA-4/02 M. (1999).

3. Study of the In-Zr system

3.1. Introduction

The indium-zirconium system is significant in the context of the modeling of the interaction between the Ag-In-Cd control rod and the zircaloy guide tube, as was mentioned in Chapter 1. This system is largely unknown, nevertheless, the existence of various intermetallic compounds (In_3Zr, In_2Zr, InZr, $InZr_2$, and $InZr_3$) is established. If they are characterized from a structural point of view, there is a lack of experimental thermodynamic data since only a measurement of standard enthalpy formation of In_2Zr is available. There is also little information on the invariant transformations both on the Zr -rich and In-rich sides of the system.

The work discussed in this chapter aims to contribute to a deeper understanding of this system. This goal has been accomplished by using many experimental techniques, i.e. equilibrating different In-Zr alloys at constant temperature followed by metallography (SEM), X-ray diffraction analysis, differential thermal analysis (DTA), dissolution and direct reaction calorimetry.

We had optimistically anticipated more important results at the beginning of this work, but we encountered many difficulties in the preparation of the samples, which was somewhat expected given the previous unsuccessful synthesis attempts.

The reasons for the difficulties encountered in preparing the samples are:

- Immiscibility of liquid Zr and In at high temperature,
- A steep difference in their melting points,
- High vapor pressure of In at melting point of Zr which makes it difficult to fuse them by arc-welding without mass loss of In,
- High oxygen affinity for both elements.

Despite these difficulties, a satisfactory method of elaboration was finally developed, which allowed us to obtain new relevant results which are reported in this Chapter.

The structure of this chapter is as follows:

- First, we provide a thorough description of the available experimental information, equilibrium phase diagram and thermodynamic properties on the In-Zr binary system.
- Then, the results obtained from the experimental techniques presented in chapter 2, X-ray diffraction analysis (XRD), scanning electron microscopy (SEM), dissolution and direct reaction calorimetry are presented and then discussed. The objective is that these new experimental data will serve as an input for the CALPHAD modeling of the In-Zr system carried out in IRSN.
- Finally, conclusion and perspectives are outlined.

3.2. Bibliography

3.2.1. In-Zr System

The different reviews of available data in the In-Zr system performed successively by Lustman et al. [1] and Okamoto [2] show that there is a very limited number of studies, even though some experimental investigations have been recently performed [3-5]. It must be also highlighted that no CALPHAD assessment of the In-Zr system was published. An unpublished and very preliminary modelling of the system was nevertheless performed by E. Fischer [6] in the framework of the NUCLEA database currently under development which will be presented in this document.

The In-Zr phase diagram assessed by Okamoto [2] in **Figure 18** is based on very limited experimental information obtained by Betterton and Noyce in the zirconium-rich region [7], by Dieva [8] in the indium-rich region and by Schubert et al. [9, 10] who identified five intermetallic compounds.

Betterton and Noyce [7] performed an experimental study of the Zr-rich side (0-26 at% In) by using X-ray and metallography. The alloys were prepared from 99.95% iodide zirconium and 99.99% In starting materials and were arc cast and then annealed in silica capsules with protective foils of zirconium and molybdenum in a temperature range of 773 K-1573 K. Indium was found to dissolve appreciably in both hexagonal (α) and cubic (β) zirconium. The α-phase was shown to be involved in a peritectoid reaction with the β phase and a fcc cubic phase (γ) of stoichiometry $InZr_3$ (with a large non stochiometric domain) at 1276 ± 20 K (**Figure 17**), as follows:

$$\beta(9.3\text{ at.\% In}) + \gamma\ (22.4\text{ at.\% In}) \leftrightarrow \alpha\ (10.1\text{ at.\% In}).$$

X-ray examination of the γ-phase showed that its crystal structure was face-centered cubic, similar to that of copper, with a lattice parameter $a = 4.45 \pm 0.01$ Å.

Betterton and Noyce [7] also mentioned a eutectic transformation between liquid, β and γ according to the reaction:

$$\beta + \gamma \leftrightarrow L\ (22\text{ at.\% In})$$

but without giving any value of the eutectic temperature.

In the indium-rich region, the solubility of zirconium in liquid indium measured by Dieva [8], in the temperature range 600-1240 K, led to the following correlation:

$$\log C = 1.87 - 3100/T \qquad (3.1)$$

where C is the composition in Zr (in at.%) in the liquid, T is temperature in K and log is the logarithm with base 10.

Equation (3.1) gives very low solubility of zirconium in liquid indium, indicating a tendency to immiscibility between both chemical elements, previously predicted from a theoretical point of view by Dasarathy [11].

According to this author, the liquid immiscibility of a binary alloy (A and B) can be calculated using the Mott's number.

$$\frac{1}{2}\frac{(V_A+V_B)(\delta_A-\delta_A)^2-2RT}{23.060(X_A-X_B)^2} \tag{3.2}$$

where:

- V_A and V_B are the atomic volumes of components A and B,
- X_A and X_B are the electronegativities of the two elements. T is the melting point of the more refractory component of the system, zirconium in the In-Zr case.
- $\delta_A = \left(\frac{\Delta E_A^V}{V_A}\right)^{\frac{1}{2}}$ and $\delta_B = \left(\frac{\Delta E_B^V}{V_B}\right)^{\frac{1}{2}}$ are called solubility parameters. These parameters are regarded as the binding energies of the components, ΔE^V being the component vaporization energies.

Dasarathy [11], reported that if the Mott's number of a binary system was greater than the maximum number of Pauling bonds which the two metals could form, then liquid immiscibility is expected. For In and Zr, with electronegativity of 1.48 and 1.78 respectively, the calculation made using the respective maximum valences, the Mott's number obtained was ∞. This implies that strong liquid immiscibility is predicted in alloys of indium with zirconium.

Five intermetallic compounds were reported in the In-Zr system [9, 10, 13]: In_3Zr, In_2Zr, InZr, $InZr_2$, $InZr_3$. Their invariant transformations and melting points are largely unknown as shown in **Figure 18**. The structures of the phases were reported to be:

- InZr face centered cubic [9],
- In_2Zr centered tetragonal [10],
- α-In_3Zr tetragonal (16 atoms) at low temperature and β-In_3Zr tetragonal (8 atoms) at high temperature [10],
- $InZr_2$ tetragonal [10],
- γ-$InZr_3$ simple cubic of type $AuCu_3$ [12, 13].

The details of the crystal structures and the values of the lattice parameters for In-Zr intermetallic compounds are summarized in **Table 5** and **Table 6** respectively.

Table 5. Crystal structures for the intermetallic compounds in the In-Zr system.

Phase	Pearson Symbol	Space group	Strukturberichte	Prototype	Reference
In	tI2	I4/mmm	A6	In	[14]
β-In_3Zr	tI8	I4/mmm	$D0_{22}$	Al_3Ti	[10]
α-In_3Zr	tI16	I4/mmm	$D0_{23}$	Al_3Zr	[10]
In_2Zr	tI24	I41/amd	-	$HfGa_2$	[3, 4, 10]
InZr	cF4	$Fm\bar{3}m$	A1	Cu	[9]
$InZr_2$	tP4	P4/mmm	$L1_0$	AuCu	[9]
$InZr_3$	cP4	$Pm\bar{3}m$	$L1_2$	$AuCu_3$	[13]
β-Zr	cI2	$Im\bar{3}m$	A2	W	[15]
α-Zr	hP2	P63/mmc	A3	Mg	[14]

Table 6. Lattice parameter data for the intermetallic compounds in the In-Zr system.

Compound	Composition (at% In)	Lattice parameters		Reference
		a (nm)	b (nm)	
In	100	0.32512	0.4967	[16]
β-In$_3$Zr	75	0.4238	0.9786	[10]
α-In$_3$Zr	75	0.4303	1.894	[10]
In$_2$Zr	66.7	0.4387	2.7238	[4]
In$_2$Zr	66.7	0.4381	2.7220	[5]
In$_2$Zr	66.7	0.4385	2.7230	[10]
InZr	50	0.4418		[9]
InZr$_2$	33.3	0.442	0.4460	[9]
InZr$_3$	24-25	0.445(6)		[10]
β-Zr	0	0.3609		[16]
α-Zr	0	0.32316	0.51475	[17]

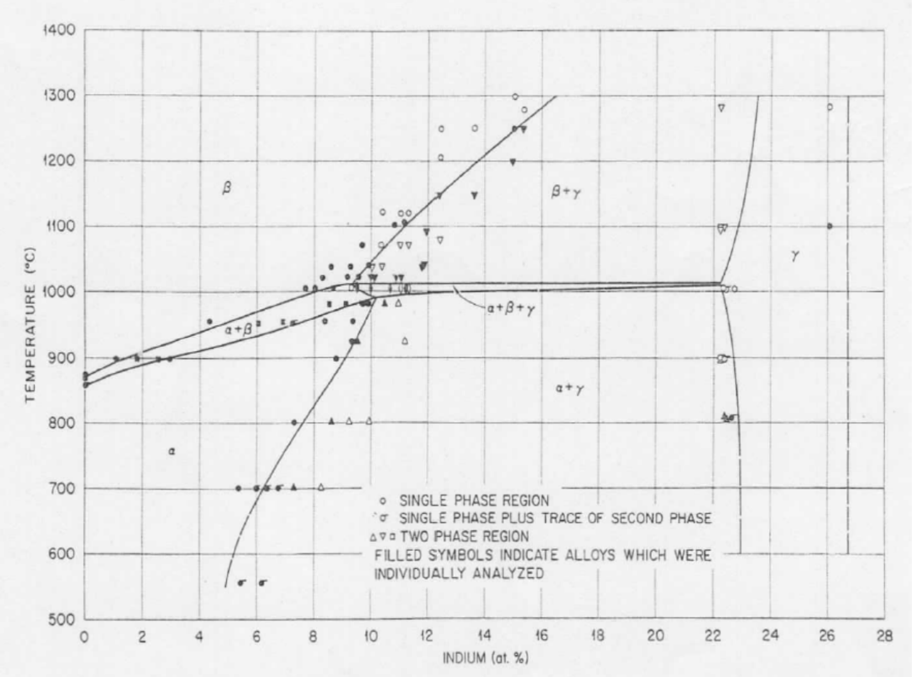

Figure 17. Zr-rich region of the In-Zr diagram by Betterton and Noyce [7].

The previous studies guided Okamoto [2] to propose the tentative diagram reported on **Figure 18**.

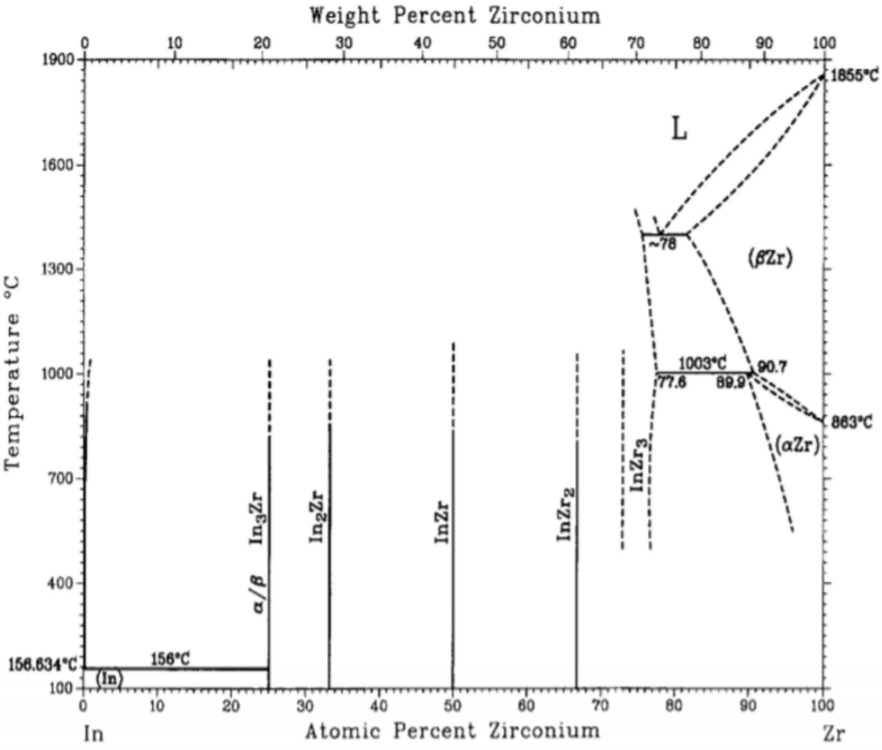

Figure 18. In-Zr phase diagram according to Okamoto [2].

More recently, the X-ray diffraction study of the Ag-In-Zr ternary isothermal section at 870 K by Gulay et al. [3], confirmed the existence of the five intermetallic binary compounds In_3Zr, In_2Zr, InZr, $InZr_2$ and $InZr_3$.

Later on the crystal structure and properties of In_2Zr were examined by Zumdick et al. [4] using single crystal X-ray diffraction data. The charge distributions and chemical bonding were also investigated by electronic structure calculations. The results obtained in terms of crystallographic structure and lattice parameter data were in agreement with previous data reported by Schubert et al. [10].

Saitovitch et al. [5], investigated intermetallic compounds of the In-Zr system as a function of temperature ($15 \leq T \leq 1200$ K), using perturbed angular correlation (PAC) spectroscopy. The samples with Zr/In ratio of 1/2, 1/3, 2/1 and 3/1 were prepared by arc melting and doped with ^{111}In, by diffusion at 1200 K. Before doping, the compounds were characterized by X-ray diffraction (XRD) analysis, both as-cast and after annealing. It was found that in the as-cast state the compounds were usually not obtained as single-phase materials. The comparison of the XRD spectrum of the as-cast Zr/In 1/2 to that of indium metal (**Figure 19**) showed that, although the sample was remelted several times in the furnace most of its strong X-ray reflections were from indium metal. Only a few weak, broad lines (red) belong to the intermetallic phase In_2Zr. By contrast, the X-ray pattern of the annealed sample changed to that of an $HfGa_2$-type compound and the room temperature lattice parameters a = 0.4381 nm, c = 2.722 nm derived from **Figure 19** were in very good agreement with the values reported by Schubert et al. [10] and Zumdick et al. [4]. The results obtained for XRD spectrum of Zr/ In =1/3 was similar to Zr/In = 1/2 showing only broad reflections belonging – with comparable intensities – to indium metal and to the intermetallic compound In_2Zr. It was interpreted that In_3Zr has probably a non-congruent melting. When the Zr/In=1/3 ingot was annealed at 1200 K for 24 hrs, the reflections of In-metal disappeared as in the case of Zr/In=1/2. The remaining narrow lines however, were only those of the phase In_2Zr and the authors were surprisingly unable to detect any signature of In_3Zr. In contrast to Zr/In = 1/2 and Zr/In = 1/3, the XRD pattern of as-cast Zr/In = 2 and Zr/In = 3 contained no In-metal reflections. The AuCu and Au_3Cu structures of respectively $InZr_2$ and $InZr_3$, were observed. In these cases, annealing at 1200 K for 24hrs reduced the line widths, but left the spectra otherwise unchanged. These two compounds have probably congruent melting or form easily on cooling from the liquid.

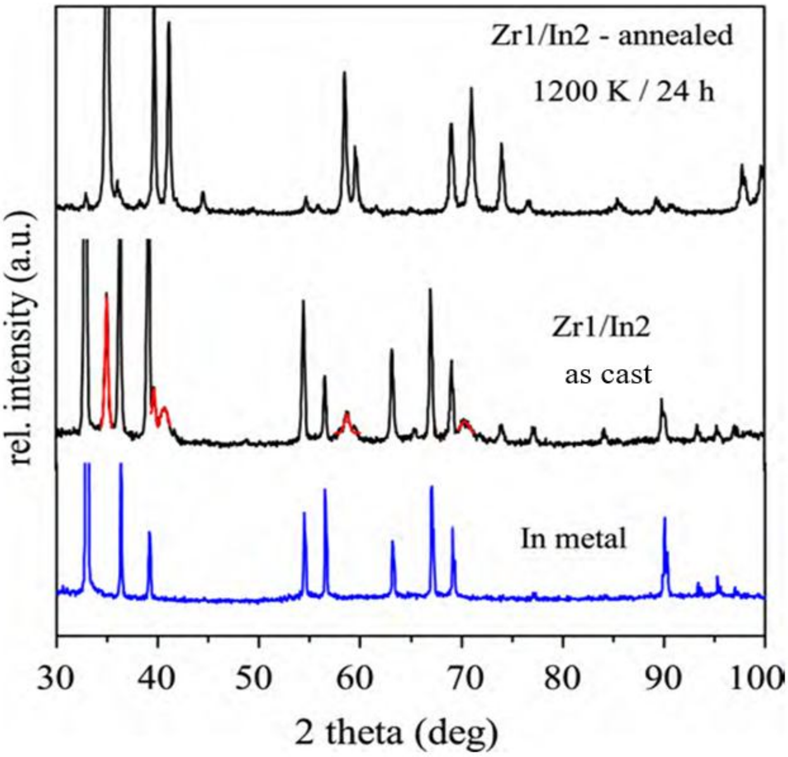

Figure 19. XRD diffraction spectra of In metal and Zr/In = 1/2 alloy in the as-cast state and after annealing 24 h at 1200K [5].

Very recently, the Zr-rich part (at.% Zr >74) of the In-Zr phase diagram already investigated by Betterton and Noyce [7] was confirmed by the metallographic investigations of Gajavalli [18]. As a representative example, the microstructure obtained for the 84.75 at.%Zr sample showed that $InZr_3$ in equilibrium with β-Zr had a composition of 79.23 at.%Zr, confirming the finding of Betterton and Noyce [7] that this compound had a rather large stability domain around its 75 at.% theoretical stoichiometric composition. However, the results from Gajavalli [18] indicated a larger $InZr_3$ stability domain than found by Betterton and Noyce [7]. According to Betterton and Noyce [7], this domain ranges from at least 73.9 at.%Zr up to 77.4 at.%Zr (**Figure 17**), whilst combining the SEM-EDS analyses obtained on various samples, Gajavalli [18] concluded that this domain extends roughly from 72 at.%Zr up to 79 at.%Zr. Gajavalli [18] mentioned that further investigation using EPMA-WDS were needed to obtain more reliable information in the 50-75 at.%Zr region of the In-Zr phase diagram.

3.2.2. Thermodynamic properties

Kneip et al. [19] measured the specific heat of dilute alloys of indium in hexagonal zirconium between 1.2 K and 4.5 K by using adiabatic calorimetry. This study brings no relevant information for assessing high temperature equilibria.

Meschel and Kleppa [20] tried to measure the standard enthalpy of formation of In_3Zr, In_2Zr, InZr and $InZr_2$ intermetallic compounds by using high temperature direct synthesis calorimetry, in the frame of a more general study aiming to determine the standard enthalpies of formation of some transition metal-indium compounds. The experiments were performed at 1273 K under a protective atmosphere of argon gas, which was purified by passing it over titanium chips at 1173 K. A boron nitride (BN) crucible was used to contain the samples. In and Zr powders were mixed in appropriate molar ratios and dropped from room temperature into the calorimeter maintained at 1273 K. They observed that the predominant phase identified by XRD in all samples was In_2Zr. On this basis, they concluded that In_2Zr was probably congruent and the most stable compound in the system [20]. In their experiment, the following reaction was expected to take place in the calorimeter:

$$\mathrm{Zr\ (s,\ 298\ K) + 2In\ (s,\ 298\ K) = In_2Zr\ (s\ or\ l,\ 1273\ K)} \quad \Delta H_1 \qquad (3.3)$$

The reacted pellets were then reused to determine their heat contents in a successive measurement, corresponding to the following reaction:

$$\mathrm{ZrIn_2\ (s,\ 298\ K) = In_2Zr\ (s\ or\ l,\ 1273\ K)} \quad \Delta H_2 \qquad (3.4)$$

The standard enthalpy of formation of In_2Zr was then deduced from the difference; $\Delta H_1 - \Delta H_2$:

$$\Delta_f H^\circ_{In_2Zr} = -114.9 \pm 6.9\ kJ.mol^{-1}\ i.e,\ \Delta_f H^\circ_{In_2Zr} = -38.3 \pm 2.3\ kJ.mol^{-1}.at^{-1}$$

These results have been recently confirmed by Gajavalli [18] who measured the standard enthalpy of formation of the In_2Zr compound using the same technique at the same temperature, 1273 K. The samples for the experiment were prepared inside a glove box under flowing purified argon. The standard molar enthalpy of formation of In_2Zr compound obtained in [18] -36.5 ± 0.9 $kJ.mol^{-1}.at^{-1}$ was in quantitative agreement with the Meschel and Kleppa's [20] value (**Table 7**).

Table 7. Comparison of the measured standard enthalpies of formation of In_2Zr.

T/K	$\Delta_f H^\circ_{In_2Zr}$ $kJ.mol^{-1}.at^{-1}$	Uncertainty $kJ.mol^{-1}.at^{-1}$	Calorimetry technique	Reference
1273	-38.3	2.3	Direct synthesis	[20]
1273	-36.5	0.9	Direct synthesis	[18]

3.2.3. Calphad modelling

E. Fischer [6] performed a very preliminary CALPHAD modelling based on the previously discussed experimental results and this assessment is integrated into the thermodynamic NUCLEA database currently developed at IRSN. The stoichiometric phases (In_3Zr, In_2Zr, InZr, $InZr_2$, $InZr_3$) were modelled as line compounds whilst substitutional model was used for the solution phases (bcc_A2, hcp_A3, liquid) where the excess interaction parameters were described by a Redlich-Kister polynomial and optimized by using the Lukas et al. computer program [21].

For this calculation:

- The formation enthalpy of In_2Zr at 298 K from Meschel and Kleppa [20] was fixed. In_2Zr was considered as the most stable compound at room temperature according to Meschel and Kleppa's suggestion.
- The formation enthalpies for the other compounds In_3Zr, InZr and $InZr_2$ were adjusted to satisfy the conditions so that the compounds are stable at room temperature and have non-congruent melting.
- The entropy of $InZr_3$ compound was first obtained in accordance with the portion of the diagram rich in Zr. Additional entropy term was added to destabilize other compounds so that they are not too stable in the diagram. This entropy was estimated to be of the same order of magnitude as that of $InZr_3$.
- The heat capacities of the compounds were estimated by the Neumann-Kopp rule.
- A sub-regular interaction parameter was added to reproduce a low solubility of Zr in the liquid in equilibrium with the In_3Zr compound.

The optimized parameters and the corresponding calculated diagram are given in **Table 8** and **Figure 20** respectively. The following observations can be made:

- The central part of the diagram remains largely estimated as, in particular, no information was available on the melting temperature of the compounds.
- The In solubility limits in the Zr hcp_A3 (α phase) and bcc_A2 (β phase) in equilibrium with $InZr_3$ reproduce the results obtained by Betterton and Noyce [7].
- In_2Zr is considered the most stable compound which decomposes by congruent melting at 1959 K.
- The experimental liquidus points obtained by Dieva [8] are well reproduced by the assessment.
- The model is in agreement with experimental information obtained from [3, 5] which are not in favor with the stability of In_3Zr compound at high temperature. In the calculated diagram, In_3Zr decomposes into (L + In_2Zr) at 1771K and it is difficult to destabilize this compound at a lower temperature while maintaining a low solubility in liquid In.

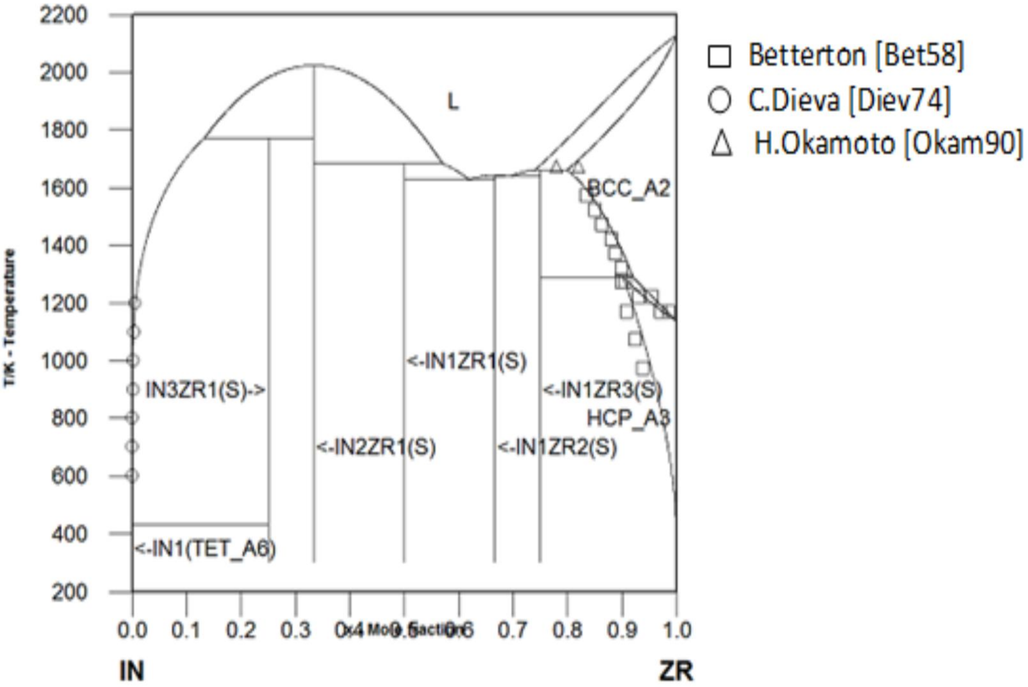

Figure 20. Calculated In-Zr phase diagram from NUCLEA [6].

Table 8. Thermodynamic parameters of In-Zr system obtained ($J.mol^{-1}$) [6].

Liquid

$^{\circ}L^{Liq}_{In,Zr} = -68186.41$

$^{1}L^{Liq}_{In,Zr} = 9416.72$

Bcc_A2

$^{\circ}L^{bcc\_A2}_{In,Zr} = -66483.68$

Hcp_A3

$^{\circ}L^{hcp\_A3}_{In,Zr} = -71786.87$

In_3Zr_1

$^{\circ}G_{In3Zr} = -130000 + 8.44904*T + 3*^{\circ}G_{In(tet\_A6)} + {}^{\circ}G_{Zr(hcp\_A3)}$

In_2Zr_1

$^{\circ}G_{In2Zr} = -114900 + 7.34*T + 2*^{\circ}G_{In(tet\_A6)} + {}^{\circ}G_{Zr(hcp\_A3)}$

In_1Zr_1

$^{\circ}G_{InZr} = -70000 + 5.22*T + {}^{\circ}G_{In(tet\_A6)} + {}^{\circ}G_{Zr(hcp\_A3)}$

In_1Zr_2

$^{\circ}G_{In1Zr2} = -88500 + 7.34*T + {}^{\circ}G_{In(tet\_A6)} + 2*^{\circ}G_{Zr(hcp\_A3)}$

In_1Zr_3

$^{\circ}G_{In1Zr3} = -100000 + 8.44904*T + {}^{\circ}G_{In(tet\_A6)} + 3*^{\circ}G_{Zr(hcp\_A3)}$

A summary of the invariant phase equilibria of the In-Zr diagram of **Figure 20** are shown in **Table 9**.

Table 9. Summary of invariant equilibria in the In-Zr system [6].

Reaction	Temperature (K)	Type of reaction	Phase	Composition (at %)	
				In	Zr
L ⇄ bcc_A2	2127.86	Congruent	L, bcc_A2	0.0	100.0
L ⇄ In_2Zr	2023.42	Congruent	L, In_2Zr	66.7	33.3
L+In_2Zr ⇄ In_3Zr	1764.04	Peritectic	L In_2Zr In_3Zr	86.7 66.7 75.0	13.3 33.3 25.0
L+In_2Zr ⇄ InZr	1684.63	Peritectic	L In_2Zr InZr	43.0 66.7 50.0	57.0 33.3 50.0
L+ bcc_A2⇄ $InZr_3$	1654.06	Peritectic	L bcc_A2 $InZr_3$	28.0 21.3 25.0	72.0 78.7 75.0
L⇄ $InZr_2$	1643.02	Congruent	L, $InZr_2$	33.3	66.7
L ⇄ InZr+$InZr_2$	1600.07	Eutectic	L InZr $InZr_2$	39.1 50.0 33.3	60.9 50.0 66.7
$InZr_3$+ bcc_A2 ⇄ hcp_A3	1250.02	Peritectoid	$InZr_3$ bcc_A2 hcp_A3	25.0 7.5 9.0	75.0 92.5 91.0
bcc_A2 ⇄ hcp_A3	1139.00	Allotropic	bcc_A2, hcp_A3	0.0	100.0
L ⇄ tet_A6	429.76	Congruent	L, tet_A6	100.0	0.0
L ⇄ tet_A6+In_3Zr	429.75	Eutectic	L tet_A6 In_3Zr	100.0 100.0 75.0	0.0 0.0 25.0

The standard enthalpies of formation of the In-Zr compounds obtained by CALPHAD modeling at 298 K and by Density Functional Theory (DFT) calculations at 0 K are compared in **Figure 21**. The DFT calculations were done using Generalized Gradient Approximation (GGA) and Vienna Ab-initio Simulation Package (VASP). The results were extracted from two open databases called Open Quantum Mechanical Database and Materials project [22, 23] and the study of Guo et al. [24].

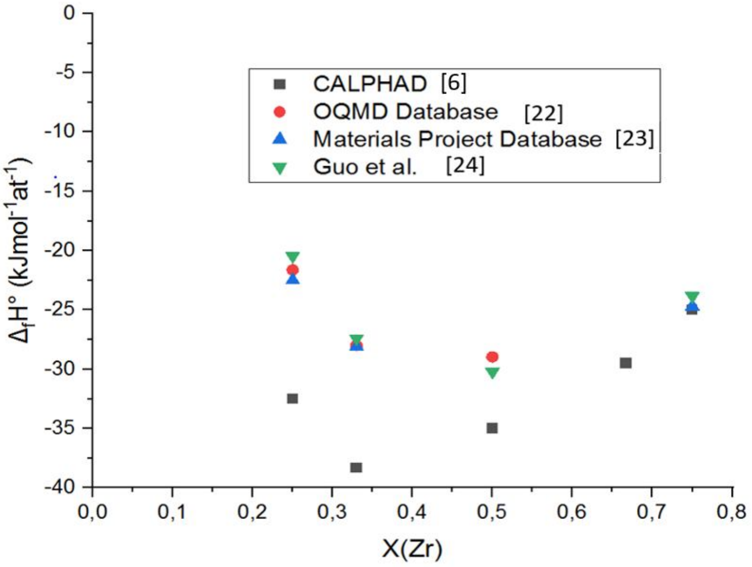

Figure 21. Comparison of standard formation enthalpies of In-Zr compounds at 298 K from CALPHAD assessment [6] with DFT values calculated at 0 K [22 - 24].

It is not straightforward to compare various DFT studies in term of a single convex-hull graphical construction since, in each individual study, formation enthalpy values were not systematically calculated for all In-Zr compounds and all possible structures at each stoichiometry. The calculated formation enthalpies and corresponding structures of the In-Zr compounds are also compared numerically in **Table 10**. This table provides a preliminary estimate of the likely range of values to be expected in a future experimental determination.

Table 10. A comparison of $\Delta_f H^\circ$ (kJ. mol^{-1} at^{-1}) values of In-Zr compounds by CALPHAD modelling and DFT calculations.

InZr	CALPHAD [6]	OQMD [22]		Materials Project [23]		Guo et al. [24]	
Comp	$\Delta_f H^\circ$ (298 K)	$\Delta_f H^\circ$ (0 K)	Structure	$\Delta_f H^\circ$ (0 K)	Structure	$\Delta_f H^\circ$ (0 K)	Structure
InZr	-35	-28.956	$Fm\bar{3}m$	-32.06	P4/mmm	-30.204	$Fm\bar{3}m$
In_2Zr	-38.3	-27.991	I41/amd	-28.088	I41/amd	-27.408	I41/amd
In_3Zr	-32.5	-21.6207	I4/mmm	-22.489	I4/mmm	-20.458	I4/mmm
$InZr_2$	-29.5						
$InZr_3$	-25	-21.717	$Pm\bar{3}m$	-24.709	$Pm\bar{3}m$	-23.835	$Pm\bar{3}m$

In a more recent study, C. Colinet [25] performed DFT calculations to determine the enthalpy of formation of In-Zr intermetallic compounds at 0 K in a more systematic way. She investigated different possible crystallographic structures at numerous stoichiometries, In/Zr = 1/3, 1/2, 2/3, 1, 4/3, 3/2, 5/2, 3. Structures and stoichiometric ratios were selected on the basis of a previous study she performed on the Ga-Zr system. The results reported on **Figure 22** shows that $L1_2$ ($Pm\bar{3}m$), $L1_0$ (P4/mmm), tP10 (P4/m), tI24 (I41/amd), tP14 (P4/mbm), and $D0_{22}$ (I4/mmm) should be the stable structures corresponding to the stoichiometries $InZr_3$, InZr, In_3Zr_2, In_2Zr, In_5Zr_2 and In_3Zr respectively at 0 K in the In-Zr system. In contrast to the experimental observations, two additional compounds are predicted by the calculations, In_3Zr_2, and In_5Zr_2. By examining the convex hull construction of **Figure 22**, it can be stated that, In_3Zr_2 (X_{In} = 0.6) and In_5Zr_2 ($X_{In} \approx 0.714$) are only marginally more stable compared to the biphasic equilibrium between InZr and In_2Zr, and In_2Zr and In_3Zr respectively, in such a way that their formation could not have been observed experimentally at room temperature.

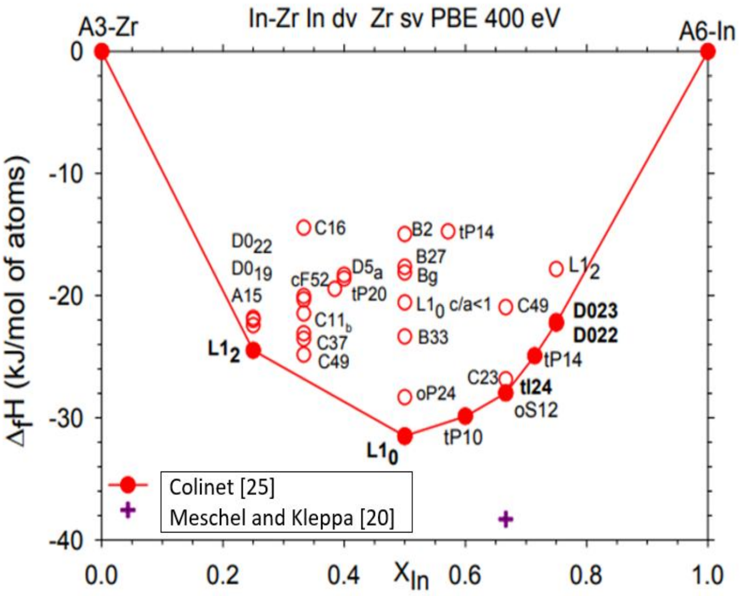

Figure 22. Comparison of standard formation enthalpies calculated by DFT by Colinet at 0 K [25] with Meschel and Kleppa calorimetric value at 298 K [20].

3.3. In-Zr binary phase diagram investigation

The revised phase diagram of the In–Zr system drawn on the basis of the present experimental work and literature results is presented in **Figure 23**. This diagram will serve as a basis for a future CALPHAD reassessment of the system at IRSN.

The main differences between this new phase diagram and preliminary assessments (see **Figure 20**) which will be discussed in the next sections are as follow:

- the peritectic decomposition of the (In) at 157 °C,
- the peritectic decomposition of the In_3Zr at 592 °C,
- the peritectic decomposition of the In_2Zr at 1133 °C,
- the peritectic decomposition of the In_3Zr_2 at 1279 °C,
- the liquidus temperatures of the indium rich compositions,
- the solubility limit of Zr in liquid In at 592 °C is 1.0 ± 0.1 at% Zr,
- the solubility limit of Zr in liquid In at 1133 °C is 3.7 ± 1.7 at%Zr.

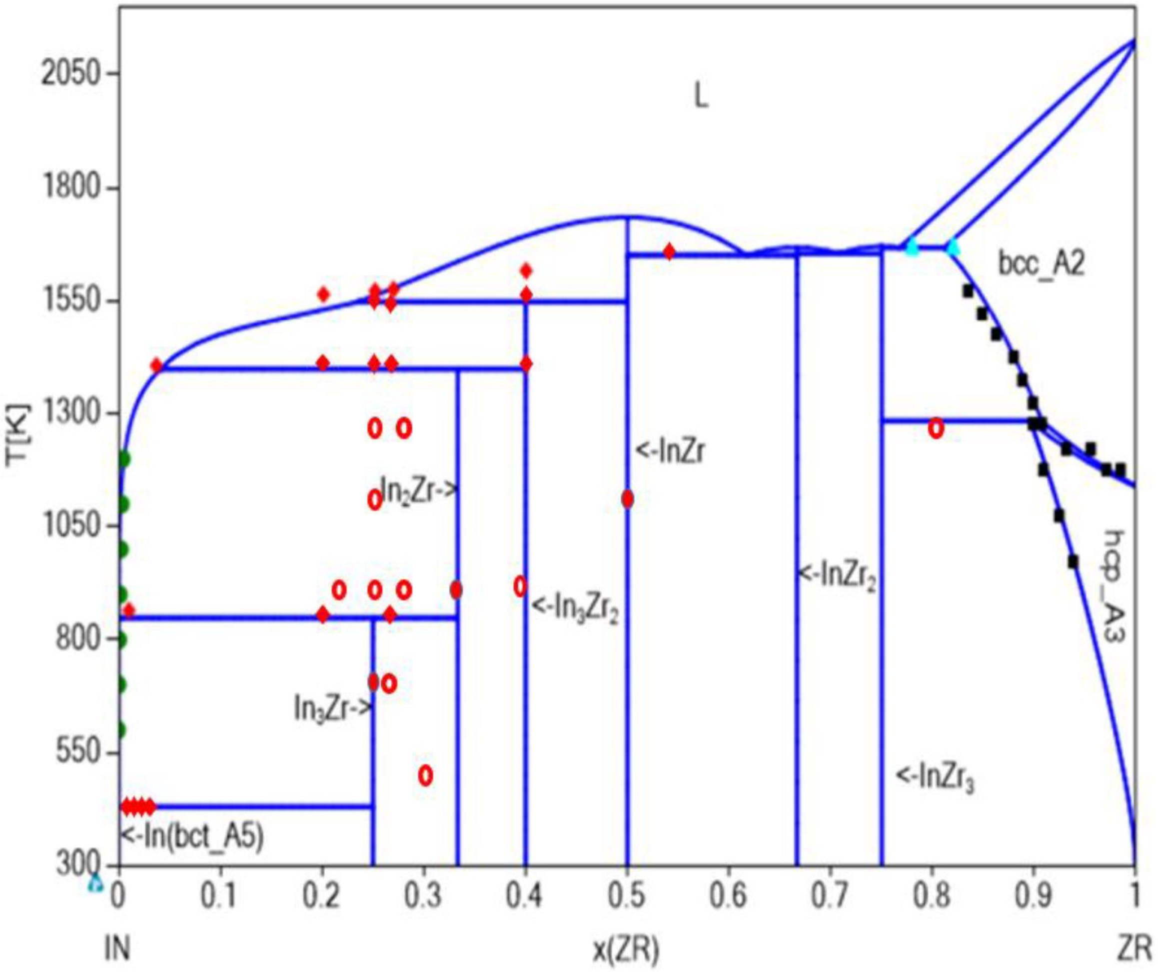

Figure 23. The revised In–Zr phase diagram. This work, annealed single phase (●), annealed 2-phase (o), DTA event (♦) – Betterton and Noyce [7] (■) – Dieva [8] (●) – Okamoto [2] (▲).

3.3.1. Phase equilibria of In-Zr system

The compositions of the samples investigated, the corresponding annealing conditions and the results of the metallographic examinations and XRD analyses are summarized in **Table 11**. As a representative example, some of the XRD spectra and micrographs are shown below. When the amount of a phase determined by XRD is very small, it is sometimes difficult to detect this phase by SEM, which explains some of the inconsistencies between SEM and XRD results in **Table 11**.

Table 11. Compositions, annealing conditions and the phases identified by XRD and SEM.

Annealing Conditions	Composition (at%Zr)	Phases identified by SEM	Phases identified by XRD
200°C (1 month)	25.63	In_2Zr + In_3Zr	In (14.9 %) + In_2Zr (48.3 %) + αIn_3Zr (36.8 %)
	30.35	In_2Zr + In_3Zr	In (4.9 %) + In_2Zr (64.9 %) + αIn_3Zr (30.2 %)
400°C (1 month)	25.53	In_2Zr + In_3Zr	In_2Zr (3.7 %) + βIn_3Zr (96.3 %)
	27.79	In_2Zr + In_3Zr	In_2Zr (10.7 %) + βIn_3Zr (89.3 %)
400°C (2 months)	25.53	N.A	βIn_3Zr (100 %)
600°C (2 months)	23.68	In + In_2Zr	In (49.6 %) + In_2Zr (50.4 %)
	28.44	In + In_2Zr	In (31.1 %) + In_2Zr (68.9 %)
	35.02	In_2Zr	In_2Zr + InZr + ZrO_2
	39.99	N.A	In_2Zr + InZr + ZrO_2+ In_2O_3
	44.96	InZr	In_2Zr + InZr + ZrO_2+ In_2O_3
	60.00	$InZr_2$ + InZr + Zr solid solution + eutectoid	$InZr_2$ + InZr + $\alpha Zr^{?}$ + $\beta Zr^{?}$ + ZrO_2
	66.00	$InZr_2$ + InZr + Zr solid solution + eutectoid	$InZr_2$ + InZr + $\alpha Zr^{?}$ + $\beta Zr^{?}$ + ZrO_2
800°C (1 Week)	25.19	N.A	In (51.9 %) + In_2Zr (48.2 %)
	27.93	N.A	In (29.2 %) + In_2Zr (70.8 %)
	40.61	N.A	In + In_2Zr + InZr + ZrO_2
	50.21	InZr	InZr+ ZrO_2 + In_2O_3
1000°C (24 hours)	24.90	In + In_2Zr	In (54.4 %) + In_2Zr (45.6 %)
	27.65	In + In_2Zr	In (30.9 %) + In_2Zr (69.1 %)
	33.17	N.A	In (4.4 %) + In_2Zr (95.6 %)
	39.64	N.A	In + In_2Zr + InZr + ZrO_2
	75.38	αZr + $InZr_3$	αZr + $InZr_3$
	80.92	αZr + $InZr_3$	αZr + $InZr_3$
Post DTA	20.13	In_3Zr + In_2Zr + In_3Zr_2+ In	
Post DTA	27.00	In_2Zr + In_3Zr_2+ In	
Post DTA	40.03	In_2Zr + In_3Zr_2+ In	
Post DTA	54.43	InZr + $InZr_2$ + eutectic	
Post DTA	81.53	βZr + $InZr_3$ + eutectoid	
As cast	53.89*	InZr	
As cast	76.09*	$InZr_3$	

$^{?}$*not so sure about the presence of the phase because of peaks overlapping with other phases. *as cast samples after arc-melting.*

Lattice parameters of the intermetallic phases obtained from the different annealing conditions are summed up in **Table 12**.

Table 12. Lattice parameters of phases identified in heat-treated In-Zr alloys as obtained from XRD.

		Lattice parameters of phases (nm)			
	Alloy (at%Zr)	In	αIn_3Zr	βIn_3Zr	In_2Zr
		a = 0.3215 c = 0.4967 [16]	a = 0.4303 c = 1.894 [10]	a = 0.4238 c = 0.9786 [10]	a = 0.4387 c = 2.7238 [4]
1000°C (24 hours)	24.90	a = 0.3250 c = 0.4945			a = 0.4386 c = 2.7253
	27.65	a = 0.3251 c = 0.4943			a = 0.4386 c = 2.7224
	33.17	a = 0.3253 c = 0.4942			a = 0.4382 c = 2.7236
800°C (1 week)	25.19	a = 0.3252 c = 0.4944			a = 0.4385 c = 2.7263
	27.93	a = 0.3248 c = 0.4944			a = 0.4384 c = 2.7237
600°C (2 months)	23.68	a = 0.3249 c = 0.4942			a = 0.4381 c = 2.7272
	28.44	a = 0.3252 c = 0.4946			a = 0.4385 c = 2.7255
400°C (1 month)	25.53			a = 0.4243 c = 0.9795	a = 0.4383 c = 2.7239
	27.79			a = 0.4243 c = 0.9794	a = 0.4384 c = 2.7232
400°C (2 month)	25.53			a = 0.4248 c = 0.9785	
200°C (1 month)	25.63	a = 0.3253 c = 0.4946	a = 0.4308 c = 1.8941		a = 0.4387 c = 2.7236
	30.35	a = 0.3252 c = 0.4945	a = 0.4307 c = 1.8938		a = 0.4386 b =2.7232

The 5 different intermetallic phases In_3Zr, In_2Zr, InZr, $InZr_2$ and $InZr_3$ reported by Okamoto [2], have been confirmed in this work (see **Table 11**).

Up to now, there was no information about the nature and temperature of decomposition of the indium richest compound, In_3Zr. According to Okamoto's diagram [2], the In_3Zr compound is expected to be stable at least up to around 800°C. Above 800°C, the stability of this compound is indicated as hypothetical by the same author while the preliminary CALPHAD assessment [6] of the system previously presented predicts a peritectic decomposition but at much higher temperature (1491°C). In an unpublished study, G. Collins [30] also reported a peritectic decomposition of In_3Zr around 660°C. Our results clearly indicate a much lower decomposition temperature for In_3Zr, 591.6°C (see **Figure 30**).

According to the previous descriptions, in the composition range $20 < x < 33$ at.% Zr, it was expected to detect In_3Zr up to relatively high temperature. Both XRD and SEM analyses consistently show that this phase was not stable for temperatures equal to or higher than 600°C since it was not detected in the samples with compositions 23.68 at.%Zr, 28.44 at.%Zr annealed at 600°C for 2 months, 25.19 at.%Zr, 27.93 at.%Zr annealed at 800°C for 1 week and 24.90 at.%Zr, 27.65 at.%Zr annealed at 1000°C for 24 hours (see **Table 11**). The absence of In_3Zr phase in the samples annealed at $T \geq 600$°C is also in agreement with the results previously obtained by Saitovich et al. [5] who did not detect In_3Zr on a 25 at.%Zr composition sample annealed at 927°C during 24 h.

The comparison of the spectra for two samples, 25.53 at.%Zr annealed at 400°C and 25.19 at.%Zr annealed at 800°C is illustrated in **Figure 24**. From **Figure 24**, it can be seen that the X-ray diffraction patterns of In_2Zr and In_3Zr compounds from Zumdick et al.[4] and Schubert et al. [10] overlaps, especially in the angle range of the high intensity diffracted peaks. However, the peaks labeled by green arrows show that the In_3Zr phase is only detected in the 25.53 at.%Zr sample annealed at 400°C. This is attributed to the fact that the 800°C annealing temperature of 25.19 at.%Zr is above the temperature of the peritectic decomposition of In_3Zr. It is hence concluded that the decomposition temperature of In_3Zr is between 400°C to 600°C, lower than the temperature previously estimated experimentally by G. Collins [30] and in the tentative CALPHAD assessment [6].

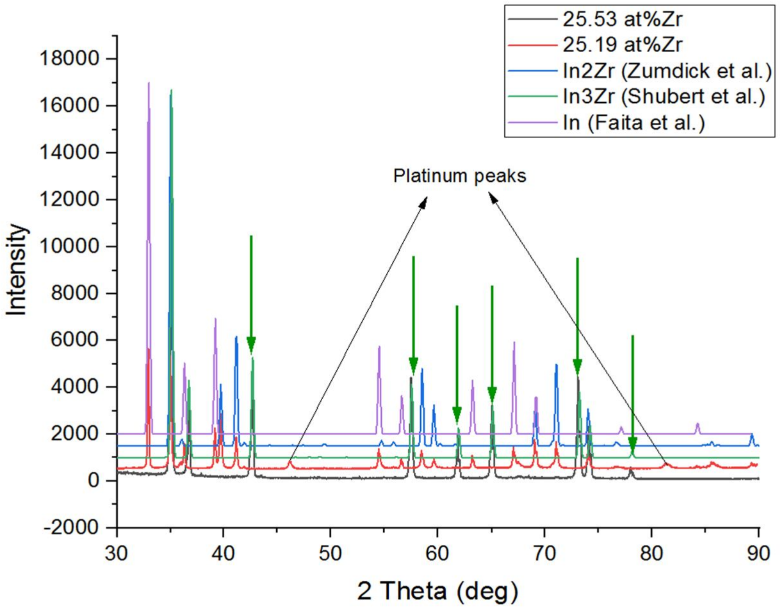

Figure 24. XRD patterns of the 25.53 at.%Zr and 25.19 at.%Zr annealed at 400°C for 2 months and 800 °C for 1 week respectively compared with the XRD pattern of In_2Zr [4], In_3Zr [10] and In [27]. The In_3Zr compound is not detected in the ≈ 25 at.%Zr alloy annealed at 800°C (red diffractogram) but clearly detected (green arrows) when a similar composition is annealed at 400°C. Extra peaks indicated by black arrows are platinum peaks coming from the sample holder.

The lattice parameters (see **Table 12**) of the compounds derived from the diffractograms of **Figure 24** are coherent with the values reported in the literature (see **Table 6**).

Three phases (α-In_3Zr + In_2Zr + In) were detected in the 25.63 at.%Zr and 30.35 at.%Zr samples, showing that these samples had not reached equilibrium (see **Table 11**).

Two micrographs having similar composition ≈ 28 at%Zr but annealed at different (400 and 1000°C) temperatures are compared in **Figure 25**. Under these conditions, a 2-phase mixture (In_3Zr + In_2Zr) was expected for both temperatures on the basis of Okamoto's diagram [2]. However, the 27.65 at.%Zr alloy annealed at 1000°C for 24 hours did not show the presence of In_3Zr whereas this phase was detected in the micrograph of the 27.79 at.%Zr alloy annealed at 400°C for 2 months. The absence of In_3Zr at 1000 °C confirms that this temperature is above the decomposition temperature of In_3Zr.

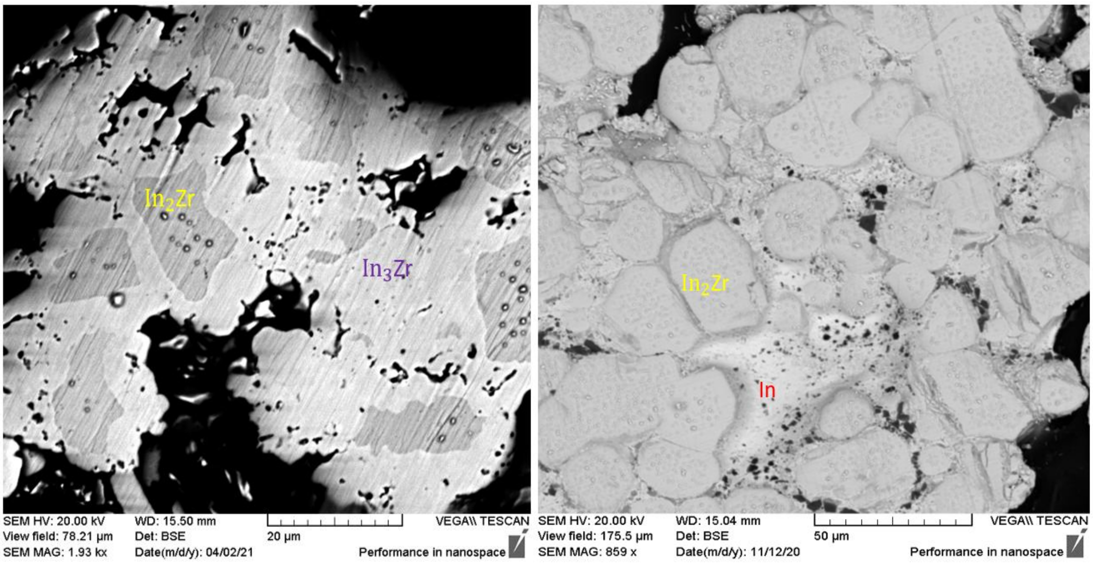

(a) (b)

Figure 25. BSE image of (a) 27.79 at.%Zr sample annealed at 400°C for 1 month and (b) 27.65 at.%Zr sample annealed at 1000°C for 24 hours. In_3Zr phase is not detected in the ≈ 28 at.%Zr alloy annealed at 1000 °C (a) but is observed when a similar composition is annealed at 400 °C (b). The black part are holes in the samples.

In analysing the In-Zr alloys with compositions between 33 and 50 at.%Zr where InZr and In_2Zr phases were expected [2], InZr, In_2Zr together with ZrO_2 and In_2O_3 phases were detected. Although the precautions taken to avoid oxidation of the samples were applied in a similar way for all the compositions studied, the X-ray diffraction patterns show the presence of ZrO_2 and In_2O_3 oxide phases in this specific compositional range. This observation most likely reflects a greater sensitivity of these compositions to oxidation at room temperature.

EPMA carried out on some of the compositions in this range showed a high oxygen concentration (≈ 60%). It was difficult to determine the exact amount of phases present in these alloys by XRD due to the overlap of some peaks belonging to different phases.

In **Figure 26 a**, we compare the intensities of the peaks of the two main phases (In_2Zr and InZr) in two samples (35.02 at.%Zr and 39.99 at.%Zr). At angles around 64°, 66° and 82° (indicated by blue arrows), the intensities of In_2Zr peaks are lower in the ≈ 40% alloy (red XRD pattern) than in the ≈ 35% alloy (black XRD pattern). Moreover, In_2Zr peaks around 71° and

92° (blue arrows) disappear in the ≈ 40% alloy (red XRD pattern). In **Figure 26 b**, around 47° (indicated by green arrow), a more intense peak of InZr is present in the 39.99 at.%Zr sample than in the 35 at%Zr sample. Despite their qualitative nature, these observations are consistent with an expected higher InZr phase fraction in the 40 at.% Zr sample than in the 35 at.% Zr sample.

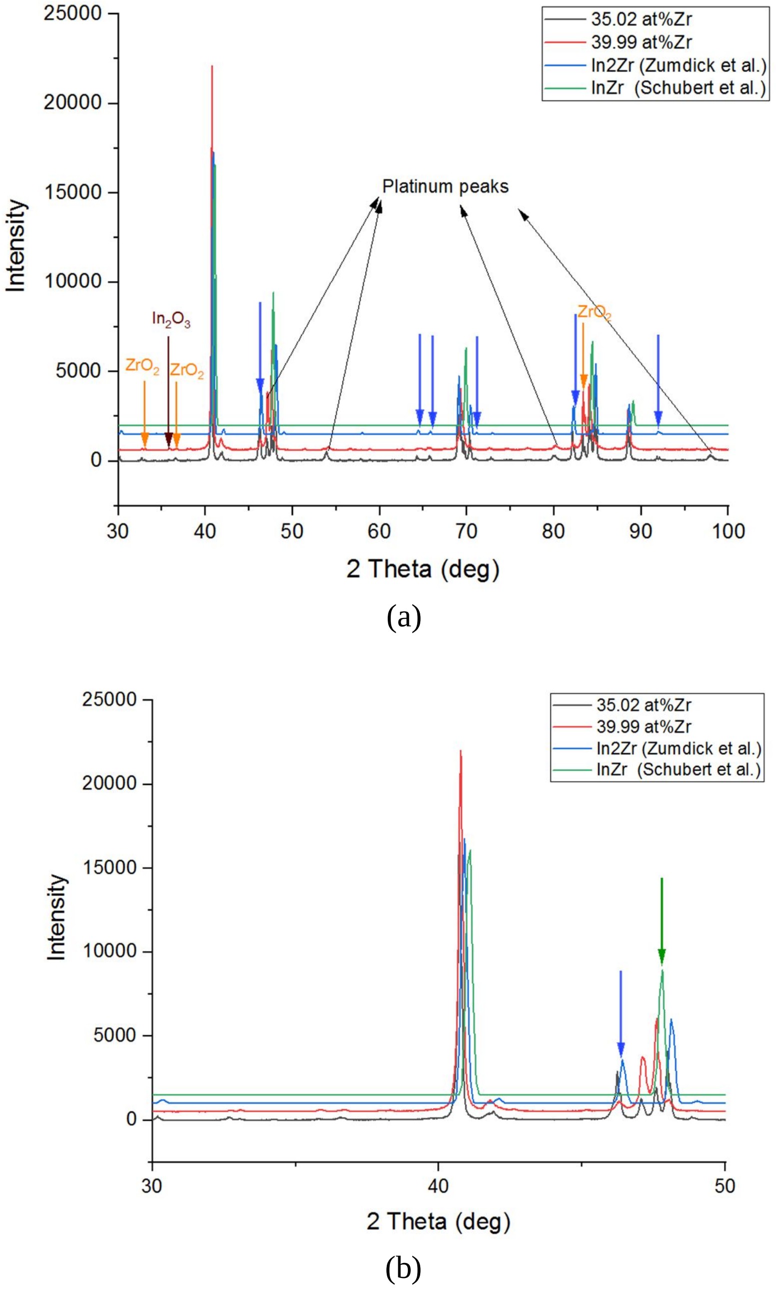

(a)

(b)

Figure 26. Comparison of XRD patterns of the 35.02 at.%Zr and 39.99 at.%Zr alloys annealed at 600°C for 2 months with the XRD pattern of In_2Zr [4] and InZr [9]. Orange and brown arrows are the oxide peaks. The blue arrows indicate In_2Zr peaks detected in the ≈ 35at.%Zr alloy (black XRD pattern) which decrease in intensity or disappear in the ≈ 40 at.%Zr alloy (red XRD pattern). Extra peaks indicated by black arrow are platinum peaks coming from the sample holder. (b) A zoom into the angle region around the 47° peak (green arrow) of InZr.

InZr and $InZr_2$ phases found in the samples with composition in the range 55 to 66 at.%Zr are coherent with the diagram of Okamoto [2]. Nevertheless, it must be underscored that the X-ray diffraction patterns of InZr and $InZr_2$ compounds from Schubert et al. [9] overlap, especially in the angle range of the high intensity diffracted peaks, making it difficult to decide about the nature of the detected phases. Traces of Zr peaks were also seen in the XRD results which put into questioning the complete equilibration of the sample (see **Table 11**).

Metallographic examinations of the 60 at.%Zr and 66 at.%Zr revealed the presence of InZr and $InZr_2$ and areas having a multiphase microstructure looking like a eutectoid decomposition (see **Figure 27**). The multiphase “eutectoid” zones (see **Figure 27**) are composed of needle shaped crystals, probably $InZr_2$, surrounded by a very fine 2-phase microstructure. It was not possible to determine the compositions of the phases involved in this fine microstructure by SEM/EDX due to their small size. This microstructure could result from the incomplete conversion of prior Zr grains into In-Zr compounds during annealing, the duration of which (2 months at 600°C) would be insufficient to obtain the equilibrium phase microstructures, i.e. InZr + $InZr_2$ in the 60% Zr sample and single-phase $InZr_2$ in the 66% Zr sample.

InZr phase is observed in the periphery of the grains. This phase has grown during annealing and as it is very sensitive to oxygen and brittle it is quite easy to identify in the microstructure (we can observe some cracks around the InZr phase as well as grey contrast due to oxidation) (see **Figure 27**).

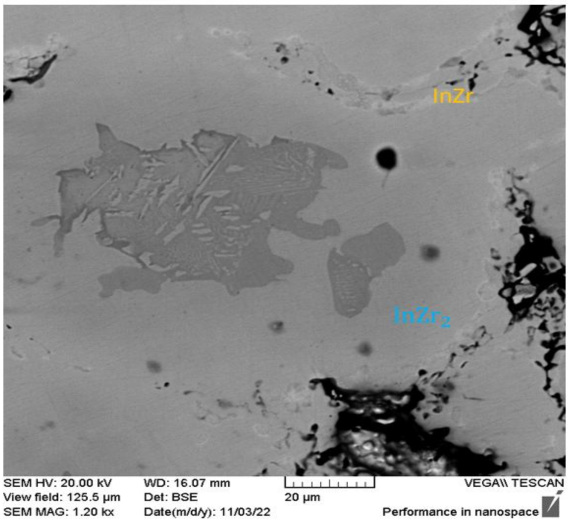

Figure 27. BSE images of the 66 at.%Zr alloy annealed 2 months at 600°C revealing the formation of InZr, $InZr_2$, and “eutectoid” microstructure.

Additional investigations on the Zr rich side of the diagram, 75.38 at.%Zr and 80.92 at.%Zr alloys, indicate the formation of $InZr_3$ and αZr phases in agreement with Okamoto’s diagram [2]. Comparing the XRD patterns of the 2 alloys (see **Figure 28**), there seem not to be any difference in the amount of phases. As seen in the micrographs (**Figure 29**), the phase fraction of $InZr_3$ seems to be higher in the 75.38 at.%Zr sample than in 80.92 at.%Zr.

From the micrograph (see **Figure 29**) it was difficult to determine if there is a peritectoid reaction as suggested by Betterton and Noyce [7] because the annealing temperature was slightly below the peritectoid temperature. The composition (73.9 - 75.5 at.%Zr) measured for the grey phase in the micrograph (**Figure 29**) confirms the finding of Betterton and Noyce [7] and Gajavalli [18] that the $InZr_3$ compound has a large stability domain around 72 at.%Zr to 79 at.%Zr stoichiometric composition.

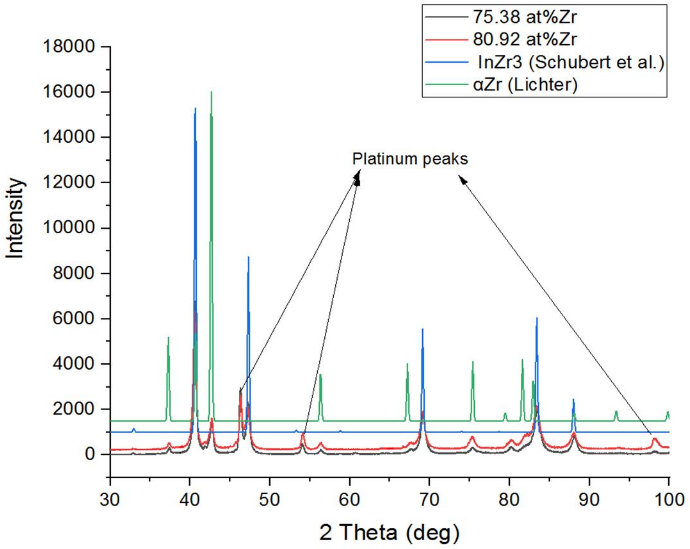

Figure 28. Experimental powder XRD pattern of the 75.38 at.%Zr and 80.92 at.%Zr samples annealed 24 h at 1000°C compared with diffraction patterns of $InZr_3$ [10] and αZr [26]. Black arrows mark the positions of the platinum peaks coming from the sample holder.

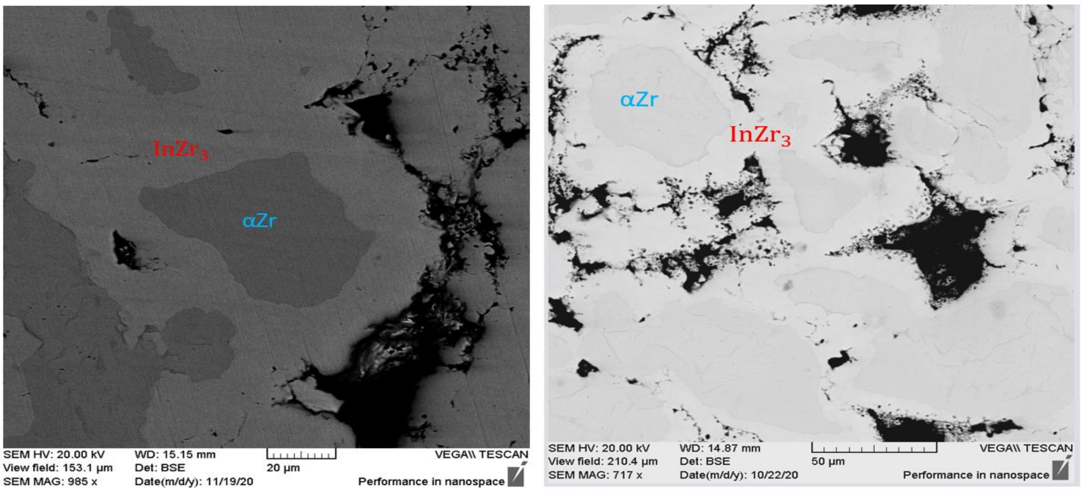

(a) (b)

Figure 29. BSE image showing the 2-phase microstructure of (a) the 75.38 at.%Zr and (b) the 80.92 at.%Zr alloys, both annealed 24 h at 1000°C. The grey matrix phase has a composition of 73.9 - 75.5 at.%Zr, and the dark phase has a 89.7 at.%Zr composition in agreement with the solubility of In in αZr determined by Betterton and Noyce [7] at similar temperature.

3.3.2. Phase transformation temperatures

The composition range 20 < x ≤ 40, where x is the atomic percent of zirconium, is firstly investigated by DTA at a 5°C/min constant rate.

A first small endothermic peak is detected at 156.8 ± 0.4°C (see **Figure 30 a)**, this value is very close to the melting temperature of pure indium. This peak undoubtedly corresponds to the invariant melting reaction involving the indium-rich solid solution. The temperature measured is coherent with the temperature proposed by Okamoto [2] and in the tentative CALPHAD assessment of Fischer [6]. In the subsequent sections it is shown that a peritectic transformation occurs (see **Figure 34**) in this region contrary to the eutectic reaction formerly assumed [2, 6].

Between 500°C and 1200°C, the heating curves of the 20.13 at.%Zr, 25.19 at.%Zr and 27 at.%Zr alloys show two endothermic peaks, whereas only one such peak is observed in the DTA curve of the 40.03 at.%Zr alloy. The first one is detected around 591.6 ± 2.4°C in the 20.13 at.%Zr, 25.19 at.%Zr and 27 at.%Zr samples. This peak most certainly corresponds to the peritectic decomposition of In_3Zr. The measured temperature (591.6°C) of this peritectic decomposition also explains why the In_3Zr compound was not observed by XRD and SEM in the samples annealed between 600 and 1000°C in this composition range. The measured peritectic temperature 591.6°C is lower than the 660°C value suggested by G. Collins [30].

A new phase, In_3Zr_2, was identified by SEM/EDX during the post DTA examinations of three different samples (**Figure 36**). Hence, the second peak detected at 1132.9 ± 1.8 °C in the four samples is interpreted as the peritectic decomposition of $In_2Zr \leftrightarrow In_3Zr_2 + L$ (see **Figure 30 a),** whereas In_2Zr had a congruent melting at 1370°C in the tentative CALPHAD assessment of the In-Zr system of the NUCLEA database [6].

A last invariant peak is detected at a temperature of 1279 ± 6°C before a monovariant endothermic thermal effect whose end corresponds to the liquidus temperature. Taking into account the In_3Zr_2 phase, the invariant peak at 1279 °C in **Figure 30 a**, is interpreted as the peritectic decomposition of $In_3Zr_2 \leftrightarrow InZr + L$. The Liquidus temperatures for the different In-Zr alloys are shown in **Figure 30 a**. It is observed that the liquidus temperature increases with the zirconium content of the alloy.

The thermal effects detected during cooling (**Figure 30 b**) present the following notable differences. The liquidus temperatures are lower due to undercooling. The peaks corresponding to the peritectic invariant of In_2Zr have a considerably smaller area as a result of incomplete peritectic reaction. The peaks corresponding to the peritectic reaction of the In_3Zr compound disappear. The invariant reaction corresponding to the solidification of the last In-rich liquid is very clearly detected at 156.9 °C because, during cooling, the signal does not suffer from baseline oscillations due to electrical noise created by the power control during heating.

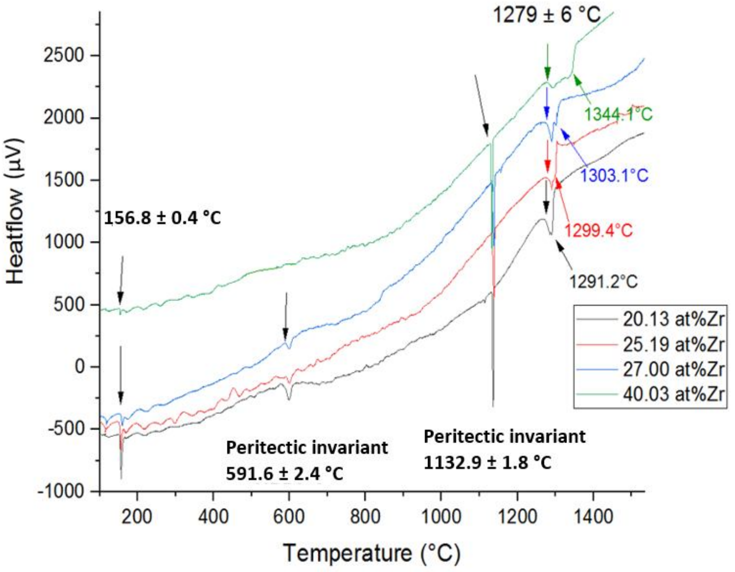

(a)

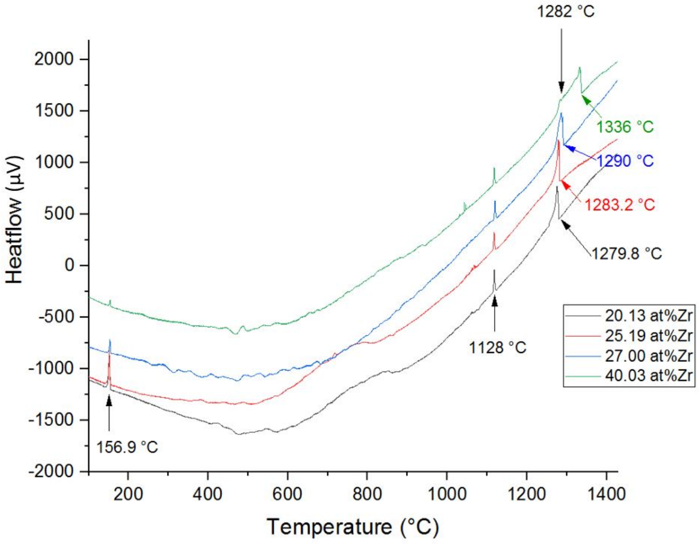

(b)

Figure 30. DTA curves showing the onset temperatures measured for 4 binary In-Zr alloys at a rate of 5°C/min under purified Ar. (a) the invariant reaction corresponding to the In-rich solid solution is observed at 156.8 ± 0.4°C, the peritectic decompositions of In_3Zr, In_2Zr and In_3Zr_2 are detected around 591.6 ± 2.4 °C, 1132.9 ± 1.8 °C and 1279 ± 6 °C respectively. The arrows indicate where the characteristic temperatures were taken. (b) Cooling curves. The oscillations in the curves are due to electrical noise from the furnace power control.

The endothermic peak at 591.6°C and 1132.9°C in **Figure 30 a** can undoubtedly be assigned to the peritectic decompositions of In_3Zr and In_2Zr respectively, but precise determinations of the characteristic compositions of these peritectic plateaus were performed using Tammann analysis. A Tammann diagram shows the variation of the enthalpy associated with a first-order transformation as a function of concentration as required by the lever rule [28]. **Figure 31 a** illustrates the Tammann analysis applied to the peritectic plateau at 591.6°C. The invariant starts at 1.0 ± 0.1 at.% Zr composition of the liquid and ends at 33 at. % Zr, where the endothermic effect corresponding to another invariant at 1132.9 ± 1.8 °C is maximum. At 1133°C, the peritectic plateau starts at ~ 3.7 ± 1.7 at.%Zr composition of the liquid (**Figure 31 b**).

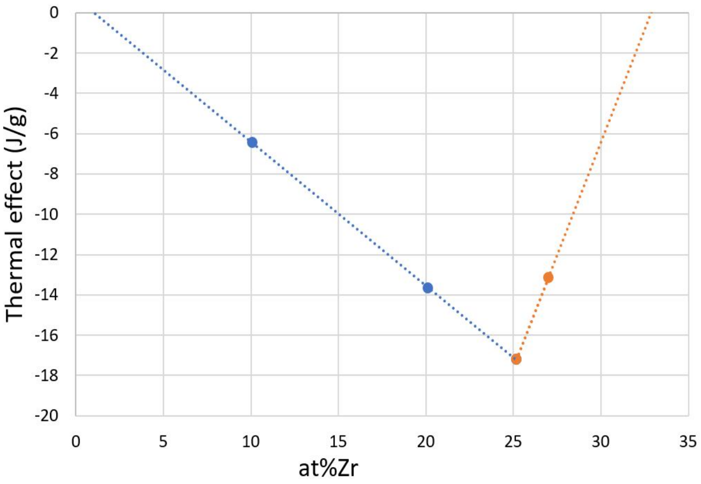

(a)

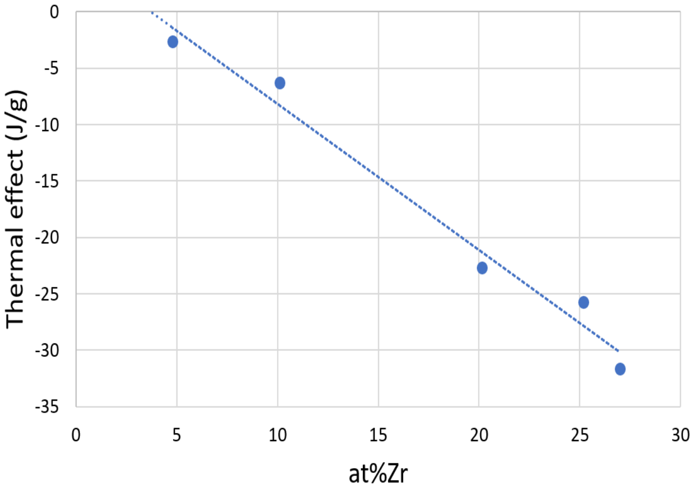

(b)

Figure 31. Tammann analysis performed on the peritectic plateau at (a) 591.6 °C shows that the extrapolation of the data sets the limits of the plateau at approximately 1.0 ± 0.1 at.% Zr for the In-rich liquid on one side and at 33 at%Zr = In_2Zr composition on the other side (b) 1132.9 °C, linear extrapolation of the measured heat effects sets the In-rich liquid composition at 3.7 ± 1.7 at%Zr.

The 25.53 at.%Zr sample was repeatedly cycled from 25°C to 700°C (**Figure 32**) using a Setaram scanning calorimeter (DSC 111 model). The endothermic peak at 155°C corresponds to the invariant reaction involving the In-rich solid solution and another endothermic peak corresponding to the invariant transformation of In_3Zr was found at 593.5 ± 2.4 °C in agreement with former DTA results. In addition to the invariant endothermic peaks, additional peaks of an exothermic nature were observed during heating and were interpreted as resulting from an incomplete peritectic reaction during prior cooling (see **Figure 32**).

On cooling at 10 or 5°C/min, there is not enough time for the completion of peritectic reaction therefore, in the subsequent heating runs, nonequilibrated sample are analysed and exothermic extra peaks are systematically observed. The exothermic peaks disappear in R5 and R6 because the sample was slowly cooled at 2°C/min and 1°C/min respectively before these runs.

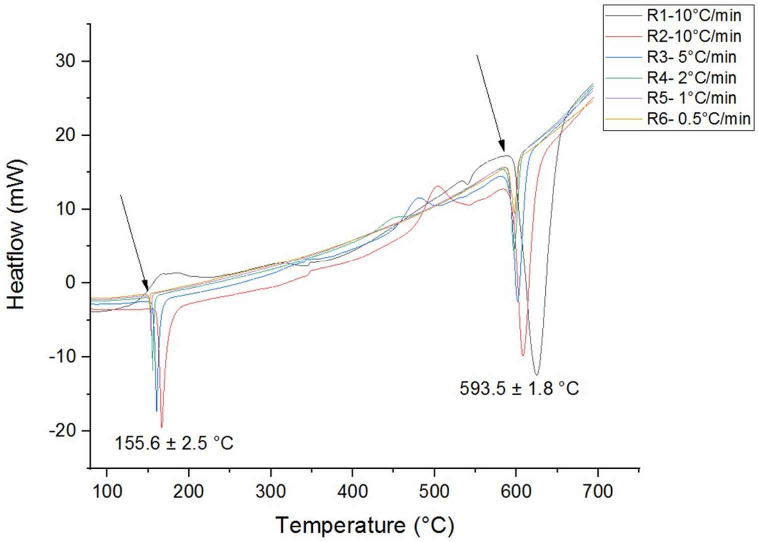

Figure 32. Low temperature range DTA curves showing the invariant temperatures measured for the 25.53 at.%Zr alloy at various heating rates under purified argon. At 155.6 ± 2.5°C, the invariant reaction corresponding to the In-rich solid solution is observed and the peritectic decompositions of In_3Zr are detected around 593.5 ± 1.8 °C. Additional peaks observed in some of the runs (R2, R3, R4) are as a result of incomplete peritectic reaction during prior cooling.

In an earlier version of the In–Zr system [2], a eutectic L ↔ αIn_3Zr + In reaction at 156.6 °C was reported. We performed simple DTA measurements both on the pure indium used as a starting material in this work and on 0.55 at.%Zr, 0.9 at.%Zr, 2 at.%Zr and 4.8 at.%Zr samples, which were prepared using mixture of pure indium and In_3Zr powder, to estimate the transition temperatures and the energy of the transformation.

Our DTA measurements show that the invariant reaction in the indium rich region occurs at 156.8 ± 0.3 °C (see **Figure 33**), which is consistent with the previous results but slightly higher than the melting point of pure indium (156.5 °C). This suggests that the samples containing less than 25 at.%Zr could undergo a peritectic, rather than eutectic, transformation of the indium-rich solid solution (In) ↔ αIn_3Zr + Liquid.

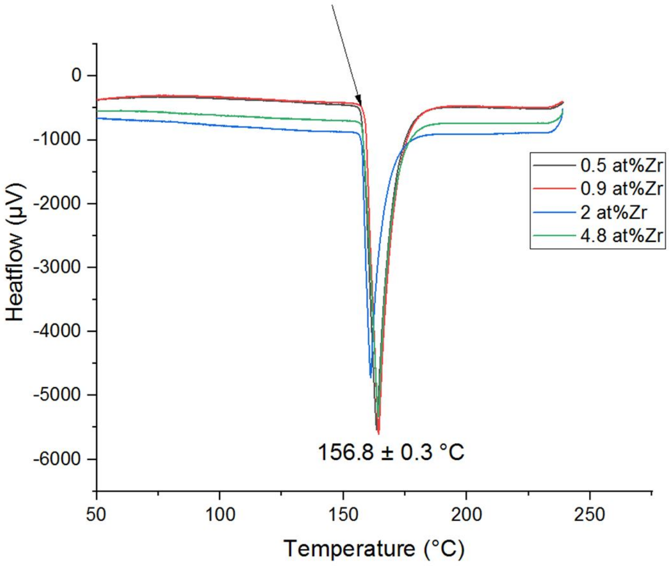

Figure 33. DTA curve for indium rich samples showing a peritectic invariant at 156.8 ± 0.3 °C.

Hence, in order to completely elucidate the exact nature of the invariant reaction that occurs at low temperature in the indium rich region, bi-differential thermal analysis was carried out. An S-type DTA sensor equipped with alumina crucibles was used for this purpose. Samples of composition 0.55 at.% Zr, 0.9 at.%Zr, 2 at.%Zr or 4.8 at.%Zr were alternately placed in the sample crucible while pure indium serving as internal reference was systematically placed in the reference crucible.

The sensor of the DTA instrument is connected in such a way that an endothermic effect on the sample side gives a downward peak while an endothermic effect on the reference side gives an upward peak. On heating, if the first thermal event detected is the melting of indium, it can be concluded that the reaction is peritectic whereas it will be eutectic if the sample melts first. Five successive thermal analysis cycles were performed to check the reproducibility of the measurements.

As illustrated in **Figure 34 a**, the first detected thermal event corresponds to the melting of pure indium placed in the reference cell, followed by the invariant reaction occurring in the alloy. This result suggests that the reaction is peritectic: (In) ↔ αIn_3Zr +Liquid.

To confirm this result and rule out the possibility that it could be due to a temperature gradient within the apparatus, an additional bi-differential experiment was carried out, this time placing a 0.9% Zr binary alloy in the reference cell while pure indium was placed in the sample cell. In this configuration (**Figure 34 b**), again, the melting of indium occurred first followed by the invariant transformation in the alloy definitely confirming the peritectic nature of the invariant plateau.

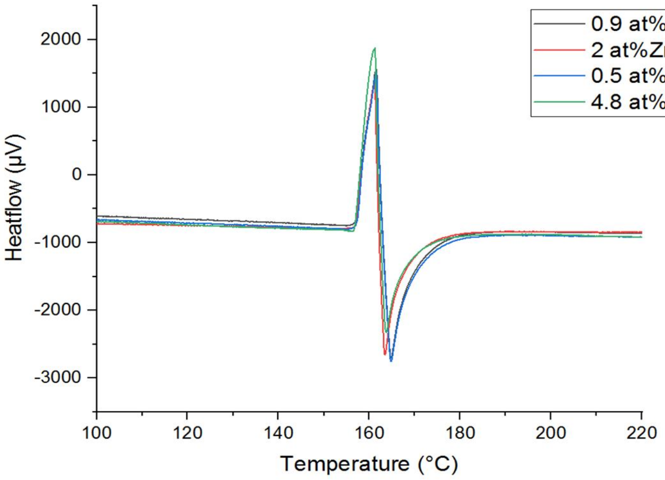

(a)

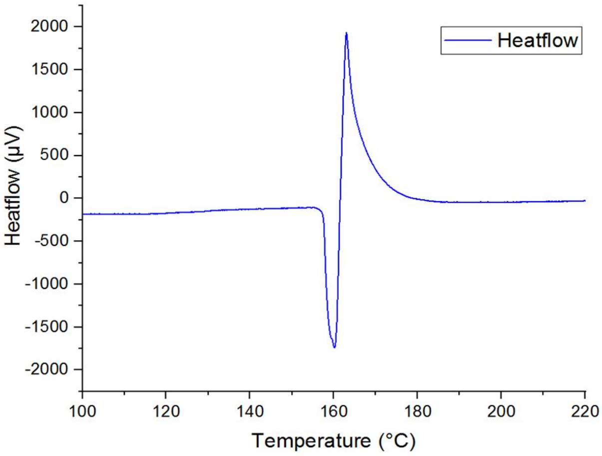

(b)

Figure 34. Bi-differential thermal analysis of indium rich samples versus pure indium on heating at 5°C /min. An endothermic effect on the sample side gives a downward deflection from the baseline. An endothermic effect on the reference side gives an upward deflection. (a) Alloy samples placed in the sample cell whilst pure indium is in the reference cell. (b) 0.9 at.% Zr alloy sample in the reference cell whilst pure indium is placed in the sample cell.

The Zr-rich end of the invariant plateau, now identified as peritectic, was determined by Tammann analysis. The linear extrapolation of the measured heat effects reaches zero at 25 ± 3.8 at.% Zr (**Figure 35**), the precise composition of In_3Zr as expected. At this composition, the endothermic effect corresponding to the peritectic decomposition of In_3Zr at 591.6 ± 2.4 °C is maximum (**Figure 31 a)**.

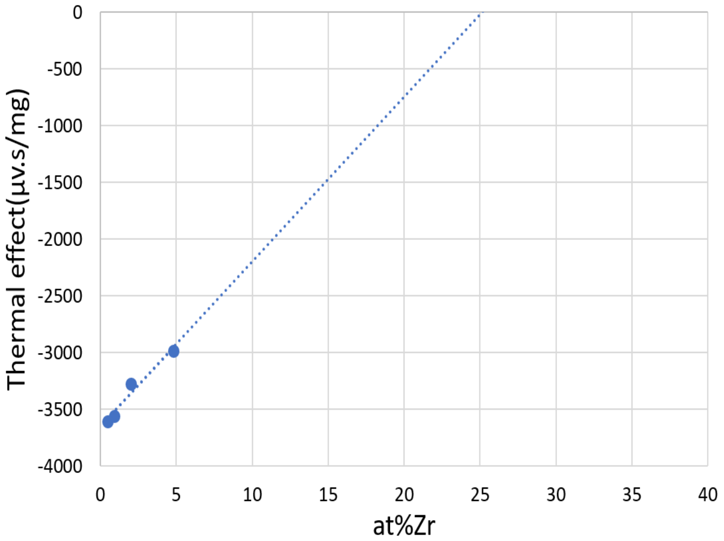

Figure 35. Tammann analysis performed on peritectic plateau at 156.8 ± 0.3 °C. The extrapolation of the data sets the limit of the plateau at approximately 25 ± 3.8 at.%Zr.

In order to check for the behavior of the different samples after DTA, micrographic examinations by means of scanning electron microscopy (SEM) were performed on the 20.13 at.%Zr, 27.00 at.%Zr and 40.03 at%Zr samples. Quantitative analysis of elements in individual phases was performed by EDX without standard.

- In the three samples (see **Figure 36**) we can observe, a dark grey phase with composition close to In_3Zr_2 and a light grey phase having a In_2Zr composition. No previous experimental studies have reported the existence of a phase with the stoichiometry In_3Zr_2. However, DFT calculations done by Colinet [25] suggest the possible stability of this phase.

- In_3Zr phase was seen in the 20 at.%Zr sample (**Figure 36 a**) but difficult to find in the other samples. The white particles on the grains are indium.

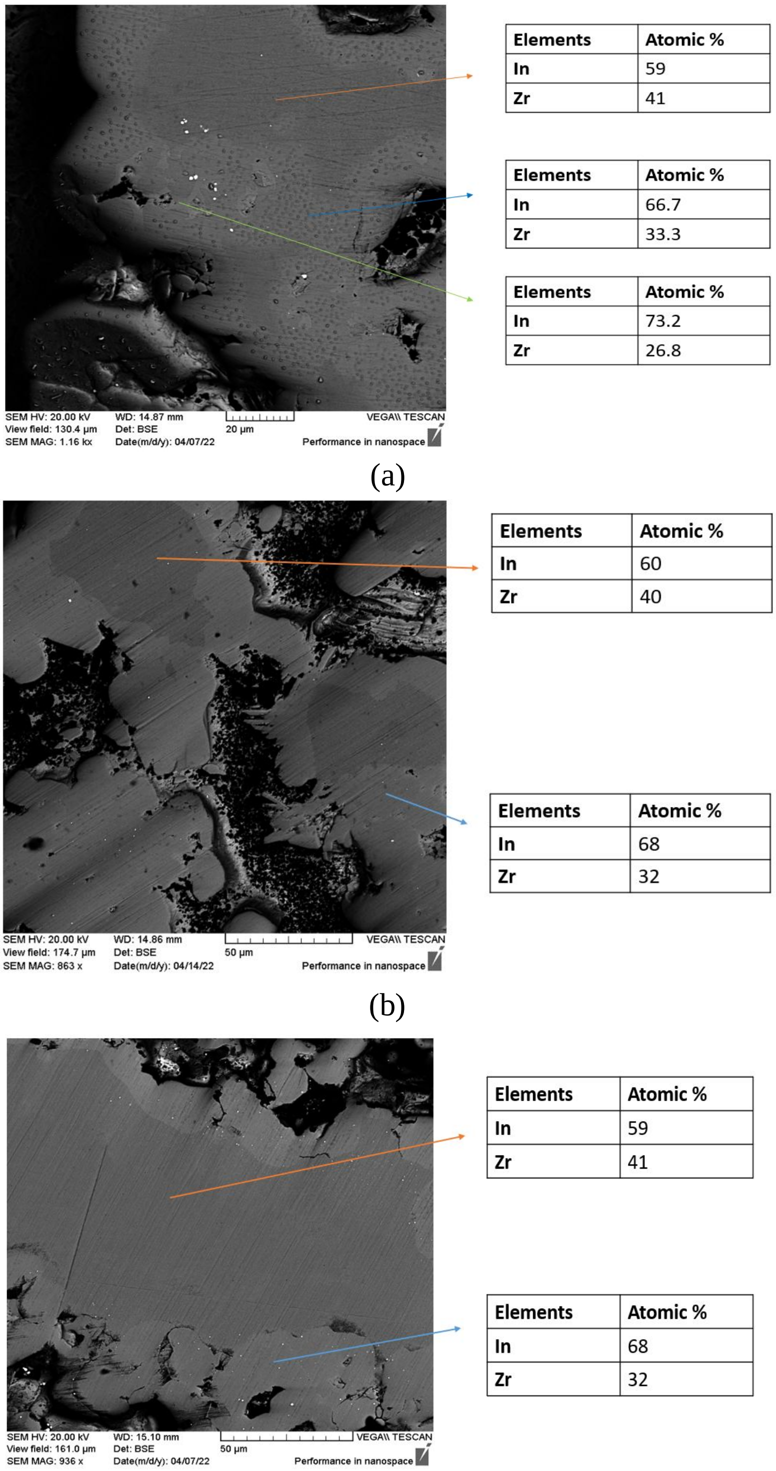

Elements	Atomic %
In	59
Zr	41

Elements	Atomic %
In	66.7
Zr	33.3

Elements	Atomic %
In	73.2
Zr	26.8

(a)

Elements	Atomic %
In	60
Zr	40

Elements	Atomic %
In	68
Zr	32

(b)

Elements	Atomic %
In	59
Zr	41

Elements	Atomic %
In	68
Zr	32

(c)

Figure 36. SEM observation of post DTA samples; (a) 20.13 at.%Zr (b) 27.00 at.%Zr and (c) 40.03 at%Zr. The dark matrix phase has compositions close to In_3Zr_2 and the grey matrix is In_2Zr phase. The white particles on the grains are indium.

3.4. Thermodynamics contribution

3.4.1. Dissolution calorimetry measurements

Prior to the calorimetry measurements, XRD was performed on the synthesized In_3Zr and In_2Zr samples. The obtained diffractograms (**Figure 37**) confirm the single phase character of both samples.

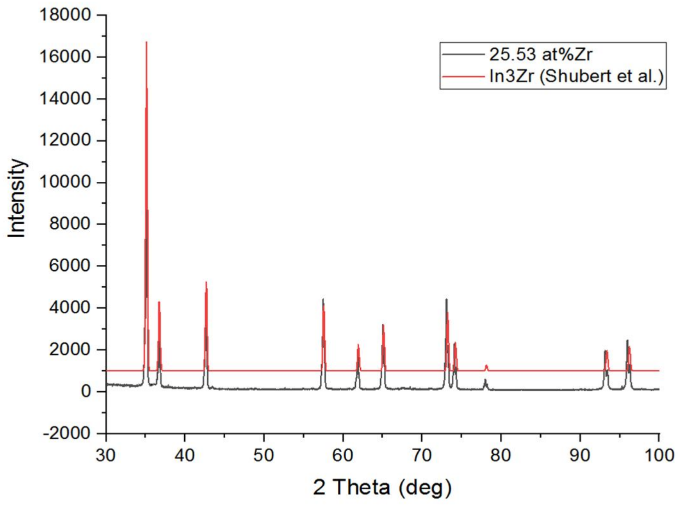

(a)

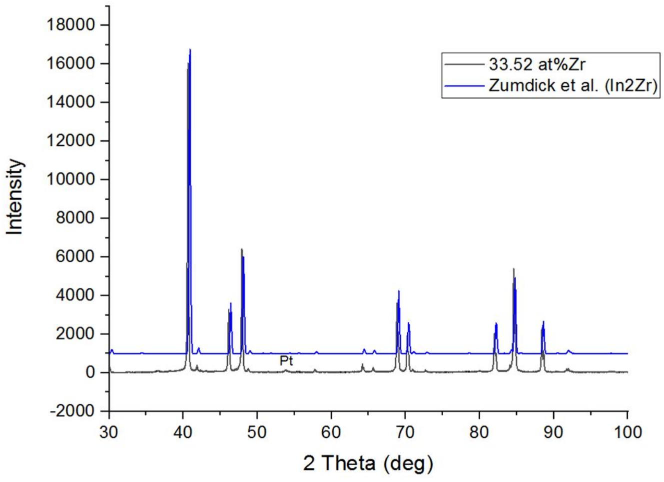

(b)

Figure 37. XRD evidencing the formation of single phase (a) In_3Zr in 25.53 at%Zr annealed 2 months at 400°C and (b) In_2Zr in 33.52 at%Zr annealed 48 h at 600°C.

3.4.1.1. Dissolution of In_3Zr in aluminum at 1173K

For these experiments, the In_3Zr samples were cut into small pieces (masses of 10 to 24 mg) and dropped into an Al bath at 1173K. Four runs of In_3Zr dissolution calorimetry measurements in Al were performed in the atomic composition range $0 < x_{\mathrm{In_3Zr}} < 0.000434$. Within one run, after each In_3Zr drop (of δn moles) in the bath containing N moles of Al and M moles of In and J moles of Zr (N >> M, J), a heat effect $Q_{\mathrm{In_3Zr}}$ was measured, corresponding to the following equation:

$$\delta n\langle \mathrm{In_3Zr}\rangle_{s,298} + ((N\mathrm{Al}, M\mathrm{In}, J\mathrm{Zr}))_{l,1173} \rightarrow ((N\mathrm{Al}, (M + 3\delta n)\mathrm{In}, (J + \delta n)\,\mathrm{Zr}))_{l,1173};\quad Q_{\mathrm{In_3Zr}} \tag{3.5}$$

After each drop, a thermal effect was registered before the signal has returned to the baseline (see Appendix). The associated heat effects $Q_{\mathrm{In_3Zr}}$ which have been measured, are reported under the heading the partial drop solution enthalpy value for In_3Zr defined by $\Delta_{ds}\overline{H}^{1173K}_{In_3Zr,298K} = Q_{\mathrm{In_3Zr}}/\delta n$ which are gathered in **Table 13**. The measured heat effect, $Q_{\mathrm{In_3Zr}}$ is plotted vs. number of moles in **Figure 38**.

The partial drop solution enthalpy for In_3Zr at infinite dilution ($x_{\mathrm{In_3Zr}} \rightarrow 0$), $\Delta_{ds}\overline{H}^{\infty,1173\,K}_{In_3Zr,298\,K}$, is calculated by taking the slope value for the blue points in **Figure 38**. These blue points in **Figure 38** are the values in bold in **Table 13** while the orange points are the values in italics. The rationale for the distinction between these two subsets of data is discussed in more detail in section 3.5.

The selected partial drop solution enthalpy of In_3Zr at infinite dilution is $\Delta_{ds}\overline{H}^{\infty,1173K}_{In_3Zr,298K} = 203.5 \pm 7.1\ \mathrm{kJ\ mol^{-1}}$ with reference states corresponding to solid In_3Zr at 298 K and liquid aluminum at 1173 K.

Table 13. Partial drop-solution enthalpy of In_3Zr in liquid Al at 1173 K in $kJ.mol^{-1}$, $\Delta_{ds}\bar{H}^{1173K}_{In_3Zr,298K}$, measured by dissolution calorimetry. The references states are solid In_3Zr at 298 K and liquid aluminum at 1173 K. M^{int}_{Al} and δm_{In_3Zr} in mg, δn in mol, M^{int}_{Al} is the sum of the bath mass plus the masses of the 4 aluminum calibration samples. X_{In_3Zr} is the molar fraction of In_3Zr.

Run	M^{init}_{Al} / mg	δm_{In_3Zr} /mg	δn_{In_3Zr} / mol	x_{In_3Zr}	$\Delta_{ds}\bar{H}^{1173\ K}_{In_3Zr,298\ K}$ / $kJ.mol^{-1}$
1	10491.91	16.84	3.865E-05	4.97E-05	**204.966**
		15.95	3.661E-05	1.46E-04	**200.630**
		10.62	2.438E-05	2.25E-04	**211.519**
		10.69	2.454E-05	2.88E-04	**220.892**
2	10369.65	20.54	4.714E-05	6.13E-05	*175.373*
		19.99	4.588E-05	1.82E-04	*159.197*
		21.16	4.857E-05	3.05E-04	**203.192**
		22.00	5.050E-05	4.34E-04	**202.095**
3	10256.57	18.22	4.182E-05	5.50E-05	*164.030*
		19.55	4.487E-05	1.69E-04	**191.689**
		21.67	4.974E-05	2.93E-04	*163.445*
		21.96	5.040E-05	4.25E-04	*174.309*
4	10473.85	23.36	5.362E-05	6.91E-05	*170.971*
		20.90	4.797E-05	2.00E-04	**216.099**
		15.27	3.505E-05	3.07E-04	*171.297*
		14.49	3.326E-05	3.95E-04	**190.309**

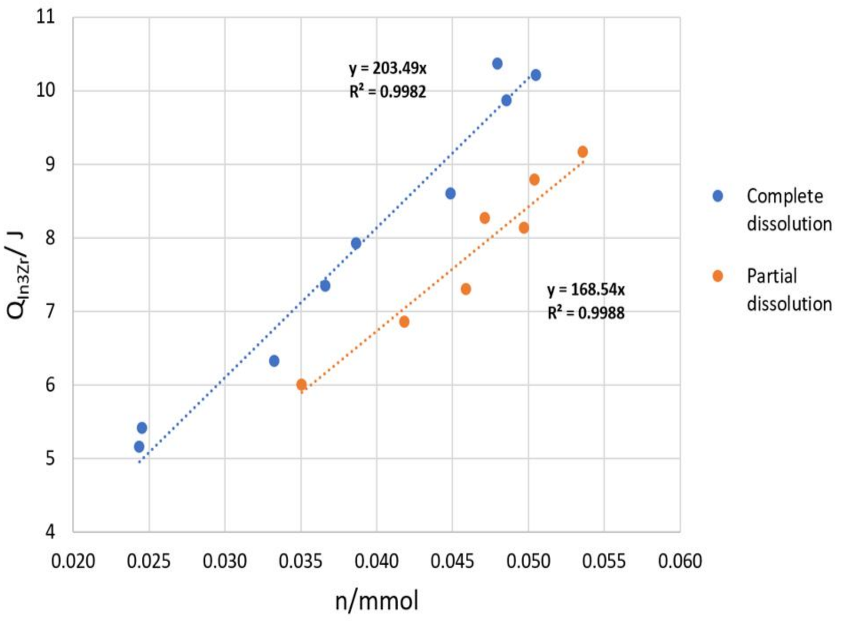

Figure 38. Measured thermal effects associated to the drop of In_3Zr in liquid Al, Q_{In_3Zr}, vs the number of moles. The blue points indicate the values measured for complete dissolution (values in bold in Table 13) while the orange is for partial dissolution (values in italics in Table 13).

3.4.1.2. Dissolution of In_2Zr in aluminum at 1173K

The synthesized single phase In_2Zr samples were cut into small pieces (masses of 9 to 22 mg) and dropped into an Al bath at 1173 K. Four runs of In_2Zr dissolution calorimetry measurements in Al were performed in the atomic composition range $0< x_{In_2Zr} < 0.000506$. The In_2Zr dissolution reaction in Al is given by:

$$\delta n\langle In_2Zr\rangle_{s,298} + ((NAl, MIn, JZr))_{l,1173} \rightarrow ((NAl, (M + 2\delta n)In, (J + \delta n)Zr))_{l,1173} \quad ;Q_{In_2Zr} \qquad (3.6)$$

The partial drop solution enthalpy value for In_2Zr, $\Delta_{ds}\overline{H}_{In_2Zr,298K}^{1173K} = Q_{In_2Zr}/\delta n$ at 1173K are gathered in **Table 14** and plotted vs. X_{In_2Zr} in **Figure 39**.

The partial drop solution enthalpy for In_2Zr at infinite dilution $\Delta_{ds}\overline{H}_{In_2Zr,298K}^{\infty 1173K}$ is calculated by taking the average of the, $\Delta_{ds}\overline{H}_{In_2Zr,298K}^{1173K}$ values. The partial drop solution enthalpy of In_2Zr at infinite dilution is $\Delta_{ds}\overline{H}_{In_2Zr,298K}^{\infty 1173K} = 101.4 \pm 3.9$ kJ mol^{-1}, the references states are solid In_2Zr at 298 K and liquid aluminum at 1173 K. The uncertainty in the enthalpies was calculated by assuming that all experimental values have the same weight and it can be observed that the experimental scattering is larger than this calculated, likely to be underestimated, uncertainty. Indeed, the quality of the baseline can change from one experiment to another (see Appendix) and sometimes within the same experiment. Hence all calculated peak areas do not necessarily have equal uncertainties, e.g. if the signal undergoes or not a baseline shift during a drop. A more thorough analysis should take into account individual error bars affecting each point, giving more weight to the points having the smaller error bars. In Run 4 (**Table 14**), the baseline was quite stable and the points were less scattered than in the other runs.

Table 14. Partial drop-solution enthalpy of In_2Zr in liquid Al at 1173 K in $kJ.mol^{-1}$, $\Delta_{ds}\overline{H}^{1173K}_{In_2Zr,298K}$, measured by dissolution calorimetry. The references states are solid In_2Zr at 298K and liquid aluminum at 1173K. M_{Al}^{int} and δm_{In_2Zr} in mg, δn in mol, M_{Al}^{int} is the sum of the bath mass plus the masses of the aluminum calibration samples. X_{In_2Zr} is the molar fraction of In_2Zr.

Run	M_{Al}^{init} / mg	δm_{In2Zr} /mg	δn_{In_2Zr} / mol	x_{In_2Zr}	$\Delta_{ds}\overline{H}^{1173\ K}_{In_2Zr,298\ K}$ / $kJ.mol^{-1}$
1	10784.66	14.44	4.500E-05	5.63E-05	104.177
		13.63	4.248E-05	1.66E-04	100.469
		9.01	2.808E-05	2.54E-04	85.414
2	10505.45	21.31	6.642E-05	8.53E-05	111.645
		16.68	5.199E-05	2.37E-04	91.933
		20.69	6.448E-05	3.87E-04	105.514
		9.06	2.824E-05	5.06E-04	102.860
3	10153.14	14.62	4.557E-05	6.05E-05	100.829
		8.86	2.761E-05	1.58E-04	90.900
		14.34	4.469E-05	2.54E-04	98.164
		14.45	4.504E-05	3.73E-04	109.061
4	10281.73	13.09	4.080E-05	5.35E-05	102.088
		13.22	4.120E-05	1.61E-04	106.123
		14.57	4.541E-05	2.75E-04	105.280
		14.21	4.429E-05	3.92E-04	106.039

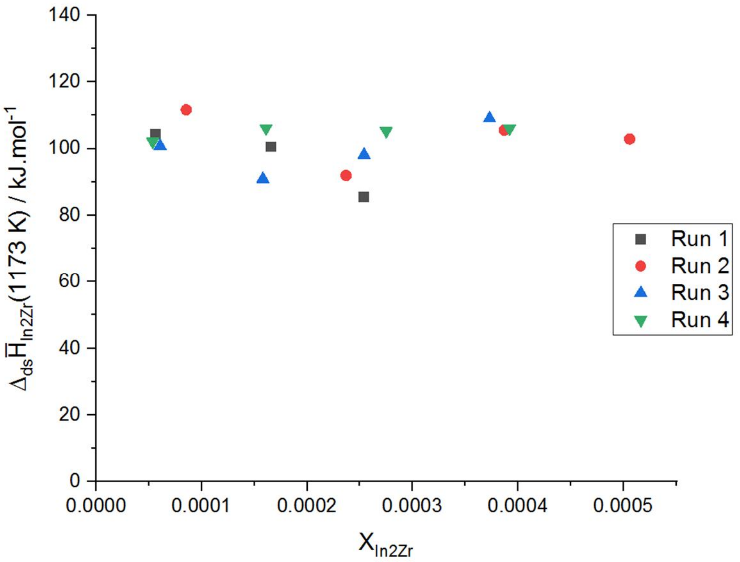

Figure 39. Drop solution enthalpy measurements of In$_2$Zr in liquid Al at 1173 K.

3.4.1.3. Standard formation enthalpy of In$_3$Zr and In$_2$Zr derived from dissolution calorimetry

The standard formation enthalpy of In$_3$Zr, $\Delta_f H^{\circ}_{In_3Zr}$ or In$_2$Zr, $\Delta_f H^{\circ}_{In_2Zr}$ is computed from the partial drop solution enthalpies at infinite dilutions of Zr, In and In$_3$Zr or In$_2$Zr measured by using the dissolution calorimetry technique. The $\Delta_f H^{\circ}_{In_3Zr}$ or $\Delta_f H^{\circ}_{In_2Zr}$ is then given by;

$$\Delta_f H^{\circ}_{In_3Zr} = 3\Delta_{ds}\overline{H}^{\infty,1173K}_{In,298K} + \Delta_{ds}\overline{H}^{\infty,1173K}_{Zr,298K} - \Delta_{ds}\overline{H}^{\infty,1173K}_{In_3Zr,298K} \quad (3.7)$$

$$\Delta_f H^{\circ}_{In_2Zr} = 2\Delta_{ds}\overline{H}^{\infty,1173K}_{In,298K} + \Delta_{ds}\overline{H}^{\infty,1173K}_{Zr,298K} - \Delta_{ds}\overline{H}^{\infty,1173K}_{In_2Zr,298K} \quad (3.8)$$

The determinations of the partial drop solution enthalpy at infinite dilution of Zr and In in liquid Al at 1173 K were reported by [29, 18] respectively. We only recall thereafter obtained results:

- The partial drop solution enthalpy of Zr in Al at infinite dilution at 1173K was found to be $\Delta_{ds}\overline{H}^{\infty,1173K}_{Zr,298K}$ = –130 ± 9 kJ.mol^{-1}[29].
- The partial drop solution enthalpy of In in Al at infinite dilution at 1173K was found to be $\Delta_{ds}\overline{H}^{\infty,1173K}_{In,298K}$ = 58.4 ± 0.7 kJ.mol^{-1}[18].

Taking into account the partial drop solution enthalpy of In$_3$Zr at infinite dilution $\Delta_{ds}\overline{H}^{\infty,1173K}_{In_3Zr,298K}$ = 203.5 ± 7.1 kJ mol^{-1} calculated by taking the slope values for the blue points in **Figure 38** (values in bold in **Table 13**) and In$_2$Zr at infinite dilution $\Delta_{ds}\overline{H}^{\infty 1173K}_{In_2Zr,298K}$ = 101.4 ± 3.9 kJ mol^{-1} calculated by taking the average of all the values in **Table 14**, then the standard formation enthalpy of In$_3$Zr and In$_2$Zr at 298K, are determined to be, $\Delta_f H^{\circ}_{In_3Zr}$=-39.7 ± 2.9 kJ.mol^{-1}.at^{-1} and $\Delta_f H^{\circ}_{In_2Zr}$=-38.2 ± 3.3 kJ.mol^{-1}.at^{-1} .

3.4.1.4. Micrographic examinations

In order to check for the successive dissolution of the In_3Zr and In_2Zr samples in liquid Al, micrographic examination by means of scanning electron microscopy (SEM) was performed on the ingot. After cooling of the crucible containing the bath, the solidified ingots were longitudinally cut, embedded in resin, polished and examined.

In all the regions of the ingot (**Figure 40** and **Figure 41**) we can observe that:

- The light grey phase is the aluminum matrix.
- White crystals are indium. Pure indium is detected in all micrographs at grain boundaries because indium is immiscible with aluminum at room temperature.
- Al_3Zr needles were detected at the bottom of In_2Zr ingot (**Figure 41 c**). Their elongated shape results from their rapid growth because of the high cooling rate. Even though the zirconium was initially dissolved in liquid aluminum at the calorimeter temperature, Al_3Zr precipitates on cooling when the crucible is extracted from the calorimeter.

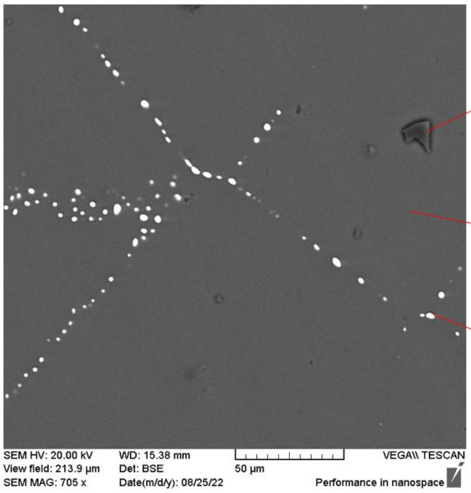

Elements	Mass %	Atomic %
Al	57.9	46.5
Zr	3.1	0.7
O	39.0	52.8

Elements	Mass %	Atomic %
Al	100	100

Elements	Mass %	Atomic %
Al	4.9	17.9
In	95.1	82.1

(a)

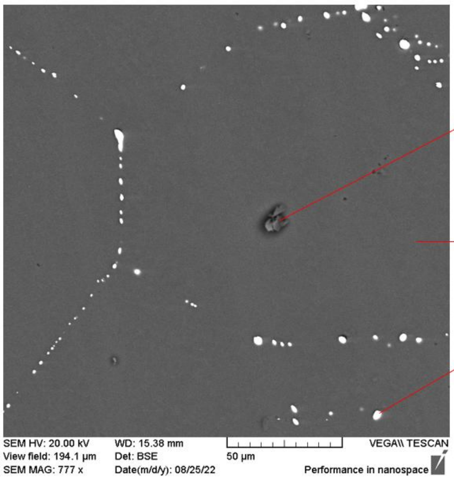

Elements	Mass %	Atomic %
Al	66.5	55.4
Zr	2.1	0.5
O	31.4	44.1

Elements	Mass %	Atomic %
Al	100	100

Elements	Mass %	Atomic %
Al	3.9	14.7
In	96.1	85.3

(b)

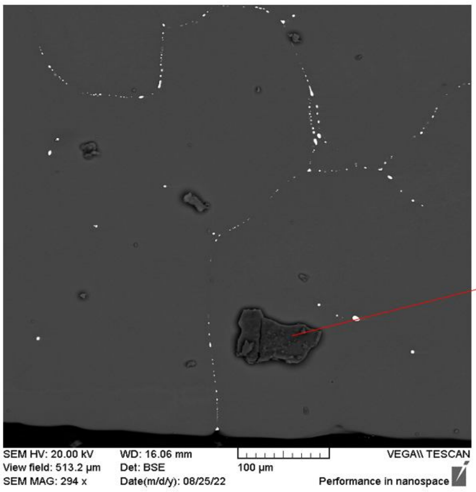

Elements	Mass %	Atomic %
Al	23.6	14.1
Zr	7.4	2.0
O	69	83.9

(c)

Figure 40. SEM observation of (a) Upper (b) Middle and (c) bottom region of the In_3Zr ingot. White crystals are indium and the light grey phase is the aluminum matrix.

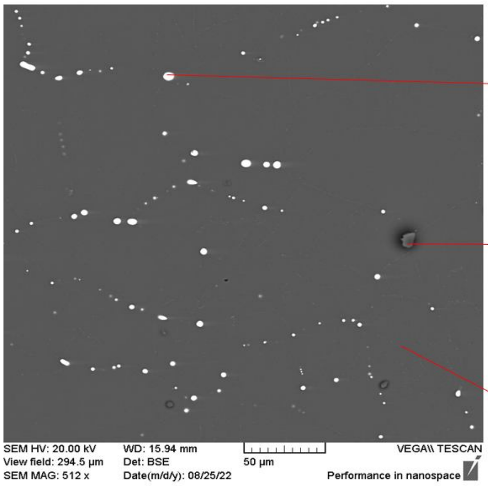

Elements	Mass %	Atomic %
Al	4.7	17.3
In	95.3	82.7

Elements	Mass %	Atomic %
Al	19.9	14.1
Zr	9.9	2.0
O	70.2	83.9

Elements	Mass %	Atomic %
Al	100	100

(a)

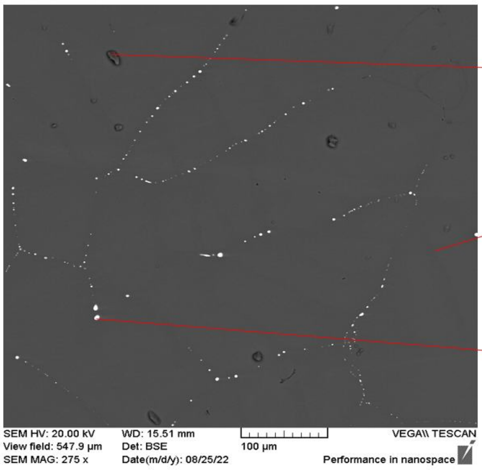

Elements	Mass %	Atomic %
Al	47.7	43.9
Zr	19.4	5.2
O	32.9	50.9

Elements	Mass %	Atomic %
Al	100	100

Elements	Mass %	Atomic %
Al	4.9	17.9
In	95.1	82.1

(b)

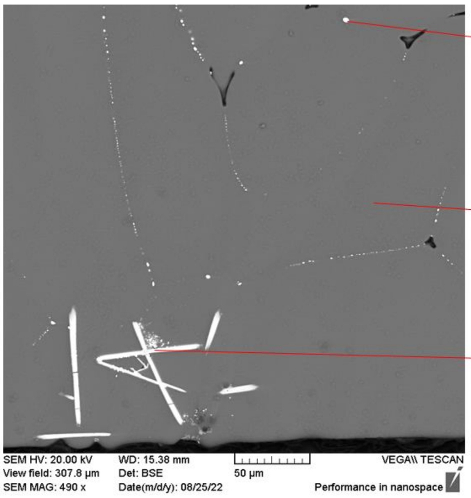

Elements	Mass %	Atomic %
Al	3.9	14.7
In	96.1	85.3

Elements	Mass %	Atomic %
Al	100	100

Elements	Mass %	Atomic %
Al	45.9	74.2
Zr	54.1	25.8
Total	100	100

(c)

Figure 41. SEM observation of (a) Upper (b) Middle and (c) bottom regions of the In_2Zr ingot. Indium is observed in the form of intergranular white crystals in all regions. Few white needles of Al_3Zr are found at the bottom of the ingot.

3.4.2. Direct reaction calorimetry

3.4.2.1. Heat increment measurements of In_2Zr

The already synthesized single phase In_2Zr pellets were dropped into calorimeter in order to measure the enthalpy increment of In_2Zr, ΔH_3, from room temperature to 1273 K.

$$\langle In_{0.667}Zr_{0.333}\rangle_{s,T_0} \rightarrow \langle In_{0.667}Zr_{0.333}\rangle_{s,1273\ K};\ \Delta H_3 \qquad (3.9)$$

The results of the measurements are given in **Table 15**. The heat increment of In_2Zr from room temperature to 1273 K is calculated by taking the average of the values and the error is calculated using the procedure stated in section 2.5.1. The heat increment of In_2Zr is measured as $\Delta H_3 = 27.1 \pm 2.4$ kJ.mol^{-1}at^{-1}.

Table 15. Heat increment measurement of In_2Zr from room temperature to 1273 K, ΔH_3.

Measurements	ΔH_3 / kJ.mol^{-1}at^{-1}
1	24.812
2	24.845
3	24.512
4	27.238
5	31.607
6	31.246
7	26.938
8	25.874

3.4.2.2. Standard enthalpy of formation of In_2Zr

The standard formation enthalpy of In_2Zr is computed from direct reaction and heat increment of In_2Zr. The sample pellets were dropped from room temperature ($T_0 \approx 298.15\ K$) to the calorimeter temperature (Tc = *1273 K*), corresponding to the following reaction:

$$0.667\langle In\rangle_{s,T_0} + 0.333\langle Zr\rangle_{s,T_0} \rightarrow \langle In_{0.667}Zr_{0.333}\rangle_{s,T_c}\ ;\ \Delta H_2 \qquad (3.10)$$

The determinations of the enthalpy (ΔH_2) associated to this reaction was reported by [18] as –8.9 ± 0.9 kJ.mol^{-1}at^{-1}.

Combining reactions (3.9) and (3.10), the standard molar enthalpy of formation of In_2Zr compound ($\Delta_f H^0_{298K}$) can be written as:

$$\Delta_f H^{\circ}_{298K} = \Delta H_2 - \Delta H_3$$

Then, the standard enthalpy of formation of In_2Zr was determined to be -36 ± 2.6 kJ.mol^{-1}at^{-1}.

3.5. Discussion

The revised In-Zr diagram established on the basis of the present work and literature data is presented in **Figure 23**.

When analyzing the different compositions by XRD, it was sometimes difficult to be definite about the exact nature of the phases present because of the many overlapping peaks between the different phase structures. Some of the results obtained in XRD were not fully consistent with the SEM observations (see **Table 11**). In fact, when the quantity of a given phase determined by XRD is very small, this secondary phase can be missed phase in the SEM investigations. EPMA analyses have shown that samples having compositions around 50 at.%Zr have greater sensitivity to oxidation at room temperature.

This work has confirmed the existence of In_3Zr, In_2Zr, InZr, $InZr_2$ and $InZr_3$ intermetallic phases previously reported in the literature and an additional phase In_3Zr_2 was found by SEM/EDX.

In the investigation of the indium rich region, it has been shown that there is a peritectic (In) ↔ α-In_3Zr + Liquid reaction at 156.8 ± 0.3 °C contrary to the eutectic reaction formerly proposed in the assessment of Okamoto [2]. The peritectic invariant at 156.8 ± 0.3 °C ends at 25 ± 3.8 at. % Zr, where the endothermic effect corresponding to another invariant at 591.6 ± 2.4 °C is maximum. We also showed that both In_3Zr and In_2Zr have non-congruent melting and decompose peritectically according to β-In_3Zr ↔ In_2Zr + L at 591.6 ± 2.4 °C and In_2Zr ↔ In_3Zr_2 + L at 1132.9 ± 1.8 °C respectively.

The liquid compositions of the peritectic plateaus at 591.6 ± 2.4 °C and 1132.9 ± 1.8 °C are 1.0 ± 0.1 at.% Zr and 3.7 ± 1.7 at.% Zr respectively. These two values are considerably higher than the Zr solubility limits, 0.02 at.% Zr and 0.5 at.% Zr, that can be calculated at the same temperatures using the correlation of Dieva [8].

According to G. Collins [30], the solid-solid transition temperature of α-In_3Zr to β-In_3Zr is around 270°C ± 50 °C but it was impossible to detect this transition temperature by DTA. From **Figure 22**, it can be seen that the energies of the two phases α-In_3Zr ($D0_{23}$) and β-In_3Zr ($D0_{22}$) are almost identical making it impossible to detect this quasi-athermal phase transition with DTA.

On cooling, all the peaks observed during former heating are seen, except the peritectic invariant of In_3Zr (see **Figure 30 b**) however, nucleation problems shift the temperatures at which new phases appear to lower values. Furthermore, in peritectic reactions, the kinetics can be slowed down as the precipitation of the peritectic phase can isolate the primary phase from the melt. For these reasons, only thermal events detected on heating of equilibrated samples were taken into consideration.

In_3Zr_2 phase was found in the 20.13 at.%Zr, 27.00 at.%Zr and 40.03 at%Zr samples investigated by SEM/EDX after DTA (see **Figure 36**). The fact that this phase was systematically observed in the three samples examined after DTA suggest that this phase could be stable even at room temperature. This hypothesis finds an additional support in the DFT calculations of C. Colinet [25] which show that In_3Zr_2 lies on the convex hull. The invariant peak at 1279°C in **Figure 30 a** is hence interpreted as the peritectic decomposition of $In_3Zr_2 \leftrightarrow InZr + L$ in the samples.

To further investigate this issue, an ≈ 40 at.%Zr sample annealed at 600°C for 2 months was analyzed by XRD (see **Figure 42**). According to Colinet [25], In_3Zr_2 has the Ga_3Ti_2 prototype. In **Figure 42**, it is seen that the diffractogram of the ≈ 40 at.%Zr sample does not show the characteristic peaks (red arrows) of the In_3Zr_2 phase but In_2Zr, InZr, ZrO_2 and In_2O_3 phases are detected and it was not possible to definitely confirm the existence of In_3Zr_2.

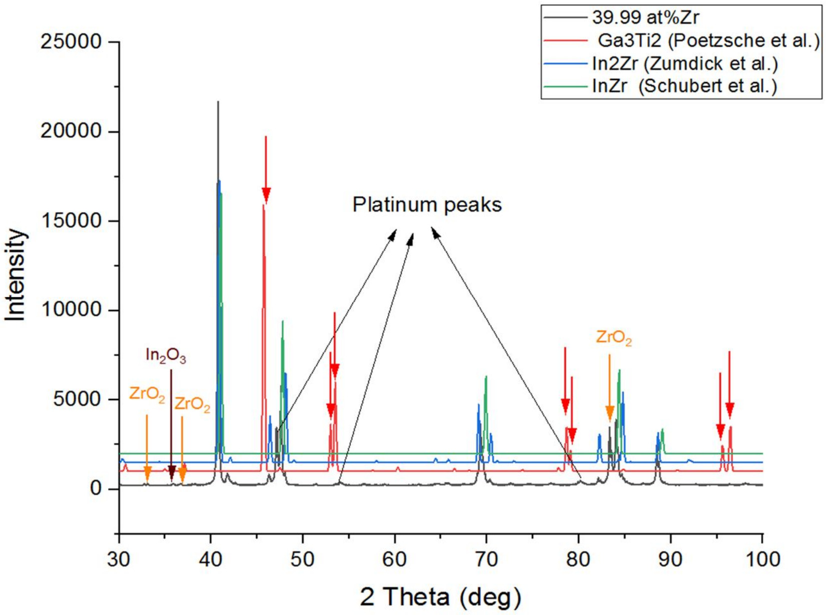

Figure 42. Diffractogram of 39.99 at.%Zr sample annealed at 600°C for 2 months compared with XRD spectra of Ga_3Ti_2 (prototype for In_3Zr_2) by Poetzschke et al. [31], InZr by Schubert et al. [10] and In_2Zr by Zumdick et al. [4]. Red arrows indicate the position of the reference In_3Zr_2 peaks that are not found in the spectra of 39.99 at.%Zr (black XRD pattern). The Extra peaks indicated by orange arrows are ZrO_2, brown arrows are In_2O_3 and black arrows are platinum peaks.

In the In-Zr phase diagram of **Figure 23**, InZr is considered to decompose by congruent melting. This choice is based on the micrograph of the arc-melted 53.89 at.%Zr alloy at the as-cast state (**Figure 43**) which shows an almost single phase InZr and eutectic structure at the grain boundaries. This observation is also fully consistent with i) the DFT calculations of Colinet [25], InZr being calculated as the most stable compound on the convex hull at 0 K (see **Figure 22**), and ii) the attribution of the peritectic at 1279°C to In_3Zr_2.

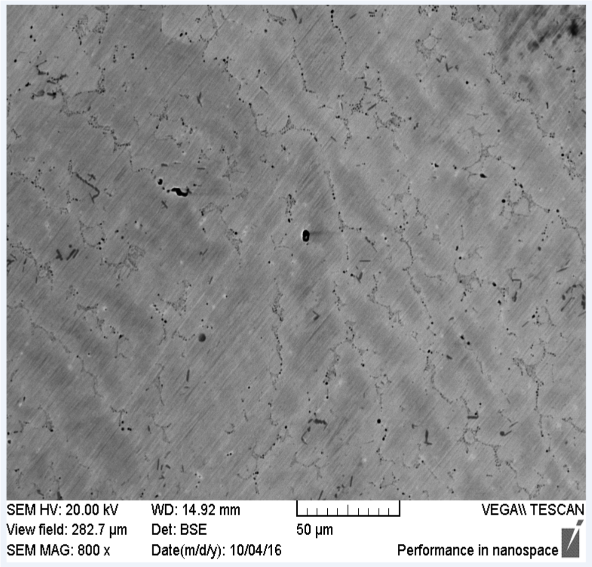

Figure 43. BSE image of arc-melted as cast 53.89 at%Zr sample showing almost single InZr phase.

In the phase diagram of **Figure 23**, a eutectic reaction is suggested between InZr and $InZr_2$ on the basis of the metallographic examination of the 54.43 at.%Zr sample after DTA. The micrograph (**Figure 44**) shows a mixture of InZr and $InZr_2$ phases. We do not see the usual lamellar eutectic structure but $InZr_2$ rather forms facet rods because of its preferential way of crystallization. This would also be consistent with the fact that both InZr and $InZr_2$ have congruent melting.

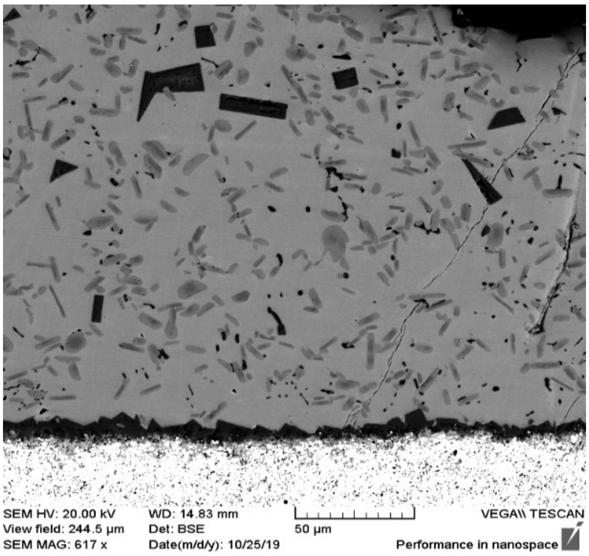

Figure 44. Micrograph of 54.34 at.%Zr sample after DTA sample showing divorced eutectic between InZr and $InZr_2$. Light grey matrix phase has InZr composition whiles the dark grey rod-like phase is $InZr_2$. The black particles are oxides.

Eutectic reaction between $InZr_2$ and $InZr_3$ was adopted in **Figure 23**, with the 2 compounds decomposing by congruent melting. This assumption is complemented with the findings of Betterton and Noyce [7] who believed $InZr_3$ decomposes by congruent melting because they did not observe a 3-phase peritectic structure for alloys with a content between 23 and 26 at.%In. Gajavalli [18] also reported the formation of single $InZr_3$ phase in 75.29 at.%Zr annealed at 1000°C for 18 days. Furthermore, the arc-melted 76.09 at.%Zr sample examined as as-cast state was also a single-phase $InZr_3$ (see **Figure 45**). It is consistent with the elaborations of Saitovich et al. [5] which mentioned that monophasic $InZr_2$ and $InZr_3$ were directly obtained from the liquid state by arc-melting.

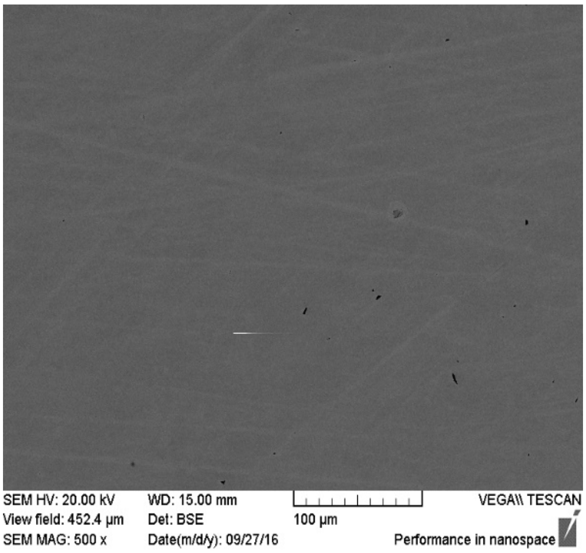

Figure 45. BSE image of the as cast 76.09 at.%Zr sample showing single $InZr_3$ phase. The lines in the micrograph come from polishing.

In **Figure 23**, the eutectic $\beta Zr + InZr_3 \leftrightarrow L$ and peritectoid $\beta Zr + InZr_3 \leftrightarrow \alpha Zr$ reactions are adopted on the basis of the work of Betterton and Noyce [7]. Surprisingly, microstructures having lamellar structures **(Figure 46)**, hence suggesting a eutectoid reaction $\beta Zr \leftrightarrow InZr_3 + \alpha Zr$, were observed when analyzing various compositions in the range 74-82 at.%Zr after DTA. However, at these compositions, the DTA analyses themselves were not conclusive enough to prove this eutectoid reaction, so we decided to stick with the findings of Betterton and Noyce [7] for this Zr-rich part of the phase diagram (**Figure 23**), which rely on a large number of samples. Future studies could be conducted in this compositional range to better interpret these conflicting observations.

The experimental standard enthalpies of formation of In_2Zr and In_3Zr compound have been measured by dissolution calorimetry in liquid Al at 1173 K. In each case the complete dissolutions of the elements and the compound are required in order to obtain an accurate result. Post-mortem metallographic examinations of the calorimetric ingots revealed no evidence of incomplete dissolution of either the In_2Zr or In_3Zr samples.

We start by discussing In_2Zr results. During the drop/solution of In_2Zr samples, the observed calorimetric peaks (e.g. the 4 last peaks in the thermogram given in the Appendix for In_2Zr/run 3) are composed of an initial fast endothermic deflection, interpreted as the heating of the sample up to the calorimeter temperature, followed by an endothermic shoulder corresponding to its slower melting/dissolution, assumed to be also endothermic. By contrast, the calibration peaks corresponding to pure Al drops (2 first peaks seen in the thermogram given in the

Appendix for In_2Zr/run 3,) do not show the endothermic shoulder but a fast return of the signal to the baseline. The retained value of the drop solution enthalpy of In_2Zr was calculated as the average from 4 experiments (see **Table 14**).

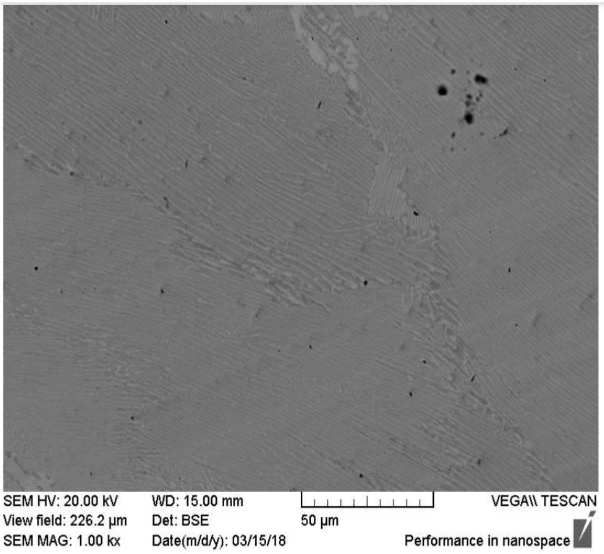

Figure 46. Micrograph of lamellar, eutectoid-like, microstructure in the 81.53 at.%Zr alloy after DTA. Exact compositions of the different contrasts could not be determined due to the small interlamellar spacing.

A new and more reliable value of the heat increment of In_2Zr at 1273 K was also obtained during the course of this thesis and was used, in conjunction with former direct reaction calorimetry results, to calculate a more accurate value of the formation enthalpy of In_2Zr.

Table 16 show that all experimental values of the formation enthalpy of In_2Zr are consistent considering the uncertainties. These values are also consistent with the CALPHAD assessment but are more exothermic than the values calculated by DFT (compare with **Table 10** and in **Figure 47**).

Table 16. Comparison of the measured standard enthalpies of formation for In_2Zr compound studied in this work with literature.

T/K	$\Delta_f H^\circ_{298K}(In_2Zr)$ / kJ.mol^{-1}at^{-1}	Uncertainty / kJ.mol^{-1}at^{-1}	Calorimetric technique	References
1273	-38.3	2.3	Direct synthesis	[20]
1273	-37.5	1.4	Direct synthesis	[18]
1273	-36.5	2.6	Direct synthesis	This work
1173	-38.2	3.3	Dissolution	This work

In_3Zr results are now discussed.

In numerous cases, the shape of the calorimetric peak following an In_3Zr drop was found to be similar to the shape observed for an In_2Zr drop (e.g. peaks 2 and 4 in the thermogram given in the Appendix for In_3Zr/run 4). However, the endothermic shoulder was absent in a significant number of peaks (e.g. peaks 1 and 3 in the thermogram given in the Appendix for In_3Zr/run 4).

Based on the presence/absence of an endothermic shoulder, the peaks were sorted into two populations (**Table 13**) and an average value was calculated for each subset of the data (**Figure 38**). It was also assumed that the most exothermic peaks, those with a marked endothermic shoulder and an average drop solution enthalpy value $\Delta_{ds}\overline{H}^{\infty,1173K}_{In_3Zr,298K}$ = 203.5 ± 7.1 kJ mol^{-1}, correspond to the complete dissolution, assumed to be endothermic, of the In_3Zr samples while dissolution remains incomplete, if it occurs at all, in the other population for which the average value is $\Delta_{ds}\overline{H}^{\infty,1173K}_{In_3Zr,298K}$ = 168.5 ± 5.7 kJ.mol^{-1}.

A more quantitative assessment of this last interpretation is now being made. The enthalpy increment of In_3Zr from 298 to 1173 K could not be directly measured as there were not enough samples available. A Neumann-Kopp Rule calculation using SGTE data of BCC Zr and tetragonal In gives an estimated value of 103 kJ mol^{-1} which is less than the average value, 168.5 ± 5.7 kJmol^{-1}, obtained for the least exothermic population. It is concluded that the measured heat effect does not simply correspond to the heating of the In_3Zr sample. This result is not surprising because, according to our DTA results, In_3Zr undergoes a peritectic melting at 592°C (865 K), a temperature which is lower than the calorimeter temperature (1173 K). Repeating the NKR calculation using SGTE data of liquid In and Zr (in fact a metastable liquid state for Zr at 1173 K), yields 128 kJ mol^{-1}, in closer agreement but still significantly lower than the measured value 168.5 ± 5.7 kJmol^{-1}. It is concluded at this point that this last value could be consistent with a thermal effect including the heat increment and a partial dissolution of the samples.

A second scenario that could give a less endothermic net heat effect would be a dissolution of In_3Zr followed by an exothermic re-precipitation of Zr as Al_3Zr aluminide due to local Zr saturation of the aluminum bath. This scenario is quantified below.

The chemical process occurring can be written as:

$$\langle \mathrm{In_3Zr} \rangle_{s,298\,K} + n(\mathrm{Al})_{1173\,K} \rightarrow \big((3\mathrm{In},(n-3)\mathrm{Al})\big)_{1173\,K} + \big((\mathrm{Al_3Zr})\big)_{1173\,K} \qquad (3.11)$$

The enthalpy of reaction (3.11), $\Delta H_{3.11}$, can be estimated by the following Hess cycle:

$$\Delta H_{3.11} = -\Delta_f H°_{In_3\mathrm{Zr},298K} + \Delta_f H°_{\mathrm{Al_3Zr},298K} + \Delta H^{1173K}_{\mathrm{Al_3Zr},298K} + 3\Delta_{ds}\overline{H}^{\infty,1173K}_{\mathrm{In},298K} - 3\Delta H^{1173K}_{\mathrm{Al},298K} \qquad (3.12)$$

Fischer [6] estimated the standard enthalpy of formation of the In_3Zr compound by CALPHAD modeling as:

$$\Delta_f H°_{In_3\mathrm{Zr},298K} = -130\ kJ\ mol^{-1}$$

Meschel and Kleppa [32] measured by high-temperature direct synthesis calorimetry the enthalpy of formation of Al_3Zr as:

$$\Delta_f H°_{Al_3Zr,298.15\ K} = -193.6 \pm 5.2\ kJ\ mol^{-1}$$

The heat increment of the aluminide from room temperature to calorimeter temperature (1173 K) was calculated using classical thermodynamic relations from the Gibbs energy function of Al_3Zr assessed by Fischer and Colinet [33]:

$$\Delta H_{Al_3Zr,298.15\ K}^{1173\ K} = 91.2\ kJ\ mol^{-1}$$

The heat increment of pure aluminum from the room temperature to the calorimeter temperature was calculated using the SGTE data for pure elements [34]:

$$\Delta H_{Al,298.15\ K}^{1173\ K} = 36.4\ kJ\ mol^{-1}$$

The partial drop solution enthalpy of In in liquid Al at infinite dilution at 1173 K was reported by Gajavalli [18] to be:

$$\Delta_{ds}\overline{H}_{In,298K}^{\infty,1173K} = 58.4 \pm 0.7\ kJ\ mol^{-1}$$

Considering all the values into equation 3.12, the enthalpy of reaction $\Delta H_{3.11}$, is determined to be, $\Delta H_{3.11}$= 93.6 ± 5.2 kJ.mol^{-1}. This value is much less than the average value 168.5 ± 5.7 kJmol^{-1} for the second population. Moreover, a transient precipitation of Al_3Zr would likely be accompanied a visible exothermic signature which was not observed during the experiments. This scenario can reasonably be discarded.

As a final conclusion, we select the most endothermic value for the drop solution enthalpy of In_3Zr and calculate $\Delta_f H^{\circ}_{In_3Zr}$= -39.7 ± 2.9 kJ.mol^{-1}.at^{-1}. We are not aware of any previous experimental determination of this enthalpy. This value is slightly more exothermic than the formation enthalpy of In_2Zr with overlapping uncertainty intervals but is also more exothermic than the values calculated by DFT (compare with **Table 10** and in **Figure 47**)

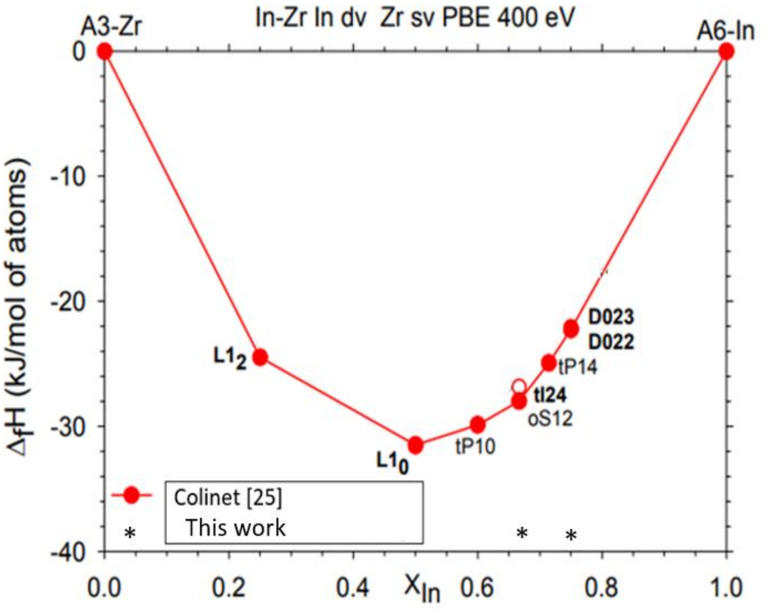

Figure 47. Comparison of standard formation enthalpies calculated by DFT by Colinet at 0 K [25] with the values measured by liquid Al solution calorimetry in this work for In_3Zr and In_2Zr.

3.6. Conclusion

A revised In-Zr phase diagram (**Figure 23**) has been proposed on the basis of detailed metallographic observations, X-ray diffraction analyses, different thermal analysis and calorimetric techniques and literature data. This new diagram will serve as a basis for a future CALPHAD reassessment of the system in the NUCLEA database which will also allow the internal consistency of the experimental results to be tested.

The existence of the intermetallic compounds (In_3Zr, In_2Zr, InZr, $InZr_2$ and $InZr_3$) previously reported by Schubert et al. [9, 10, 13] has been confirmed. Around the equiatomic composition (InZr), the X-ray powder diffraction analyses and EPMA have shown that the alloys are sensitive to oxidation at room temperature. An additional phase of In_3Zr_2 composition was found by SEM examination of 20-40 at.%Zr alloys after DTA. Existence of this phase is also supported by DFT calculations [25] but we have not been able to confirm it by XRD.

The transition temperatures of the different phases have been determined. We showed that there is peritectic reaction (In) ↔ αIn_3Zr + Liquid at low temperature (156.8 ± 0.3 °C), peritectic decomposition of In_3Zr ↔ In_2Zr + L at 591.6 ± 2.4 °C, In_2Zr ↔ In_3Zr_2 + L at 1132.9 ± 1.8 °C and In_3Zr_2 ↔ InZr + L at 1279 ± 6 °C. It was impossible to determine the phase transition temperature of αIn_3Zr to βIn_3Zr by DTA due to the quasi athermal character of the transition.

The central part of the diagram in **Figure 23** remains largely estimated as, in particular, no information is available on the melting and invariant temperature of the compounds.

On the Zr rich side, the peritectoid reaction reported by Betterton and Noyce [7] was adopted in **Figure 23**. However, metallographic investigations on few alloys in this compositional range after DTA have surprisingly shown lamellar, eutectoid-like, microstructures. Future studies need to be done in order to draw a definite conclusion about the type of invariant reaction.

The experimental standard enthalpy of formation of In_3Zr and In_2Zr compounds have been determined by dissolution calorimetry at 1173 K. For In_2Zr, the enthalpy value obtained by dissolution calorimetry was further complemented by drop calorimetry at 1273 K. The values obtained for In_2Zr are consistent with the NUCLEA database, -38.3 $kJ.mol^{-1}.at^{-1}$ whiles the value obtained for In_3Zr is more exothermic than NUCLEA, -32.5 $kJ.mol^{-1}.at^{-1}$ [6]. The standard enthalpy of formation of In_2Zr determined by both direct reaction and dissolution calorimetry are consistent. The results obtained for In_2Zr are also in agreement with the experimental data [18, 20].

3.7. Appendix

Thermograph for In_3Zr dissolution in liquid Al (Run 4)

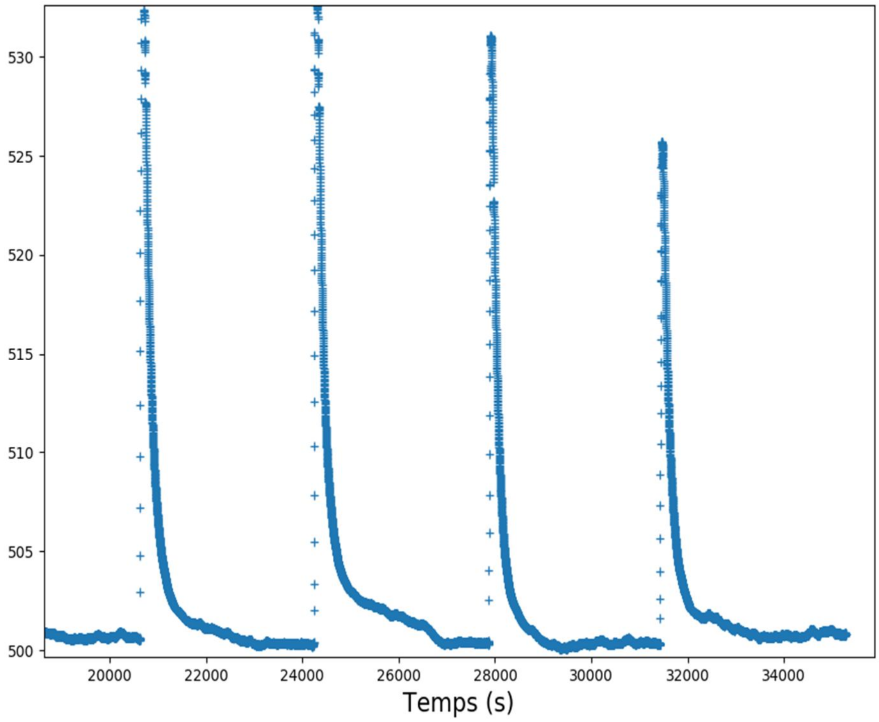

Thermograph for In_2Zr dissolution in liquid Al (Run 3)

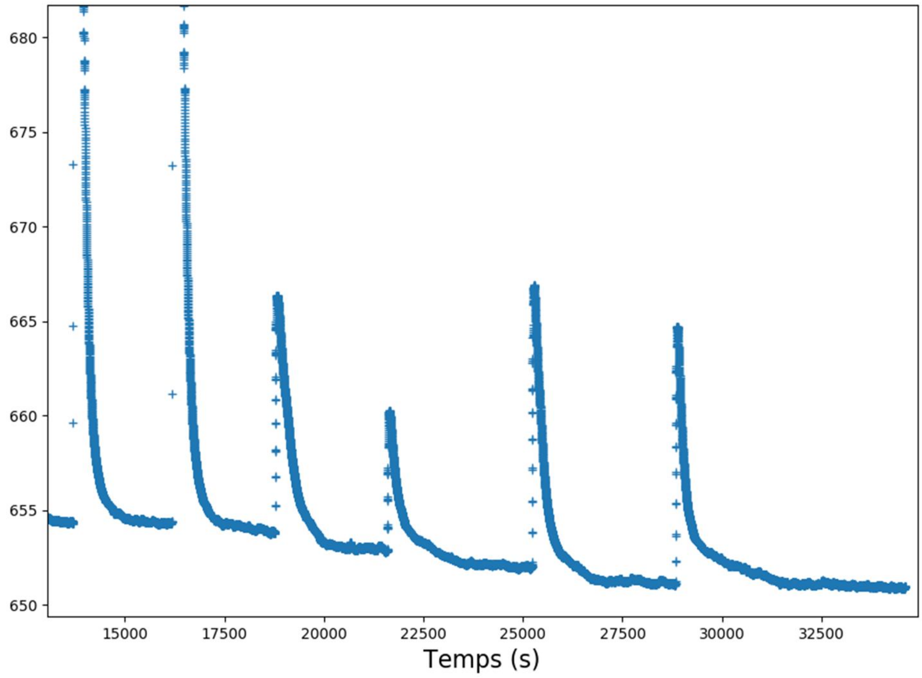

3.8. References

1. Lustman B., Kerze F., Metallurgy of Zirconium, McGraw-Hill Book. 458-460 (1965).
2. Okamoto H., The Indium-Zirconium System. Bull. Alloy Phase Diag. 11(2):150–152 (1990).
3. Gulay L.D., Zaremba V.I., Stepien-Damm J., Kalychak. Y.M., Interactions between the Components in the Zr-Ag-In System at 870 K. Polish J. Chem. 72: 1886–1889 (1998).
4. Zumdick M. F., Gregory A. L., Dronskowski R., Hoffmann R.D., Pöttgen R., Structure, Chemical Bonding, and Properties of $ZrIn_2$, $IrIn_2$, and $Ti_3Rh_2In_3$. J. Solid State Chem. 150 (1): 19–30 (2000).
5. Saitovitch H., Silva P.R.J., Cavalcante J.T., Forker M., Zirconium–Indium Intermetallic Compounds Investigated by Measurements of Nuclear Electric Quadrupole Interactions. J. Alloys Compd. 505 (1): 157–62 (2010).
6. Fischer E., Thermodynamic database NUCLEA (IRSN) (2014).
7. Betterton J.O., Noyce W.K. The Equilibrium Diagram of Indium-Zirconium in the Region 0-26 At. Pct In. Trans. Metall. Soc. AIME. 212 (6): 340–342 (1958).
8. Dieva E.N., Solubility of Metals of the Fifth and Sixth Periods in Liquid Indium: Physicochemical Studies of Liquid Metals and Alloys, V.G. Bamburov, Ed., Izd. Ural'sk. Nauch. Tsentra Akad. Nauk SSSR, Sverdlovsk. 105–110 in Russian (1974).
9. Schubert, K., Meissner H.G., Raman A., Rossteutscher W., Einige Strukturdaten Metallischer Phasen (9). Die Naturwissenschaften. 51 (12): 287–287 (1964).
10. Schubert K., Frank K., Gohle R., Maldonado A., Meissner H.G., Raman A., et al., Einige Strukturdaten Metallischer Phasen (8). Die Naturwissenschaften. 50 (2): 41–41 (1963).
11. Dasarathy C., Liquid Immiscibility in Binary Indium Alloys. Trans. Metall. Soc. AIME. 245(9), 2015–2019 (1969).
12. Anderko K., Beitrag Zu Den Binaren Systemen Des Titans Mit Gallium, Indium Und Germanium Und Des Zirkons Mit Gallium Und Indium. Zeitschrift Für Metallkunde. 49 (4): 165– 172 (1958).
13. Schubert K., Meissner H.G., Potzschke M., Rossteutscher W., Stolz E., Einige Strukturdaten Metallischer Phasen (7). Die Naturwissenschaften. 49 (3): 57–57 (1962).
14. King H.W., Crystal Structures of the Elements at 25°C. Bull. Alloy Phase Diag. 2:401–402 (1981).
15. King H.W., Temperature Dependent Allotropic Structures of the Elements. Bull. Alloy Phase Diag. 3: 276–276 (1982).
16. Pearson W.B., Handbook of Lattice Spacings and Structures of Metals and Alloys. Physics Today. 11(9): 36-36 (1958).
17. Massalski T., Subramanian P. R., Kacprzak L., Scott W.W., Bull. Alloy Phase Diag. ASM International. 3 (1986).
18. Gajavalli J., Experimental Contribution to Thermodynamics of the Ag-Cd-In, In-Zr and In_2O_3-ZrO_2 Systems. PhD Thesis, Aix Marseille University (2019).
19. Kneip G. D., Betterton J.O., Scarbrough J.O., Specific Heats of Zirconium Alloys at Low Temperatures. Physical Review. 131(6):2425–2432 (1963).

20. Meschel S.V., Kleppa O.J., Standard Enthalpies of Formation of Some Transition Metal Indium Compounds by High Temperature Direct Synthesis Calorimetry. J. Alloys Compd. 333:91–98 (2002).
21. Lukas H.L., Henig E.T., Zimmermann B., Optimization of Phase Diagrams by a Least Squares Method Using Simultaneously Different Types of Data. Calphad. 1(3): 225–236 (1977).
22. Saal J.E., Kirklin S., Aykol M., Meredig B., Wolverton C., Materials Design and Discovery with High-Throughput Density Functional Theory: The Open Quantum Materials Database (OQMD). Journal of Management. 65(11):1501–1509 (2013).
23. Jain A., Ong S.P., Hautier G., Chen W., Richards W.D. et al., Commentary: The Materials Project: A Materials Genome Approach to Accelerating Materials Innovation: APL Materials. 1(1):011002 (2013).
24. Guo F., Wu J., Liu S., Zhan Y., The Effect of Indium Concentration on the Structure and Properties of Zirconium Based Intermetallics: First-Principles Calculations. Adv. Condense Matter Phys. (2016).
25. Colinet C. “Private communication (2019)”.
26. Lichter B.D., Precision Lattice Parameter of Zirconium Oxygen Solid Solution. Trans. Metall. Soc. AIME. 218:1015 -1018 (1960).
27. Faita F.L., Ersching K., Acuna J.J.S., Campos C.E.M., Pizani P.S., Structure and Microstructure of In_4Te_3 Nano-Powders Prepared by Solid State Reaction. Materials Chemistry and Physics. 130 (3): 1361-1365 (2011).
28. Guenet J.M., Contributions of Phase Diagrams to the Understanding of Organized Polymer-Solvent Systems. Thermochim Acta. 284:67–83 (1996).
29. Gajavalli K., Barrachin M., Benigni P., Rogez J., Mikaelian G., Fischer E., Determination of Solution Enthalpy of Zirconium in Liquid Aluminum. J. Chem. Thermodyn. 135: 198–204 (2019).
30. Gary S. Collins. “Private communication (2021)”.
31. Poetzschke M., Schubert K., Zum Aufbau einiger T(4)-B(3) homologer und quasihomologer Systeme. I. Die Systeme Ti-Ga, Zr-Ga und Hf-Ga. Zeitschrift fuer Metallkunde. 53 : 474 – 488 (1962).
32. Meschel S. V., Kleppa O.J., Standard Enthalpies of Formation of 4d Aluminides by Direct Synthesis Calorimetr. J. Alloys and Compd. 191: 111–116 (1993).
33. Fischer E., Colinet C., An Updated Thermodynamic Modeling of the Al-Zr System. J. Phase Equilibria and Diffus. (2015).
34. Dinsdale A.T., SGTE Data for Pure Elements. Calphad. 15: 317-425 (1991).

4. Enthalpies of formation of the AgZr and Fe_2Zr intermetallic compounds

4.1. Introduction

As stated in Chapter 1, most pressurized water reactor (PWR) control rods are composed of Ag-In-Cd neutron absorber alloy (80 wt. % Ag, 15 wt. % In, 5 wt. % Cd) inside a stainless steel (AISI 304 or 316) cladding and inserted into a Zircaloy-4 guide tube.

In the event of a severe accident in a PWR, the Ag-Cd-In absorbing alloy is expected to interact with the Zircaloy guide tubes at high temperature due to the failure of stainless steel, leading to the formation of Ag-In-Zr-O and Fe-Zr-(Cr-Ni-O) mixtures. They form quasi-immiscible mixtures because most stainless steel components (Fe, Cr, Ni) are very lowly soluble with the main elements of the absorber materials (Ag, In) even at high temperature (Ag-Fe [1], Ag-Cr [2] Ag-Ni [3], In-Fe- [4] and In-Cr [5]). To address the issue of control rod and Zircaloy interactions during the early stages of the progression of a severe accident in a nuclear reactor, accurate knowledge of the binary and ternary subsystems of the quaternary Ag-In-Zr-O phase diagram as well as those of the quinary Fe-Zr-(Cr-Ni-O) one is required. Information on these systems, in particular, aids in determining the liquid fraction of the melts during their progression, as well as their ability to flow down in the colder region of the core which have a significant impact on the progression of the accident in terms of core degradation and in terms of silver and cadmium released fractions, which have a significant impact on iodine behavior in the primary circuit and nuclear reactor containment.

The thermodynamic behavior of these two relevant systems (Ag-In-Zr-O, Fe-Cr-Ni-Zr-O) can be predicted from the modeling of their binary and ternary subsystems. Among the subsystems of interest, the Ag-Zr and Fe-Zr systems will be addressed in this chapter. It must be underscored that during the advanced phase of the progression of severe accident in a nuclear reactor, the study of the complex multiphase system (U-O-Zr-Fe) is of great importance for understanding core degradation and in this framework, a better characterisation of the Fe-Zr is also a key contribution.

Despite numerous studies on these two binary systems, it can be noted that few studies concerning the measurements of thermodynamic properties of the intermetallic compounds in the Ag-Zr and Fe-Zr systems are available. Our experiments will be focused on the determination of the thermodynamic properties of the AgZr and Fe_2Zr intermetallic compounds, specifically, their standard enthalpy of formation. In order to determine the standard enthalpy of formation of these compounds, we used the high temperature dissolution calorimetry technique in liquid aluminum.

After a short review of the data available in the literature, we present our experimental data on the partial drop solution enthalpies of AgZr and Fe_2Zr at infinite dilution in liquid aluminum at 1173 K, which will be combined, for the determination of the standard enthalpies of formation, with the partial drop solution enthalpies of Zr and Ag in liquid Al recently determined in a PhD work performed in our laboratory [6], [7] and partial drop solution enthalpy of Fe in liquid Al critically assessed in this work from literature results [8-20].

4.2. Bibliography

4.2.1. Fe-Zr system

There have been numerous investigations of the Fe-Zr phase diagram, ever since Svechnikov [21, 22] performed the first experiments aimed at establishing the phase diagram over the entire composition range. Both the cubic C15-$ZrFe_2$ phase and the Zr_3Fe phase were discovered, however no compounds in the Zr-rich composition range were detected.

Later critical evaluation by Arias and Abriata [23] has produced a phase diagram based on new experimental findings [21, 22, 24-29] where four compounds Zr_3Fe, C15-$ZrFe_2$, Zr_2Fe, and $ZrFe_3$ were shown to be stable. Thermodynamic analyses made later [30–33] reflected inconsistencies in the literature on phase stabilities. Stein et al. [34] conducted experiments on phase equilibria to resolve a number of inconsistencies and uncertainties. In particular, they suggested that the Zr_6Fe_{23} ($ZrFe_3$) phase did not belong to the binary Fe-Zr equilibrium diagram but was rather a ternary (Fe-Zr-O) phase stabilized by oxygen impurity. However, Du et al. [35] have recently challenged this conclusion. These last authors concluded that Zr_6Fe_{23} was indeed a true binary phase.

On the Zr rich side of the diagram, the works of Malakhova [36] and Malakhova and Alexeyeva [26] showed that Zr_3Fe was stable below 1158 K while the Zr_2Fe phase was only stable between 1048 and 1247 K. Stein et al. [34] confirmed and slightly modified the stability ranges of these phases. **Figure 48** displays the phase diagram for the Fe-Zr binary system established by Stein et al. [34].

Table 17 contains a list of all stable phases of the Zr-Fe system along with a description of their crystal structures.

Table 17. Crystal structures for the solid phases in the Fe-Zr system.

Phase	Pearson Symbol	Space group	Strukturbericht	Prototype	Reference
α-Fe	cI2	$Im\bar{3}m$	A2	W	[41]
γ-Fe	cF4	$Fm\bar{3}m$	A1	Cu	[41]
δ-Fe	cI2	$Im\bar{3}m$	A2	W	[41]
Zr_6Fe_{23}	cF116	$Fm\bar{3}m$	D8a	$Mn_{23}Th_6$	[35]
C36-$ZrFe_2$	hP24	$P6_3/mmc$	C36	$MgNi_2$	[34]
C15-$ZrFe_2$	cF24	$Fd\bar{3}m$	C15	$MgCu_2$	[34]
Zr_2Fe	tI12	I4/mcm	C16	Al_2Cu	[34]
Zr_3Fe	oC16	Cmcm	$E1_a$	Re_3B	[34]
αZr	hP2	$P6_3/mmc$	A3	Mg	[41]
βZr	cI2	$Im\bar{3}m$	A2	W	[41]

In the optimizations carried out by Guo et al. [30], Yang et al. [37], Rigaud et al. [38], Lafaye et al. [39] and Saenko et al. [40] the phase diagram established by Stein et al [34] was approved. While Yang [37] put more weight to the thermodynamic data and ab-initio calculations, which led to a significantly worse agreement with the established phase diagram [34], Guo et al. [30]'s thermodynamic assessment fits better with the experimental findings of Stein et al. [34]. In contrast with the above mentioned optimizations of Guo et al. [30], Rigaud et al. [38], Saenko et al. [40] and Lafaye et al. [39], the very recent reassessment of Du et al. [35] reintegrates the Zr_6Fe_{23} phase.

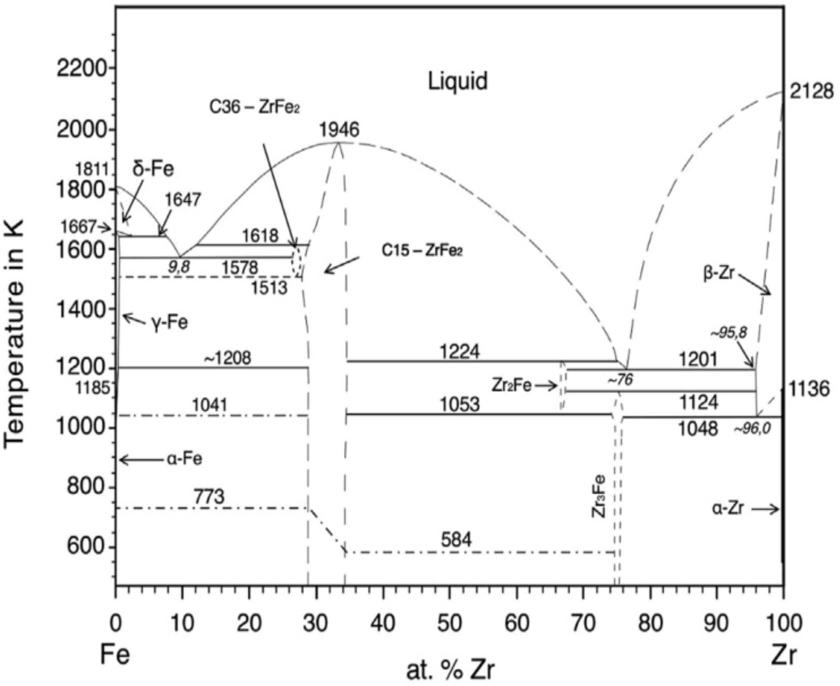

Figure 48. Fe–Zr phase diagram presented by Stein et al. [29].

The enthalpies of formation of different Fe-Zr compounds using different techniques and assessment reported by different authors are summarized in **Table 18** and **Table 19**. The values reported by Gachon and Hertz [42] and Rosner-Kuhn et al. [43] for C15-$ZrFe_2$ are consistent while Schneider at al. [44] and Sidorov et al. [45] obtained less exothermic values (see **Table 18**).

It should be noted that, all ab-initio calculations for the compounds C15-$ZrFe_2$ and C36-$ZrFe_2$ show strong agreement with each other and within the limits of experimental uncertainty, with data obtained by Gachon and Hertz [42] for C15-$ZrFe_2$.

Table 18. Comparison of experimental data of standard enthalpies of formation of the Fe-Zr compounds by different authors using different techniques.

Compound	$\Delta_f H$ (298 K) kJ/(mol at)	Technique	References
C15- $ZrFe_2$	-29.7 ± 1.7	Direct reaction calorimetry	[42]
	-31.93	Levitation Alloy calorimetry.	[43]
	-24.69 ± 1.4	Solution calorimetry.	[44]
	-22.0 ± 2	Solution calorimetry.	[45]

Table 19. Comparison of the enthalpy of formation of the stable intermediate phases in the Fe–Zr system by DFT at 0 K and CALPHAD at 298 K reported by different authors.

Compounds	$\Delta_f H$ kJ/ (mol at)	Technique	References
C15-$ZrFe_2$	-30.45	CALPHAD	[30]
	-28.95	CALPHAD	[37]
	−29.77	CALPHAD	[40]
	-27.79	DFT	[47]
	−28.07	DFT	[50]
	−27.0	DFT	[46]
	−27.40	DFT	[51,52]
	−26.98	DFT	[53]
C36-$ZrFe_2$	-26.34	DFT	[46]
	-27.59	DFT	[50]
	-26.63	DFT	[51,52]
	-27.78	CALPHAD	[30]
	-28.23	CALPHAD	[37]
	-28.86	CALPHAD	[40]
Zr_2Fe	−16.07	DFT	[49]
	−18.76	DFT	[48]
	−16.02	DFT	[50]
	−13.51	DFT	[46]
	−13.70	DFT	[51,52]
	−13.49	DFT	[53]
	−15.43	CALPHAD	[37]
	−11.70	CALPHAD	[40]
Zr_3Fe	−11.62	DFT	[47]
	−14.34	DFT	[49]
	−14.47	DFT	[50]
	−11.77	DFT	[46]
	−12.35	DFT	[51,52]
	−11.56	DFT	[53]
	−12.38	CALPHAD	[40]
	−14.46	CALPHAD	[37]

4.2.2. Ag-Zr System

Several studies have been carried out on investigating the Ag-Zr phase diagram [54-64]. In studying the crystallographic structure of the Ag-Zr system, five phases were reported: a silver rich solid solution (Ag), two Zirconium-rich solid solutions; (αZr) and (βZr) and two intermetallic compounds corresponding to the AgZr and $AgZr_2$ phases (see **Figure 49**).

Existence of $AgZr_3$ compound was also mentioned by [59] but the later studies, in particular that of Betterton and Easton [56], reported that it was a matter of erroneous identification of the $AgZr_2$ phase. The phases present in the Ag-Zr phase equilibrium diagram are shown in **Table 20** with their crystallographic data. The experimental data regarding the Ag–Zr equilibrium phase diagram successively obtained by Raub and Engel [54], Betterton and Easton [56], Loboda et al. [57], Zhang et al. [58] and Decreton [64] are reported on **Figure 49**.

Table 20. Crystal structures of the phases of the Ag-Zr system.

Phase	Pearson Symbol	Space group	Strukturbericht	Prototype	Reference
(Ag)	cF4	$Fm\bar{3}m$	A1	Cu	[60]
AgZr	tP4	P4/nmm	B11	γCuTi	[58] [61]
$AgZr_2$	tI6	I4/mmm	$C11_b$	$MoSi_2$	[58] [61]
αZr	hP2	$P6_3/mmc$	A3	Mg	[41]
βZr	cI2	$Im\bar{3}m$	A2	W	[41]

The list of invariant transformations reported by the different authors is given in **Table 21**. This table highlights the controversies about notably the nature of the transformations of the intermediate compounds AgZr and $AgZr_2$. The diagrams have been recently assessed by different authors [65- 67] in order to propose a CALPHAD modeling of the system. There are large discrepancies between the different available versions, regarding notably the nature of the invariant reactions in the system between 0 and 50 at. % Ag, reflecting the different experimental data obtained in the past. The controversies have been recently solved in the PhD work of Decreton [64] which shows that AgZr and $AgZr_2$ likely decomposes congruently and peritectically respectively.

For the thermodynamic properties of Ag-Zr system, there is limited experimental work available in the literature. The enthalpies of formation of different Ag-Zr compounds using different techniques reported by different authors are summarized in **Table 22** .

The enthalpies of formation of AgZr and $AgZr_2$ were firstly determined by Fitzner et al. [68]:

$$\Delta_f H^{\circ}_{AgZr} = -\,3.12 \pm 3.13 \text{ kJ.mol}^{-1}.\text{at}^{-1}.$$

$$\Delta_f H^{\circ}_{AgZr2} = -1.47 \pm 2.89 \text{ kJ.mol}^{-1}.\text{at}^{-1}.$$

The uncertainties are of the same order of magnitude as the measured values, making it difficult to determine the exothermic or weakly endothermic nature of the enthalpy of formation of the compounds.

Table 21. Summary of invariant equilibria and transformation temperatures for the Ag-Zr system reported in past studies [54-59, 62-64].

Reactions	Temperature (K)	Type of reaction	References
L ⇄ Ag	1235	Congruent	[63]
L ⇄ (Ag)+AgZr	1228	Eutectic	[54]
	1208		[57]
	1226		[58]
	1232		[64]
L ⇄ AgZr$_2$ +AgZr	1437	Eutectic	[57]
	1438		[64]
L + AgZr$_2$ ⇄ AgZr	1408	Peritectic	[59]
L⇄ AgZr	>1456	Congruent	[64]
L+ AgZr⇄ AgZr$_2$	1426	Peritectic	[58]
L⇄ AgZr$_2$+ (βZr)	1523	Eutectic	[55]
	1422		[58]
L + (βZr) ⇄ AgZr$_2$	≤ 1464	Peritectic	[56]
	1443		[57]
	1459		[64]
(βZr) ⇄ αZr +AgZr$_2$	1083	Eutectoid	[55]
	1093		[62]
	1094		[56]
	~1098		[64]
L ⇄ (βZr)	2128	Congruent	[63]
(βZr) ⇄ αZr	1136	Allotropic	[63]

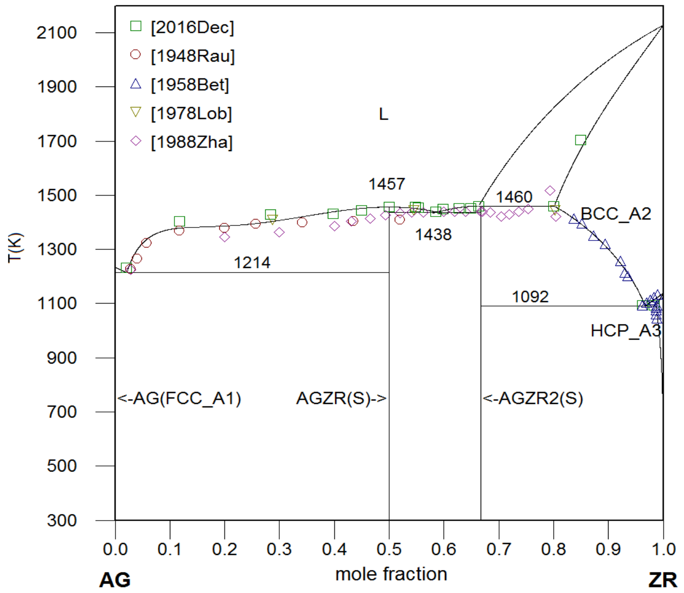

Figure 49. Calculated Ag-Zr diagram with superimposed experimental points of 54, 56-58 and 64.

Recently, Decreton [64] tried to measure the formation enthalpies of AgZr and $AgZr_2$ by acid solution calorimetry using HF-HNO_3 mixtures at room temperature. For AgZr, he obtained $\Delta_f H^{\circ}_{AgZr}$= -22.3 ± 10 kJ.mol^{-1} at^{-1}. For $AgZr_2$ and its corresponding mechanical mixture, the enthalpies of dissolution measured were very scattered with very large standard deviations around 100 kJ.mol^{-1}. Hence, it was not possible to derive a reliable estimate of the formation enthalpy of $AgZr_2$.

Decreton [64] also tried to carry out new thermodynamic measurements in determining the enthalpy of formation of AgZr by dissolution calorimetry taking into account the drop solution enthalpy of Ag, Zr, AgZr in liquid Al at T=996 K.

$$\Delta_f H^{\circ}_{AgZr} = \Delta_{ds}\overline{H}^{\infty,T}_{Ag,298\ K} + \Delta_{ds}\overline{H}^{\infty,T}_{Zr,298\ K} - \Delta_{ds}\overline{H}^{\infty,T}_{AgZr,298\ K} \quad (4.1)$$

Decreton [64] measured the partial drop solution enthalpies of Ag and AgZr at infinite dilution in liquid Al at 996 K finding $\Delta_{ds}\overline{H}^{\infty,996\ K}_{Ag,298\ K}$= 40.9 ± 0.8 kJ.mol^{-1} and $\Delta_{ds}\overline{H}^{\infty,996\ K}_{AgZr,298\ K}$ = -146.8 ± 9.6 kJ.mol^{-1}. He did not succeed in measuring the partial drop solution enthalpies of Zr in liquid Al at 996 K. Later on, Gajavalli et al. [6] indirectly measured the partial drop solution enthalpies of Zr at infinite dilution in liquid Al, but at higher temperature, 1173 K:

$$\Delta_{ds}\overline{H}^{\infty,1173\ K}_{Zr,298\ K} = -130 \pm 9\ \text{kJ.mol}^{-1}.$$

The Decreton's [64] and Gajavalli's [6] works can be combined to have an estimate of the enthalpy of formation of AgZr. Nevertheless, some assumptions have to be done since all the drop solution enthalpy measurements of Ag, AgZr (996 K) and Zr (1173 K) at infinite dilution in liquid aluminum were not performed at the same working temperature.

One can assume that the partial mixing enthalpy value of Zr in Al at infinite dilution at 1173 K is the same at the 996 K:

$$\Delta_{mix}\overline{H}^{\infty,996\ K}_{Zr} = \Delta_{mix}\overline{H}^{\infty,1173\ K}_{Zr} = -175 \pm 10\ \text{kJ.mol}^{-1.}$$

From this value, considering the heat increment of Zr from room temperature to 996 K and the fusion enthalpy of Zr at 996 K, the drop dissolution enthalpy of Zr in liquid Al at infinite dilution at 996 K:

$$\Delta_{ds}\overline{H}^{\infty,996\ K}_{Zr,298\ K} = -136.2 \pm 10\ \text{kJ.mol}^{-1}.$$

Substituting the values in Equation (4.1), the enthalpy of formation of AgZr, $\Delta_f H^{\circ}_{AgZr}$ was calculated as 51.5 ± 13.6 kJ.mol^{-1}. The estimation for the standard enthalpy of formation of AgZr is endothermic, which is in contradiction with the state of the art of Ag-Zr phase diagram in which AgZr is a stable compound at 298 K. It puts in question the dissolution measurements of AgZr. Therefore, new measurements of AgZr dissolution in liquid Al at 1173 K have been decided and presented in this work.

The Ag–Zr system was thermodynamically assessed by He et al. [66]. It can be checked from Figure 3 of reference [66] that the calculated enthalpies of formation of the AgZr phase were slightly more exothermic than the measured values by Fitzner et al. [68]. Assessment was also done by Hsiao et al. [65] and obtained the enthalpies of formation of the AgZr and $AgZr_2$ phases as −5.5 kJ.mol^{-1} at^{-1} and −3.62 kJ.mol^{-1} at^{-1} respectively.

The standard enthalpy of formation of the Ag-Zr compounds obtained by CALPHAD modeling at 298 K and by Density Functional Theory (DFT) calculation at 0 K are reported in **Table 23**. It must be underscored that DFT calculations from Curtarolo et al. [69] predicted the stability at 0 K of the Ag_2Zr and $AgZr_3$ compounds which have never been identified in the various experimental studies on the system Ag-Zr. For the compounds effectively present in the Ag-Zr system, the standard enthalpy of formation of the AgZr and $AgZr_2$ compounds obtained by CALPHAD modeling at 298 K are less exothermic than by DFT calculation.

At this stage, if all the available values of standard enthalpy of formation (DFT, CALPHAD and experimental) seem to converge to a slightly exothermic one, there is a need for a definitive experimental confirmation.

Table 22. Comparison of experimental data of standard enthalpies of formation of the Ag-Zr compounds by different authors using different techniques.

Compound	$\Delta_f H$ (298 K) kJ/(mol at)	Technique	References
AgZr	− 3.12 ± 3.13 -22.3 ± 10	Direct synthesis calorimetry Acid solution calorimetry	[68] [64]
$AgZr_2$	−1.47 ± 2.89	Direct synthesis calorimetry	[68]

Table 23. Comparison of the enthalpies of formation of the intermediate phases calculated at 298.15 K and 0 K by CALPHAD and DFT respectively in the Ag–Zr system.

Compounds	$\Delta_f H$ kJ/ (mol at)	Technique	References
AgZr	−5.5	CALPHAD	[65]
	−12.06	DFT	[53]
	−14.18	DFT	[69]
	−17.6	CALPHAD	[70]
	−11.67	DFT	[51]
$AgZr_2$	−3.62	CALPHAD	[65]
	−10.61	DFT	[53]
	−11.36	DFT	[69]
	−12.21	CALPHAD	[70]
	−10.23	DFT	[51]
$AgZr_3$	−8.6	DFT	[69]
	1.64	DFT	[53]
	2.22	DFT	[51]
Ag_2Zr	−12.5	DFT	[69]
	−4.92	DFT	[53]
	−4.63	DFT	[51]

4.3. Dissolution calorimetry measurements

4.3.1. Dissolution of Fe_2Zr in liquid Al at 1173 K

The synthesized Fe_2Zr was elaborated at LM2T/CEA Saclay. Prior to the measurements, XRD was performed on the synthesized Fe_2Zr sample in order to check its single phase character. The diffractogram (**Figure 50**) shows the absence of the peaks of the starting elements (Fe and Zr) and the very good matching with the Fe_2Zr pattern of Israel et al. [71]. Therefore, it is concluded that the sample is single phase Fe_2Zr.

For our dissolution experiments, the Fe_2Zr slugs were cut into small pieces (masses of 9 to 17 mg) and dropped into an Al bath at 1173 K. Six runs of Fe_2Zr dissolution calorimetry measurements in Al were performed in the atomic composition range $0 < X_{Fe2Zr} < 0.0005988$. Within one run, after each Fe_2Zr drop (of δn moles) in the bath containing N moles of Al and M moles of Fe and J moles of Zr (N >> M, J), a heat effect Q_{Fe2Zr} was measured, corresponding to the following reaction:

$$\delta n\langle Fe_2Zr\rangle_{s,298} + ((NAl, MFe, JZr))_{l,1173} \rightarrow ((NAl, (M+2\delta n)Fe, (J+\delta n)\,Zr))_{l,1173};\, Q_{Fe_2Zr} \quad (4.3)$$

The measured heat effect, Q_{Fe_2Zr}, is divided by the number of moles (δn) to obtain the partial drop solution enthalpy value, $\Delta_{ds}\overline{H}^{1173\ K}_{Fe_2Zr,298\ K} = Q_{Fe_2Zr}/\delta n$. The values obtained at 1173 K are gathered in **Table 24** and plotted vs. x_{Fe_2Zr} in **Figure 51**.

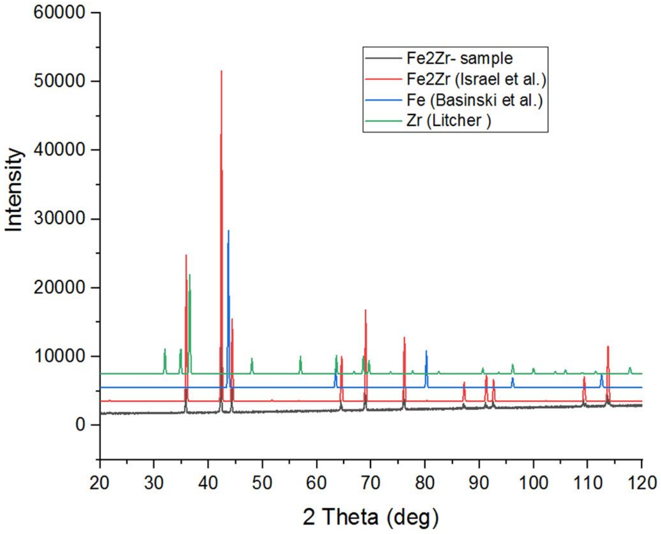

Figure 50. Diffractogram evidencing the formation of single phase Fe_2Zr. Comparison of the obtained XRD spectra (black curve) with spectra of Fe_2Zr by Israel et al. [71] (red), Fe by Basinski et al. [72] (blue) and αZr by Litcher [73] (green). All spectra for were taken with Cu Kα radiation at room temperature.

The measured values for the enthalpies of dissolution as a function of the composition are dispersed, therefore, the partial drop solution enthalpy for Fe_2Zr at infinite dilution ($x_{Fe_2Zr} \rightarrow 0$), $\Delta_{ds}\overline{H}^{\infty,1173\ K}_{Fe_2Zr,298\ K}$, is calculated by taking by taking the average of the $\Delta_{ds}\overline{H}^{1173\ K}_{Fe_2Zr,298\ K}$ values in bold (see **Table 24**). This selection of these particular values is discussed in section 4.5. The expanded uncertainty $U = t_{\nu,p}.\, u$ is calculated using the same procedure discussed in Chapter 2.

The partial drop solution enthalpy of Fe_2Zr at infinite dilution is $\Delta_{ds}\overline{H}^{\infty,1173\ K}_{Fe_2Zr,298\ K}$ = -186.3 ± 4.2 kJ mol^{-1} with a reference state corresponding to the solid state at 298K.

Table 24. Partial drop-solution enthalpy of Fe_2Zr in liquid Al at 1173 K, $\Delta_{ds}\overline{H}^{1173K}_{Fe_2Zr,298K}$, measured by dissolution calorimetry. The references states are solid Fe_2Zr at 298 K and liquid aluminum at 1173 K. M^{int}_{Al} and δm_{Fe2Zr} in mg, δn in mol, M^{int}_{Al} is the sum of the bath mass plus the masses of the 4 Al calibration samples. Bold values are only retained in the calculation of the drop solution enthalpy at infinite dilution.

Run	M^{init}_{Al} / mg	δm_{Fe_2Zr} /mg	δn_{Fe_2Zr} / mol	x_{Fe_2Zr}	$\Delta_{ds}\overline{H}^{1173K}_{Fe_2Zr,298K}$ / kJ.mol^{-1}
1	10655.07	10.41	5.130E-05	6.495E-05	**-187.556**
		15.82	7.796E-05	2.286E-04	-215.147
		9.70	4.780E-05	3.877E-04	-222.122
		9.47	4.667E-05	5.072E-04	-219.354
2	10665.47	14.25	7.023E-05	8.876E-05	-212.531
		12.00	5.914E-05	2.523E-04	**-190.810**
		13.13	6.471E-05	4.088E-04	-213.101
		14.15	6.973E-05	5.787E-04	-236.397
3	10445.29	13.34	6.574E-05	8.490E-05	**-187.999**
		10.71	5.278E-05	2.379E-04	**-184.063**
		12.40	6.111E-05	3.849E-04	**-180.780**
		10.69	5.268E-05	5.318E-04	**-187.947**
4	9981.57	11.72	5.776E-05	7.806E-05	-206.645
		11.88	5.855E-05	2.352E-04	**-176.388**
		13.20	6.505E-05	4.022E-04	-204.069
		16.35	8.058E-05	5.988E-04	-212.460
5	9935.32	14.73	7.259E-05	9.856E-05	-209.203
		13.10	6.456E-05	2.847E-04	**-186.435**
		14.97	7.378E-05	4.724E-04	-232.821
6	10140.96	16.43	8.097E-05	1.077E-04	**-195.379**
		10.26	5.056E-05	2.826E-04	-232.396
		13.35	6.579E-05	4.373E-04	-232.211
		10.57	5.209E-05	5.940E-04	-215.955

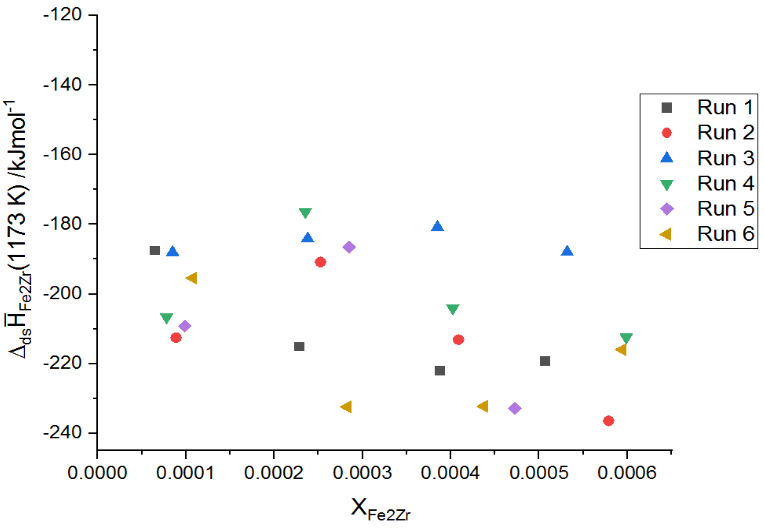

Figure 51. Partial drop solution enthalpy of Fe_2Zr, $\Delta_{ds}\overline{H}^{1173K}_{Fe2Zr,298K}$, in liquid Al between 298 and 1173 K as a function of Fe_2Zr mole fraction.

4.3.2. Enthalpy of formation of Fe_2Zr

The standard formation enthalpy of Fe_2Zr, $\Delta_f H^{\circ}_{Fe_2Zr}$ is computed from the partial drop solution enthalpies at infinite dilutions of Zr, Fe and Fe_2Zr measured by using the dissolution calorimetry technique. The $\Delta_f H^{\circ}_{Fe_2Zr}$ is then given by;

$$\Delta_f H^{\circ}_{Fe_2Zr} = 2\Delta_{ds}\overline{H}^{\infty,1173\ K}_{Fe,298\ K} + \Delta_{ds}\overline{H}^{\infty,1173\ K}_{Zr,298\ K} - \Delta_{ds}\overline{H}^{\infty,1173\ K}_{Fe_2Zr,298\ K} \qquad (4.4)$$

The determination of the partial drop solution enthalpy at infinite dilution of Zr in liquid Al at 1173 K was reported by Gajavalli [6], $\Delta_{ds}\overline{H}^{\infty,1173\ K}_{Zr,298\ K} = -130 \pm 9$ kJ.mol^{-1}.

Different authors have investigated the thermodynamics of the Fe solution in liquid Al at different temperatures. In carrying out a comparison and checking consistency of the results, all enthalpies were converted to a standard liquid reference state (partial mixing enthalpies, $\Delta_{mix}\overline{H}^{\infty}_{Fe,\ T_{exp}}$) at the corresponding experimental temperature T_{exp} and infinite dilution by taking into consideration enthalpy increment and enthalpy of fusion for the different temperatures (see **Table 25**) which can be obtained from SGTE data [63].

The variation of the partial mixing enthalpy of Fe at infinite dilution in liquid Al is plotted as a function of temperature in **Figure 52**. The data indicate a strong temperature dependence, the values becoming less exothermic at high temperature. The results of Antony et al. [15] and Lee et al. [13] are outside the general trend and can be discarded. A regression line through all remaining data gives at the temperature used in this work: $\Delta_{mix}\overline{H}^{\infty}_{Fe,1173\ K} = -123.9$ kJ.mol^{-1}. Then, from this value, considering the heat increment of Fe from room temperature to 1173 K, the drop dissolution enthalpy of Fe in liquid Al at infinite dilution at 1173 K is calculated as $\Delta_{ds}\overline{H}^{\infty,1173K}_{Fe,298K} = -76.6$ kJ.mol^{-1}.

Table 25. Comparison of literature values of the partial solution $\Delta_{sol}\overline{H}_{Fe,\,T_{exp}}^{\infty}$ or drop solution $\Delta_{ds}\overline{H}_{Fe,298.15\,K}^{\infty,T_{exp}}$ enthalpies of Fe at infinite dilution in liquid aluminum measured at different temperatures T_{exp}. Corresponding mixing enthalpies $\Delta_{mix}\overline{H}_{Fe,\,T_{exp}}^{\infty}$ calculated by us are reported in the last column. X_{Fe}^{max} is the maximum Fe mole fraction reached in the binary Fe-Al liquid during the experiments. The solubility limit X_{Fe}^{sat} is calculated using the NUCLEA database developed at IRSN [70].

Reference	Technique	T_{exp} / K	X_{Fe}^{max}	X_{Fe}^{sat}	$\Delta_{\mathrm{ds}}\overline{H}_{Fe,298.15\,K}^{\infty,T_{exp}}$ / $kJ\ mol^{-1}$	$\Delta_{mix}\overline{H}_{Fe,\,T_{exp}}^{\infty}$ / $kJ\ mol^{-1}$**
Matthieu et al. [14]	Drop sol. calo.	971	≤ 0.006	0.0135	-90.7 ± 2.7**	-131.2 ± 2.7
Saadi et al. [8]	Drop sol. calo.	976	<0.008	0.0142	-94.8 ± 1.3*	-135.5 ± 1.2
Labroche et al. [9]	Drop sol. calo.	988	Not specified	0.0157	-93.7 ± 2.0*	-134.8 ± 2.0
Antony et al. [15]	Drop sol. calo.	994	≤ 0.033	0.0165	-76.9 ± 2.5*	-118.1 ± 3.1
Dannöhl and Lukas [16]	Isothermal sol. calo.	1023	≤ 0.021	0.0208	$\Delta_{sol}\overline{H}_{Fe,1023\,K}^{\infty}$ = -109.3 ± 10.3**	-125.5 ± 0.3
Zubkov [17]	Drop sol. calo.	1073	≤ 0.0071	0.0297	$\Delta_{sol}\overline{H}_{Fe,1073\,K}^{\infty}$ = -106.7 ± 1.8*	-123.7 ± 1.9
Breuer et al. [10]	Isothermal sol cal	1073	≤ 0.0082	0.0297	$\Delta_{sol}\overline{H}_{Fe,1073\,K}^{\infty}$ = -112.6 ± 1.3*	-127.9 ± 1.2
Norgren et al. [11]	Drop sol. calo.	1100	Not specified	0.0354	-83.0 ± 1.4*	-127.8 ± 2
Kek et al. [12]	Drop sol. calo.	1123	≤ 0.019	0.0408	-79.4 ± 1.6*	-125.8 ± 2.9
Gasior [18]	Drop sol. calo.	1158 ± 2	Not specified	0.0500	$\Delta_{mix}\overline{H}_{Fe,1158\,K}^{\infty}$ = -123.1 ± 2.3*	-123.1 ± 5.6
Pool et al. [19]	Drop sol. calo.	1173	Not specified	0.0543	$\Delta_{sol}\overline{H}_{Fe,1173\,K}^{\infty}$ = -113.0*§	-127.2
Lee et al. [13]	Drop sol. Calo	1212	≤ 0.013	0.0667	$\Delta_{mix}\overline{H}_{Fe,1212\,K}^{\infty}$ = -110.8 ± 3*	-110.8 ± 3.1
Labroche et al. [9]	Drop sol. calo.	1244	< 0.028	0.0785	-71.1 ± 1.6	-121.8 ± 2.7
Gasior [18]	Drop sol. calo.	1273 ± 2	Not specified	0.0906	$\Delta_{mix}\overline{H}_{Fe,1273\,K}^{\infty}$ = -120.0 ± 0.7*	-120.0 ± 0.7
Gasior [18]	Drop sol. calo.	1383 ± 2	Not specified	0.161	$\Delta_{mix}\overline{H}_{Fe,1383\,K}^{\infty}$ = -115.2 ± 1.4*	-115.2 ± 1.2
Petrushevskiy [20]	Drop sol. calo.	1873	1	1	$\Delta_{mix}\overline{H}_{Fe,1873\,K}^{\infty}$ = -95.2*§	-95.2

* *reported value (and uncertainty),* § *no reported uncertainty,* ** *value and uncertainty calculated by us.*

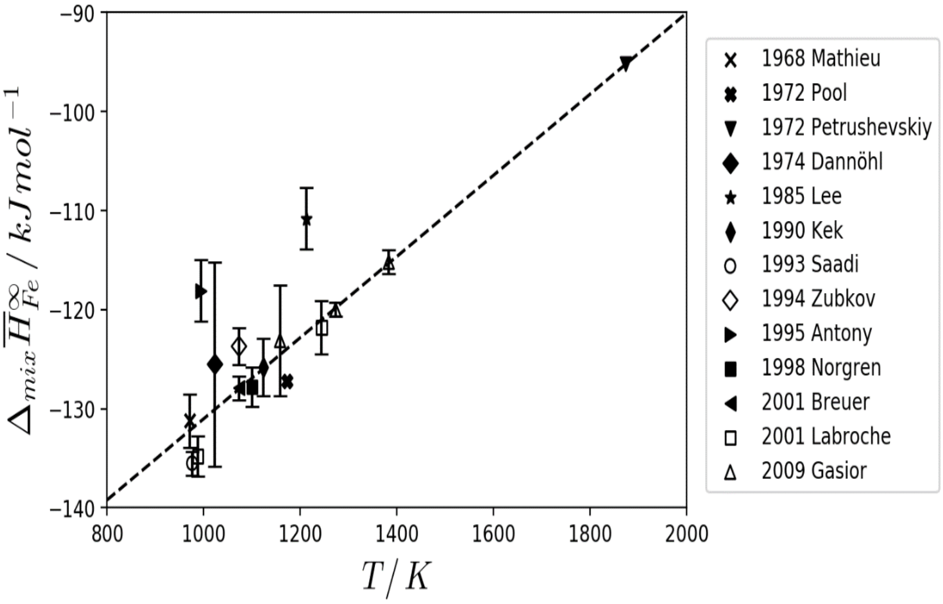

Figure 52. Partial mixing enthalpy of Fe at infinite dilution in liquid Al plotted vs. temperature. Reference state: both elements at the liquid state at the considered temperature. The dashed straight line is a regression line through all the data, after discarding the results of Lee et al.[13] and Antony et al. [15].

Taking into consideration all the values into Equation (4.4), the standard formation enthalpy of Fe_2Zr, at 298K, is determined to be, $\Delta_f H^{\circ}_{Fe_2Zr}$= -32.2 ± 3.3 $kJ.mol^{-1}.at^{-1}$.

4.3.3. Dissolution of AgZr in liquid Al at 1173 K

In order to form and use a single phase AgZr sample for the experiment, reference sample preparation and annealing conditions were chosen in this work. In Figure 22 of Decreton [64], single phase AgZr was formed after annealing the arc melted sample at 900°C for 40 days. Following the same procedure AgZr sample was prepared by arc melting and annealed at 900 °C for 40 days.

The bigger the mass the more the probability of obtaining heterogeneous samples during arc melting sample preparation. Considering difficulties in obtaining homogeneous sample by arc melting, two separate masses of the samples with the same composition were prepared, therefore XRD and dissolution calorimetry were not performed on the same sample.

XRD performed on one of the synthesized AgZr after annealing at 900°C for 40 days, showed the presence of AgZr, Ag and ZrO_2 phases (**Figure 53**). The presence of ZrO_2 phase results from the sensitivity of equiatomic Ag-Zr composition to oxygen. Due to the large difference in the relative intensities between the reference pattern and our pattern, it was impossible to know the exact quantity of the phases using Rietveld analysis. Using DIFFRAC EVA software we were able to get an approximate quantity of the two major phases, thus 84 wt% AgZr and 16 wt% Ag phases. Considering the small intensity of Ag and ZrO_2 (see **Figure**

53), the calculations were done without taking into account the secondary phases. The presence of platinum peaks in the XRD comes from the sample holder.

The AgZr samples were cut into small pieces (masses of 8 to 23 mg) and dropped into an Al bath at 1173 K. Three runs of AgZr dissolution calorimetry measurements in liquid Al were performed in the atomic composition range $0 < X_{AgZr} < 0.0006860$.

After each AgZr drop (of δn moles) in the bath containing N moles of Al and M moles of Ag and J moles of Zr (N >> M, J), the heat effect Q_{AgZr} measured, corresponded to the equation:

$$\delta n\langle AgZr\rangle_{s,298} + ((NAl, MAg, JZr))_{l,1173} \rightarrow ((NAl, (M+\delta n)Ag, (J+\delta n)\,Zr))_{l,1173};\ Q_{AgZr} \quad (4.5)$$

The measured heat effect, Q_{AgZr}, is divided by the number of moles (δn) to obtain the partial drop solution enthalpy value, $\Delta_{ds}\overline{H}^{1173\ K}_{AgZr,298\ K} = Q_{AgZr}/\ \delta n$. The obtained values are gathered in **Table 26** and plotted in **Figure 54**.

The partial drop solution enthalpy of AgZr at infinite dilution is calculated by taking the average of the $\Delta_{ds}\overline{H}^{1173\ K}_{AgZr,298\ K}$ values in Run 3 excluding the underlined value (see **Table 26**) to obtain $\Delta_{ds}\overline{H}^{\infty,1173\ K}_{AgZr,298\ K} = -44.1 \pm 6.9\ kJmol^{-1}$ with reference state corresponding to the solid state at 298 K. The reason for the choice of Run 3 is discussed in section 4.5.

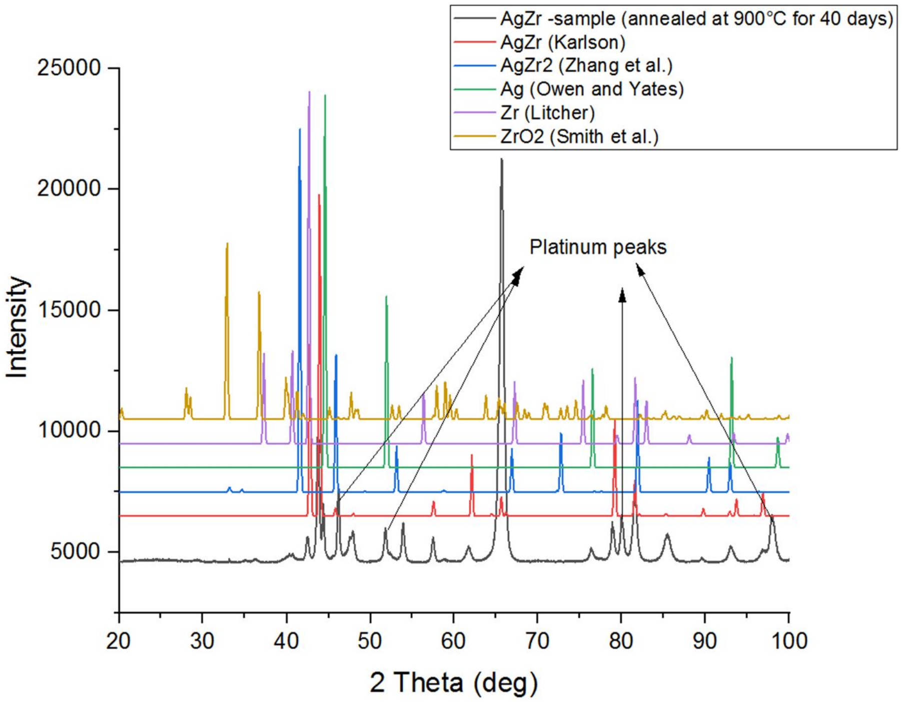

Figure 53. XRD evidencing the phases formed after annealing synthesized AgZr sample. Comparison of the obtained XRD spectra (black curve) with XRD spectra of AgZr by Karlsson [59] (red), $AgZr_2$ by Zhang et al. [58] (blue), Ag by Owen and Yates [74] (green), αZr by Litcher [73] (purple) and ZrO_2 by Smith et al. [75] (gold). All spectra were taken with Co Kα radiation at room temperature.

Table 26. Partial drop-solution enthalpy of AgZr in liquid Al at 1173 K in kJ.mol^{-1}, $\Delta_{ds}\overline{H}^{1173\ K}_{AgZr,298\ K}$, measured by dissolution calorimetry. The references states are solid AgZr at 298 K and liquid aluminum at 1173 K. M^{int}_{Al} and δm_{AgZr} in mg, δn in mol, M^{int}_{Al} is the sum of the bath mass plus the masses of the 4 aluminum calibration samples. x_{AgZr} is the molar fraction of AgZr. The meaning of the police (bold, italics and underlined) chosen for the different values is discussed in Section 4.5.

Run	M^{init}_{Al} / mg	δm_{AgZr} /mg	δn_{AgZr} / mol	x_{AgZr}	$\Delta_{ds}\overline{H}^{1173}_{AgZr,298}$ / kJ.mol^{-1}
1	10570.84	15.15	7.610E-05	9.711E-05	*-60.688*
		22.89	1.150E-04	3.408E-04	**-103.507**
		10.48	5.264E-05	5.546E-04	**-125.421**
		10.06	5.053E-05	6.861E-04	**-118.956**
2	10551.75	14.00	7.032E-05	8.990E-05	*-52.390*
		13.63	6.846E-05	2.673E-04	*-64.386*
		15.33	7.700E-05	4.531E-04	**-94.156**
		20.22	1.016E-04	6.812E-04	**-106.603**
3	10597.80	10.09	5.068E-05	6.451E-05	*-43.484*
		9.66	4.852E-05	1.908E-04	*-47.185*
		8.80	4.420E-05	3.087E-04	*-41.685*
		10.55	5.299E-05	4.324E-04	-14.723

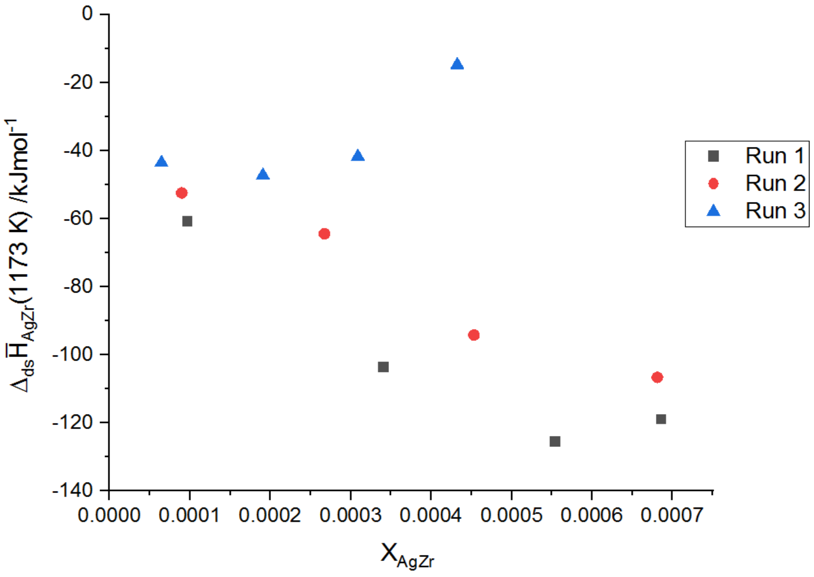

Figure 54. Partial drop solution enthalpy of AgZr, $\Delta_{ds}\overline{H}^{1173\ K}_{AgZr,298\ K}$,in liquid Al between 298 and 1173 K as a function of AgZr mole fraction.

4.3.4. Enthalpy of formation of AgZr

The standard formation enthalpy of AgZr, $\Delta_f H^\circ_{AgZr}$ is computed from the partial drop solution enthalpies at infinite dilutions of Zr, Ag and AgZr measured by using the dissolution calorimetry technique. The $\Delta_f H^\circ_{AgZr}$ is then given by;

$$\Delta_f H^\circ_{AgZr} = \Delta_{ds}\overline{H}^{\infty,1173\ K}_{Ag,298\ K} + \Delta_{ds}\overline{H}^{\infty,1173\ K}_{Zr,298\ K} - \Delta_{ds}\overline{H}^{\infty,1173\ K}_{AgZr,298\ K} \qquad (4.6)$$

The determinations of the partial drop solution enthalpy at infinite dilution of Zr and Ag in liquid Al at 1173 K were reported by [6] and [7] respectively. We only recall thereafter obtained results:

- The partial drop solution enthalpy of Zr in Al at infinite dilution at 1173K was found to be $\Delta_{ds}\overline{H}^{\infty,1173K}_{Zr,298\ K}$ = –130 ± 9 kJ.mol^{-1}.
- The partial drop solution enthalpy of Ag in Al at infinite dilution at 1173 K was found to be $\Delta_{ds}\overline{H}^{\infty,1173K}_{Ag,298\ K}$ = 42.2 ± 0.2 kJ.mol^{-1}.

Taking into account the partial drop solution enthalpy of AgZr at infinite dilution $\Delta_{ds}\overline{H}^{\infty,1173\ K}_{AgZr,298\ K}$ = –44.1 ± 6.9 calculated by taking the average of the Run 3 values (see **Table 26**) then the standard formation enthalpy of AgZr, $\Delta_f H^\circ_{AgZr}$ = –21.8 ± 5.7 kJ.mol^{-1}.at^{-1}.

4.4. Metallographic examinations

In order to check for the successful dissolution of the Fe_2Zr and AgZr samples in liquid Al, micrographic examinations by means of scanning electron microscopy (SEM) were performed on Run 1 (**Figure 55**) and Run 3 (**Figure 56**) of Fe_2Zr ingots and Run 1 (**Figure 57**) and Run 3 (**Figure 58**) of AgZr ingots. The solidified ingots were longitudinally cut, embedded in resin, and polished. The quantitative analysis of elements in individual phases was measured by EDX without standard.

In the upper and middle region of Fe_2Zr ingots (see **Figure 55 a, b** and **Figure 56 a, b**), we can observe:

- The dark phase which is the aluminum matrix.
- The grey interdendritic precipitates having a composition of around 97 at.%Al, indicates the eutectic reaction between FCC_Al solid solution and Al_3Fe [76] also named $Al_{13}Fe_4$ in Zheng et al. [77].

  In the lower region of the Fe_2Zr ingot (see **Figure 55 c** and **Figure 56 c**), we can observe:

- White crystals at the bottom having a needle shape with an Al_3Zr composition. Their elongated shape results from their rapid growth because of the high cooling rate.
- Also, white needlelike interdendritic precipitates are Al_3Zr. Their interdendritic position indicates that the invariant reaction between FCC_Al solid solution and Al_3Zr is probably of eutectic rather than peritectic nature as stated by Janghorban et al. [78].

In both ingots there was similar observation. Large clusters of primary Al_3Zr precipitates which would have indicated unsuccessful dissolution of samples were not seen.

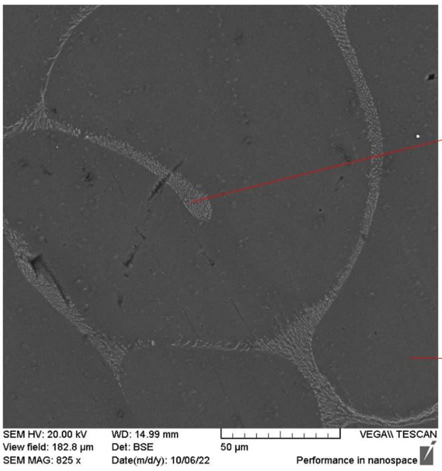

Elements	Mass %	Atomic %
Al	93.8	96.9
Fe	6.2	3.1
Total	**100**	**100**

Elements	Mass %	Atomic %
Al	**100**	**100**

(a)

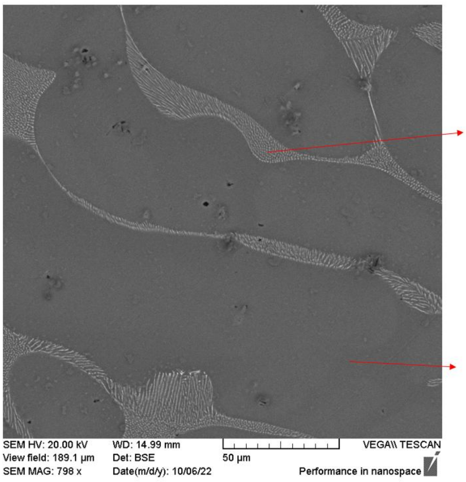

Elements	Mass %	Atomic %
Al	93.5	96.7
Fe	6.5	3.3
Total	**100**	**100**

Elements	Mass %	Atomic %
Al	**100**	**100**

(b)

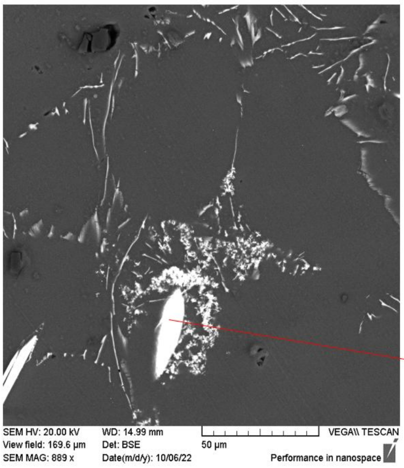

Elements	Mass %	Atomic %
Al	48.1	75.8
Zr	51.9	24.2
Total	**100**	**100**

(c)

Figure 55. SEM observation of (a) upper (b) middle and (c) bottom of Run 1 of Fe_2Zr ingot.

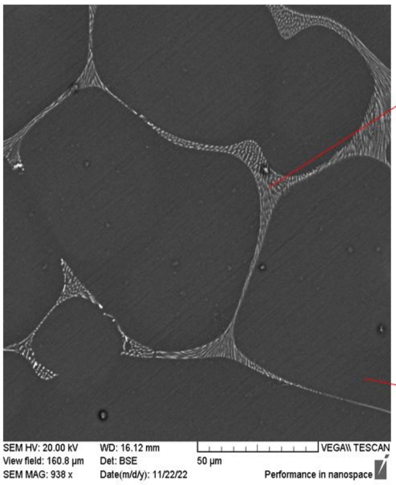

Elements	Mass %	Atomic %
Al	93.9	97.0
Fe	6.1	3.0
Total	100	100

Elements	Mass %	Atomic %
Al	100	100

(a)

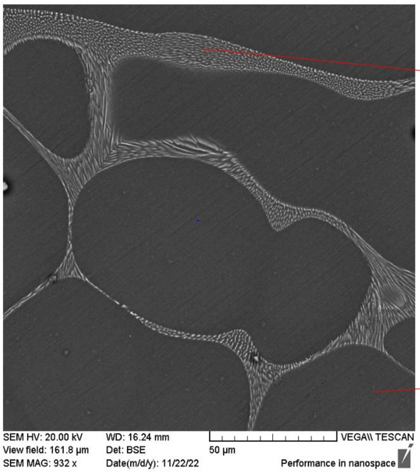

Elements	Mass %	Atomic %
Al	94.3	97.1
Fe	5.7	2.9
Total	100	100

Elements	Mass %	Atomic %
Al	100	100

(b)

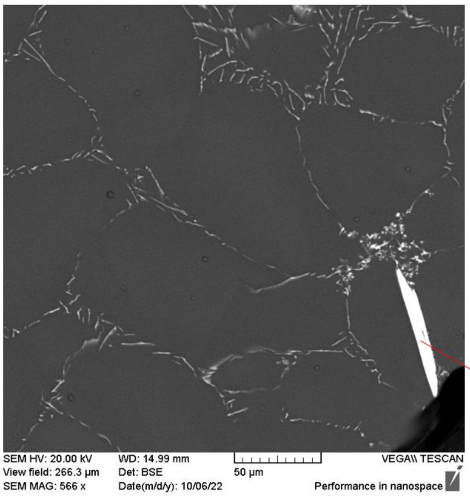

Elements	Mass %	Atomic %
Al	44.8	73.2
Zr	55.2	26.8
Total	100	100

(c)

Figure 56. SEM observation of (a) upper (b) middle and (c) bottom of Run 3 of Fe_2Zr ingot.

In the AgZr ingots (Run 1 and Run 3) we observe:

- White interdendritic precipitates and white crystals having a needle shape (see **Figure 57 b** and **Figure 58 c**), which are Al_3Zr $D0_{23}$ crystals as shown by Khvan et al. [79].
- Clusters of Al_3Zr of typical size comparable to the dropped fragments were only detected at the bottom of the Run 1 ingot (see **Figure 57 a** and **c**).
- Dark particles consisting of Al, Ag and O.

Most of the primary Al_3Zr particles would settle down to the bottom of the ingot due to the larger density of Al_3Zr compared to liquid aluminum. The clusters of Al_3Zr precipitates seen at the bottom of the ingot (see **Figure 57 a** and **c**) are likely to have precipitated at the calorimeter temperature and not dissolving afterwards.

The Al_3Zr precipitates appear brighter than the Al matrix because Zr has higher atomic number than Al.

4.1. Discussion

The available experimental values of the formation enthalpies of Fe_2Zr and AgZr are widely used in literature as input data in the Calphad assessments of the Fe-Zr and Ag-Zr binary systems and as a benchmark for DFT calculations. In this work the enthalpies of formation of Fe_2Zr and AgZr were determined using drop solution calorimetry at high temperature.

In drop solution calorimetry the enthalpy of formation is calculated by considering the partial drop solution enthalpies of the elements (Ag, Fe, Zr) and the compounds (Fe_2Zr and AgZr). In each case the complete dissolutions of the elements and the compound are required in order to obtain an accurate result.

During the drop/solution experiments of Fe_2Zr and AgZr samples, the observed calorimetric peaks (see Appendix A) are composed of an initial endothermic contribution, associated with the heating/melting of the sample, followed by a strong exothermic contribution which corresponds to its dissolution in liquid aluminum accompanied by the formation of Al_3Zr. These first two observed contributions are quite frequently, but not systematically, followed by a 3^{rd} endothermic effect. When it occurs, this third effect is interpreted as the dissolution of Al_3Zr, a reaction whose endothermic character was highlighted in a previous study performed in our laboratory [6]. The lack of systematic observation of the dissolution of Al_3Zr is probably linked to a local saturation in Zr of the aluminum bath in the vicinity of the dissolving samples. This saturation is all the more probable as the number of samples already dissolved in the bath is high. Thus, it is often the first falls that show a marked final endothermic contribution, this contribution tending to fade with the successive drops. This problem is compounded by the fact that the high density of the compounds compared to that of the liquid aluminum leads to an accumulation of samples towards the bottom of the crucible.

It was sometimes difficult to be sure if there was successful complete dissolution of the sample in liquid Al by just checking the shape of the peak after each drop. Complementary and useful information about dissolution of the samples (Fe_2Zr and AgZr) in liquid Al is gained through post-mortem metallographic examination by means of scanning electron microscopy (SEM).

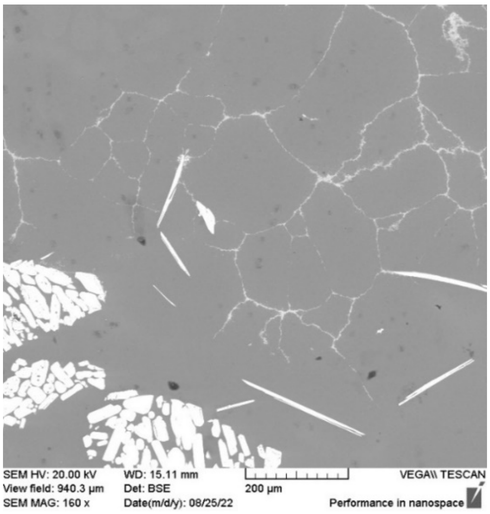

(a)

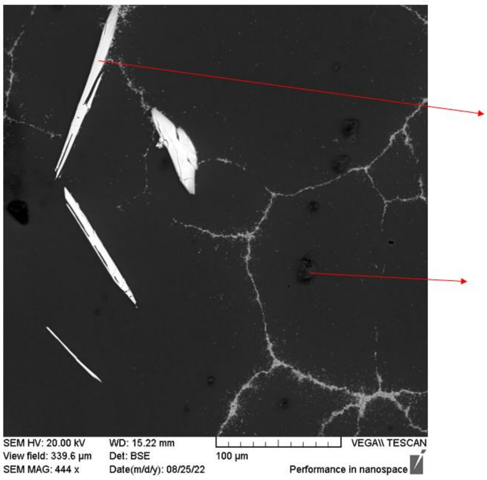

Elements	Mass %	Atomic %
Al	44.2	72.8
Zr	55.8	27.2
Total	100	100

Elements	Mass %	Atomic %
Al	47.3	41.8
Ag	16.2	3.7
O	36.5	54.5

(b)

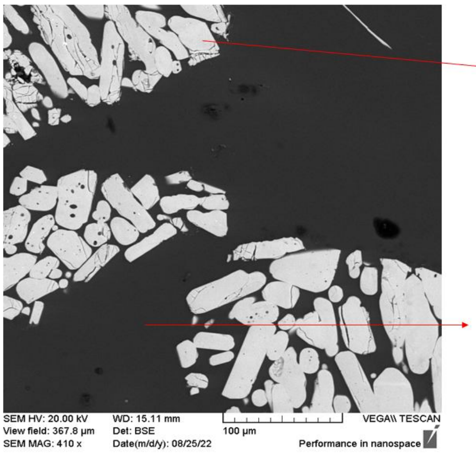

Elements	Mass %	Atomic %
Al	43.9	72.5
Zr	56.1	27.5
Total	100	100

Elements	Mass %	Atomic %
Al	100	100

(c)

Figure 57. SEM observation of ingot for Run 1 of AgZr (a) the region near the bottom of the ingot at low magnification showing both (b) needlelike shape Al_3Zr particles and interdendritic Al_3Zr and (c) clusters of Al_3Zr primary precipitates in pure Al matrix.

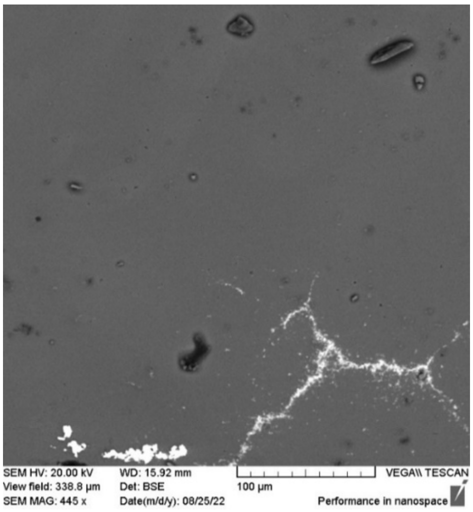

(a)

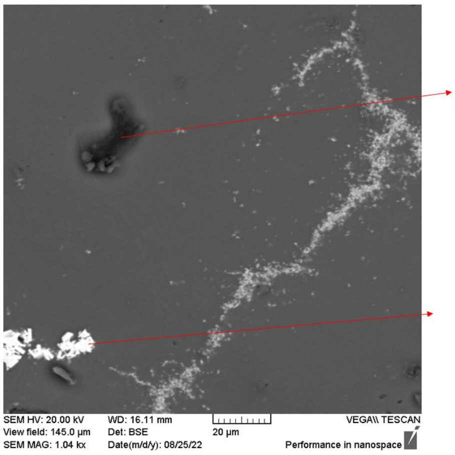

Elements	Mass %	Atomic %
Al	55.6	36.9
Ag	2.3	0.5
O	42.1	62.6

Elements	Mass %	Atomic %
Al	44.5	73.0
Zr	55.5	27.0
Total	100	100

(b)

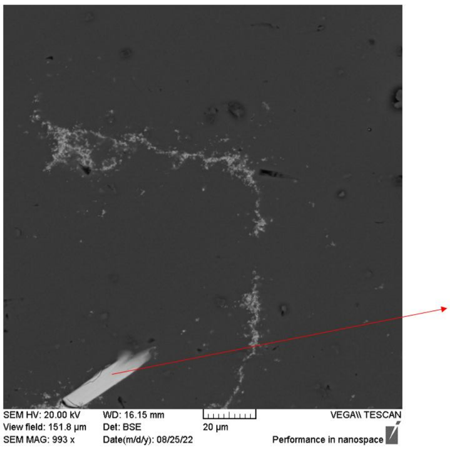

Elements	Mass %	Atomic %
Al	46.5	74.6
Zr	53.5	25.4
Total	100	100

(c)

Figure 58. SEM observation of (a) the AgZr ingot (for Run 3) showing the (b) interdendritic Al_3Zr particles and (c) needlelike shape Al_3Zr in the lower region. Large clusters of Al_3Zr were not found.

In the metallographic examination of the Fe_2Zr ingots for Run 1 and Run 3, large clusters of primary Al_3Zr precipitates were not found indicating that a significant fraction of the samples are likely to be completely dissolved but considering the scattering of the calorimetric values and different peak shapes (see Appendix A) maybe not all samples.

From the micrographs (see **Figure 55** and **Figure 56**) it is shown that when Fe_2Zr sample is dropped in the calorimeter, it dissociates, with Fe and Zr dissolving successfully in liquid Al. We observe eutectic reaction between FCC_Al solid solution and Al_3Zr [76] (see **Figure 55 a**, **b** and **Figure 56 a**, **b**) and a needlelike shape with a composition related to Al_3Zr (see **Figure 55 c** and **Figure 56 c**). Even though Zr successful dissolved in liquid Al but on cooling they formed Al_3Zr.

In conclusion we selected the less exothermic values and obtained the enthalpy of formation of the Fe_2Zr, as $\Delta_f H^{\circ}_{Fe_2Zr}$= -32.2 ± 3.3 $kJ.mol^{-1}.at^{-1}$. These values were selected because, even though there is similar microstructure on both ingots (see **Figure 55** and **Figure 56**) but looking at Appendix A, the thermograph with all peak phenomena explained above are less exothermic than the ones without the last endothermic peak. The measured value is in agreement with values obtained by other experimental techniques (see **Table 18**) and by DFT calculation (see **Table 19**).

For AgZr, the investigation of successful dissolution was thoroughly checked by comparing the thermographs (Appendix A) and micrographs (**Figure 58**) considering the extreme large scattering of the values (see **Table 26**). The behavior of the thermographs in Appendix A has been explained earlier. For the thermograph of Run 1 (see Appendix A), we can see the presence of the last endothermic peak which corresponds to the complete dissolution of AgZr in the first peak and slightly in the second peak but cannot be seen in the third and fourth. For the thermograph of Run 3, we observe all the three phenomena in all the peaks, thus endothermic peak first followed by exothermic peak and lastly endothermic peak.

Comparing the behavior of the signals to the values in **Table 26**, the peaks that shows all the three phenomena are less exothermic than the peaks that do not show the last endothermic peak.

We used the following 3 arguments to select the accurate values:

- Shape of the thermogram (see Appendix A).
- We observe that the values become more exothermic on successive additions, so progressive saturation of the bath (see **Table 26**).
- We have proved that in some cases the dissolution is not finished as seen in the ingot of Run 1 (see **Figure 57**), but no evidence of incomplete dissolution for ingot of Run 3 as no large clusters of Al_3Zr particles were seen (see **Figure 58**).

In the calculation for partial drop solution enthalpy of AgZr at infinite dilution two assumptions can be considered based on the thermal effect detected after each drop (see Annex A).

- Complete dissolution of AgZr in liquid Al (see **Table 26** values in italics).
- Dissolution of AgZr in liquid Al followed by the re-precipitation of the excess quantity of Zr in the form of Al_3Zr aluminide (see **Table 26** values in bold).

For the first assumption, the partial drop solution enthalpy of AgZr at infinite dilution calculated by taking the average of the $\Delta_{ds}\overline{H}^{1173\ K}_{AgZr,298\ K}$ values (see **Table 26** values in italics) is $\Delta_{ds}\overline{H}^{\infty,1173\ K}_{AgZr,298\ K}$ = -51.6 ± 9.7 kJ.mol^{-1} with reference state corresponding to the solid state at 298 K.

For the second assumption, the partial drop solution enthalpy of AgZr at infinite dilution calculated by taking the average of the $\Delta_{ds}\overline{H}^{1173\ K}_{AgZr,298\ K}$ values (see **Table 26** values in bold) is $\Delta_{ds}\overline{H}^{\infty,1173\ K}_{AgZr,298\ K}$ = -109.7 ± 15.5 kJ.mol^{-1} with reference state corresponding to the solid state at 298 K.

Considering all the values into Equation (4.6), the standard formation enthalpy of AgZr at 298K, is determined to be, $\Delta_f H^{\circ}_{AgZr}$= -18.1 ± 6.6 kJ.mol^{-1}.at^{-1} for the first assumption and $\Delta_f H^{\circ}_{AgZr}$= 10.9 ± 8.9 kJ.mol^{-1}.at^{-1} for second assumption.

The enthalpy of formation for the second assumption is strongly positive $\Delta_f H^{\circ}_{AgZr}$= 10.9 ± 8.9 kJ.mol^{-1}.at^{-1} which would indicate the instability of this phase at 298.15 K, in remarkable contradiction to the state of knowledge on the Ag-Zr system.

However, considering the metallographic examination on the AgZr ingot (see **Figure 57**), it can be assumed that the dissolution of AgZr in liquid Al is accompanied by the re-precipitation of the excess quantity of Zr in the form of Al_3Zr aluminide. Therefore, calculations are done to check the suspicion. Taking into account this assumption, the chemical process can be written as;

$$\langle AgZr\rangle_{s,298\ K} + n(Al)_{1173\ K} \rightarrow \big((Ag,(n-3)Al)\big)_{1173\ K} + \big((Al_3Zr)\big)_{1173\ K} \qquad (4.7)$$

The enthalpy of reaction (4.7), $\Delta H_{4.7}$, can be estimated by the following Hess cycle:

$$\Delta H_{4.7} = -\Delta_f H^{\circ}_{AgZr,298K} + \Delta_f H^{\circ}_{Al_3Zr,298K} + \Delta H^{1173K}_{Al_3Zr,298K} + \Delta_{ds}\overline{H}^{\infty,1173K}_{Ag,298K} - 3\Delta H^{1173K}_{Al,298K} \qquad (4.8)$$

Decreton et al. [64] estimated the standard enthalpy of formation of the AgZr compound, using acid dissolution calorimetry:

$$\Delta_f H^{\circ}_{AgZr,298.15\ K} = -44.6 \pm 20\ kJ.mol^{-1}.$$

Meschel and Kleppa [80] measured by high-temperature direct synthesis calorimetry the enthalpy of formation of Al_3Zr as:

$$\Delta_f H^{\circ}_{Al_3Zr,298.15\ K} = -193.6 \pm 5.2\ kJ.mol^{-1}.$$

The heat increment of the aluminide from room temperature to calorimeter temperature (1173 K) was calculated using classical thermodynamic relations. The value can be calculated from the Gibbs energy function of Al_3Zr assessed by Fischer and Colinet [81]:

$$\Delta H^{1173\ K}_{Al_3Zr,298.15\ K} = 91.2\ kJ.mol^{-1}.$$

The heat increment of pure aluminum from the room temperature to the calorimeter temperature was calculated using the SGTE data for pure elements [63]:

$$\Delta H^{1173\ K}_{Al,298.15\ K} = 36.4\ kJ.mol^{-1}.$$

The partial drop solution enthalpy of Ag in liquid Al at infinite dilution at 1173 K was reported by Gajavalli [7] to be:

$$\Delta_{ds}\overline{H}^{\infty,1173K}_{Ag,298K} = 42.2 \pm 0.2\ kJ.mol^{-1}.$$

Considering all the values into equation 4.8, the enthalpy of reaction $\Delta H_{4.7}$, is determined to be, $\Delta H_{4.7}$= -124.8 ± 20.7 kJ.mol^{-1}.

The above calculated value is not very far from the partial drop solution enthalpy of AgZr in liquid Al at infinite dilution at 1173 K measured in this work considering the second assumption of incomplete dissolution which is $\Delta_{\mathrm{ds}}\overline{\mathrm{H}}^{\infty,1173\mathrm{K}}_{\mathrm{AgZr},298\mathrm{K}}$ = -109.7 ± 15.5 kJ.mol^{-1}.

In this case for Run 1 it can be assumed that for the first drop there was complete dissolution of AgZr in liquid Al, but for the subsequent drops there is dissolution accompanied by the re-precipitation of the excess quantity of Zr in the form of Al_3Zr aluminide hence, these large clusters of Al_3Zr found at the lower region of the ingots in the micrographs.

But for the micrograph of Run 3 (see **Figure 58**), we do not observe large clusters of Al_3Zr at the lower region of the ingot which means there is complete dissolution and it is consistent with the behavior of the thermograph (see Appendix A). Taking into account the metallographic result, it was more suitable to use the values obtained for Run 3 for calculating the formation enthalpy of AgZr. The last value of Run 3 (underlined value in **Table 26**) was discarded. This is due to the fact that the charge corresponding to the 4th drop was made from the grouping of the only 3 small pieces of AgZr remaining, that is a total mass of 10.55 mg. Looking at the value obtained (see **Table 26**) it can be concluded that the small fragments floated on the bath but did not dissolve. By taking the mean value for the rest of the values for Run 3 (see **Table 26**), the partial drop solution enthalpy at infinite dilution of AgZr in liquid Al was $\Delta_{\mathrm{ds}}\overline{\mathrm{H}}^{\infty,1173\ \mathrm{K}}_{\mathrm{AgZr},298\ \mathrm{K}}$ = 44.1 ± 6.9 kJmol^{-1}, then, the standard formation enthalpy of AgZr at 298K, is determined to be, $\Delta_f H^{\circ}_{AgZr}$= -21.8 ± 5.7 kJ.mol^{-1}.at^{-1}.

As already seen in the bibliography section, there is limited experimental work available in the literature for the thermodynamic properties of the solid and liquid phases of Ag-Zr system. The results obtained by He et al. [66] seems to deviate from the experimental data of Fitzner and Kleppa [68] while the optimized results by Hsiao et al. [65] are within the error bar of the experimental dataset [68] and the DFT calculations are more exothermic (see **Table 22** and **Table 23**). The enthalpy of formation for AgZr obtained in this work -21.8 ± 5.7 kJ.mol^{-1}.at^{-1}, is consistent with the result obtained by Decreton et al. [64] and DFT calculations [70] within the error bar, but more exothermic than the experimental data by Fitzner and Kleppa [68] and the optimized enthalpy of formation of the AgZr phase, −5.5 kJ.mol^{-1}at^{-1} reported by Hsiao et al. [65].

4.2. Conclusion

The Fe_2Zr and AgZr compounds are key phases for the accurate description of the Fe-Zr and Ag-Zr systems.

However, a single experimental determination of the enthalpy of formation of the AgZr stoichiometric composition is published and the value was measured by high-temperature direct synthesis calorimetry. Most of the Calphad and DFT models of this phase rely on this value to support their validation. In this chapter, we have re-determined the enthalpy of formation of AgZr by dissolution calorimetry and obtained a good agreement with the acid solution calorimetry result of Decreton [64]. Our value (-21.8 ± 5.7 $kJ.mol^{-1}.at^{-1}$) is more exothermic than the value obtained by direct reaction [68]. Within the experimental error limit, the results obtained is consistent with the recent Calphad model of the Ag-Zr system performed by Fischer in the NUCLEA database [70] integrating the phase diagram relations determined in the Decreton's work [64], -17.6 $kJ.mol^{-1}.at^{-1}$.

The experimental standard enthalpy of formation of Fe_2Zr has also been determined by dissolution calorimetry and it is in agreement with literature values. The thermodynamic evaluation of the Fe-Zr system existing in the NUCLEA database was done in 1998 and revised in 2003. Since 2003, no new experimental thermodynamic properties are available except Calphad and ab-initio calculations (see **Table 19**). In the very recent Calphad modelling done by Fischer in NUCLEA [70], the value obtained, -27.5 $kJ.mol^{-1}.at^{-1}$ is consistent with our results in this study (-32.2 ± 3.3 $kJ.mol^{-1}.at^{-1}$).

4.3. Appendix

Thermograph for AgZr dissolution in liquid Al (Run 1)

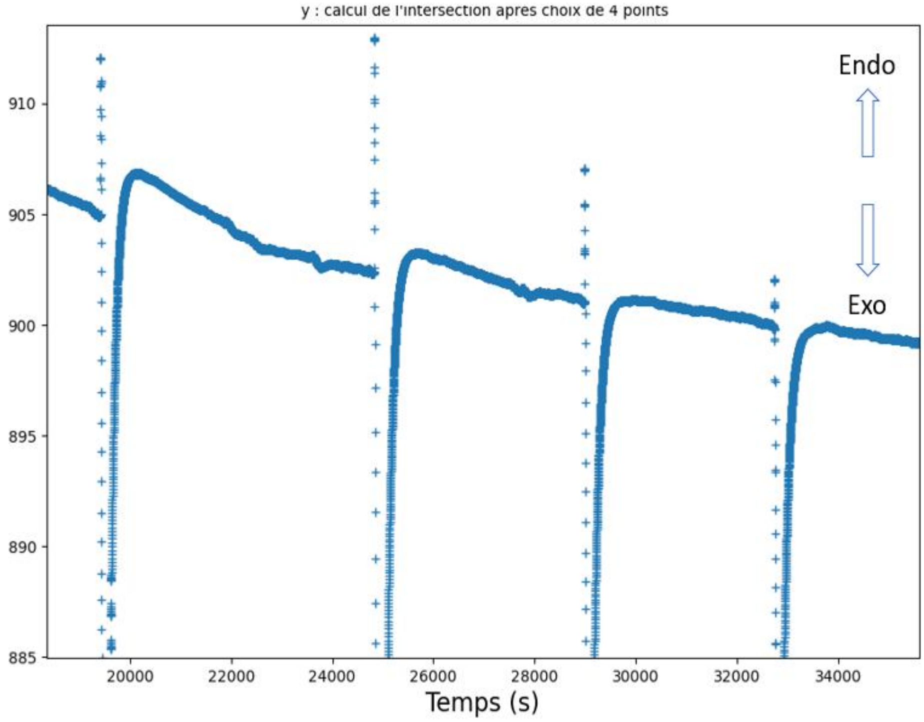

Thermograph for AgZr dissolution in liquid Al (Run 3)

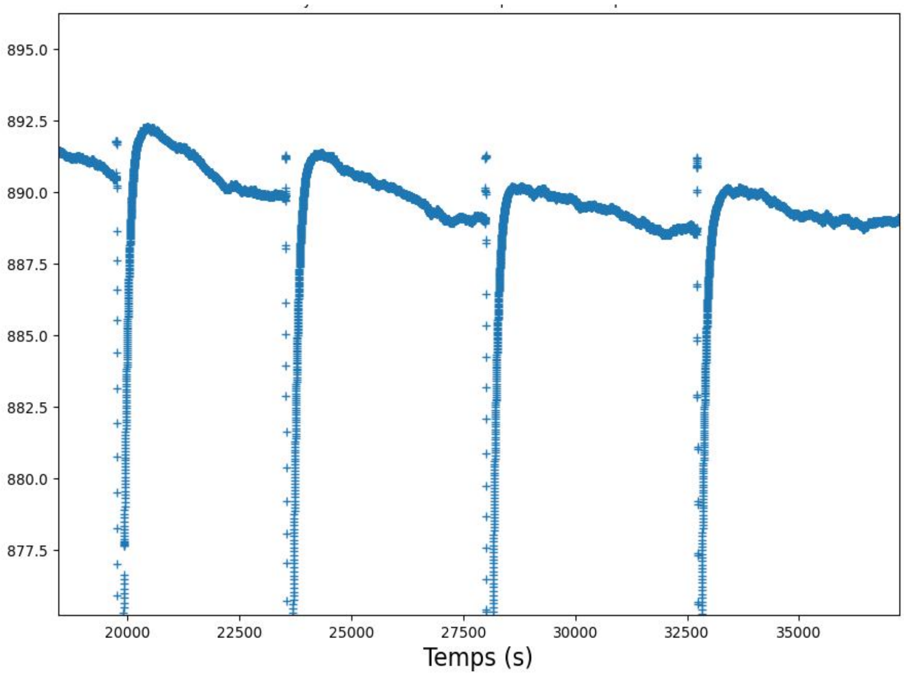

Thermograph for Fe_2Zr dissolution in liquid Al (Run 1)

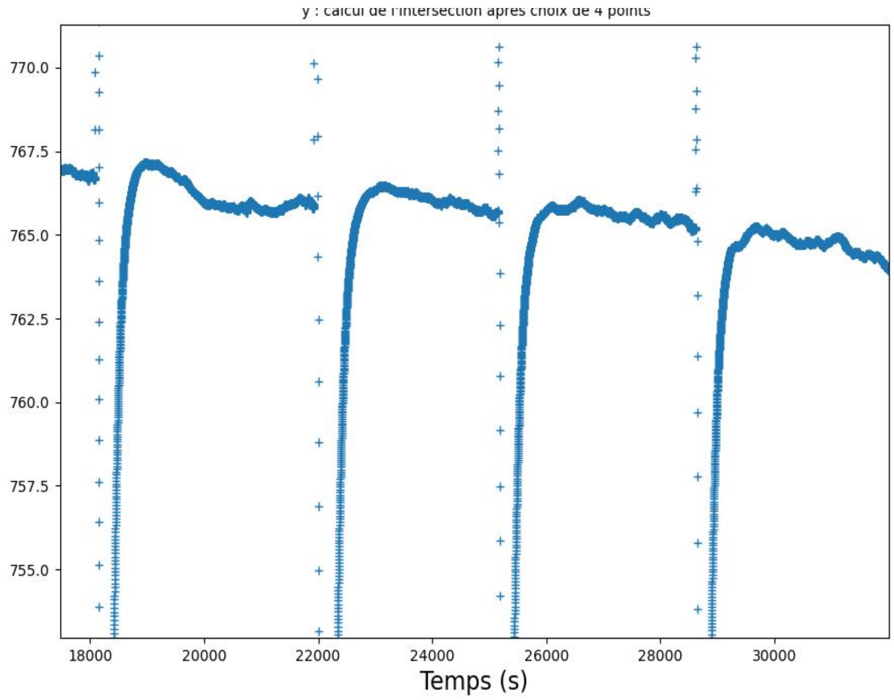

Thermograph for Fe_2Zr dissolution in liquid Al (Run 3)

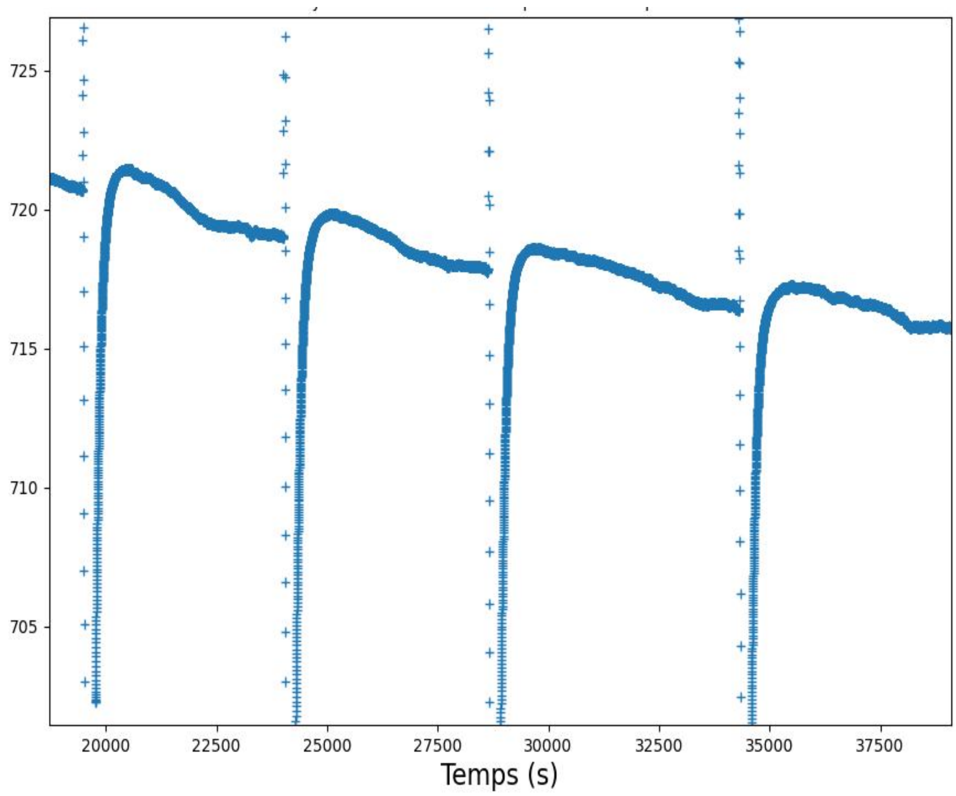

4.4. References

1. Swartzendruber L. J., The Ag-Fe (Silver-Iron) System. Bull. Alloy Phase Diag. 5: 560–564 (1984).
2. Venkatraman M., Neumann, J.P., The Ag-Cr (Silver-Chromium) System. Bull. Alloy Phase Diag. 11: 263–265 (1990).
3. Singleton M., Nash P., The Ag-Ni (Silver-Nickel) System. Bull. Alloy Phase Diag. 8:119–121 (1987).
4. Okamoto H., The Fe-ln (Iron-Indium) System. Bull. Alloy Phase Diag. 11: 143–146 (1990).
5. Dasarathy C., Immiscible Behaviour in the Chromium-Indium System. Naturwissenschaften. 4: 179 (1968).
6. Gajavalli K., Barrachin M., Benigni P., Rogez J., Mikaelian G., Fischer E., Determination Of Solution Enthalpy of Zirconium in Liquid Aluminum. J. Chem. Thermodyn. 135: 198–204 (2019).
7. Gajavalli K., Experimental Contribution to Thermodynamics of the Ag-Cd-In, In-Zr and In2O3-ZrO2 Systems, PhD Thesis, Aix Marseille University (2019).
8. Saadi N., Harmelin M., Legendre B., Determination of the Formation Enthalpy of Crystalline and Quasicrystalline Phases of the Al-Cu-Fe System by Solution Calorimetry. J. Chem. Phys. 90: 355-366, (1993).
9. Labroche D., Dugne O., Rogez J., New Thermodynamic Measurements in the U-Fe system, in: INIS/AIEA (Ed.), 9th Int. Conf. Nucl. Eng. Nice, Acrop. (France); Nice (France), 8-12 Apr 2001.
10. Breuer J., Grün A., Sommer F., Mittemeijer E.J., Enthalpy of Formation of B2-Fe_{1-x} Al_x and B2-$(Ni,Fe)_{1-x}$ Al_x. Metallurgical and Materials Transactions B. 32B: 913–918 (2001).
11. Norgren S., Hodaj F., Azay P., Colinet C., Experimental Investigation on the Enthalpy of Formation of DyFe2, DyFe3, Dy2Fe17, ErFe2 and ErFe3 Intermetallic Compounds. Metallurgical and Materials Transactions A. 29A: 1367 (1998).
12. Kek S., Rzyman C., Sommer F., Determination of the Enthalpy of Formation of Ternary Ni3Al-based Alloys. Anal. Fisica B. 86: 31-38 (1990).
13. Lee J. J., Sommer F., Determination of the partial enthalpies of mixing of Aluminum rich alloy melts by solution calorimetry. Z. Metallkd. 76: 750-754 (1985).
14. Mathieu J.C., Jounel B., Desre P., Mesure de la Chaleur de Formation de Compose FeSi par Calorimetrie de Dissolution dans l'Aluminium, C. R. Acad. Sc. Paris. 266 : 773-776 (1968).
15. Antony M.P., Babu R., Mathews C.K., Varada Raju U.V., Enthalpies of Formation of UNi5, UNi2 and UFe2 by Solution Calorimetry. J. Nucl. Mater. 223: 213, (1995).
16. Dannöhl H.D., Lukas H.L., Calorimetric Determination of the Enthalpies of Formation of Some Intermetallic Compounds. Z. Metallkd. 65(10): 642-649 (1974).
17. Zubkov A.A., Dissolution Enthalpies of 3d transition metals in Liquid Aluminium. J. Chem. Thermodyn. 26: 1267-1274 (1994).

18. Gasior W., Moser Z., Debski A., Heat of Formation of FeNi70, FeNi73.5 and FeNi80 Ordered Alloys from the Homogenous Region of the FeNi3 Phase. J. Alloys and Compd. 487: 132–137 (2009).
19. Pool H.J., Starr J., Griffith W.W., Heats of Formation of Nickel-Aluminum and Nickel-Iron Alloys, Thermodynamik der Legierungen. 36-37 (1972).
20. Petrushevskiy M.S., Esin Y.O., Gel'd P.V., V.M. Sandakov, Concentration Dependence of the Enthalpy of Formation of Liquid Iron-Aluminium Alloys. Russ. Metall. 6: 149-53 (1972).
21. Svechnikov V.N., Pan V.M., Spektor A.T., Intermediate phases in the iron-zirconium system. Zh. Neorg. Khim. 8: 2118–2123 (1963).
22. Svechnikov V.N., Spektor A.T., The Fe-Zr phase diagram. Dokl. Akad. Nauk SSSR. 143: 613–615 (1962).
23. Arias D., Abriata J.P., The Fe−Zr (Iron-Zirconium) System. Bull. Alloy Phase Diag. 9: 597–604 (1988).
24. Hayes E.T., Roberson A.H., Obrien W.L., Constitution and Mechanical Properties of Zirconium-Iron Alloys. Trans. Am. Soc. Met. 43: 888–905 (1951).
25. Tanner L.E., Levinson D.W., Observations on the System Zirconium-Iron. Trans. Am. Inst. Min., Metall. Pet. Eng. 215: 1066–1067 (1959).
26. Malakhova T.O., Alekseyeva Z.M., The Zr-Fe Phase Diagram in the Range 20–40 at.% Fe and the Crystalline Structure of the Intermetallic Compound Zr3Fe. J. Less Common Met. 81: 293–300 (1981).
27. Malakhova T.O., Kobylkin A.N., The Zr-Fe Phase-Diagram (0-66.6 at.% Fe). Izv. Akad. Nauk. SSSR, Met. 2: 205–209 (1982).
28. Aubertin F., Gonser U., Campbell S.J., Wagner H.-G., An Appraisal of the Phases of the Zirconium-Iron System. Z. Metallkd. 76: 237–244 (1985).
29. Stupel M.M., Bamberger M., Weiss B.Z., Determination of Fe solubility in αZr by Mössbauer Spectroscopy. Scripta Metall. 19: 739–740 (1985).
30. Guo C., Du Z., Li C., Zhang B., Tao M., Thermodynamic Description of the Al–Fe–Zr System. Calphad. 32: 637–649 (2008).
31. Pelton A.D., Leibowitz L., Blomquist R.A., Thermodynamic Analysis of Phase Equilibria in the Iron—Zirconium System. J. Nucl. Mater. 201: 218–224 (1993).
32. Servant C., Gueneau C., Ansara I., Experimental and Thermodynamic Assessment of the Fe2Zr Syste. J. Alloys and Compd. 220: 19–26 (1995).
33. Jiang M., Oikawa K., Ikeshoji T., Wulff L., Ishida K., Thermodynamic Calculations of Fe-Zr and Fe-Zr-C Systems. J. Phase Equilibria. 22: 406–417 (2001).
34. Stein F., Sauthoff G., Palm M., Experimental Determination of Intermetallic Phases, Phase Equilibria, and Invariant Reaction Temperatures in the Fe-Zr System. J. Phase Equilibria. 23: 480–494 (2002).
35. Du Zt., Zou L., Guo Cp., et al., Phase Stability of $Fe_{23}Zr_6$ and Thermodynamic Reassessment of Fe–Zr system. J. Iron and Steel Res. Intern. 28: 1375–1389 (2021).
36. Malakhova T.O., Investigation of the Phase Diagram of Zirconium Part of the Zr-Fe, Zr-Cr-Fe and Zr-Cr-Cu Systems, in: O.S. Ivanov, Z.M. Alekseeva (Eds.). Alloys for Atomic Energy, Nauka, Moscow. 123–130 (1979).

37. Yang Y., Tan L., Bei H., Busby J.T., Thermodynamic Modeling and Experimental Study of the Fe–Cr–Zr System. J. Nucl. Mater. 441: 190–202 (2013).
38. Rigaud V., Sundman B., Daloz D., Lesoult G., Thermodynamic Assessment of the Fe–Al–Zr Phase Diagram. Calphad. 33: 442–449 (2009).
39. Lafaye P., Toffolon-Masclet C., Crivello J-C., Joubert J-M., Thermodynamic Modelling of the Fe-Sn-Zr System Based on New Experiments and First- Principles Calculations. J. Alloys and Compd, Elsevier. 821: 153200 (2020).
40. Saenko I., Kupravaa A., Udovskyb A., Fabrichnaya O., Heat Capacity Measurement of Zr_2Fe and Thermodynamic Re-Assessment of the Fe–Zr System. Calphad. 66: 101625 (2019).
41. Massalski T.B., Binary Alloy Phase Diagrams. Metals Park, Ohio, (1991).
42. Gachon J.C., Hertz J., Enthalpies of Formation of Binary Phases in the Systems FeTi, FeZr, CoTi, CoZr, NiTi, and NiZr, by Direct Reaction Calorimetry. Calphad. 7:1–12 (1983).
43. Rosner-Kuhn M., Qin J.P., Schaefers K., Thiedemann U., Frohberg M.G., Temperature-Dependence of the Mixing Enthalpy and Excess Heat-Capacity in the Liquid-System Iron-Zirconium. Z. Metallkd. 86: 682–685 (1995).
44. Schneider A., Klotz H., Stendel J., G. Strauß, Zur thermochemie von Legierungen, Pure Appl. Chem. 2: 13–16 (1961).
45. Sidorov O.Y., Esin Y., Geld P.V., Enthalpies of Formation of Zirconium Alloys with Iron, Cobalt, Nickel, and Copper. *Rasplavy*. (3): 28-33 (1989).
46. Ali K., Arya A., Ghosh P.S., Dey G.K., A First Principles Study of Cohesive, Elastic and Electronic Properties of Binary Fe–Zr Intermetallics. Comput. Mater. Sci. 112: 52–66 (2016).
47. Mukhamedov B.O., Saenko I., Ponomareva A., Kriegel M.J., Chugreev A., Udovsky A., Fabrichnaya O., Abrikosov I., Thermodynamic and Physical Properties of Zr3Fe and ZrFe2 Intermetallic Compounds. Intermetallics. 109: 189–196 (2019).
48. Tao X., Zhu J., Guo H., Ouyang Y., Du Y., Phase Stability, Thermodynamic and Mechanical Properties of AlZr2, FeZr2 and Al2FeZr6 from First-Principles Calculations. J. Nucl. Mater. 440: 6–10 (2013).
49. Ohodnicki P.R., Cates N.C., Laughlin D.E., McHenry M.E., Widom M., Ab Initio Theoretical Study of Magnetization and Phase Stability of the (Fe,Co,Ni)23B6 and (Fe,Co,Ni)23Zr6 Structures of Cr23C6 and Mn23Th6 Prototypes. J. Alloys and Compd. 78: 207 (2008).
50. Mihalkovič M., Widom M., Ab Initio Calculations of Cohesive Energies of Fe Based Glass Forming Alloys. Phys. Rev. B. 70: 177 (2004).
51. Materials Project, https://materialsproject.org (accessed 12 March 2019).
52. Jain A., Ong S.P., Hautier G., Chen W., Richards W.D., Dacek S., Cholia S., Gunter D., Skinner D., Ceder G., Persson K.A., Commentary: The Materials Project: A Materials Genome Approach to Accelerating Materials Innovation. APL Materials. 1: 11002 (2013).
53. OQMD, The Open Quantum Materials Database, Chris Wolverton's group, http:// www.oqmd.org, Accessed date: 12 March 2019.

54. Raub E., Engel M., Alloys of Zirconium with Copper, Silver, and Gold. Z. Metallkd. 39: 172-177 (1948).
55. Kemper R.S., The Zirconium-Silver System, Thesis for the degree of Master of Sciences. Oregon State College, (1952).
56. Betterton J.O., Easton D.S., The Silver-Zirconium System. T. Metall Soc AIME. 212: 470-475 (1958).
57. Loboda T.P., Pyatnitskii V.N., Raevskaya M.V., Sokolovskaya E.M., Study of the Zirconium-Silver System by Differential Thermal Analysis. Vestn Mosk U Khim. 19(3): 298-301 (1978).
58. Zhang K., Zhao H., Zhou Y., An Investigation of the Silver-Zirconium Phase Diagram. J. Less-Common Met. 138(2): 173-177 (1988).
59. Karlsson N., An X-Ray Study of the Phases in the Silver-Zirconium System. Acta Chem Scand. 6: 1424-1430 (1952).
60. Pravoverov N., Kolonin Y., Solubility of Zirconium in Silver. Izv Akad Nauk SSSR, Metally. 2: 188-190 (1969).
61. Taguchi O., Iijima Y., Reaction Diffusion in Silver-Zirconium System. Mater T JIM. 35(10): 673-678 (1994).
62. Scott J.L., A Calorimetric Investigation of Zirconium, Titanium, and Zirconium Alloys from 60 to 960°C, Oak Ridge National Laboratory, (1957).
63. Dinsdale A.T., SGTE Data for Pure Elements. Calphad. 15: 317-425 (1991).
64. Decreton A. Contribution Expérimentale à l'Etude Thermodynamique des Systèmes Ag-Zr et Ag-Cd-In. PhD Thesis, Aix Marseille University, (2016).
65. Hsiao H-M., Liang S-M, Rainer S-F., Yen Y., Thermodynamic Assessment of the Ag-Zr and Cu-Zr Binary Systems. CALPHAD. 55(2): 77-87 (2016).
66. He X.C., Wanga H., Liua H.S., Jina Z.P., Thermodynamic Description of the Cu–Ag–Zr System. Computer Coupling of Phase Diagrams and Thermochemistry. 30: 367–374 (2006).
67. Kang D.H., Critical Thermodynamic Evaluation and Optimization of the Ag–Zr, Cu–Zr and Ag–Cu–Zr Systems and its Applications to Amorphous Cu–Zr–Ag Alloys. Intermetallics. 18: 815 (2010).
68. Fitzner K., Kleppa O.J., James F., Thermochemistry of Binary Alloys of Transition Metals: the Me-Titanium, Me-Zirconium and Me-Hafnium (Me = silver, gold) Systems. Metall Trans A. 23(3): 997-1003 (1992).
69. Curtarolo S., Morgan D., Ceder G., Accuracy of Ab Initio Methods in Predicting the Crystal Structure of Metals: a Review of 80 Binary Alloys. Calphad. 29(3): 163-211 (2005).
70. E. Fischer, NUCLEA Thermodynamic Database for Corium; Institut de Radioprotection et Sûreté Nucléaire: St Paul lez Durance, France, 2022.
71. Israel A., Jacob I., Soubeyroux J.L., Fruchart D., Pinto H., Melamud M., Neutron Diffraction Study of Atomic Bonding in the Hydrogen-Absorbing Zr (Alx Fe1-X)2 System. J. Alloys and Compd. 253: 265-267 (1997).
72. Basinski Z.S., Hume-Rothery W., Sutton A.L., The Lattice Expansion of Iron, Proceedings of the Royal Society of London, Series A. Mathematical and Physical and Engineering Sciences. 229: 459-467 (1955).

73. Lichter B.D., Precision Lattice Parameter of Zirconium Oxygen Solid Solution. Trans. Metall. Soc. AIME. 218: 1015 -1018 (1960).
74. Owen E.A., Yates Z.L., Precision measurements of crystal parameters. Philosophical Magazine. 15: 472-488 (1933).
75. Smith D. K., Newkirk W., The Crystal Structure of Baddeleyite (Monoclinic ZrO_2) and its Relation to the Polymorphism of ZrO_2. Acta crystalographica. 18(6): 983-991 (1965).
76. Kattner U.R. and Burton B.P., Al-Fe (Aluminum-Iron), Phase Diagrams of Binary Iron Alloys. H. Okamoto, Ed., ASM International. 12–28 (1993)
77. Zheng W., Shuang H., Malin S., Yanlin H., et al., Thermodynamic Assessment of the Al-C-Fe System. Calphad. 58: 34-49 (2017).
78. Janghorban A., Antoni-Zdziobek A., Lomello-Tafin M., Antion C., et al., Phase Equilibria in the Aluminium-Rich Side of the Al–Zr System. J. Therm. Analy. Calorim. 114: 1015–1020 (2013).
79. Khvan A. V., Eskin D.G., Starodub K.F., Dinsdale A.T., Wang F., Fang C., et al., New Insights into Solidification and Phase Equilibria in the Al-Al3Zr System: Theoretical and Experimental Investigation. J. Alloys and Compd. 743: 626-638 (2018).
80. Meschel S. V., Kleppa O.J., Standard Enthalpies of Formation of 4d Aluminides by Direct Synthesis Calorimetr., J. Alloys and Compd. 191: 111–116 (1993).
81. Fischer E., Colinet C., An Updated Thermodynamic Modeling of the Al-Zr System. J. Phase Equilibria and Diffus. (2015).

5. Enthalpy of formation of UZr_2

5.1. Introduction

As mentioned in Chapter one, in the simulations of the advanced phase of severe nuclear reactor accidents, an important issue is to be able to calculate the heat flux imposed by the corium on the vessel in order to determine the time and location of the vessel rupture and the initial conditions of the corium-concrete interaction. Knowing the final state of the fuel debris inside the reactor vessel is also crucial for developing appropriate strategies to contain the corium inside the vessel in the event of severe accidents for future (Generation III) reactors.

The analysis of the potential situations shows that the different components in the corium melts cannot be treated independently since their interaction may lead to different situations more or less threatening to the vessel confinement. Thermodynamic equilibrium plays an important role for the formation of various phases of the complex system of molten core materials, including U, Zr, O, stainless steel and control rod materials Depending on the oxygen potential conditions, metallic phases including uranium, zirconium and stainless steel components can be formed in the lower part of the vessel. Among the different binary systems of interest for the modelling of such phases, the U-Zr system for which few data are available is important to model. For severe accident applications, the U-Zr system has been modelled by Chevalier et al. [1] [2] and more recently by Quaini et al. [3]. In a very different context, the U-Zr system has received a lot of attention both experimentally and theoretically. It can be firstly attributed to its importance in the development of metallic nuclear fuels for fast neutron reactors, as a binary subsystem of the U-Pu-Zr ternary. To be able to predict the behavior of such fuels for various composition and temperature ranges, Calphad modellings based on critical assessments of the available experimental thermodynamic and phase diagram data have been successively published by Leibowitz et al. [4], Ogawa et al. [5], Kurata et al. [6] [7] and more recently by Xiong et al. [8].

Despite these numerous studies, there are some controversies about the available data of the U-Zr system. Among these data, the revisit of the thermodynamic properties related to phases in the U-Zr system, specifically the standard enthalpy of formation of UZr_2 (only intermetallic phase in the system) has been the object of intense debate between different theoretical teams in the framework of validation of ab initio calculations.

This chapter then focuses on the standard enthalpy of formation of UZr_2. It comprises of an analysis of bibliography available for this phase, the reinterpretation of standard enthalpy of formation of UZr_2 obtained in the past by Nagarajan et al. [9] and lastly discussion of the new experimental results obtained in this work by high temperature dissolution calorimetry technique.

5.2. Bibliography

It is well established [10] that the U-Zr phase diagram exhibits at high temperature, a body centered cubic solution (γ-U,β-Zr) with complete mutual solubility of U and Zr. At lower temperature, this phase forms a very flat miscibility gap ranging between 10 and 40 at% Zr and having a critical point at 995 K and 30 at.% Zr (see **Figure 59**). The so-called **δ** phase, which is the subject of this chapter, is the only intermetallic phase in the system. This intermediate phase, whose composition could be approximated as stoichiometric UZr_2 and which is stable below its transition temperature around 880 K [11], has a significant homogeneity composition range extending from 64.2 to 78.2 at.% Zr at 873 K and from 66.5 to 80.2 at.% Zr at 823 K according to Akabori et al. [12]. The **δ** phase has a hexagonal structure (c = 3.08 Å, a = 5.03 Å) [13] with three atoms in the conventional cell in which the (0, 0, 0) sites are occupied by zirconium atoms while the (2/3, 1/3, 1/2) and (1/3, 2/3, 1/2) sites are randomly filled by uranium and zirconium atoms. In the Calphad assessments, this phase is conventionally modelled using a two-sublattice model (either $(Zr)_1(U,Zr)_2$ adopted in [8] [2] [3] consistently with the experimental crystallographic description of **δ** or $(U,Zr)_1(U,Zr)_2$ considered in [7]).

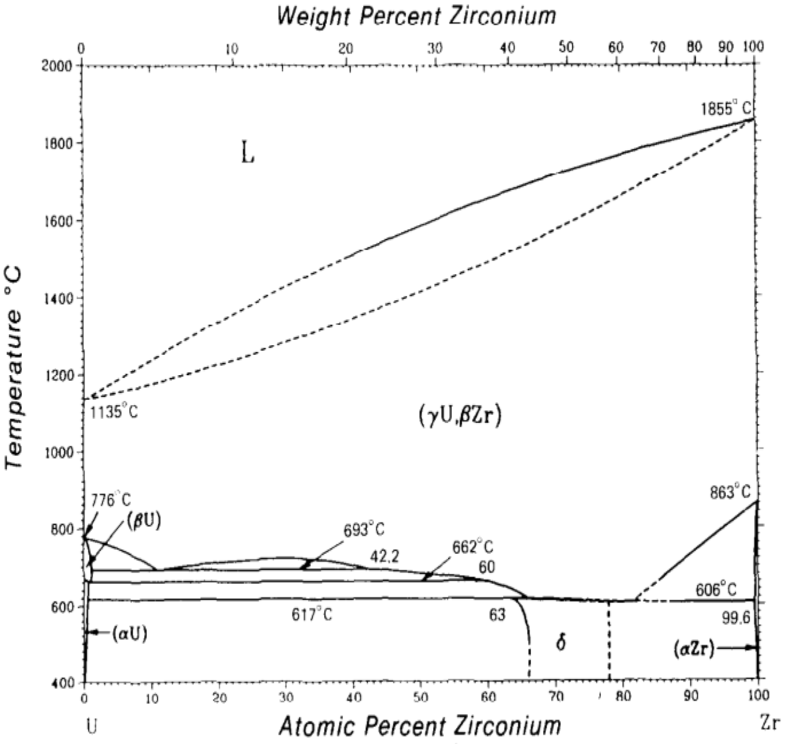

Figure 59. U–Zr phase diagram presented by Sheldon and Peterson [10].

The thermodynamic experimental data related to the **δ**-phase are rather limited since only the enthalpy of formation at the composition U/Zr=1/2 was determined to be (−4.0 ± 10.1 kJ/mol[a]) at 298.15 K by Nagarajan et al. [9] using dissolution calorimetry in liquid

---

[a] The mole here is UZr_2, hence containing 3 moles of atoms. In the following, we will use the unit $kJ.mol^{-1}$ to specify it. When enthalpies are referred to one mole of atoms, that is to say to the formula $U_{1/3}Zr_{2/3}$, we will use the unit kJ mol at^{-1}. The misunderstanding of this basic distinction is the source of considerable confusion in the comparison between literature results.

aluminum at high temperature and the uranium activity in the compound was later measured by Murakami et al. [14] using EMF method.

In [9], the enthalpy of formation of UZr2 at 298.15 K, $\Delta_f H^{\circ}_{UZr_2}$, is obtained through a Hess cycle combining the drop-solution enthalpies at infinite dilution, $\Delta_{ds}\overline{H}^{\infty,T}_{X,298.15\ K}$, for X=U, Zr and UZr2 separately measured in an aluminum bath at T=991 K according to the following equation:

$$\Delta_f H^{\circ}_{UZr_2,298.15\ K} = \Delta_{ds}\overline{H}^{\infty,T}_{U,298.15\ K} + 2\Delta_{ds}\overline{H}^{\infty,T}_{Zr,298.15\ K} - \Delta_{ds}\overline{H}^{\infty,T}_{UZr_2,298.15\ K} \qquad (5.1)$$

A first point about the data reported in [9] was stressed by Ogawa et al. [15]. In such determination, a rather significant error is inevitable, since $\Delta_f H^{\circ}_{UZr_2}$ is calculated from the linear combination of three large values, $\Delta_{ds}\overline{H}^{\infty,T}_{X,298.15\ K}$, for $X = U, Zr$ and UZr_2 ranging between 100 and 200 kJ mol at^{-1}. Since the absolute value of $\Delta_f H^{\circ}_{UZr_2,298.15\ K}$ is small, its corresponding uncertainty (± 10.1 kJ. mol^{-1}) is inevitably large.

The second point is more fundamental since it puts into question the experimental determination itself. We have recently shown [16] that in most of the experimental studies dealing with zirconium dissolution in liquid aluminum around 1000 K (**Table 27**), including the one of Nagajaran et al. [9] and in spite of their consistency, the recorded thermal effects probably did not correspond to a dissolution phenomenon but to a partial or total transformation of Zr into a zirconium aluminide (Al_3Zr).

Table 27. Partial drop-solution enthalpies of zirconium in liquid aluminum at infinite dilution around 1000 K. The references states are solid zirconium at 298.15 K and liquid aluminum at the calorimeter temperature T_{cal}.

References	T_{cal} / K	x_{Zr}	$\Delta_{ds}\overline{H}^{\infty,T}_{Zr,298.15K}$ / $kJ\ mol^{-1}$
Ansara et al. [19]	984	≤ 0.0014	-212.4
Nagarajan et al. [9]	991	≤ 0.0267	-220.3 ± 9.5
Turchanin et al. [20] [21] [22]	1026	≤ 0.0044	-217.4 ± 8.5
Gomozov et al. [23]	1030	≤ 0.0006	-203.3 ± 4.9
Turchanin et al. [18] [24]*	1022	≤ 0.0055	-235.0 ± 4.3*
Decreton et al. [25]	996	≤ 0.0022	-221.5 ± 5.8
Maciag et al. [26]	1073	Not reported	-244.5 ± 5.4
Gajavalli et al. [17]	1173	≤ 0.001	-130 ± 9

** The most recent values of Turchanin et al. are considered, according to the authors [18], to be a refinement of the previously published ones.*

To overcome this difficulty, the partial drop-solution enthalpy of zirconium at infinite dilution has been recently indirectly determined by [17] from Al_3Zr dissolution in liquid aluminum at 1173 K, leading to a much less exothermic value -130 ± 9 kJ mol^{-1}. Combining this new value for Zr and those from [9] for U and UZr_2 in equation (5.1) reveals that the enthalpy of formation of UZr_2 would become strongly positive (about 55 kJ mol at^{-1}), which is in complete contradiction with the proven stability of the **δ**-phase at room temperature. This implies that the thermal effects related to the dissolution of uranium and UZr_2 in liquid aluminum measured in [9] must likely be reinterpreted.

The values from the various Calphad assessments of the U-Zr system are listed in **Table 28**. Chevalier adopted the experimental value ($\Delta_f H^{\circ}_{UZr_2,298.15\ K} = -4/3$ kJ mol at^{-1}) of Nagarajan et al. [9] in his first assessment [1] but revised the value to zero in a later article [2]. Kurata followed a similar reasoning modifying his initial value -13.394 kJ mol^{-1} adopted in [7] to zero in a later description of U-Zr-O [3]. We can thus note that all the authors finally agreed to choose an enthalpy of formation very close to zero at the stoichiometric UZr_2 composition.

The enthalpy of formation of this phase obtained at 0 K by electronic structure calculations are listed in **Table 29**. Depending on the authors and calculation methods, both positive and negative values are obtained with large differences in absolute magnitude.

Table 28. Description of δ-phase in the different Calphad modellings.

References	Thermodynamic model	Enthalpy of formation of **δ** for the composition U/Zr=1/2 / kJ mol^{-1}	Selected reference for the enthalpy of formation of **δ**
Chevalier et al. [1]	δ-phase modelled as U_3Zr_7	-13.333 $(= 10 \times -4/3)$	[9]
Chevalier et al. [2]	$(Zr)_1(U,Zr)_2$	0	Not explicitly mentioned
Kurata et al. [7]	$(U,Zr)_1(U,Zr)_2$	−13.394	Not explicitly mentioned
Xiong et al. [8]	$(Zr)_1(U,Zr)_2$	0.016	Not explicitly mentioned
Quaini et al. [3]	$(Zr)_1(U,Zr)_2$	-0.113	[9]

Table 29. Enthalpy of formation of UZr_2 determined from electronic structure calculations. SOC stands for Spin-Orbit Coupling. * The value $-23.1\ kJ\ mol^{-1}$ is reported by the authors in the core of the text however, the value $23.1\ kJ\ mol\ at^{-1}$ can be calculated from the total energies given in eV/at in Table II of the original article. This result is therefore highly questionable both in terms of sign and magnitude.

References	$\Delta_f H°$ of $\boldsymbol{\delta}$ for the composition U/Zr=1/2 / $\mathrm{kJ\ mol^{-1}}$ at 0 K	DFT method
Landa et al. [27]	-18.863	GGA
Basak et al. [28]	-14.61	GGA PBE
Xie et al. [29]	16.787/12.445 7.725/2.605 4.052/-1.737	GGA without/with SOC GGA + U(1.24eV) without/with SOC GGA + U(1.49eV) without/with SOC
Matar [30]	-2.895 ordered structure -38.594 disordered structure	GGA PBE
Seong et al. [31]	-23.1*	GGA PBE
Basak and Poswal [32]	61.654/90.889 ordered structure 76.416 disordered structure	GGA PBE
Ghosh et. al.[33]	15.948	GGA PBE
Zhang et al. [34]	76.708/85.392 54.42/58.761	GGA without/with SOC GGA + U (1 eV) without/with SOC
OQMD [35]	39.945	GGA
Materials Project [36]	63.970	GGA

5.3. Reinterpretation of the measured thermal effect in Nagarajan et al.'s [9] experiments

5.3.1. Zirconium solution in liquid aluminium

A thorough critical evaluation of literature data concerning the dissolution of zirconium in liquid aluminum was recently presented in [16] [17]. It was concluded that, in most of the calorimetric studies performed around 1000 K, the heat effect recorded was misinterpreted as the dissolution of zirconium whereas the phenomenon occurring in the calorimeter was more likely to be the formation of the Al_3Zr aluminide. This striking argument is applied to the measurements performed by Nagarajan et al. [9].

The calorimeter temperature selected in this literature study is 991 K (717.85°C). At this temperature, it can be checked from Figure 3 of reference [37] that the solubility limit of zirconium in an aluminum rich liquid is around 0.05 at.%. After the drop of the first Zr sample in the liquid Al bath, the Zr concentration already reaches 0.52 at.% as shown in Table 1 of [9] that is ten times the solubility limit value. Then, the amount of zirconium in excess of the solubility limit will precipitate as Al_3Zr aluminide crystals. The four subsequent Zr samples are dropped in an Al-rich Zr-saturated liquid and the expected reaction to occur is the full conversion of the Zr pieces into Al_3Zr according to the chemical reaction:

$$\langle \mathrm{Zr} \rangle_{298.15\,\mathrm{K}} + 3(\mathrm{Al})_{991\,\mathrm{K}} \rightarrow \langle \mathrm{Al_3Zr} \rangle_{991\,\mathrm{K}} \qquad \Delta H_2 \qquad (5.2)$$

Moreover, the plausibility of the above scenario can be quantitatively tested as the enthalpy ΔH_2 of reaction (5.2) can be calculated from the following Hess cycle:

$$\langle \mathrm{Zr} \rangle_{298.15\,\mathrm{K}} + 3\langle \mathrm{Al} \rangle_{298.15\,\mathrm{K}} \rightarrow \langle \mathrm{Al_3Zr} \rangle_{298.15\,\mathrm{K}} \qquad \Delta H_3 \qquad (5.3)$$

$$\langle \mathrm{Al_3Zr} \rangle_{298.15\,\mathrm{K}} \rightarrow \langle \mathrm{Al_3Zr} \rangle_{991\,\mathrm{K}} \qquad \Delta H_4 \qquad (5.4)$$

$$\langle \mathrm{Al} \rangle_{298.15\,\mathrm{K}} \rightarrow (\mathrm{Al})_{991\,\mathrm{K}} \qquad \Delta H_5 \qquad (5.5)$$

Then: $\Delta H_2 = \Delta H_3 + \Delta H_4 - 3\Delta H_5$

The enthalpy of reaction (5.3) is the standard formation enthalpy of Al_3Zr at room temperature. This value was measured by high-temperature direct synthesis calorimetry by Meschel and Kleppa [38]:

$$\Delta H_3 = \Delta_f H^{\circ}{}_{\mathrm{Al_3Zr},298.15\,\mathrm{K}} = -193.6 \pm 5.2\ \mathrm{kJ\,mol^{-1}}.$$

The enthalpy of reaction (5.4) represents the heat increment of the aluminide between the room and calorimeter temperatures. Using classical thermodynamic relations, this value can be calculated from the Gibbs energy function of Al_3Zr assessed by Fischer and Colinet [39]:

$$\Delta H_4 = \Delta H^{991\mathrm{K}}_{\mathrm{Al_3Zr},298.15\,\mathrm{K}} = 69.8\ \mathrm{kJ\,mol^{-1}}.$$

The enthalpy of reaction (5.5) represents the heat increment of pure aluminum between the room and calorimeter temperatures. This value can be calculated using the SGTE data for pure elements [40]:

$$\Delta H_5 = \Delta H^{991\mathrm{K}}_{\mathrm{Al},298.15\,\mathrm{K}} = 30.7\ \mathrm{kJ\,mol^{-1}}.$$

Neglecting the uncertainty affecting the enthalpy increment values, expected to be one order of magnitude smaller than the one affecting the formation enthalpy of Al_3Zr, we finally calculate: $\Delta H_1 = -215.9 \pm 5.2\ \mathrm{kJ\,mol^{-1}}$. This value is indeed in very good agreement with the average value $Q^{E,\infty}_{Zr} = -220.3 \pm 9.5\ \mathrm{kJ\,mol^{-1}}$ measured by Nagarajan et al. [9].

Two additional arguments can be put forward to contest the possibility to dissolve solid zirconium in liquid aluminum under the experimental conditions used by Nagarajan et al. [9].

First, even if the solubility limit is not exceeded, the time required to fully dissolve, at this temperature, a small solid piece of Zr having a mass of 3.5 mg in 9.1 grams of liquid Al is in the range 22000 - 24000 s, as can be estimated using a diffusion/convection modelling (see Fig. 1 of [16]). In the Nagarajan experiments, Zr samples have masses around 10 mg and the expected dissolution time would certainly be larger than this conservative estimate. It should be added that such a long dissolution time rules out the possibility of accurately measuring the enthalpy of dissolution with a high temperature calorimeter such as the HT 1500 model, considering the unavoidable fluctuations of the baseline of the calorimetric signal.

Second, as demonstrated in [17], accepting both the measured values of Nagarajan et al. around 1000 K and the ones obtained by calorimetry in the 1693-2045 K range by other groups of researchers would imply an unrealistic variation of the mixing enthalpy of Zr at infinite dilution in liquid Al with temperature. Moreover, the CALPHAD optimization by Fischer and Colinet [39] showed that a consistent modelling of the Al-Zr system could only be obtained relying on the 1693-2045 K range calorimetry results for the liquid phase, without taking into account any temperature variation of the liquid mixing enthalpy.

As a conclusion of this section, we reject the value of the partial enthalpy of Zr solution in liquid Al measured by Nagarajan et al. Adopting instead the partial enthalpy of mixing of Zr in liquid Al determined in our laboratory [17], $\Delta_{\mathrm{mix}}\overline{\mathrm{H}}^{\infty}_{\mathrm{Zr,1173\ K}} = -175 \pm 10\ \mathrm{kJ\ mol^{-1}}$, further assuming that this value remains constant between 991 and 1173 K and using SGTE data of pure Zr, we finally estimate $\Delta_{\mathrm{ds}}\overline{\mathrm{H}}^{\infty,991\ \mathrm{K}}_{\mathrm{Zr,298.15\ K}} = -136.4 \pm 10\ \mathrm{kJ\ mol^{-1}}$.

5.3.2. Uranium solution in liquid aluminum

The thermodynamics of the U-Al liquid has been investigated by various groups. Colinet et al. [41], Nagarajan et al. [42] and Labroche et al. [43] all used drop-solution calorimetry in liquid aluminum. In this technique, the solid samples are maintained at room temperature before being dropped in liquid aluminum held at the high calorimeter temperature $\mathrm{T_{exp}}$. The measured quantity is the partial drop solution enthalpy of uranium between 298.15 K and $\mathrm{T_{exp}}$ denoted $\Delta_{\mathrm{ds}}\overline{\mathrm{H}}^{\infty,\mathrm{T_{exp}}}_{\mathrm{U,298.15\ K}}$ where the ∞ superscript means that the results are extrapolated to infinite dilution in liquid aluminum. Dannöhl and Lukas [44] adopted isothermal solution calorimetry in the same solvent. In their method, the solid samples are maintained at the same temperature as the calorimeter and the liquid aluminum. The measured enthalpy is, in this case, the partial isothermal solution enthalpy of uranium at $\mathrm{T_{exp}}$ denoted $\Delta_{\mathrm{sol}}\overline{\mathrm{H}}^{\infty}_{\mathrm{U,T_{exp}}}$. Lebedev et al. [45] measured the activity of U in liquid U-Al alloys by EMF technique. From the second-law processing of the EMF measurements vs. temperature at various compositions, they derive the partial mixing enthalpy of U at infinite dilution at the average temperature $\mathrm{T_{exp}}$ of the measurements denoted $\Delta_{\mathrm{mix}}\overline{\mathrm{H}}^{\infty}_{\mathrm{U,\ T_{exp}}}$.

The experimental conditions and partial enthalpies of uranium reported in these studies are summarized in **Table 30.** However, to check the consistency of the results, it is required to perform a prior conversion of all enthalpies to a common liquid reference state for both elements at the corresponding experimental temperature and infinite dilution. The SGTE data [40] are used to make the calculations and the obtained isothermal partial mixing enthalpies of uranium at $\mathrm{T_{exp}}$ and infinite dilution, denoted $\Delta_{\mathrm{mix}}\overline{\mathrm{H}}^{\infty}_{\mathrm{U,\,T_{exp}}}$, are given in the last column of **Table 30** for each study with, when it was possible, a re-estimation of the associated uncertainty.

Table 30. Comparison of literature values of the partial solution $\Delta \boldsymbol{H_U}$ and partial mixing enthalpies $\Delta_{\boldsymbol{mix}}\overline{\boldsymbol{H}}^{\infty}_{\boldsymbol{U,\,T_{exp}}}$ of uranium at infinite dilution in liquid aluminum measured at different temperatures $\boldsymbol{T_{exp}}$. $\boldsymbol{X_U^{max}}$ is the maximum uranium mole fraction reached in the binary U-Al liquid during the experiments. $\boldsymbol{X_U^{sat}}$ is the U mole fraction at saturation, i.e. the U mole fraction in the U-Al liquid in equilibrium with $\mathbf{UAl_4}$ or $\mathbf{UAl_3}$ depending on temperature, as calculated using the Calphad modelling of Wang et al. [46].

References	Technique	$\mathrm{T_{exp}}$ / K	$\mathrm{X_U^{max}}$	$\mathrm{X_U^{sat}}$	Reported $\Delta\overline{\mathrm{H}}_{\mathrm{U}}$ / kJ mol^{-1}	$\Delta_{\mathrm{mix}}\overline{\mathrm{H}}^{\infty}_{\mathrm{U,\,T_{exp}}}$ / kJ mol^{-1}
Nagarajan et al. [42]	Drop sol. calo.	980	≤ 0.0166	0.0266	-117.5 ± 7.1*	-155 ± 8.8#
Colinet et al. [41]	Drop sol. calo.	986	≤ 0.0009	0.0273	-96.65 ± 1.5*	-134.5 ± 1.1#
Labroche et al. [43]	Drop sol. calo.	988	≤ 0.011	0.0276	-105.0 ± 2.3**	-142.9 ± 2.3** -145.4 ± 6.4#
Lebedev et al. [45]	EMF	1000	≤ 0.0275	0.0291	-138.9 ± 2.9**	-138.9 ± 2.9**
Dannöhl and Lukas [44]	Isothermal sol. calo.	1023	≤ 0.045	0.0317	-132.4***	-142.4*** -142.4 ± 4.3#
Labroche et al. [43]	Drop sol. calo.	1244	≤0.010	0.0611	-79.3 ± 1.7**	-129.7 ± 1.7** -128.9 ± 3.7#

** reported standard deviation, ** reported uncertainty, *** uncertainty not reported by the authors, # value and expanded uncertainty re-estimated by us for a 95% confidence level.*

To gain a better insight into the literature results, the partial mixing enthalpy of U is plotted vs. uranium mole fraction in **Figure 60**. The experimental data points of Dannöhl and Lukas [44] and Labroche et al. [43] are digitized from the relevant figures of the original articles. Only the values at infinite dilution are reported in the articles of Colinet [41] and Lebedev et al. [45] and hence further analysis of these two experimental studies was not possible.

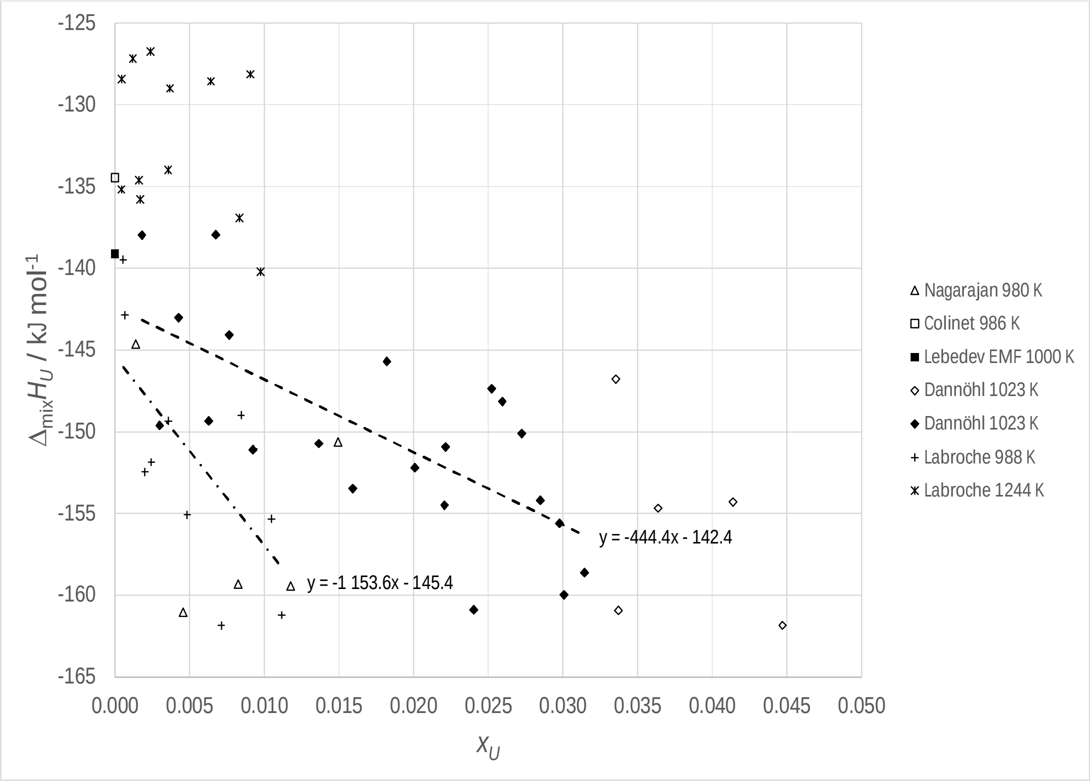

Figure 60. Partial mixing enthalpy of U plotted vs. U mole fraction in liquid Al at various temperatures. Reference state: both elements at the liquid state at the considered temperature. The dashed and dash-dotted lines are linear regressions to the data points of Dannöhl and Lukas (1023 K) and Labroche et al. (988 K) respectively. The corresponding regression equations are superimposed on the graph. The Dannöhl and Lukas data points plotted using empty diamonds exceed the solubility limit at 1023 K and were not considered for linear regression.

Several important points follow from the observation of **Figure 60**.

Dannöhl and Lukas [44] fit their results referred to solid U and liquid Al with a quadratic polynomial, obtaining the value $-132.4\ \mathrm{kJ\ mol^{-1}}$ at infinite dilution, corresponding to a mixing enthalpy $\Delta_{\mathrm{mix}}\overline{\mathrm{H}}^{\infty}_{\mathrm{U,1023\ K}} = -142.4\ \mathrm{kJ\ mol^{-1}}$. However, it can be checked that five data points (empty diamonds) of Dannöhl and Lukas [44] exceed the solubility limit and hence should not be considered further in the analysis. Despite this shortcoming, the results of Dannöhl and Lukas [44] at 1023 K clearly show that the mixing enthalpy varies linearly with the U mole fraction. We reprocess their data using a simple regression line excluding these five points and finally estimate from the line intercept $\Delta_{\mathrm{mix}}\overline{\mathrm{H}}^{\infty}_{\mathrm{U,1023\ K}} = -142.4 \pm 4.3\ \mathrm{kj\ mol^{-1}}$ (**Table 30** and **Figure 60**) a value which is identical to the initial estimate of Dannöhl and Lukas [44] given above.

A linear trend is also confirmed by the results of Labroche et al. [43] at 988 K. Hence, around 1000 K, it is confirmed that the values at infinite dilution should be estimated from the intercepts of regression lines. In the original article, the intercepts are determined by a complex coupled regression procedure involving the simultaneous determinations of several regression lines corresponding to the calorimetric data of several elements and compounds. This procedure is impossible to reproduce without all the original data. The uncertainties on the intercepts were estimated to be 2.2% of the value. Here, we adopted a different approach, we fitted the U data of Labroche et al. at 988 K by a simple regression but the uncertainty was estimated by the 95% confidence interval on the intercept yielding $\Delta_{\mathrm{mix}}\overline{\mathrm{H}}_{\mathrm{U,988\ K}}^{\infty} = -145.4\ \mathrm{kJ} \pm 6.4\ \mathrm{mol}^{-1}$. At 1244 K, the results of Labroche et al. show no clear slope vs. U mole fraction. Hence, the value at infinite dilution was estimated by simply taking the mean of all results giving $\Delta_{\mathrm{mix}}\overline{\mathrm{H}}_{\mathrm{U,1244\ K}}^{\infty} = -128.9\ \mathrm{kJ} \pm 3.7\ \mathrm{mol}^{-1}$. Both values, at 988 and 1244 K, remain consistent with those determined in the original paper, but the magnitude of the uncertainties is considered more realistic.

The scattering affecting the five points (empty triangles in **Figure 60**) of Nagarajan et al. [42] is large. In view of this scattering, these authors logically calculated the enthalpy at infinite dilution by taking a simple average of the five values. However, by comparison with the results of Dannöhl and Lukas and the ones of Labroche at 988 K, it can be realized that, even if most of the experimental points of Nagarajan et al. are consistent with the other studies, taking a simple average is an improper procedure, which leads to underestimate the mixing enthalpy value around $-155\ \mathrm{kJ\ mol}^{-1}$ (**Table 30**) whereas values in the range $\{-145\ ;\ -135\ \mathrm{kJ\ mol}^{-1}\}$ can be inferred from other literature results obtained at temperatures between 980 and 1023 K.

The variation of the partial mixing enthalpy of U at infinite dilution in liquid Al is plotted as a function of temperature in **Figure 61**. As explained above, the value of Nagarajan et al. is underestimated and all other results obtained at temperatures close to 1000 K are around $-140 \pm 5\ \mathrm{kJ\ mol}^{-1}$. The single value obtained at a significantly higher temperature (1244 K) by Labroche et al. suggests that the partial enthalpy of U would become less exothermic as temperature is increased. However, it is worth noting that, in the CALPHAD assessments of Kassner et al. [47] and Wang et al. [46], this possible enthalpy variation with temperature is not considered and constant values were adopted. We have also to keep in mind that any value of the partial mixing enthalpy of uranium in the 980 – 1244 K temperature range of the measurements relies on the estimation of the melting enthalpy of U at undercoolings ranging from 164 to 428 K, the uncertainty on this value remains difficult to assess. Further investigations would be required to clarify this issue.

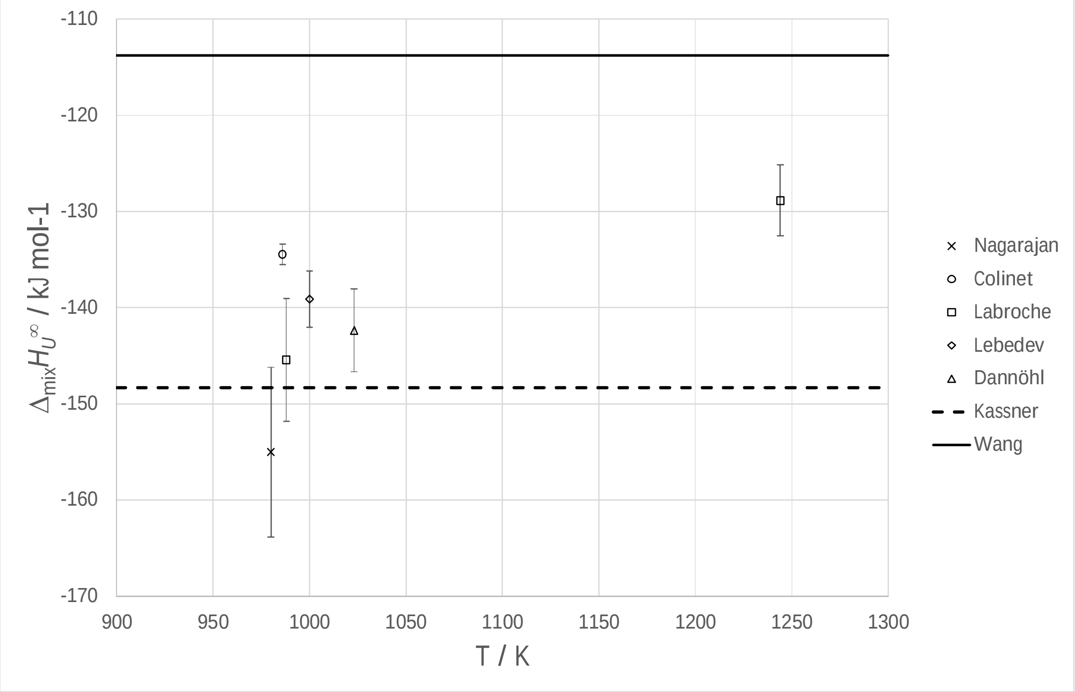

Figure 61. Partial mixing enthalpy of U at infinite dilution in liquid Al plotted vs. temperature U mole fraction in liquid Al. Reference state: both elements at the liquid state at the considered temperature. The constant values that can be calculated from the optimized coefficients of the CALPHAD assessments of Kassner et al. [47] and Wang et al. [46] are plotted as horizontal dashed and solid lines respectively.

At this stage of our critical analysis, we select the value of Labroche et al. corrected by us $\Delta_{mix}\overline{H}_U^{\infty} = -145.4 \text{ kJ} \pm 6.4 \text{ mol}^{-1}$ as a reliable estimate of the partial mixing enthalpy of U around 1000 K. This value, obtained by the IM2NP laboratory 20 years ago, is consistent with the determination of both Dannöhl and Lukas [44] and Lebedev et al. [43].

The exothermic character of the measured thermal effects recorded during the calorimetric experiments implies that a chemical reaction did occur when the solid U samples are immersed in liquid Al. To ensure that this effect corresponds to the actual dissolution of U, we performed a kinetic calculation.

At 980 K, the solubility of uranium in liquid aluminum is approximately 50 times higher than the one of zirconium. Moreover, and in contrast to what occurred in the Zr drop-solution experiments, this solubility limit was not crossed during the U drop-solution experiments of Nagarajan et al. (and of other studies). So, there was a non-zero thermodynamic driving force for U dissolution. It is then interesting to check if the kinetics of this dissolution is fast enough to allow the calorimetric measurement of its associated heat effect. A dissolution model has been developed by [16] to estimate the duration of the thermal effect in case the dissolution process is driven by diffusion and natural convection induced by the density difference between the metal (M) to be dissolved and liquid aluminum. More details on the model and the input parameters can be found in Appendix A. We have simulated the experimental conditions of the three drop-solution calorimetry studies (**Table 31**). In the experiments of Nagarajan et al. [42]

as well as in those of Colinet et al. [41] and Labroche et al. [43], the geometry and then the surface area S of the dropped uranium samples are not known. We will assume a spherical geometry. According to the isoperimetric inequality [48], for a given mass (so for a given volume at fixed density), the spherical geometry leads to minimize the surface of the sample and then to increase the dissolution time. The calculated dissolution time will have to be considered as an upper bound.

Table 31. Experimental conditions in the different dissolution calorimetry experiments of uranium in liquid aluminum and reported duration of the heat effect. T_{exp} is the calorimeter temperature.

References	T_{exp} / K	Dropped mass of U / mg	Mass of liquid aluminum bath / g	Experimental dissolution time / s
Nagarajan et al. [42]	980	50	> 0.4	No information
Colinet et al. [41]	986	20	200	Lower than 900 s
Labroche et al. [43]	988	28.6 (1st drop)	3	No information
Labroche at al. [43]	1244	23 (1st drop)	3	< 1200

Our calculations (**Figure 62**) show that, for all experimental conditions, dissolution is achieved in less than one hour. In high-temperature calorimetry, the occurrence of drift and/or baseline fluctuations is very likely over durations longer than one hour. The short durations which are calculated indicate that the dissolution enthalpy can be measured without too much uncertainty. Moreover, the calculated dissolution times are of the same order of magnitude or lower than the reported experimental ones. For example, in the experiments of Labroche et al. [43] at 1244 K, the observed dissolution time (< 1200 s) is much longer than the few hundred seconds calculated using our model. In fact, this duration of 1200 s probably corresponds to the time constant of the Tian-Calvet calorimeter. Colinet et al. [41] confirmed that the dissolution rate of uranium in liquid aluminum is very fast, even at 986 K. We conclude that the dissolution kinetics is not the phenomenon that limited the return of the calorimetric signal to its baseline.

To conclude this section, and in contrast to the zirconium case, the most likely scenario is that, during calorimetric experiments performed in the range 980-1023 K, uranium, because of its much larger solubility and sufficiently fast kinetics of the reaction, is effectively dissolved in liquid aluminum. So, the resulting estimate of the partial mixing enthalpy of uranium around 1000 K is then: $\Delta_{\mathrm{mix}}\overline{\mathrm{H}}_{\mathrm{U}}^{\infty} = -145.4\ \mathrm{kJ} \pm 6.4\ \mathrm{mol}^{-1}$. The corresponding drop solution enthalpies at 980 K (temperature of Nagarajan et al.'s experiments on U) and 991 K (temperature of Nagarajan et al.'s experiments on Zr and $\mathrm{UZr_2}$) are respectively $\Delta_{\mathrm{ds}}\overline{\mathrm{H}}_{\mathrm{U},298.15\ \mathrm{K}}^{\infty,980\ \mathrm{K}} = -107.9 \pm 6.4\ \mathrm{kJ\ mol}^{-1}$ and $\Delta_{\mathrm{ds}}\overline{\mathrm{H}}_{\mathrm{U},298.15\ \mathrm{K}}^{\infty,991\ \mathrm{K}} = -107.4 \pm 6.4\ \mathrm{kJ\ mol}^{-1}$.

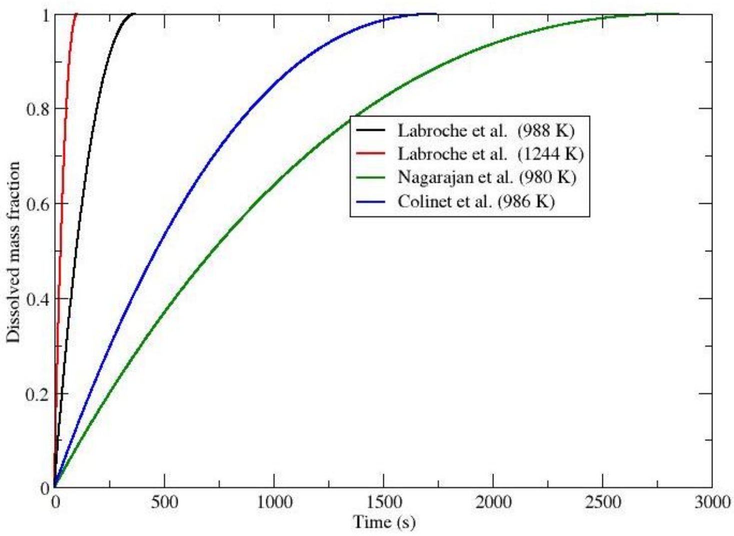

Figure 62 . Calculated evolutions of the dissolved fraction of the first dropped uranium sample in the experimental conditions of Nagarajan et al. [42], Colinet et al. [41] and Labroche et al. [43].

5.3.3. UZr_2 solution in liquid aluminum

The enthalpy of formation of UZr_2 at room temperature, which can be calculated combining our assessed solution enthalpies of zirconium (Section 5.3.1) and uranium (Section 5.3.2) in liquid aluminum with the solution enthalpy of UZr_2 reported by Nagarajan et al., is again strongly positive. It would be indicative of the instable character of this phase at 298.15 K, in remarkable contradiction to the state of knowledge on the U-Zr system which establishes the stability of this phase at room temperature. So from this first argument, it seems doubtful that the thermal effect reported by Nagarajan et al. could correspond to the effective dissolution of UZr_2 samples in liquid aluminum assumed by the authors.

According to the Calphad modelling of the Al-U-Zr system of Rabin et al. [49], it can be checked that Nagarajan et al. investigated in their UZr_2 dissolution experiments at 991 K, ranges of uranium and zirconium concentrations, leading to solid precipitation and this, from the first drop. Indeed, using Rabin's modelling, the calculated thermodynamic equilibrium is found to be biphasic, liquid + Al_3Zr (**Table 32**), and this equilibrium is calculated to prevail after each of the five UZr_2 additions. The corresponding equilibrium points are labelled as Q_N, N=1, 2,… 5 on the isothermal ternary section of **Figure 63**. The solubility limit of Zr in the ternary Al-rich liquid is so small that it appears as a line almost merged with the U-Al binary border in **Figure 63 a** and its value is almost constant in the explored composition range (**Figure 63 b**). As this limit is largely exceeded from the first drop during the calorimetric experiments of Nagarajan et al., it can be assumed that the dissolution of UZr_2 in liquid Al is accompanied by the re-precipitation of the excess quantity of Zr in the form of Al_3Zr aluminide. The calculation from Rabin's Calphad model shows that after the first drop, assuming that the Q1 thermodynamic equilibrium is established and then the liquid composition is at P1, about 85 wt% of zirconium from the UZr_2 dropped sample is not dissolved in the liquid and have precipitated as Al_3Zr while 15 wt% of zirconium is dissolved in liquid. For the following drops, according to the phase equilibrium is given respectively Q_2, Q_3, Q_4 and Q_5 no more zirconium dissolution in liquid phase is possible and then zirconium introduced in the bath fully precipitates in Al_3Zr.

This chemical process then occurring in the calorimeter could be written as:

$$\langle UZr_2\rangle_{298.15\,K} + n(Al)_T \rightarrow \left((U,(n-6)Al)\right)_T + 2\langle Al_3Zr\rangle_T \qquad (5.6)$$

The enthalpy of reaction (5.6), ΔH_6, can be estimated by the following Hess cycle:

$$\Delta H_6 = -\Delta_f H°_{UZr_2,298.15\,K} + 2\Delta_f H°_{Al_3Zr,298.15\,K} + 2\Delta H^{991K}_{Al_3Zr,298.15\,K} + \Delta_{ds}\overline{H}^{\infty,991\,K}_{U,298.15\,K} - 6\Delta H^{991K}_{Al,298.15\,K}$$

In which $\Delta_f H°_{Al_3Zr,298.15\,K} = -193.6 \pm 5.2$ kJ mol^{-1}, $\Delta H^{991K}_{Al_3Zr,298.15\,K} = 69.8$ kJ mol^{-1} and $\Delta H^{991K}_{Al,298.15\,K} = 30.7$ kJ mol^{-1} as already reported in section 5.3.1.

From the assessment presented in section 5.3.2, we select $\Delta_{ds}\overline{H}^{\infty,991\,K}_{U,298.15\,K} = -107.4 \pm 6.4$ kJ mol^{-1}.

For $\Delta_f H°_{UZr_2}$, the values calculated by DFT are spread over a large range, including both exothermic and largely endothermic values. However, considering that the compound is stable at room temperature but decomposes at a rather moderate temperature around 880 K [11], the absolute value of its formation enthalpy should be small. Moreover, considering that values close to zero were adopted in the most recent CALPHAD assessments (**Table 28**), a reasonable estimate of the formation enthalpy could be: $\Delta_f \overset{\circ}{H}_{UZr_2,298.15\,K} \approx 0 \pm 5$ kJ mol^{-1}.

Table 32. Phase mass fractions at thermodynamic equilibrium during the calorimetric experiments of Nagarajan et al. [9] at 991 K, as calculated with the Calphad modelling of the Al-U-Zr system by Rabin et al. [49]. Initial mass of aluminum equal to 595.59 mg as reported by Nagarajan et al. [9].

Dropped masses of UZr_2 / mg	Mass fraction of liquid phase	Mass fraction of Al_3Zr	Points on **Figure 63**
20.32	0.977	0.023	Q_1 : equilibrium between liquid of P_1 composition and Al_3Zr
24.67	0.947	0.053	Q_2 : equilibrium between liquid of P_2 composition and Al_3Zr
22.43	0.921	0.079	Q_3 : equilibrium between liquid of P_3 composition and Al_3Zr
17.57	0.901	0.099	Q_4 : equilibrium between liquid of P_4 composition and Al_3Zr
26.00	0.874	0.126	Q_5 : equilibrium between liquid of P_5 composition and Al_3Zr

Neglecting the uncertainties on the enthalpy increments of Al and Al_3Zr expected to be small compared to the ones affecting the other terms in the sum, it follows that $\Delta H_6 \approx -539.2 \pm 13.2$ kJ mol^{-1} ($\approx -179.6 \pm 4.4$ kJ mol at^{-1}), in rather good agreement with the value reported by Nagarajan et al., -554.7 ± 9.6 kJ mol at^{-1} (-184.9 ± 3.2 kJ mol at^{-1}). Moreover, it can be checked that the reported uncertainty ± 3.2 kJ mol at^{-1} is in fact the standard deviation of the five measured values given in Table 2 of [9]. The expanded uncertainty corresponding to a 95 % confidence interval is then ±4.0 kJ mol at^{-1}. So the uncertainty range of both values largely overlap and that means that the thermal effects measured by Nagarajan et al. can also be interpreted quantitatively in terms of dissolution of uranium and precipitation of Al_3Zr.

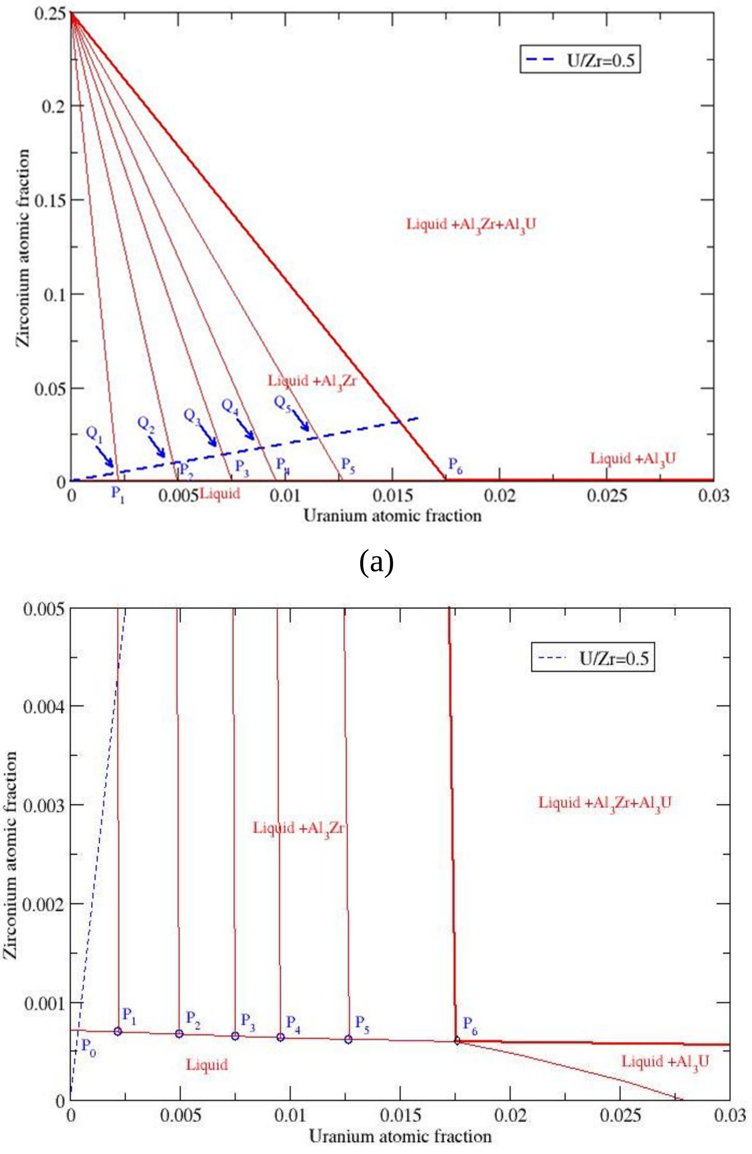

(a)

(b)

Figure 63. (a) Al-rich corner of the 991 K isothermal section of the Al-U-Zr phase diagram as modelled by Rabin et al. [44]. (b) Enlarged view at low Zr content.

Assuming that the thermal effect measured by Nagarajan et al. during the "dissolution" of UZr_2 corresponds to reaction (5.6), the standard enthalpy of formation of UZr_2 can be calculated from the following equation:

$$\Delta_f H°_{UZr_2,298.15\,K} = -\Delta H_6 + 2\Delta_f H°_{Al_3Zr,298.15\,K} + 2\Delta H^{991K}_{Al_3Zr,298.15\,K} + \Delta_{ds}\overline{H}^{\infty,991\,K}_{U,298.15\,K} - 6\Delta H^{991K}_{\mathrm{Al},298.15\,K}$$

Taking $\Delta H_6 = -184.9 \pm 4.0\ kJ\ mol\ at^{-1}$ and other auxiliary values already used in previous sections, we finally estimate:

$$\Delta_f H°_{UZr_2,298.15\ K} = 15.5 \pm 17.1\ kJ\ mol^{-1} = 5.2 \pm 5.7\ kJ\ mol\ at^{-1}.$$

The value is endothermic and again the absolute values of the enthalpy and its uncertainty are comparable. Finally, the enthalpy estimate is not greatly improved but results from combining values in which we can put more confidence. This modest improvement, in addition obtained from indirect procedure, underscores the need for additional measurements if a refined value for the enthalpy of formation of UZr_2 is desired. This is the topic of the two next sections.

5.4. New measurements of UZr_2 dissolution in liquid Al

An UZr_2 sample was elaborated at UCCS (Lille University). An arc-melted sample of composition U (51.45 wt.%) Zr (48.55 wt.%) was annealed during 2h below the eutectoid plateau at 853 K. No quantitative detection of carbon and oxygen was possible (**Figure 64 a**). Prior to the measurements, XRD was also performed on the synthesized $UZr_{2.46}$ (**Figure 64 b**) in order to be sure of the formation of expected single phase. In **Figure 64 b**, we observe that all the peaks obtained belong to UZr_2 phase, confirming the monophasic character of the sample.

The synthesized single phase $UZr_{2.46}$ samples were cut into small pieces (masses of 7 to 22 mg) and dropped into an Al bath at 1173 K. Four runs of $UZr_{2.46}$ dissolution calorimetry measurements in Al were performed in the atomic composition range $0 < X_{UZr2.46} < 0.0002765$. Within one run, each drop of dn moles of $UZr_{2.46}$ in the bath containing initially N moles of Al, M moles of U and J moles of Zr, corresponds to the following reaction:

$$\delta n\langle UZr2.46\rangle_{s,298} + ((NAl, MU, JZr))_{l,1173} \rightarrow ((NAl, (M+\delta n)U, (J+2.46\delta n)\ Zr))_{l,1173};\quad Q_{UZr2.46} \tag{5.7}$$

The differential signal of the calorimeter was continuously recorded during the dissolution process. After each drop, a thermal effect was registered before the signal has returned to the baseline (see Appendix C). The return to the baseline can be in some cases difficult to assess. It is considered that our measurements of thermal effects are accurate within ±5%. The associated heat effects $Q_{UZr2.46}$ which have been measured, are reported under the heading the partial drop solution enthalpy value for $UZr_{2.46}$ defined by $\Delta_{ds}\overline{H}^{1173K}_{UZr_{2.46},298K} = Q_{UZr2.46}/\delta n$ which are gathered in **Table 33** and plotted vs. $X_{UZr2.46}$ in **Figure 65**.

In the investigated composition range, $\Delta_{ds}\overline{H}^{1173K}_{UZr2.46,298K}$ can be represented by a linear function of the composition $X_{UZr2.46}$ and extrapolated to infinite dilution ($X_{UZr2.46} \rightarrow 0$) in order to calculate $\Delta_{ds}\overline{H}^{\infty 1173K}_{UZr2.46,298K}$. Discarding the value outside the general trend in bold (see **Table 33**), the partial drop solution enthalpy of UZr_2 at infinite dilution is $\Delta_{ds}\overline{H}^{\infty 1173K}_{UZr2.46,298K} = -365.1 \pm 6.6\ kJ\ mol^{-1}$, with reference state corresponding to the solid state at 298K.

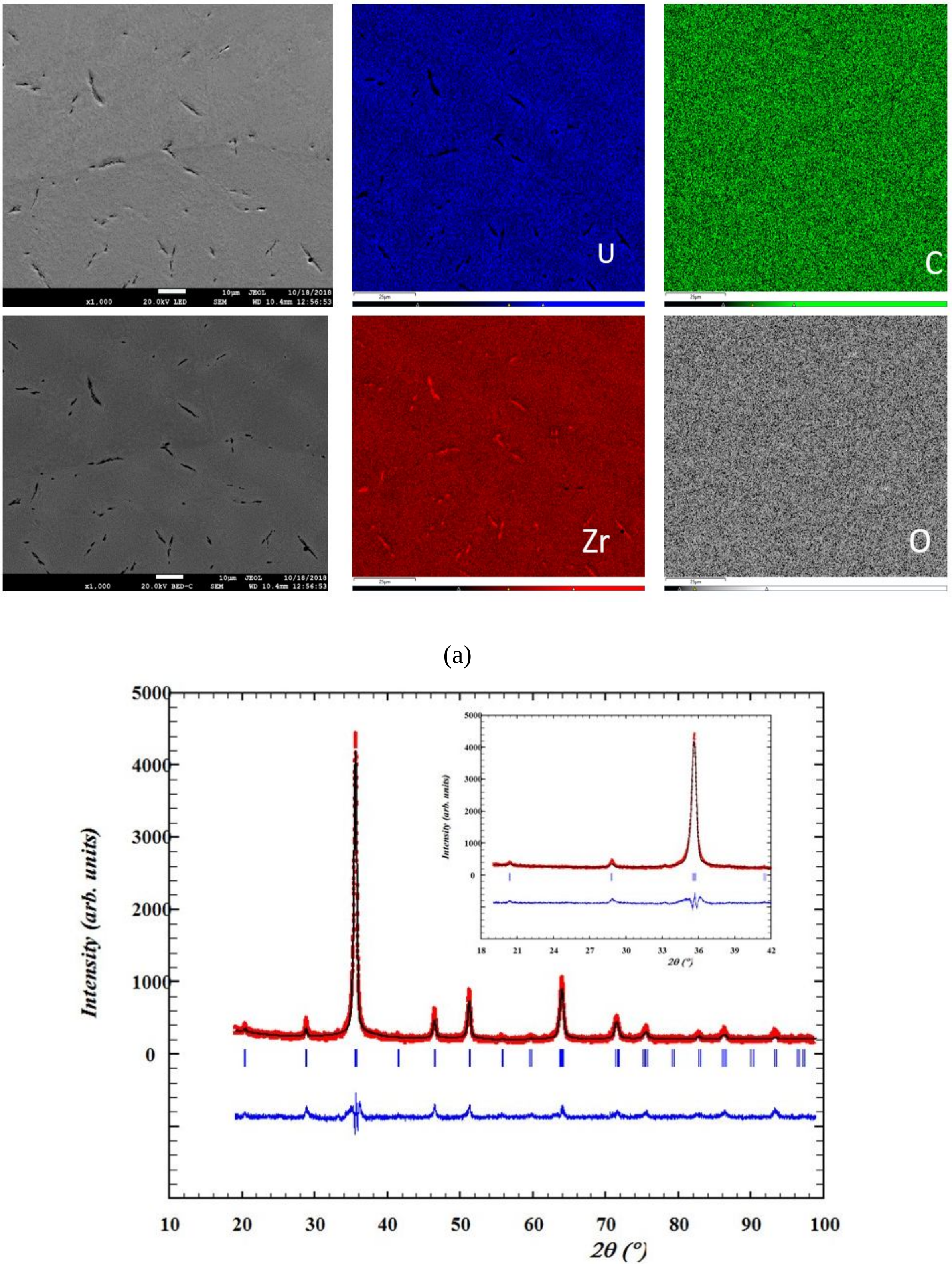

(a)

(b)

Figure 64. (a) SEM observation of UZr2.46 sample and (b)Refinement plot with the UHg_2 type of structure of the X-ray pattern of the $UZr_{2.46}$ sample annealed at 580°C for 2h.

Table 33. Partial drop-solution enthalpy of $UZr_{2.46}$ in liquid Al at 1173 K in $kJ.mol^{-1}$, $\Delta_{ds}\overline{H}^{1173K}_{UZr_{2.46},298K}$, measured by dissolution calorimetry. The references states are solid $UZr_{2.46}$ at 298 K and liquid aluminum at 1173K. M^{int}_{Al} and $\delta m_{UZr2.46}$ in mg, $\delta n_{UZr2.46}$ in mol, M^{int}_{Al} is the sum of the bath initial mass plus the masses of the 4 aluminum calibration samples. $X_{UZr2.46}$ is the molar fraction of $UZr_{2.46}$. Masses were weighed on a balance of 10^{-5} g accuracy. Thermal effects are accurate within ±5%.

Run	M^{init}_{Al} / mg	$\delta m_{UZr_{2.46}}$ /mg	$\delta n_{UZr_{2.46}}$ / mol	$x_{UZr_{2.46}}$	$\Delta_{ds}\overline{H}^{1173}_{UZr_{2.46},298}$ / $kJ.mol^{-1}$
1	10531.02	7.72	1.669E-05	2.138E-05	-355.554
		12.99	2.808E-05	7.872E-05	-420.172
		18.43	3.984E-05	1.657E-04	-482.400
		21.60	4.669E-05	2.765E-04	-527.098
2	10095.41	9.55	2.064E-05	2.758E-05	-375.009
		8.34	1.803E-05	7.925E-05	-407.199
		14.71	3.180E-05	1.458E-04	-466.951
3	10153.63	9.79	2.116E-05	2.812E-05	-386.405
		17.51	3.785E-05	1.065E-04	-445.02
		8.40	1.816E-05	1.809E-04	-467.085
4	10175.76	7.23	1.563E-05	2.072E-05	-381.014
		7.26	1.569E-05	6.224E-05	**-311.437**
		8.41	1.818E-05	1.071E-04	-452.886

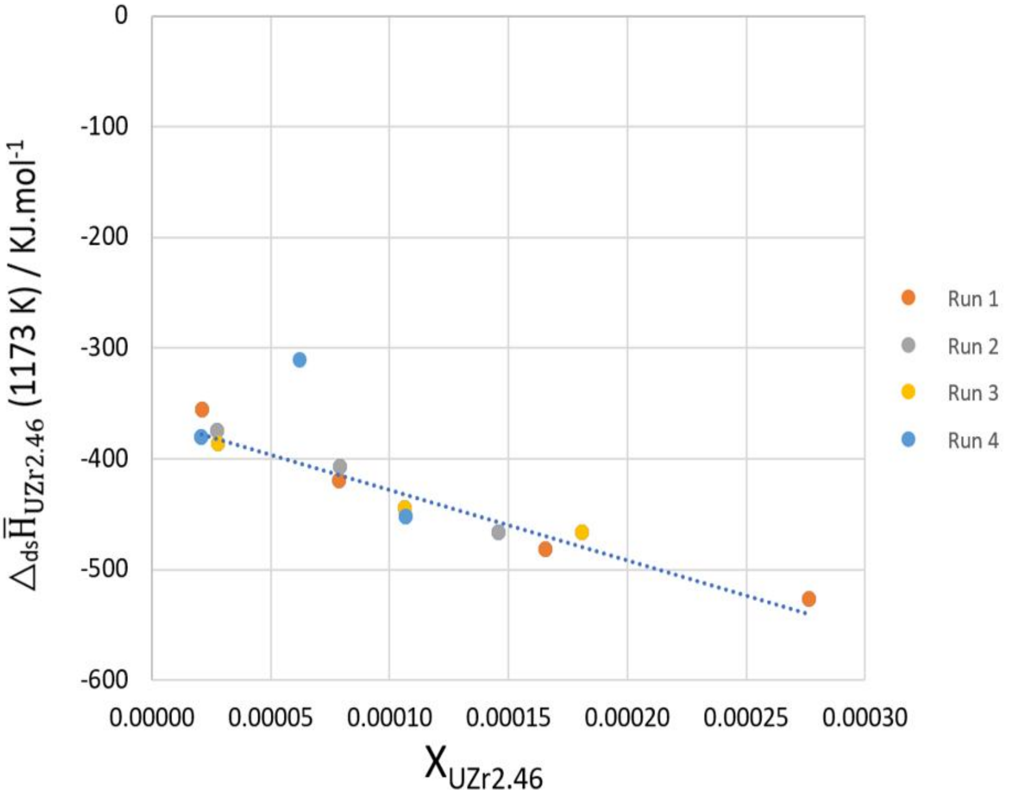

Figure 65. Partial drop solution enthalpy of UZr$_{2.46}$, $\Delta_{ds}\overline{H}^{1173K}_{UZr_{2.46},298K}$, in liquid Al between 298 and 1173 K as a function of UZr$_{2.46}$ mole fraction.

5.5. New determination the enthalpy of solution of UZr$_2$

The standard formation enthalpy of UZr$_{2.46}$, $\Delta_f H^\circ_{UZr2.46}$ is computed from the partial drop solution enthalpies at infinite dilutions of Zr, U and UZr$_{2.46}$ in liquid aluminum at 1173 K measured by using the dissolution calorimetry technique.

The $\Delta_f H^\circ_{UZr2.46}$ is then given by :

$$\Delta_f H^\circ_{UZr_{2.46},298.15\ K} = \Delta_{ds}\overline{H}^{\infty,1173\ K}_{U,298.15\ K} + 2.46\Delta_{ds}\overline{H}^{\infty,1173\ K}_{Zr,298.15\ K} - \Delta_{ds}\overline{H}^{\infty,1173\ K}_{UZr_{2.46},298.15\ K} \qquad (5.8)$$

The values of the quantities in the previous equation have determined as follows:

- The partial drop solution enthalpy of Zr in Al at infinite dilution at 1173 K was determined in our laboratory [17] $\Delta_{ds}\overline{H}^{\infty,1173K}_{Zr,298K} = -130 \pm 9$ kJ.mol^{-1}.
- The partial drop solution enthalpy of U in Al at infinite dilution at 1173 K was extrapolated from literature. A regression line through the data of Labroche [43] and Dannöhl and Lukas [44] (see **Table 30**) gives the partial mixing enthalpy at the temperature used in this work: $\Delta_{mix}\overline{H}^{\infty}_{U,1173\ K} = -133.3$ kJ.mol^{-1}.

Then from this value, considering the heat increment of U from room temperature to 1173 K, $\Delta H^{1173K}_{U,298K}$, and the enthalpy of fusion of uranium at 1173 K, $\Delta_{fus} H^{1173K}_{U}$, the drop dissolution enthalpy of U in liquid Al at infinite dilution at 1173 K is calculated from equation (5.9):

$$\Delta_{ds}\overline{H}^{\infty,1173K}_{U,298K} = \Delta_{mix}\overline{H}^{\infty,1173\,K}_{U} + \Delta H^{1173K}_{U,298K} + \Delta_{fus} H^{1173K}_{U} \tag{5.9}$$

i.e : $\Delta_{ds}\overline{H}^{\infty,1173K}_{U,298K} = -86.3$ kJ.mol^{-1}.

- The partial drop solution enthalpy of $UZr_{2.46}$ in Al at infinite dilution at 1173 K is measured in this study (previous section) $\Delta_{ds}\overline{H}^{\infty,1173K}_{UZr2.46,298K}$ = -365.1 ± 6.6 kJ.mol^{-1}.

Taking into consideration all the values into equation (5.8), the standard formation enthalpy of $UZr_{2.46}$ at 298K, is determined to be, $\Delta_f H^{\circ}_{UZr2.46}$= - 11.9 ± 6.7 kJ.mol^{-1}.at^{-1}.

5.6. Summary and discussion

The single available experimental value of the formation enthalpy of UZr_2 measured by Nagarajan et al. [9] ($\Delta_f H^{\circ}_{UZr_2,298.15\,K} = -4.0 \pm 10.1\ kJ\ mol^{-1}$) has been widely used in literature as input data in the Calphad assessments of the U-Zr binary system and as a benchmark for DFT calculations. As already mentioned previously, values of the formation enthalpy of UZr_2 very close to zero were adopted in the most recent Calphad assessments of the U-Zr system, allowing a good description of this binary. These values hence appeared to be consistent with that measured by Nagarajan et al. [9] taking into account the large experimental uncertainty, whose absolute value greater than that of the measured enthalpy itself and did not allow to have certainty on the sign of the enthalpy of formation. In the same way, a wide range of values were obtained by DFT depending on the various calculation methodologies. These ab initio calculations have been the subject of intense debate on whether the addition of the Hubbard U potential to the standard GGA functional, in the so-called DFT + U approach, could better model the energetics of binary U-Zr alloys and in particular UZr_2. Without further analysis of the DFT calculations, one could recognize that some of these values were again consistent with the experimental result of Nagarajan et al. [9]. This apparent consistency between the experimental, the CALPHAD and some of the DFT enthalpies explains why no critical analysis of the experimental value has been undertaken so far. However, the thorough analysis of the calorimetric experiments of Nagarajan et al. presented in the preceding sections shows that this agreement is largely coincidental.

Indeed, in the measurement technique adopted by this author, three (U, Zr and UZr_2) drop solution enthalpies must be measured to determine the formation enthalpy of UZr_2. We have shown that it was impossible to dissolve Zr and UZr_2 in liquid aluminum at 991 K because, in both cases, the solubility of Zr in the Al-rich liquid was largely exceeded during the experiments of Nagarajan et al. In addition, it was also shown that the enthalpy of drop-solution of U was underestimated because its linear dependence on the mole fraction of U was masked by the large dispersion of the experimental points. After reinterpretation of Nagarajan et al. [13] measurements a slightly calculated endothermic value (5.2 ± 5.7 kJ mol at^{-1}, section 5.3.3.) for standard enthalpy of formation of UZr_2 was obtained and again the absolute values of the enthalpy and its uncertainty are comparable.

The presence of the δ-phase in the U-Zr binary diagram is undeniable. This phase is considered as the only stable intermediate phase in the system as mentioned page 17 of the Metallic Fuels Handbook [50], while the α'-orthorhombic and ω-hexagonal phases are commonly accepted as being metastable (pages 20-21 of Janney's Handbook [50]). So, if we rule out the possibility that the δ phase, like Fe_3C in the Fe-C system, is metastable, then the sum of the enthalpic and entropic contributions to its Gibbs energy of formation should be negative.

With the CALPHAD description of [8] taken as an example, the formation entropy for the UZr_2 composition is calculated to be $\Delta_f S° = 0.773\, J\ (mol\ at)^{-1}\ K^{-1}$ at 298.15 K and then the entropic contribution $-T\ \Delta_f S° = -298.15 \times (0.773) \approx -230\, J\ (mol\ at)^{-1}$ is negative. These authors could adopt a very slightly endothermic formation enthalpy (see **Table 28**).

We have performed exploratory CALPHAD calculations with the NUCLEA database currently developed at IRSN [51] where the U-Zr system is modelled (**Figure 66 a**). We have estimated that the maximum endothermic value of the formation enthalpy at room temperature consistent with the available phase diagram data is $\approx +340\, J\ (mol\ at)^{-1}$. In this case, the stability domain of the δ phase gets narrower around 300 K (see **Figure 66 b**). However, it was not found possible to counterbalance an endothermic value of the formation enthalpy as large as $+5.2\ kJ\ (mol\ at)^{-1}$ by a negative entropic contribution.

Our endothermic value obtained from the interpretation of the Nagarajan's data was based on the assumption that reaction (5.6) occurred as a complete reaction. This estimate has an indirect character and its uncertainty is large, including both positive and negative values. We can therefore question whether it can be reduced by refining the estimate of the entropy. To further investigate this issue, the absolute entropy value of the δ phase was estimated from the very recent calorimetric measurements of [52] to be $S^{°}_{298.15\ K}(UZr_2) = 124.91 \pm 0.07\, J\, mol^{-1}\ K^{-1}$ (appendix B). Then the formation entropy can be calculated to be $\Delta_f S^{°}_{298.15\ K} = -1.22\, J (mol\ at)^{-1} K^{-1}$ and it is concluded that, at room temperature, the entropic contribution $-T\ \Delta_f S° = -298.15 \times (-1.22) \approx +364\, J\ (mol\ at)^{-1}$ being positive, destabilizes the compound. If this entropy value is fixed in the CALPHAD optimization (see **Figure 66 c**). then the formation enthalpy becomes negative $\Delta_f H^{°}_{298.15\ K} = -1503\ \mathrm{J\ (mol\ at)^{-1}}$ to keep the phase stable at room temperature. This conclusion must be tempered by the fact that the absolute value of the entropy of the δ phase at 298.15 K cannot be calculated directly by numerical integration of the experimental data Cp(T)/T because the high-temperature limit of the heat capacity measurements of [52] is 270 K and thus the previous value is only an extrapolated value of entropy. To definitely conclude, new measurements were necessary.

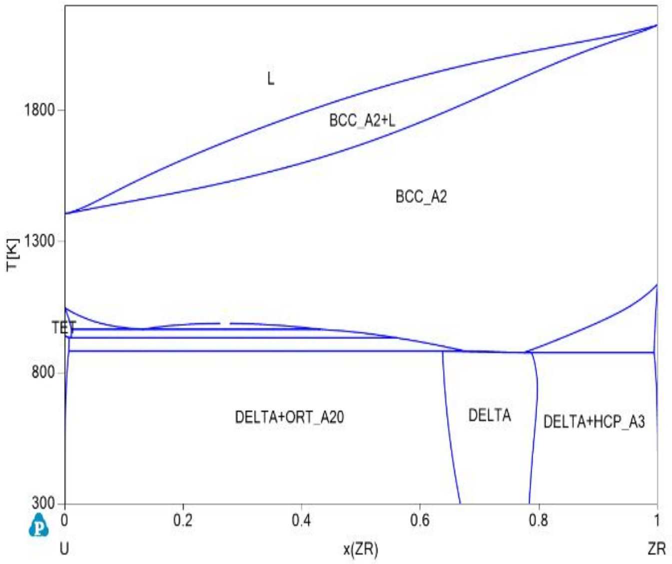

$$\Delta_f H^{\circ}_{298.15\ K} = 225\ \mathrm{J\ (mol\ at)}^{-1}$$

$$S^{\circ}_{298.15\ K} = 43.25\ \mathrm{J\ (mol\ at)}^{-1} K^{-1}$$

$$\Delta_f S^{\circ}_{298.15\ K} = = 0.40\ \mathrm{J\ (mol\ at)}^{-1} K^{-1}$$

(a)

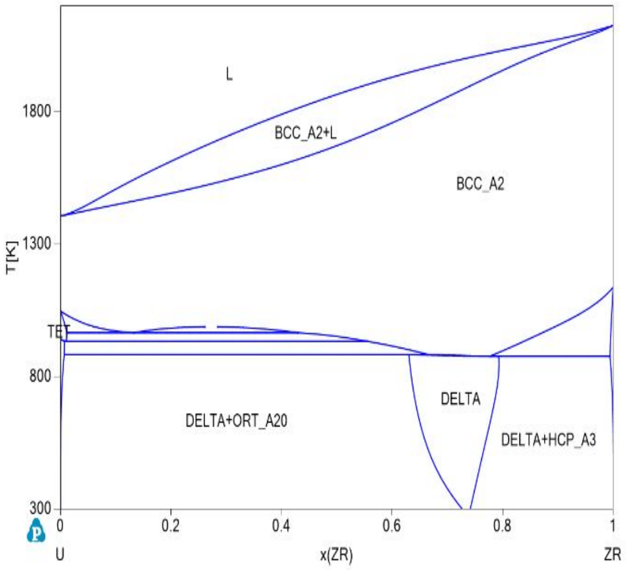

$$\Delta_f H^{\circ}_{298.15\ K} = 338\ \mathrm{J\ (mol\ at)}^{-1}$$

$$S^{\circ}_{298.15\ K} = 44\ \mathrm{J\ (mol\ at)}^{-1} K^{-1}$$

$$\Delta_f S^{\circ}_{298.15\ K} = 1.15\ \mathrm{J\ (mol\ at)}^{-1} K^{-1}$$

(b)

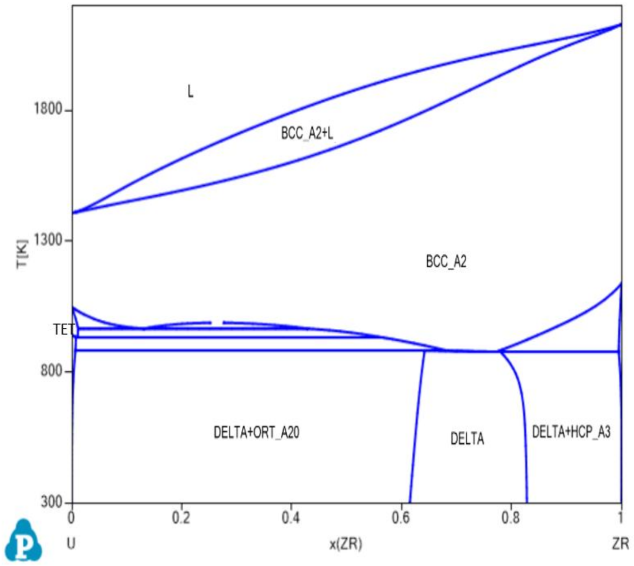

$$\Delta_f H^{\circ}_{298.15\,K} = -1503\ \mathrm{J\ (mol\ at)^{-1}}$$

$$S^{\circ}_{298.15\,K} = 41.7\ \mathrm{J\ (mol\ at)^{-1}}K^{-1}$$

$$\Delta_f S^{\circ}_{298.15\,K} = -1.15\ \mathrm{J\ (mol\ at)^{-1}}K^{-1}$$

(c)

Figure 66. U-Zr phase diagram from a) the NUCLEA Database [46] and with two amended thermodynamic description of the δ-phase (b and c). Values of the thermodynamic quantities for the δ-phase are given at the stoichiometric UZr_2 composition.

In order to make a definite conclusion, new measurements were carried under more favorable experimental conditions than those adopted by Nagarajan et al., such as a higher temperature if solution calorimetry in liquid aluminum is to be used. The standard formation enthalpy of UZr_2 at 298K, was determined as $\Delta_f H^{\circ}_{UZr2.46}$= - 11.9 ± 6.7 kJ. $(\mathrm{mol\ at})^{-1}$. The value obtained is more exothermic than the value of Nagarajan et al. [9].

5.7. Conclusion

The δ-solid solution is a key phase for the accurate description of the U-Zr system. However, a single experimental determination of the enthalpy of formation of the δ-UZr_2 stoichiometric composition is reported in the literature and the value was measured by dissolution calorimetry in liquid aluminum.

Most of the Calphad and DFT models of this phase rely on this value to support their validation. In this chapter, we have shown that this measurement must be reinterpreted and proposed a new estimate of the standard enthalpy of formation of δ-UZr_2. This new estimate confirms that the absolute value of the formation enthalpy of the δ-phase is small with an uncertainty of the same order of magnitude as the value itself. However, its value is too endothermic to allow the δ phase to appear as a stable phase in the diagram. The fact that both the available experimental value and our new estimate are questionable underscores the need for additional measurements if a refined value for the enthalpy of formation of UZr_2 is desired.

The additional measurements were done under more favorable experimental conditions than those adopted by Nagarajan et al. [9], where the standard enthalpy of formation was measured using dissolution calorimetry but at a higher temperature and the results obtained were more exothermic.

In terms of perspectives, metallographies of baths obtained after $UZr_{2.46}$ sample dissolution should be performed to check the completeness of the dissolution process of the samples in liquid aluminum. Also, the new experimental value obtained for the standard enthalpy of formation, more exothermic than the commonly accepted one until now should be introduced in the Calphad modelling of the U-Zr system to test its consistency with the other data available for this system.

5.8. Appendix

Appendix A. Kinetic model to estimate the dissolution time

A dissolution model has been developed by our team [17] in order to estimate the duration of the thermal effect expected in a dissolution. If the dissolution process of a solid metal (M) sample in liquid aluminum process is driven by diffusion and natural convection induced by the density difference between the metal (M) and liquid aluminum, the phenomenon can be described by the Nernst-Shchukarev equation [53,54]:

$$\frac{dC(t)}{dt} = K\frac{S}{V}[C_s - C(t)] \tag{5.10}$$

where $C(t)$ is the concentration of the dissolved metal in the liquid bulk at time t, C_s, the M concentration in the liquid at saturation (as given by the Al-M phase diagram), (t / s) the dissolution time, (S / m^2) the sample surface area, (V / m^3) the melt volume, and ($K / m.s^{-1}$) the mass transfer coefficient.

After some mathematics detailed in [17], the evolution of the M concentration in liquid aluminum can be expressed as:

$$\frac{dC(t)}{dt} = \frac{S}{V}B_0[C_S - C(t)] + \frac{S}{V}B_1[C_S - C(t)]^{5/4} \tag{5.11}$$

where B_0 and B_1 are defined according to:

$$B_0 = \frac{3.47D_0}{S^{1/2}} \text{ and } B_1 = 0.51\frac{D_0}{S^{1/2}}\left(\frac{A_1S^{3/2}}{D_0v}\right)^{1/4} \tag{5.12}$$

And:

$$A_1 = \frac{\rho_{l,M} - \rho_{l,Al}}{\rho_{l,Al}C_S + \rho_{l,M}(1 - C_S)} \tag{5.13}$$

with ($\rho_{l,i}$/ kg.m^{-3}) the density of 'i' at the liquid state, (ν /m^2.s^{-1}), the kinematic viscosity of liquid, (D_0 / m^2.s^{-1}) the diffusion coefficient of solute in liquid, and S, the sample surface.

To simulate the dissolution kinetics of uranium in liquid aluminum, the selected material properties and corresponding references are listed in **Table 34.** For the uranium solubility in liquid aluminum, C_s, around 1000 K, the experimental data of [55], [56] and Bitsianes and Hayes as reported in [55] are rather consistent in the vicinity of the eutectic temperature in the Al-rich region. The solubilities at the different temperatures have been calculated using the Calphad modelling of the Al-U system by Wang et al. [46].

Table 34. References of the material properties used in the dissolution simulations.

Properties	References
Density of liquid Al	Assael et al. [57]
Viscosity of Al	Assael et al. [57]
Density of solid U	Bobkov [58]
Density of liquid U	Fischer et al. [59]
U diffusion in liquid Al	Hesson et al. [60]

Appendix B. Excess heat capacity of UZr_2 between 0 and 298.15 K

The heat capacity of an UZr_2sample synthesized by arc melting and characterized by TEM and X-ray diffraction has been measured very recently by Ding et al. [52] between 2 and 270 K. Their experimental data were then fitted using a weighed sum of five Einstein functions with the help of the CpFit software [61]. The values of the parameters are given in **Table 35**. The experimental and calculated heat capacity curves of UZr_2 are plotted in **Figure 67**.

Table 35. Values of the weights and Einstein temperatures of UZr_2 optimized with the CpFit program on 151 experimental points from Ding et al. by [52]. The Δ and s values are respectively the 95% confidence interval and standard deviations of the parameters. Extra digits are indicated between brackets to avoid round-off errors.

i	α_i	$\Delta\alpha_i$	$s(\alpha_i)$	θ_i/ K	$\Delta\theta_i$ / K	$s(\theta_i)$ / K
1	0.243(4258147)	0.022	0.011	867(.4117740)	111	56
2	1.39(8804225)	0.29	0.15	248(.6742834)	17	8.8
3	1.37(1410246)	0.21	0.11	141(.8506446)	15	7.7
4	0.32(4744959)	0.13	0.063	70(.9233646)	9.0	4.5
5	0.0175(6016127)	0.0071	0.0036	19(.0967066)	4.7	2.4

For comparison, the data measured above room temperature by Fedorov and Smirnov [62] on a $U_{27}Zr_{73}$ sample by pulse joule heating and by Takahashi et al. [63] on a $U_{28}Zr_{72}$ sample by laser flash method are also plotted on the same graph together with a Neumann-Kopp estimate of the heat capacity in the same temperature range.

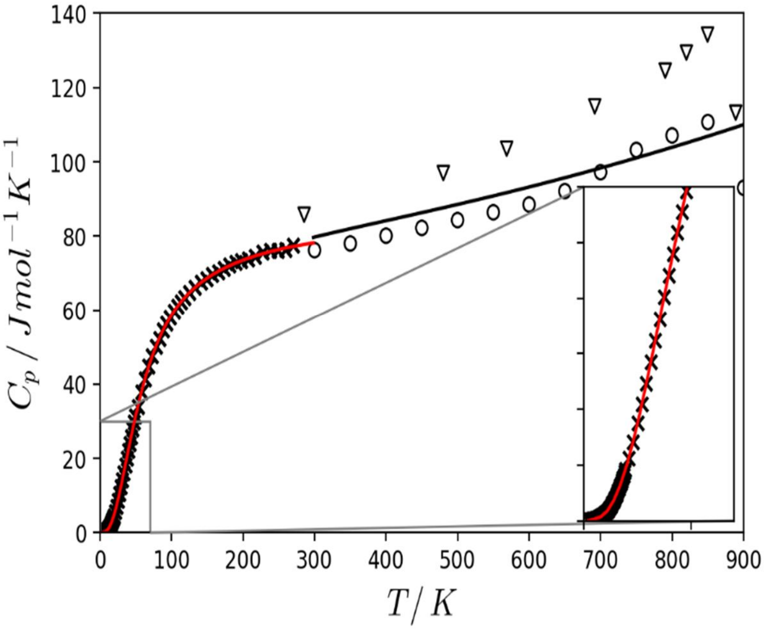

Figure 67. Heat capacity of UZr_2 vs. temperature. Scatter symbols are experimental points: (▽) from [62], (○) from [63], (✕) from [52]. The red solid line is calculated with the parameter values of Table 35. The black solid line is calculated with the Neumann-Kopp additivity Rule (NKR) for the UZr_2 stoichiometric composition using the SGTE data [40] of pure U and Zr.

Appendix C. Thermograph for UZr_2 dissolution in liquid Al (Run 1)

During the drop/solution experiments of UZr_2 samples, the observed calorimetric peaks (see **Figure 68**) are composed of an initial endothermic contribution, associated with the heating/melting of the sample, followed by a strong exothermic contribution which corresponds to its dissolution in liquid aluminum accompanied by the formation of Al_3Zr. And the third effect is interpreted as the dissolution of Al_3Zr, a reaction whose endothermic character was highlighted in a previous study [17].

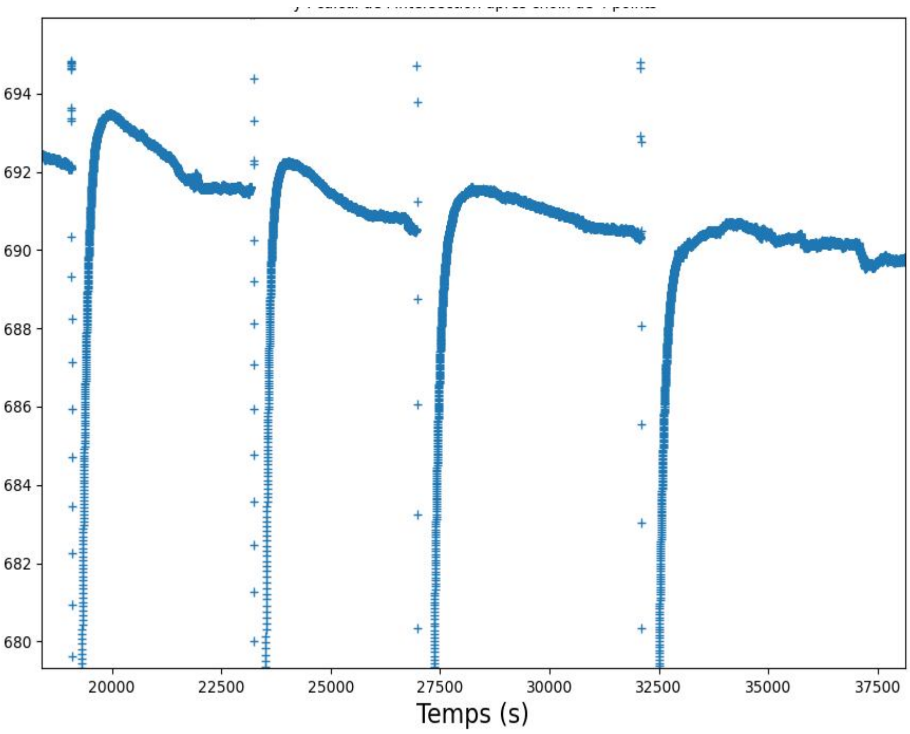

Figure 68. Thermograph for UZr2 dissolution in liquid Al (Run 1).

5.9. References

1. Chevalier P.Y., Fischer E., Thermodynamic Modelling of the O–U–Zr system. J. Nucl. Mater. 257: 213–255 (1998). https://doi.org/10.1016/S0022-3115(98)00450-4.
2. Chevalier P.Y., Fischer E., Cheynet B., Progress in the Thermodynamic Modelling of the O-U-Zr ternary system. Calphad Comput. Coupling Phase Diagrams Thermochem. 28: 15–40 (2004). https://doi.org/10.1016/j.calphad.2004.03.005.
3. Quaini A., Guéneau C., Gossé S., Dupin N., Sundman B., Brackx E., Domenger R., Kurata M., Hodaj F., Contribution to the thermodynamic description of the corium – The U-Zr-O System, J. Nucl. Mater. 501: 104–131 (2018). https://doi.org/10.1016/j.jnucmat.2018.01.023
4. Leibowitz L., Blomquist R.A., Pelton A.D., Thermodynamics of the Uranium-Zirconium System. J. Nucl. Mater. 167: 76–81 (1989). https://doi.org/10.1016/0022-3115(89)90426-1.
5. Ogawa T., Iwai T., Thermochemical Modelling of U-Zr Alloys. J. Less Common Met. 170: 101–108 (1991). https://doi.org/10.1016/0022-5088(91)90055-9.
6. Kurata M., Ogata T., Nakamura K., Ogawa T., Thermodynamic Assessment of the Fe–U, U–Zr and Fe–U–Zr Systems. J. Alloys Compd. 271–273: 636–640 (1998). https://doi.org/10.1016/S0925-8388(98)00176-5.
7. Kurata M., Thermodynamic Database on U-Pu-Zr-Np-Am-Fe Alloy System I — Re-evaluation of U-Pu-Zr alloy system. IOP Conf. Ser. Mater. Sci. Eng. 9: 012022 (2010). https://doi.org/10.1088/1757-899X/9/1/012022.
8. Xiong W., Xie W., Shen C., Morgan D., Thermodynamic Modeling of the U-Zr System - A Revisit. J. Nucl. Mater. 443: 331–341 (2013). https://doi.org/10.1016/j.jnucmat.2013.07.034.
9. Nagarajan K., Babu R., Mathews C., Enthalpy of Formation of UZr2 by Calorimetry. J. Nucl. Mater. 203: 221–223 (1993). https://doi.org/10.1016/0022-3115(93)90378-C.
10. Sheldon R.I., Peterson D.E., The U-Zr (Uranium-Zirconium) System. Bull. Alloy Phase Diagrams. 10: 165–171 (1989). https://doi.org/10.1007/BF02881432.
11. Akabori M., Ogawa T., Itoh A., Morii Y., The Lattice Stability and Structure of Delta-UZr2 at Elevated Temperatures. J. Phys. Condens. Matter. 7: 8249–8257 (1995). https://doi.org/10.1088/0953-8984/7/43/005.
12. Akabori M., Itoh A., Ogawa T., Kobayashi F., Suzuki Y., Stability and Structure of the δ phase of the U-Zr alloys. J. Nucl. Mater. 188: 249–254 (1992). https://doi.org/10.1016/0022-3115(92)90480-9.
13. Boyko E.R., The Structure of the δ phase in the Uranium–Zirconium System. Acta Crystallogr. 10: 712–713 (1957). https://doi.org/10.1107/s0365110x57002492.
14. Murakami T., Kato T., Kurata M., Yamana H., Electrochemical Formation of Uranium–Zirconium Alloy in LiCl–KCl melts. J. Nucl. Mater. 394: 131–135 (2009). https://doi.org/10.1016/j.jnucmat.2009.08.016.
15. Ogawa T., Free Energy of Formation of δ-UZr2 comment on the paper: K. Nagarajan, R. Babu and C.K. Mathews, Enthalpy of Formation of UZr2 by calorimetry. J. Nucl. Mater. 209: 107–108 (1994). https://doi.org/10.1016/0022-3115(94)90251-8.
16. Barrachin M., Gajavalli K., Decreton A., Virot F., Bénigni P., Rogez J., Mikaelian G.,

Fischer E., Lomello-Tafin M., Antion C., Janghorban A., Critical Evaluation of Experimental Data of Solution Enthalpy of Zirconium in Liquid Aluminum. J. Chem. Thermodyn. 128: 295–304 (2019). https://doi.org/10.1016/j.jct.2018.08.010.

17. Gajavalli K., Barrachin M., Benigni P., Rogez J., Mikaelian G., Fischer E., Determination of Solution Enthalpy of Zirconium in Liquid Aluminum. J. Chem. Thermodyn. 135: 198–204 (2019). https://doi.org/10.1016/j.jct.2019.03.037.
18. Turchanin A., Tomilin I., Inoue A., Zubkov A., Experimental Determination of Enthalpies of Formation of the Copper-Zirconium Amorphous Alloys. Mat. Sci. Forum 269-272. 565–570 (1998).
19. Ansara I., Pasturel A., Buschow K.H.J., Enthalpy Effects in Amorphous Alloys and Intermetallic Compounds in the System ZrCu. Phys. Status Solidi. 69: 447–453 (1982). https://doi.org/10.1002/pssa.2210690203.
20. Zubkov A.A., Turchanin A., Tomilin I.A., A High-Temperature Solution Calorimeter for Measuring the Heat of Mixing. Ind. Lab. 61: 544–547 (1995).
21. Turchanin A.A., Tomilin I.A., Inoue A., Zubkov A.A., Experimental Determination of the Formation Enthalpies of Zirconium-Nickel-Aluminium Amorphous Alloys. Mater. Sci. Eng. A. 226–228: 487–490 (1997). https://doi.org/10.1016/S0921-5093(97)80059-7.
22. Turchanin A., Tomilin I., Zubkov A., Experimental Determination of the Formation Enthalpies of Nickel-Zirconium And Nickel-Zirconium-Titanium Amorphous Alloys. Mater. Sci. Forum. 235–238: 367–372 (1997). http://www.scientific.net/MSF.235-238.367.pdf (accessed July 22, 2013).
23. Gomozov P., Zasypalov Y., Mogutnov B., Enthalpies of Formation of Intermetallic Compounds With the CsCl Structure (CoTi, CoZr, CoAl, NiTi). Russ. J. Phys. Chem. 60: 1122–1124 (1986).
24. Turchanin A.A., Tomilin I.A., Experimental Investigations of the Enthalpies of Formation of Zr-Based Metallic Amorphous Binary and Ternary Alloys. Berichte Der Bunsengesellschaft Für Phys. Chemie. 102: 1252–1258 (1998). https://doi.org/10.1002/bbpc.19981020932.
25. Decreton A., Benigni P., Rogez J., Mikaelian G., Barrachin M., Lomello-Tafin M., Antion C., Janghorban A., Fischer E., Contribution to the Description of the Absorber Rod Behavior in Severe Accident Conditions: An Experimental Investigation of the Ag–Zr Phase Diagram. J. Nucl. Mater. 465: 849–856 (2015). https://doi.org/10.1016/j.jnucmat.2015.05.039.
26. Maciąg T., Enthalpy Of Formation of Intermetallic Phases from Al–Zr System Determined by Calorimetric Solution Method. J. Therm. Anal. Calorim. 134: 423–431 (2018). https://doi.org/10.1007/s10973-017-6917-9.
27. Landa A., Söderlind P., Turchi P.E.A., Density-Functional Study of the U-Zr System. J. Alloys Compd. 478: 103–110 (2009). https://doi.org/10.1016/j.jallcom.2008.12.052.
28. Basak C.B., Neogy S., Srivastava D., Dey G.K., Banerjee S., Disordered Bcc γ-phase to $\boldsymbol{\delta}$-phase Transformation in Zr-Rich U-Zr Alloy. Philos. Mag. 91: 3290–3306 (2011). https://doi.org/10.1080/14786435.2011.577756.
29. Xie W., Xiong W., Marianetti C.A., Morgan D., Correlation and Relativistic Effects in U metal and U-Zr alloy: Validation of ab initio approaches. Phys. Rev. B - Condens.

Matter Mater. Phys. 88: 1–22 (2013). https://doi.org/10.1103/PhysRevB.88.235128.

30. Matar S.F., First Principles Studies of Hydrogen Insertion Effects on Magnetic Properties, Bonding and Structure Reordering of UZr2. Comput. Condens. Matter. 12: 19–24 (2017). https://doi.org/10.1016/j.cocom.2017.08.001.
31. Seong H.W., Ryu H.J., Ab-initio Calculation of the Metallic Fuels, in: Trans. Korean Nucl. Soc. Spring Meet. May 17-18, Jeju, Korea, pp. 17–19 (2018).
32. Basak C. B., and Poswal A. K., Structure and Stability of δ-UZr2 Phase in U-50 Wt% Zr Alloy. Philosophical Magazine. 102(9): 787–802 (2022). https://doi.org/10.1080/14786435.2021.2017050.
33. Ghosh P.S., et al., Chemical Ordering as a Precursor to Formation of Ordered δ-UZr2 phase: a Theoretical and Experimental Study. J. Phys., Condens. Matter. 33: 254003–254019 (2021). doi:10.1088/1361-648X/abf20b.
34. Zhang C.B., Li X. P., Li W. D., et al., Structural, Electronic, and Elastic Properties of Equiatomic UZr Alloys from First Principles. J. Nucl. Mater. 496: 333–42 (2017). https://doi.org/10.1016/j.jnucmat.2017.09.028.
35. OQMD, The Open Quantum Materials Database, Chris Wolverton's group, http:// www.oqmd.org, Accessed date: 12 March 2019.
36. Materials Project, https://materialsproject.org (accessed 12 March 2019).
37. Dezellus O., Gardiola B., Andrieux J., On the Solubility of Group IV Elements (Ti, Zr, Hf) in Liquid Aluminum Below 800°C. J. Phase Equilibria Diffus. 35: 120–126 (2014). https://doi.org/10.1007/s11669-013-0278-2.
38. Meschel S. V., Kleppa O.J., Standard Enthalpies of Formation of 4d Aluminides by Direct Synthesis Calorimetry. J. Alloys Compd. 191: 111–116 (1993). https://doi.org/10.1016/0925-8388(93)90280-Z.
39. Fischer E., Colinet C., An Updated Thermodynamic Modeling of the Al-Zr System. J. Phase Equilibria Diffus. (2015). https://doi.org/10.1007/s11669-015-0398-y.
40. Dinsdale A.T., SGTE Data for Pure Elements. Calphad. 15: 317–425 (1991). https://doi.org/10.1016/0364-5916(91)90030-N.
41. Colinet C., Bessoud A., Pasturel A., Müller W., Enthalpies of Formation of Rare Earth and Uranium Tin Compounds. J. Less Common Met. 143: 265–278 (1988). https://doi.org/10.1016/0022-5088(88)90049-5.
42. Nagarajan K., Babu R., Mathews C.K., Enthalpies of Formation of UAl4 and UAl3 by Calorimetry. J. Nucl. Mater. 201: 142–146 (1993). https://doi.org/10.1016/0022-3115(93)90169-Y.
43. Labroche D., Dugne O., Rogez J., New Thermodynamic Measurements in the U-Fe system, in: INIS/AIEA (Ed.), 9th Int. Conf. Nucl. Eng. Nice, Acrop. (France); 8-12 Apr 2001, Nice (France), 2001.
44. Dannöhl H.D., Lukas H.L., Calorimetric Determination of the Enthalpies of Formation of some Intermetallic Compounds. Z. Met. v. 65, no. 10, pp. 642-649. (1974). http://www.osti.gov/scitech/biblio/4260017 (accessed January 20, 2016).
45. Lebedev V.A., Sal’nikov V.I., Nichkov I.F., Raspopin S.P., Thermodynamic Properties of Uranium-Aluminum Alloys. Sov. At. Energy. 32: 129–132 (1972). https://doi.org/10.1007/BF01125089.
46. Wang J., Liu X.J., Wang C.P., Thermodynamic Modeling of the Al–U and Co–U

systems. J. Nucl. Mater. 374: 79–86 (2008). https://doi.org/10.1016/j.jnucmat.2007.06.023.

47. Kassner M.E., Adamson M.G., Adler P.H., Peterson D.E., The Al-U (Aluminum-Uranium) system. Bull. Alloy Phase Diagrams. 11: 82–89 (1990). https://doi.org/10.1007/BF02841588.
48. Andreescu T., Mushkarov O., Stoyanov L., Geometric Problems on Maxima and Minima, Birkhäuser Verlag, 2006.
49. Rabin D., Shneck R.Z., Rafailov G., Dahan I., Meshi L., Brosh E., Thermodynamic Modeling of Al–U–X (X = Si,Zr), J. Nucl. Mater. 464: 170–184 (2015). https://doi.org/10.1016/j.jnucmat.2015.04.020.
50. Janney D.E., Metallic Fuels Handbook, Part 1: Alloys Based on U-Zr, Pu-Zr, U-Pu, or U-Pu-Zr, Including Those with Minor Actinides (Np, Am, Cm), Rare-earth Elements (La, Ce, Pr, Nd, Gd), and Y, (2018). https://inldigitallibrary.inl.gov/sites/sti/sti/Sort_6065.pdf.
51. Fischer E., NUCLEA Thermodynamic Database for Corium, and Mephista Thermodynamic Database for Fuel Applications - Institut de Radioprotection et Sûreté Nucléaire: St Paul lez Durance, France, (2021).
52. Ding X., Yao T., Fu L., Hua Z., Harp J., Marianetti C., Neupane M., Manley M.E., Hurley D., Gofryk K., Magnetic, Transport and Thermal Properties of δ -phase UZr2. Philos. Mag. Lett. 101: 1–11 (2021). https://doi.org/10.1080/09500839.2020.1833375.
53. Eremenko V., Natanzon Y., Titov V., Dissolution Kinetics of the Compound $ZrAl_3$ in Liquid Aluminum.(Translation). Russ. Met. 204–208 (1981).
54. Yatsenko S.P., Sabirzyanov N. A., Yatsenko A. S., Dissolution Rates and Solubility of some Metals in Liquid Gallium and Aluminum. J. Phys. Conf. Ser. 98: 062032 (2008). https://doi.org/10.1088/1742-6596/98/6/062032.
55. Gordon P., Kaufmann A.R., The Alloy Systems Uranium-Aluminum and Uranium-Iron. JOM. 2 182–194 (1950). https://doi.org/10.1007/BF03398994.
56. Storhok V.W., Bauer A.A., Dickerson R.F., A study of the Liquidus in Aluminum-Uranium Alloys, Report No. BMI-1264, Columbus 1, Ohio, 1958. https://doi.org/10.2172/4334799.
57. Assael M.J., Kakosimos K., Banish R.M., Brillo J., Egry I., Brooks R., Quested P.N., Mills K.C., Nagashima A., Sato Y., Wakeham W.A., Reference data for the Density and Viscosity of Liquid Aluminum and Liquid Iron. J. Phys. Chem. Ref. Data. 35: 285–300 (2006). https://doi.org/10.1063/1.2149380.
58. Bobkov V.P., Thermophysical Properties of Uranium in Thermophysical Properties of Materials for Water-Cooled Reactors, IAEA-TECDOC-949. Supplement S7, Vienna, 1997.
59. Fischer E.A., Density of Liquid Uranium and Derived Equation of State, Scientific Report FZKA 6387, Karlsruhe, 2000. https://core.ac.uk/download/pdf/197567066.pdf.
60. Hesson J.C., Hootman H.E., Burris L.J., Diffusivity of Uranium in Various Liquid Metal Solutions, Electrochem. Technol. 3: 241–245 (1965).
61. Voskov A.L., Kutsenok I.B., Voronin G.F., CpFit program for Approximation of Heat Capacities and Enthalpies by Einstein-Planck Functions Sum, Calphad Comput. Coupling Phase Diagrams Thermochem. 61: 50–61 (2018).

https://doi.org/10.1016/j.calphad.2018.02.001.

62. Fedorov G.B., Smirnov E.A., Heat Capacity of Uranium-Zirconium Systems. Sov. At. Energy. 25: 795–797 (1968). https://doi.org/10.1007/BF01114245.
63. Takahashi Y., Yamamoto K., Ohsato T., Shimada H., Terai T., Yamawaki M., Heat Capacities of Uranium-Zirconium Alloys from 300 to 1100 K. J. Nucl. Mater. 167: 147–151 (1989). https://doi.org/10.1016/0022-3115(89)90436-4.

6. Conclusion

This research is part of two broader themes important to the understanding and mitigation of severe accidents in nuclear reactors.

- The first one is related to the source term determination under accident conditions and more specifically about the evaluation of fission products, such as iodine, having significant radiological consequences in short and medium term. During the early times of a severe accident in a pressurized water reactor, the Ag-Cd-In absorbing rod interacts with the Zircaloy guide tube at high temperature due to the failure of its stainless-steel cladding. This interaction leads to the formation of Ag-In-Zr-O and Fe-Zr-Cr-Ni-O mixtures and partial vaporization of Ag and Cd known to strongly impact iodine speciation and transport in the reactor primary circuit. To address the issue of control rod and Zircaloy interaction and its impact on indium and silver releases, accurate knowledge of the binary and ternary subsystems of the quaternary Ag-In-Zr-O phase diagram, as well as that of the quinary Fe-Zr-Cr-Ni-O one is required.

- The second one is linked to the interaction of the corium with the lower part of the vessel. In the late phase of the accident, when the corium has massively relocated to the lower plenum of the vessel, it is essential to be able to calculate the heat flux imposed by the corium on the vessel to determine the time and location of vessel failure and the initial conditions of the corium-concrete interaction. Thermodynamics of the complex multiphase system (U-O-Zr-Fe) of the corium plays a key role in this calculation.

This research has started between IRSN, IM2NP (Aix-Marseille University), SYMME (Savoie-Mont-Blanc University) and SIMAP (Grenoble University) in 2013. A lot of work has been done during the two previous theses [1, 2] to address the first theme. Both studies focused on the experimental determination of the Ag-Cd-In system at high temperature. Liquidus determinations obtained by an original approach [2] (Interrupted Heating Differential Technique Analysis allowing to better approach equilibrium conditions) combined with existing literature data and measurements of the mixing enthalpy of the liquid phase previously performed by [3] has allowed to propose for the first time a CALPHAD modelling of the Ag-Cd-In ternary system [4].

For the zirconium-based metallic binary systems, In-Zr and Ag-Zr, slightly less information was obtained even if, for this latter one, the limits of the phase domains, in particular involving the liquid phase, were entirely determined by Decreton [1] over the whole composition range. One of the main results was the resolution of the controversial nature of the decompositions of the two compounds in the system, AgZr and $AgZr_2$, which were shown to be congruent and peritectic respectively, in disagreement with some recent Calphad assessments of the Ag-Zr system [5, 6].

The In-Zr system was virtually unknown at the start of this research programme. Much of Gajavalli's work [2] was devoted to sample preparation, which was identified at the beginning of this work as a difficult problem due to the difference in melting point between the two elements, their relative immiscibility in the liquid state, the significant partial pressure of indium at the melting point of zirconium and finally the affinity of both elements with oxygen.

After extensive synthesis and characterization trials, mainly in the zirconium-rich part of the system, a procedure using an arc furnace was successfully developed. The Zr-rich part (at% Zr > 74) of the diagram previously established by Betterton and Noyce [7] was confirmed. Gajavalli's [2] work was complemented by melting point determinations of different compositions in the In_2O_3-ZrO_2 system using the laser flash technique at JRC Karlsruhe.

In parallel of this important phase diagram investigations, much of this past research has been devoted to determining the enthalpy of formation of compounds in the two systems. Measurements of enthalpy of formation of AgZr and In_2Zr were first attempted. For In_2Zr, direct reaction calorimetry provided a value in agreement with that measured by Meschel and Kleppa [8] while the use of high-temperature dissolution calorimetry has given rise to many problems, mainly related to the difficulty of finding a suitable solvent to dissolve zirconium at the highest temperature accessible with our calorimeter (about 1173 K). Metallic solvents, such as liquid indium, tin or aluminium, and aqueous solvents, such as HCl + HF mixtures, were tested but for most of them dissolution failed. Molten aluminium was finally chosen mainly because it has been widely used in the past to dissolve zirconium around 1000 K, apparently successfully and has led to consistent values measured by different groups of experimenters. A critical analysis of these data, including our own data, supported by the development of a kinetic model, finally showed that most of the dissolution experiments of zirconium in aluminum actually led to the (partial or total) transformation of this zirconium into zirconium aluminide (Al_3Zr) at the calorimeter temperature [9]. It was thus established, firstly, that the data obtained were unreliable, and secondly, that the values of enthalpies of formation measured by dissolution calorimetry in liquid aluminum around 1000 K in several Zr-based binary systems, such as U-Zr, Co-Zr, Ni-Zr and Cu-Zr, should be questioned.

These difficulties were then overcome by directly measuring the partial enthalpy of dissolution of Al_3Zr aluminide samples in liquid aluminum [2]. This value was then used to deduce the partial enthalpy of dissolution of zirconium in liquid aluminum by a thermodynamic cycle.

Two main challenges remained at the beginning of the present work. The first was to determine the phase equilibria in the indium-rich part of the In-Zr system. The second was to determine, by dissolution calorimetry in liquid aluminum, the standard enthalpies of formation of the different compounds of the In-Zr and Ag-Zr systems.

For the In-Zr system, we were again confronted with difficulties in preparing the samples. The procedure developed by Gajavalli for the zirconium-rich part of the diagram proved to be inapplicable to the indium-rich part, mainly due to the high volatility of indium leading to mass losses hard to anticipate and, ultimately, a great difficulty in synthesizing predefined target compositions. In this work, powder metallurgy was successfully adopted as an alternative synthesis method in the indium-rich part. This technique was extended to samples with higher zirconium content.

In-Zr alloys of different compositions were annealed at various temperatures and then analyzed by scanning electron microscopy (SEM) and X-ray diffraction (XRD) to identify the phases and measure their compositions. The existence of the previously reported intermetallic compounds (In_3Zr, In_2Zr, InZr, $InZr_2$ and $InZr_3$) was confirmed. An additional In_3Zr_2 phase was found by SEM. At this stage, the existence of this phase is also corroborated by DFT calculations [10] showing that the tP10 structure is located on the convex hull. Experimental confirmation of this phase by XRD is needed. The standard enthalpies of formation of In_3Zr and In_2Zr have been determined by dissolution calorimetry in liquid aluminum and the values are respectively -39.7 ± 2.9 $kJ.mol^{-1}.at^{-1}$ and -38.2 ± 3.3 $kJ.mol^{-1}.at^{-1}$. The standard enthalpy of formation of In_2Zr was also determined by high temperature direct synthesis calorimetry with a value consistent with the solution calorimetry one, being also in agreement with the value previously obtained by Meschel and Kleppa [8]. The overall agreement between the values obtained by various techniques for In_2Zr indirectly validates the solution enthalpy of zirconium in liquid aluminum measured by Gajavalli [2].

However, it should be noted that the experimental values for In_2Zr and In_3Zr are significantly more exothermic than the values calculated by DFT. A similar trend is observed in the Ga-Zr system [10] i.e. when indium is replaced by gallium, which is in the same column of the periodic table. This discrepancy will probably be the subject of a debate as to the qualification of the most suitable theoretical approaches for this type of chemical system.

For the first time, investigations by DTA have shown that the compounds in the indium-rich part, β-In_3Zr, In_2Zr and In_3Zr_2 decompose peritectically at 865 K, 1406 K and 1552 K respectively. Solubility of zirconium in liquid indium was indirectly estimated by a Tammann processing of DTA results and found to be larger than the values formerly reported by Dieva [11]. Finally, it was shown, by careful bi-differential thermal analyses, that the solid solution based on pure indium decomposed peritectically at 157°C in disagreement with the eutectic reaction assumed by Okamoto [12].

Due to unresolved sample preparation problems (samples containing a significant amount of oxygen), the central part of the phase diagram ($40 < at\% \ Zr < 75$ composition range) remains largely uncertain today and should be the main focus of future investigations of the In-Zr system. Measurements of indium activity in In-Zr alloys could be carried out to complete the description of the system.

For the Ag-Zr system, the formation enthalpy of the AgZr equiatomic compound was measured by dissolution calorimetry in liquid aluminium with a good agreement with the value of Decreton [1], who used room temperature solution calorimetry in a HF-HNO_3 aqueous solvent. Our value (-21.8 ± 5.7 $kJ.mol^{-1}.at^{-1}$) is much more exothermic than the value previously obtained by direct reaction [13] and subsequently accepted in various CALPHAD assessments of the Ag-Zr system. Within the experimental uncertainty, our value is nevertheless consistent with the more recent CALPHAD modelling of the Ag-Zr system performed at the SIMAP laboratory [14] on the basis of the phase diagram investigations of Decreton. Future work should be devoted to measuring the enthalpy of formation of $AgZr_2$ by dissolution calorimetry. In parallel, silver activity measurements for solid compositions on either side of the equimolar AgZr compound are currently underway at the SIMAP laboratory in order to finalise the description of the system.

The next step, after the completion of the studies of the Ag-Zr and In-Zr systems, could be the study of the Ag-In-Zr ternary system, which has received little attention so far. Two ternary compounds have been identified at 870 K [15] but their thermodynamic properties are unknown.

For the other two systems of interest investigated in this thesis, namely Fe-Zr and U-Zr, dissolution calorimetry in liquid aluminium at 1173 K was also applied to determine the enthalpy of formation of the intermetallic compounds Fe_2Zr and UZr_2.

- For UZr_2, prior to the present thesis, there was a single experimental value determined by Nagarajan et al. [16] using solution calorimetry in liquid aluminium and many CALPHAD assessments of the U-Zr system selected this value. This value is also of high relevance in the discussions between theoretical teams about the best DFT methodology (GGA or GGA+U) to calculate the enthalpy of formation of UZr_2 at 0 K. A complete reinterpretation of Nagarajan et al. value is done in the present manuscript. We show that the formation enthalpy results from a combination of different erroneous or imprecise values. This observation led us to re-measure the drop solution enthalpy of UZr_2 in liquid aluminum which, combined with those of uranium and zirconium, gives a more exothermic value (-11.9 ± 6.7 $kJ.mol^{-1}.at^{-1}$). At this stage, this new experimental value must be confirmed by additional SEM examinations of the aluminum ingots obtained at the end of the calorimetric experiments to verify the complete dissolution of UZr_2. The consistency of this new value with other experimental data available on the system has also to be checked. In parallel, the heat capacity of this phase should be measured between a few K and 298.15 K to estimate its formation entropy at 298.15 K and deduce a reliable value of its formation Gibbs energy for a future CALPHAD reassessment of the system.
- The standard enthalpy of formation of Fe_2Zr has also been determined by dissolution calorimetry for the first time. The obtained value (-32.2 ± 3.3 $kJ.mol^{-1}.at^{-1}$) is in agreement with the DFT values and those retained in CALPHAD assessments. Despite the importance of this system, as far as we know, there are no experimental thermodynamic data for other compounds in this system. A first perspective would therefore be to extend the determination of the enthalpy of formation to these compounds.

All the data obtained in this work, as well as those obtained during the previous theses of Decreton [1] and Gajavalli [2], will be introduced into the thermodynamic modeling of the NUCLEA database currently developed at IRSN with the support of the SIMAP laboratory. This database is now used through the ASTEC code, in severe accident simulations aimed at evaluating the consequences of an accident scenario.

References

1. Decreton A. Contribution Expérimentale à l'Etude Thermodynamique des Systèmes Ag-Zr et Ag-Cd-In. PhD Thesis, Aix Marseille University, (2016).
2. Gajavalli J., Experimental Contribution to Thermodynamics of the Ag-Cd-In, In-Zr and In_2O_3-ZrO_2 Systems. PhD Thesis, Aix Marseille University (2019).
3. Benigni P., Hassam S., Decreton A., Mikaelian G., Gajavalli K., Barrachin M., Fischer E., Rogez J., Enthalpy of Mixing in the Ag-Cd-In Ternary Liquid Phase. J. Chem. Thermodyn.107: 207-15 (2017).
4. Fischer E., Gajavalli K., Mikaelian G., Benigni P., Rogez J., Decreton A., Barrachin M., Experimental Study and Thermodynamic Modelling of the Ag-Cd-In System. Calphad 64: 292-305 (2019).
5. Hsiao H-M., Liang S-M, Rainer S-F., Yen Y., Thermodynamic Assessment of the Ag-Zr and Cu-Zr Binary Systems. CALPHAD. 55(2): 77-87 (2016).
6. Jin C., Hu B., Zeng G., Xie J., Sheng S., Liu S., Hu J., Experimental investigation and CALPHAD modeling of phase equilibria of the Cu–Ag–Zr system. Calphad 79: 102487 (2022).
7. Betterton J.O., Noyce W.K. The Equilibrium Diagram of Indium-Zirconium in the Region 0-26 At. Pct In. Trans. Metall. Soc. AIME. 212 (6): 340–342 (1958).
8. Meschel S.V., Kleppa O.J., Standard Enthalpies of Formation of Some Transition Metal Indium Compounds by High Temperature Direct Synthesis Calorimetry. J Alloys Compd. 333:91–98 (2002).
9. Barrachin M., Gajavalli K., Decreton A., Virot F., Bénigni P., Rogez J., Mikaelian G., Fischer E., Lomello-Tafin M., Antion C., Janghorban A., Critical Evaluation of Experimental Data of Solution Enthalpy of Zirconium in Liquid Aluminum. J. Chem. Thermodyn. 128: 295–304 (2019).
10. Colinet C. "Private communication (2019)".
11. Dieva E.N., Solubility of Metals of the Fifth and Sixth Periods in Liquid Indium: Physicochemical Studies of Liquid Metals and Alloys, V.G. Bamburov, Ed., Izd. Ural'sk. Nauch. Tsentra Akad. Nauk SSSR, Sverdlovsk. 105–110 in Russian (1974).
12. Okamoto H., The Indium-Zirconium System. Bull. Alloy Phase Diag. 11(2):150–152 (1990).
13. Fitzner K., Kleppa O.J., James F., Thermochemistry of Binary Alloys of Transition Metals: the Me-Titanium, Me-Zirconium and Me-Hafnium (Me = silver, gold) Systems. Metall Trans A. 23(3): 997-1003 (1992).
14. Fischer E., NUCLEA Thermodynamic Database for Corium; Institut de Radioprotection et Sûreté Nucléaire: St Paul lez Durance, France, 2022.
15. Gulay L.D., Zaremba V.I., Stepien-Damm J., Kalychak. Y.M., Interactions between the Components in the Zr-Ag-In System at 870 K. Polish J. Chem. 72: 1886–1889 (1998).
16. Nagarajan K., Babu R., Mathews C., Enthalpy of Formation of UZr2 by Calorimetry. J. Nucl. Mater. 203: 221–223 (1993).

Table of figures

Figure 1. Schematic representation of a PWR reactor [7]. 24

Figure 2. The nuclear fuel assembly with the rod cluster control assembly [8]. 25

Figure 3. Structure of an SIC absorber rod in a 900 MWe reactor [9]. 27

Figure 4. Reactor core degradation phenomena in relation to temperature [1]. 31

Figure 5. Main physical phenomena during a severe accident [17]. 31

Figure 6. Schematic representation of the degradation of the control rod in a severe accident scenario in case of low pressure primary circuit. (a) Control rod in nominal conditions, (b) Rise of internal pressure in the rod following the loss of cooling and progressive swelling of the stainless steel (SS) sheath, (c) SS sheath and Zry-4 guide tube rupture, and (d) relocation and vaporization of absorber materials. [4]. 32

Figure 7. Lower head geometry—stratification and interface heat exchange fluxes 34

Figure 8. (a) Powder pellet pressing die set for 5 mm diameter cylindrical sample. (b) Samples wrapped in Ta foils and sealed in a quartz ampoule under inert atmosphere, ready for subsequent annealing (c) Powder pellet pressing die set for 3 mm diameter cylindrical sample. 39

Figure 9. Glove box of the SYMME laboratory. 41

Figure 10. Arc melting furnace of the SYMME laboratory. 42

Figure 11. Comparison of XRD spectra of (a) pure powdered indium with XRD spectra of In by Faita et al. [2] and In_2O_3 by Marezio [3] and (b) pure powdered zirconium with Zr spectra of Lichter [4] and ZrO_2 by Smith and Newkirk [5]. The XRD pattern belongs to indium and zirconium, with no trace of the oxide peaks. All spectra were taken with Co K-α radiation at room temperature. 44

Figure 12. Mounting of samples using cold resin. 45

Figure 13. Graphical construction for determination of melting temperatures by the extrapolation method (T_T^{extrap}) or first deviation from baseline method (T_T^{Onset}) [2]. 47

Figure 14. (a) SETARAM TGA92 DTA instrument equipped with (b) type B sensor and tantalum crucible and (c) type S sensor and unsealed alumina crucibles (d) Setaram DSC 111 having 3-D Tian-Calvet sensors. 48

Figure 15. Onset temperature determination on DTA curve for temperature calibration performed with pure indium under purified argon (10°C/ min). It is shown that the temperature measured by the extrapolation method (T_T^{extrap} = 157.09°C) has a higher deviation from the true melting point (156.59 °C) than the temperature measured by first deviation from baseline method (T_T^{Onset} = 156.30 °C). Green arrow: extrapolated onset temperature (T_T^{extrap}). Red arrow: first deviation from baseline (T_T^{Onset}). 49

Figure 16. High temperature Tian-Calvet calorimeter. 51

Figure 17. Zr-rich region of the In-Zr diagram by Betterton and Noyce [7]. 58

Figure 18. In-Zr phase diagram according to Okamoto [2]. 59

Figure 19. XRD diffraction spectra of In metal and Zr/In = 1/2 alloy in the as-cast state and after annealing 24 h at 1200K [5]. 60

Figure 20. Calculated In-Zr phase diagram from NUCLEA [6]. 63

Figure 21. Comparison of standard formation enthalpies of In-Zr compounds at 298 K from CALPHAD assessment [6] with DFT values calculated at 0 K [22 - 24]. 65

Figure 22. Comparison of standard formation enthalpies calculated by DFT by Colinet at 0 K [25] with Meschel and Kleppa calorimetric value at 298 K [20]. 66

Figure 23. The revised In–Zr phase diagram. Temperatures in black were measured in this work, whilst the temperature in red was determined by Betterton and Noyce [7]. 67

Figure 24. XRD patterns of the 25.53 at.%Zr and 25.19 at.%Zr annealed at 400°C for 2 months and 800 °C for 1 week respectively compared with the XRD pattern of In_2Zr [4], In_3Zr [10] and In [27]. The In_3Zr compound is not detected in the ≈ 25 at.%Zr alloy annealed at 800°C (red diffractogram) but clearly detected (green arrows) when a similar composition is annealed at 400°C. Extra peaks indicated by black arrows are platinum peaks coming from the sample holder. 70

Figure 25. BSE image of (a) 27.79 at.%Zr sample annealed at 400°C for 1 month and (b) 27.65 at.%Zr sample annealed at 1000°C for 24 hours. In_3Zr phase is not detected in the ≈ 28 at.%Zr alloy annealed at 1000 °C (a) but is observed when a similar composition is annealed at 400 °C (b). The black part are holes in the samples. 71

Figure 26. Comparison of XRD patterns of the 35.02 at.%Zr and 39.99 at.%Zr alloys annealed at 600°C for 2 months with the XRD pattern of In_2Zr [4] and InZr [9]. Orange and brown arrows are the oxide peaks. The blue arrows indicate In_2Zr peaks detected in the ≈ 35at.%Zr alloy (black XRD pattern) which decrease in intensity or disappear in the ≈ 40 at.%Zr alloy (red XRD pattern). Extra peaks indicated by black arrow are platinum peaks coming from the sample holder. (b) A zoom into the angle region around the 47° peak (green arrow) of InZr. 72

Figure 27. BSE images of the 66 at.%Zr alloy annealed 2 months at 600°C revealing the formation of InZr, $InZr_2$, and “eutectoid” microstructure. 73

Figure 28. Experimental powder XRD pattern of the 75.38 at.%Zr and 80.92 at.%Zr samples annealed 24 h at 1000°C compared with diffraction patterns of $InZr_3$ [10] and αZr [26]. Black arrows mark the positions of the platinum peaks coming from the sample holder. 74

Figure 29. BSE image showing the 2-phase microstructure of (a) the 75.38 at.%Zr and (b) the 80.92 at.%Zr alloys, both annealed 24 h at 1000°C. The grey matrix phase has a composition of 73.9 - 75.5 at.%Zr, and the dark phase has a 89.7 at.%Zr composition in agreement with the solubility of In in αZr determined by Betterton and Noyce [7] at similar temperature. 74

Figure 30. DTA curves showing the onset temperatures measured for 4 binary In-Zr alloys at a rate of 5°C/min under purified Ar. (a) the invariant reaction corresponding to the In-rich solid solution is observed at 156.8 ± 0.4°C, the peritectic decompositions of In_3Zr, In_2Zr and In_3Zr_2 are detected around 591.6 ± 2.4 °C, 1132.9 ± 1.8 °C and 1279 ± 6 °C respectively. The arrows indicate where the characteristic temperatures were taken. (b) Cooling curves. The oscillations in the curves are due to electrical noise from the furnace power control. 76

Figure 31. Tammann analysis performed on the peritectic plateau at (a) 591.6 °C shows that the extrapolation of the data sets the limits of the plateau at approximately 1.0 ± 0.1

at.% Zr for the In-rich liquid on one side and at 33 at%Zr = In_2Zr composition on the other side (b) 1132.9 °C, linear extrapolation of the measured heat effects sets the In-rich liquid composition at 3.7 ± 1.7 at%Zr. 77

Figure 32. Low temperature range DTA curves showing the invariant temperatures measured for the 25.53 at.%Zr alloy at various heating rates under purified argon. At 155.6 ± 2.5°C, the invariant reaction corresponding to the In-rich solid solution is observed and the peritectic decompositions of In_3Zr are detected around 593.5 ± 1.8 °C. Additional peaks observed in some of the runs (R2, R3, R4) are as a result of incomplete peritectic reaction during prior cooling. 78

Figure 33. DTA curve for indium rich samples showing a peritectic invariant at 156.8 ± 0.3 °C. 79

Figure 34. Bi-differential thermal analysis of indium rich samples versus pure indium on heating at 5°C /min. An endothermic effect on the sample side gives a downward deflection from the baseline. An endothermic effect on the reference side gives an upward deflection. (a) Alloy samples placed in the sample cell whilst pure indium is in the reference cell. (b) 0.9 at.% Zr alloy sample in the reference cell whilst pure indium is placed in the sample cell. 80

Figure 35. Tammann analysis performed on peritectic plateau at 156.8 ± 0.3 °C. The extrapolation of the data sets the limit of the plateau at approximately 25 ± 3.8 at.%Zr. 81

Figure 36. SEM observation of post DTA samples; (a) 20.13 at.%Zr (b) 27.00 at.%Zr and (c) 40.03 at%Zr. The dark matrix phase has compositions close to In_3Zr_2 and the grey matrix is In_2Zr phase. The white particles on the grains are indium. 82

Figure 37. XRD evidencing the formation of single phase (a) In_3Zr in 25.53 at%Zr annealed 2 months at 400°C and (b) In_2Zr in 33.52 at%Zr annealed 48 h at 600°C. 83

Figure 38. Measured thermal effects associated to the drop of In_3Zr in liquid Al, QIn3Zr, vs the number of moles. The blue points indicate the values measured for complete dissolution (values in bold in Table 13) while the orange is for partial dissolution (values in italics in Table 13). 86

Figure 39. Drop solution enthalpy measurements of In_2Zr in liquid Al at 1173 K. 88

Figure 40. SEM observation of (a) Upper (b) Middle and (c) bottom region of the In_3Zr ingot. White crystals are indium and the light grey phase is the aluminum matrix. 90

Figure 41. SEM observation of (a) Upper (b) Middle and (c) bottom regions of the In_2Zr ingot. Indium is observed in the form of intergranular white crystals in all regions. Few white needles of Al_3Zr are found at the bottom of the ingot. 91

Figure 42. Diffractogram of 39.99 at.%Zr sample annealed at 600°C for 2 months compared with XRD spectra of Ga_3Ti_2 (prototype for In_3Zr_2) by Poetzschke et al. [31], InZr by Schubert et al. [10] and In_2Zr by Zumdick et al. [4]. Red arrows indicate the position of the reference In_3Zr_2 peaks that are not found in the spectra of 39.99 at.%Zr (black XRD pattern). The Extra peaks indicated by orange arrows are ZrO_2, brown arrows are In_2O_3 and black arrows are platinum peaks. 94

Figure 43. BSE image of arc-melted as cast 53.89 at%Zr sample showing almost single InZr phase. 95

Figure 44. Micrograph of 54.34 at.%Zr sample after DTA sample showing divorced eutectic between InZr and $InZr_2$. Light grey matrix phase has InZr composition whiles the dark grey rod-like phase is $InZr_2$. The black particles are oxides. 95

Figure 45. BSE image of the as cast 76.09 at.%Zr sample showing single $InZr_3$ phase. The lines in the micrograph come from polishing. 96

Figure 46. Micrograph of lamellar, eutectoid-like, microstructure in the 81.53 at.%Zr alloy after DTA. Exact compositions of the different contrasts could not be determined due to the small interlamellar spacing. 97

Figure 47. Comparison of standard formation enthalpies calculated by DFT by Colinet at 0 K [25] with the values measured by liquid Al solution calorimetry in this work for In_3Zr and In_2Zr. 99

Figure 48. Fe–Zr phase diagram presented by Stein et al. [29]. 107

Figure 49. Calculated Ag-Zr diagram with superimposed experimental points of 54, 56-58 and 64. 110

Figure 50. Diffractogram evidencing the formation of single phase Fe_2Zr. Comparison of the obtained XRD spectra (black curve) with spectra of Fe_2Zr by Israel et al. [71] (red), Fe by Basinski et al. [72] (blue) and αZr by Litcher [73] (green). All spectra for were taken with Cu Kα radiation at room temperature. 113

Figure 51. Partial drop solution enthalpy of Fe_2Zr, $\Delta dsHFe2Zr, 298K1173K$, in liquid Al between 298 and 1173 K as a function of Fe_2Zr mole fraction. 115

Figure 52. Partial mixing enthalpy of Fe at infinite dilution in liquid Al plotted vs. temperature. Reference state: both elements at the liquid state at the considered temperature. The dashed straight line is a regression line through all the data, after discarding the results of Lee et al.[13] and Antony et al. [15]. 117

Figure 53. XRD evidencing the phases formed after annealing synthesized AgZr sample. Comparison of the obtained XRD spectra (black curve) with XRD spectra of AgZr by Karlsson [59] (red), $AgZr_2$ by Zhang et al. [58] (blue), Ag by Owen and Yates [74] (green), αZr by Litcher [73] (purple) and ZrO_2 by Smith et al. [75] (gold). All spectra were taken with Co Kα radiation at room temperature. 118

Figure 54. Partial drop solution enthalpy of AgZr, $\Delta dsHAgZr, 298\ K1173\ K$,in liquid Al between 298 and 1173 K as a function of AgZr mole fraction. 119

Figure 55. SEM observation of (a) upper (b) middle and (c) bottom of Run 1 of Fe_2Zr ingot. 121

Figure 56. SEM observation of (a) upper (b) middle and (c) bottom of Run 3 of Fe_2Zr ingot. 122

Figure 57. SEM observation of ingot for Run 1 of AgZr (a) the region near the bottom of the ingot at low magnification showing both (b) needlelike shape Al_3Zr particles and interdendritic Al_3Zr and (c) clusters of Al_3Zr primary precipitates in pure Al matrix. 124

Figure 58. SEM observation of (a) the AgZr ingot (for Run 3) showing the (b) interdendritic Al_3Zr particles and (c) needlelike shape Al_3Zr in the lower region. Large clusters of Al_3Zr were not found. 125

Figure 59. U–Zr phase diagram presented by Sheldon and Peterson [10]. 138

Figure 60. Partial mixing enthalpy of U plotted vs. U mole fraction in liquid Al at various temperatures. Reference state: both elements at the liquid state at the considered temperature. The dashed and dash-dotted lines are linear regressions to the data points of Dannöhl and Lukas (1023 K) and Labroche et al. (988 K) respectively. The corresponding regression equations are superimposed on the graph. The Dannöhl and Lukas data points plotted using empty diamonds exceed the solubility limit at 1023 K and were not considered for linear regression. 145

Figure 61. Partial mixing enthalpy of U at infinite dilution in liquid Al plotted vs. temperature U mole fraction in liquid Al. Reference state: both elements at the liquid state at the considered temperature. The constant values that can be calculated from the optimized coefficients of the CALPHAD assessments of Kassner et al. [47] and Wang et al. [46] are plotted as horizontal dashed and solid lines respectively. 147

Figure 62 . Calculated evolutions of the dissolved fraction of the first dropped uranium sample in the experimental conditions of Nagarajan et al. [42], Colinet et al. [41] and Labroche et al. [43]. 149

Figure 63. (a) Al-rich corner of the 991 K isothermal section of the Al-U-Zr phase diagram as modelled by Rabin et al. [44]. (b) Enlarged view at low Zr content. 151

Figure 64. (a) SEM observation of UZr2.46 sample and (b)Refinement plot with the UHg_2 type of structure of the X-ray pattern of the $UZr_{2.46}$ sample annealed at 580°C for 2h. 153

Figure 65. Partial drop solution enthalpy of $UZr_{2.46}$, $\Delta \mathrm{dsHUZr2.46,298K1173K}$, in liquid Al between 298 and 1173 K as a function of $UZr_{2.46}$ mole fraction. 155

Figure 66. U-Zr phase diagram from a) the NUCLEA Database [46] and with two amended thermodynamic description of the δ-phase (b and c). Values of the thermodynamic quantities for the δ-phase are given at the stoichiometric UZr_2 composition. 159

Figure 67. Heat capacity of UZr_2 vs. temperature. Scatter symbols are experimental points: (▽) from [62], (○) from [63], (✕) from [52]. The red solid line is calculated with the parameter values of Table 35. The black solid line is calculated with the Neumann-Kopp additivity Rule (NKR) for the UZr_2 stoichiometric composition using the SGTE data [40] of pure U and Zr. 162

Figure 68. Thermograph for UZr2 dissolution in liquid Al (Run 1). 163